Mechatronic Design of a Magnetically Suspended Rotating Platform

Leon Jabben

Mechatronic Design of a Magnetically Suspended Rotating Platform

PROEFSCHRIFT

ter verkrijging van de graad van doctor
aan de Technische Universiteit Delft,
op gezag van de Rector Magnificus prof. dr. ir. J.T. Fokkema,
voorzitter van het College voor Promoties,
in het openbaar te verdedigen op

maandag 10 december 2007 om 10:00 uur

door

Leon JABBEN

werktuigkundig ingenieur
geboren te De Lier.

Dit proefschrift is goedgekeurd door de promotoren:
prof. dr. ir. J. van Eijk
prof. ir. O.H. Bosgra

Samenstelling promotiecommissie:

Rector Magnificus	voorzitter
prof. dr. ir. J. van Eijk	Technische Universiteit Delft, promotor
prof. ir. O.H. Bosgra	Technische Universiteit Delft, promotor
prof. Ph.D. M.S. D.L. Trumper	Massachusetts Institute of Technology
prof. dr. ir. H. van Brussel	Katholieke Universiteit Leuven
prof. ir. H.M.J.R. Soemers	Universiteit Twente
prof. dr. ir. P.M.J. van den Hof	Technische Universiteit Delft
ir. P.C.P. du Pau	OTB Group B.V.

This research was supported by IOP

ISBN 978-90-9022523-4

Printed in The Netherlands

To my parents

Voorwoord

Zo, dan is het na zeven jaar tijd om het leukste stuk van het proefschrift te schrijven. Ondertussen weet ik bijna niet meer hoe het is om zonder schuldgevoel op zaterdag avond een biertje te drinken en ik kan me ook niet meer voorstellen hoe het is om een héél weekend gewoon vrij te hebben. Maar ik weet wel dat ik daar enorm veel zin in heb (dat biertje ook trouwens)!

Iedere promotie kent wel z'n ups en downs, maar ik moet eerlijk bekennen dat ik de downs toch wel erg laag bij de grond vond. Ik ben dan ook bijzonder trots dat ik het toch heb afgerond en u dit stukje leest. Echter zonder de steun van vele mensen had ik het niet gekund, dus dit is mooi moment om iedereen te bedanken.

Om te beginnen wil ik Jan, mijn promotor, bedanken. Jouw scherpe inzichten in het systeem-ontwerpen hebben mij bijzonder geïnspireerd en ik heb genoten van onze discussies. Ook dank voor je steun in moeilijke perioden van het traject.

In de eerste jaren begreep ik maar half waar Okko in zijn gesprekken op doelde. Later werd me duidelijk dat jij er altijd naar streefde het geheel van een nog hoger niveau te bekijken. Ik heb deze gesprekken (vooral later) dan ook erg gewaardeerd.

De dag dat ik begon, moest ik mijn buro nog in elkaar zetten. Inderdaad, de vakgroep was net aan een herstart begonnen en de toko werd in die tijd praktisch door Jo en Frans gedragen. Jo bedankt voor alle morele en practische steun over de jaren. Frans "Dag, Pik", ik denk nog regelmatig aan je.

Dit onderzoek werd gefinancierd door IOP/Senter (bedankt Casper voor de prettige samenwerking). Deze instelling heeft als voorwaarde dat een gebruikerscommissie ieder half jaar op de hoogte wordt gehouden van het onderzoek. Deze meetings waren altijd erg waardevol, vooral vanwege de vele tips van mannen met onschatbare praktische ervaring. Henk, Erik, Lex, Pieter, Ed, Henk, Richard, Huub, Frank, Jos, Eddy, Lou en vooral Peter, bedankt voor het meedenken! Verder heb ik een behoorlijk aantal student mogen begeleiden in hun afstuderen. Chepa, Jeffrey, Daan, Wim, Wouter, Frederik en Stijn bedankt voor al jullie bijdragen. Ik heb ontzettend veel van jullie geleerd. De magnetisch gelagerde rotor was een team effort met Peter en Hussein. Hoewel promoveren met "team effort" bijna een contradictio in terminus is, hebben we het toch best goed gedaan. Ook Kees en

Ad, die veel aan de practische realizatie hebben bijgedragen, waren deel van het team. Verder wil ik bij AM nog de volgende mensen bedanken voor het lachen: Peter, Hussein, Warner, Dick, Sander, Jeroen, Marc, Dipali, Maarten, Hans en vele studenten.

Om mijn kunsten op control gebied op niveau te krijgen, heb ik ook anderhalf jaar bij de jongens van Systeem en Regeltechniek (tegenwoordig DCSC) gezeten. Dit was een behoorlijk hechte groep, maar ik werd meteen opgenomen. Rob, Tinus, David, Eduard, Branko, Dennis, Camile, Gideon, Martijn, Matthijs en Maria bedankt hiervoor! Ook wil ik Ton, Piet, Debby, Agnes, Sjoerd, Carsten en Peter bedanken voor de koffietafel gesprekken.

Gedurende mijn promotie heb ik een paar maanden van zonnig Californië mogen genieten. Bedankt Angelo, Ton, Joe en James voor de prettige samenwerking vooraf en tijdens deze periode.

Voor het doorlezen van verschillende stukken van het proefschrift ben ik Rob, Ad en Mishka dank verschuldigd. (Uiteraard blijf ik natuurlijk volledig aansprakelijk voor de typo's en andere fouten!)

Zonder vele vrienden en familie was ik nooit door de moeilijke perioden gekomen. Dit boekje is dus ook van jullie! Mijn ouders hebben me altijd geheel vrij gelaten in mijn keuzes en me in mijn eenmaal gemaakte keuzes altijd gesteund. Van het MAVO advies dat ik ooit kreeg en waar ik het niet mee eens was, tot en met deze promotie. Ik draag mijn proefschrift dan ook aan jullie op. En bedankt Sanneke. Je stond te vaak op de tweede plaats de afgelopen tijd, maar ik ben blij dat je nu weer op één staat!

Contents

Nomenclature

Symbols

Symbol	*Description*	*Unit*
c	velocity of sound in air $\approx 20.05\sqrt{T}$	$\mathrm{m/s}$
d	damping	$\mathrm{Ns/m}$
e_m	magnetic energy density	$\mathrm{J/m^3}$
f	frequency or force input of plant	Hz, N
f_{bw}	bandwidth, zero-dB crossing of $\lvert L(s)\rvert$	Hz
f_N	Nyquist frequency	Hz
f_r	reference force input to NLC	N
f_{rta}	force generated by an RTA	N
f_u	output of controller	N
i	current	A
i_r	current set-point to amplifier	A
i_b	bias current	A
j	imaginary unit, $j := \sqrt{-1}$	
k	stiffness	$\mathrm{N/m}$
k_p	gain of controller	
k_{rta}	RTA constant	$\mathrm{Nm^2/A^2}$
k_x	stiffness introduced by a RTA	$\mathrm{N/m}$
m	mass, or moment	kg,Nm
m_r	mass of the rotor	kg
n_c	number of coil windings	
p	air pressure	$\mathrm{N/m^2}$
q	quantization interval	
s	Laplace variable	
t	time	s
u	controller output	
x_g	air gap in RTA	mm

continued on next page...

... continued from previous page

Symbol	*Description*	*Unit*
x_n	nominal air gap in RTA	mm
x^r	position of rotor at CoG	
y_m	measured variables for feedback	
v	velocity	m/s
w	stacked physical disturbances	
$\overline{w}$	stacked normalized disturbances	
z	stacked performance variables	
$\overline{z}$	stacked normalized performance variables	
$A, B,$		
C, D	state space matrices	
$\vec{B}, B$	magnetic flux density	T
C_x	CAS of signal x	[x]
C_R	noise index	μV/V
D	damping matrix	
E_m	magnetic energy	J
$\vec{H}, H$	magnetic field intensity	A/m
$I^{n\times n}$	identity matrix of size n	
$0^{n\times m}$	zero matrix with n-rows and m-columns	
J	inertia	kgm^2
$\vec{J}$	current density	A/m^2
K	controller	
K	stiffness matrix	
K_d	differentiating part of the controller	
K_i	integrating part of the controller	
K_{ro}	roll-off part of the controller	
L	loop gain	
L_i	sound intensity level	W/m^2
L_p	sound pressure level	N/m^2
$\vec{M}, M$	magnetic susceptibility	A/m
M	mass matrix	
M_r	diagonal mass and inertia matrix of the rotor	
P	plant	
R	resistance	Ω
R_{xx}	autocorrelation of signal x	
S	sensitivity $(I+L)^{-1}$	
$S_x(f)$	power spectral density of signal x	
S_x^+	single sided power spectral density of signal x	

continued on next page...

... continued from previous page

Symbol	*Description*	*Unit*
T	complementary sensitivity $L(I+L)^{-1}$	
	temperature	K
V_x	weighting transfer function for disturbance x	
W_x	weighting transfer function for signal x	
Z	(complex) impedance	
$\mathcal{R}$	magnetic resistance	$\mathrm{A/T/m^2}$

Greek Symbols

Symbol	*Description*	*Unit*
α	auxiliary gain to obtain Pareto curve	
α_i	coefficient in integrator lag-lead filter	-
α_d	coefficient in differentiator lead-lag filter	-
χ	state space vector	
γ	confidence coefficient	
μ_r	relative permeability	
μ_x	relative permeability of material x	
σ_x	variance of x	$\mathrm{si^2}$
ω	frequency	rad/s
ω_i	end of integration action frequency	rad/s
ω_{bw}	bandwidth, zero-dB crossing of $\lvert L(s)\rvert$	rad/s
ω_{ro}	roll-off frequency	rad/s
ξ	stochastic variable	
ρ_a	density of air	$\mathrm{kg/m^3}$
ζ	relative damping	-
Λ	relative gain array	-
Φ	magnetic flux	$\mathrm{Tm^2}$
Ω	rotation velocity of the rotor	rad/s

Constants

Constant	*Description*	*Value*	*Unit*
e	Napier's constant	2.718282	-
g	standard acceleration of free fall	9.80665	$\mathrm{m/s^2}$
k	Boltzmann's constant	$1.38{\cdot}10^{-23}$	J/K
q_e	electronic charge	$1.602{\cdot}10^{-19}$	C
μ_0	permeability of vacuum	$4\pi \cdot 10^{-7}$	$\mathrm{H/m{=}N/A^2}$

Mathematical Operators and Symbols

Operator	*Description*
$\times$	element by element multiplication
$:=$	defined as
$\propto$	proportional with
$\in$	belong to
$\forall x$	for all x
$\vec{x}$	vector x
$\dfrac{\partial}{\partial x}$	partial derivative with respect to x
∇	nabla operator: $\nabla = \left[\dfrac{\partial}{\partial x}\ \dfrac{\partial}{\partial y}\ \dfrac{\partial}{\partial z}\right]^{\mathrm{T}}$
$\dot{x}$	time derivative of x: $\dot{x} = \dfrac{\mathrm{d}x}{\mathrm{d}t}$
$\overline{x}$	average of x
$\|x\|_{\mathrm{rms}}$	RMS semi-norm of x
A^{T}	transpose of A
A^*	complex conjugate transpose of A
$\mathrm{diag}\,(\vec{a})$	matrix with $\vec{a}$ as diagonal
$\mathrm{Tr}\,(A)$	trace of A, i.e. the sum of its diagonal terms
$\mathrm{Re}\,Z$	real part of Z
$\mathrm{Im}\,Z$	imaginary part of Z
E	expectation operator
$\mathrm{Prob}\,(x)$	probability of x being true
$\|G\|_2$	$\mathcal{H}_2$ system norm of G

Abbreviations and Acronyms

Abbreviation	*Description*
AC	alternating current
ADC	analogue to digital converter
AMB	active magnetic bearing
AREM	asynchronous radial error motion
BD	blu-ray disk
CAS	cumulative amplitude spectrum
CD	compact disk
CoG	centre of gravity
CPS	cumulative power spectrum
CSR	current slew rate
DAC	digital to analogue converter
DC	direct current, engineering term for steady state
DVD	digital versatile disc
DEB	dynamic error budgeting
DoF	degree of freedom
DSP	digital signal processor
EUV	extreme ultra violet
FEM	finite element model
FF	force frame
FFT	fast fourier transform
FRD	frequency response data
FSR	force slew rate
GC	gravity compensator
LSB	least significant bit
LTI	linear time invariant
LRTA	linearized reluctance type actuator
IC	integrated circuit
MEMS	micro electro-mechanical system
MF	metrology frame
MIMO	multi input, multi output
MOSFET	metal oxide silicon field effect transistor
NLC	nonlinear compensation/compensator
NL	non-linear(ity)
OD	optical disk
PAI	principal axis of inertia
PC	personal computer

continued on next page...

... continued from previous page

Abbreviation	*Description*
PDF	probability density function
P(I)D	proportional, (integral,) differential
PSD	power spectral density
PUH	pick up head
PtV	peak-to-valley
RMS	root mean square
RGA	relative gain array
RTA	reluctance type actuator
SISO	single input, single output
SNR	signal-to-noise ratio
SREM	synchronous radial error motion
STD	standard deviation
SVD	singular value decomposition
THD	total harmonic distortion
TPV	track pitch variation
TREM	total radial error motion

1 Introduction

The mastering process of an optical disk is a good example of a high precision process of which ever increasing performance is desired due to the demands from a modern society which is craving for information. A promising potential technology to increase the performance of optical disk mastering is the use of magnetic bearings. In this thesis the design of a magnetically levitated platform is described. The design aims to fulfill the specifications of modern optical disk mastering. This introductory chapter starts with an explanation of the driving force for continuous performance increase in some high precision processes, in particular optical disk mastering. After discussing magnetic bearing technology, this chapter elaborates on the mechatronic design approach. The chapter ends with the problem statement and an outline of the thesis.

1.1 High Precision Processes

Modern society is becoming more and more an society craving for information. This is best illustrated by the exponential growth of the world wide web in the last ten years. The handling of the huge amounts of data generated by modern society drives the need to rapidly increase the capability for processing, storing and viewing this data.

To fulfill the demand for ever increasing processing power requires ever more precise production processes. This becomes apparent in the production of Integrated Circuits (ICs), where the motion stages in lithography machines are positioned within nanometre accuracy. Another example is bonding machines. In a bonding machine an IC is connected to the pins of its package with gold wires

which have a diameter of less than 30 microns. Since throughput is of major importance in the IC industry, the challenge with these processes is to achieve the desired position accuracy at very high speeds.

The demand for increasing data storage capacity, drives the technology to increase the data density on hard disks and optical disks (such as the CD and DVD). The data density is increased by shrinking the area of the smallest information unit (bit). Reading out these bits requires mechanisms which position the read head with a precision better than the dimensions of the bit, while the information layer makes relatively large movements at high rotation speeds.

Lastly, the need to view the data with higher resolution and more consumer comfort, drives the demand for flat panel displays, such as Liquid Crystal Displays (LCDs), and new panels based on Organic Light Emitting Diodes (OLEDs) and Polymer Light Emitting Diodes (PLEDs). Price efficient production of large displays with small dots involves mechanical processes with high precision.

This thesis focusses on a particular step in the production process of Optical Disks (ODs), namely OD-mastering. Because of the shrinking of the bit area on the OD, this production step is becoming more and more challenging.

1.2 Optical Disk Mastering

1.2.1 About the Optical Disk

An optical disk is composed of polycarbonate and made reflective with a thin metal layer (usually aluminium). An example of an OD is the well-known Compact Disk (CD), standardized by Philips and Sony in 1981. An OD holds the information in a long spiral of pits written into the metal layer. The area between the pits is termed "land" and the edges of the pits correspond to binary ones, see [17].

After the CD, the DVD was introduced in 1995 and in 2002 the Blu-Ray Disk (BD) was added to the OD family. In 2004 the High Definition DVD (HD-DVD) was introduced, competing with the Blu-Ray standard[1]. Some of the parameters for the different families of optical disks is given in Table 1.1. The increase of data storage capacity for each member is strikingly illustrated in Figure 1.1, showing the relative pit sizes and track pitch for the CD, DVD and BD. Although ODs can have different sizes, they usually come with a diameter of 120 mm.

One reason for the huge success of the optical disks, with respect to pre-existing and alternative forms of data storage and reproduction, has been the possibility of storing relatively large amount of information on a small, light and easy

[1] Although the storage capacity of the HD-DVD is less than the BD, its main advantage is that it requires much less investments of the OD industry. Much of the DVD infrastructure can be used for the production, while the BD requires a completely new infrastructure.

Table 1.1. *Indication of the increase of information density on the subsequent optical disk families.*

	year	capacity[a] [GB]	wavelength laser [nm]	minimal pit length [nm]	track pitch [nm]
CD	1981	0.65	780	830	1600
DVD	1995	4.7	650	400	740
BD	2002	27	405	138	320
HD-DVD	2004	15	405	204	400

[a]Capacity of a single layer.

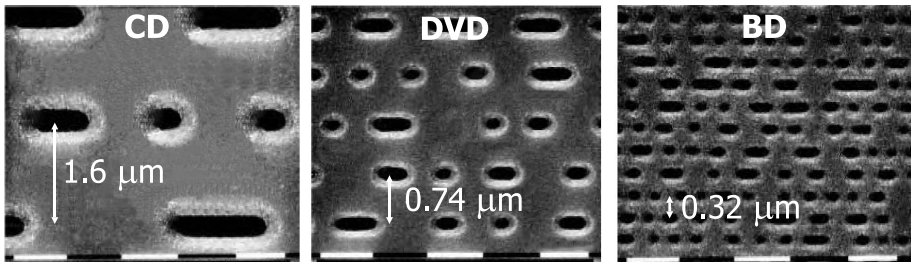

Figure 1.1. *Three photos of the pits on a CD, DVD, and Blu-Ray Disk (BRD), clearly illustrating the increased storage capacity with each generation.*

to handle removable medium. These characteristics are perfect for the exchange and the distribution of large amount of data. Furthermore, the quality of the stored information remains unchanged under playback, large temperature variations and contamination with dust and fingerprints. Another important reason contributing to the success of ODs is that the medium allows cheap mass production of pre-recorded ODs.

1.2.2 The Mastering Process

Optical disks are mass-produced by an injection molding process, in which the polycarbonate is pressed against a stamper. In the fabrication process of the stamper, the *mastering process* is the crucial step.

The fabrication of the stamper begins with a disk made of glass, called the master, which is coated with a photo-resist. Mastering is the process of writing the information pattern into the photo-resist layer. To do this, the master is placed on a rotating platform which is spun with a multiple of the final reading speed of the OD. Simultaneously, a laser spot makes a translating movement above the master and is modulated in an on/off fashion to form a latent image of the spiral

tracks with information. One of the difficulties in this process is to keep the track distance within specification. After this step the photo-resist is developed and by sputtering a metal layer onto the master a stamper is created, see [17].

Note that an OD-rom already contains an empty track. Hence, to write the information onto an OD-rom, the OD-rom writer only has to follow the existing track, instead of writing on a blank disk. This is why an OD mastering machine is a factor thousand to ten thousand more expensive than an OD-rom writer.

1.2.3 The Future of Optical Disks

The dimensions of the pit are limited by the minimal size of the spot the laser light can be focussed to during writing. The minimal spot diameter is given by:

$$d_{\text{focus}} = 0.5\frac{\lambda_{\text{light}}}{\text{NA}} \tag{1.1}$$

in which d_{focus} is the minimal diameter of the focussed spot[2], λ_{light} the wavelength of the laser light and NA the numerical aperture of the optics. The optics of a BD Pick-Up Head (PUH) has an NA of 0.85[3]. Using the information of Table 1.1, it can be seen that the minimal diameter of the spot with the BD is 240 nm, which is bigger than the minimal pit length. With this spot size the pits can be read, but they cannot be written. To write the pits of a Blu-Ray master light with a smaller wavelength must be used, such as ultra-violet light.

For the the follow-up of the Blu-Ray standard this means that, to be able to burn the pits in the glass master, EUV (Extreme (deep) Ultra violet) light or even electron beams must be used. These energy sources require vacuum conditions, which have great consequences for the production.

In current mastering machines, the rotation axes of the spindle which supports the optical disk master is held in place with air bearings. To operate air bearings under vacuum conditions, necessary for EUV or electron beams, special precautions are required which would make them expensive. Furthermore, to fulfill the more tight specifications required to master future ODs, the air bearings must be made more stiff. The stiffness of an air bearing increases if the air gap is reduced, which implies smaller machining tolerances for the bearings, making them even more expensive.

Hence, the optical disk manufacturing industry has a potential interest in an alternative bearing technology. An interesting candidate is active magnetic bearing technology.

[2]The factor 0.5 depends on the photo-resist that is being used.

[3]Increasing this value is quite difficult since the distance between the disk and the optics becomes very small. In some lithography machines the NA is increased by focussing the light into water, which allows values larger than one, see [9].

1.3 Active Magnetic Bearing Technology

In an Active Magnetic Bearing (AMB) the spindle (or a moving part) is held in place with magnetic fields. An AMB works contactless and contamination free, it can work under vacuum conditions and allows high rotation speeds. Examples of the application of AMBs are turbo molecular pumps, turbo blowers, gas compressors and high speed milling spindles. Hence, it is a well developed technology, except that it currently does not achieve the extreme accuracy that is required for OD mastering.

Besides optical disk mastering, there are more applications where AMBs can be an interesting alternative to air bearings. Air bearings always require machining of the bearing surfaces with a very high accuracy, which is not the case with magnetic bearings. Especially in processes which require vacuum operating conditions, AMBs can prove to be more cost effective than air bearings. Examples of such processes are the earlier mentioned motion stages in lithography machines or stages for manipulation of samples in scientific instruments.

A drawback to the above mentioned advantages is that multiple Degrees of Freedom (DoFs) (usually five or six) need to be actively controlled in order to have a stable configuration. The control of these DoFs adds to the complexity of the system. However, this can also turn into an advantage. If the process is measured, actuation of the magnetic fields can be used to compensate the process if it deviates from the ideal set-point, giving direct means to increase the performance. This is discussed in more detail in the next section.

1.4 A Mechatronic Design Approach

1.4.1 High Precision Through Closed Loop Control

To read out data from an OD, the lens that focusses the laser light needs to be controlled in two DoFs. The remaining DoFs are constrained mechanically. One control loop keeps the lens at constant distance to the OD such that the laser spot remains focussed. The other loop controls the radial position of the lens, such that the focussed spot follows the track. Both loops needs to compensate for the relatively very large motions at high rotation speeds of the OD during playing (and writing!). Hence, for OD playing, control is an *enabling* technology, without which the player cannot function.

For many of the processes given as examples in the first section of this chapter feedback control is the enabling technology. With feedback control a relatively high position precision can be obtained with relative inexpensive components or a very high precision is achieved which would simply not be possible otherwise.

1.4.2 Definition of Terms

To get the terminology right, some terms are defined here which are used throughout this thesis. To start with, the term *plant* is defined in the *IEEE Standard Dictionary of Electrical and Electronics Terms*, [49] as:

Definition 1.1 (Plant) *For a given system, the plant is the part which is to be controlled and whose parameters are unalterable.*

This definition of the plant is quite general. To narrow the field the following definition from [83] is given:

Definition 1.2 (Electromechanical Plant) *An electromechanical plant is a physical plant that is electrically actuated, and has mechanical position—or any of its time derivatives—as measured output.*

In which the mechanical position can be vector containing multiple positions and/or orientations. This thesis only deals with electromechanical plants, so whenever the word plant is used, it refers to an electromechanical plant.

The closed loop consisting of the plant and the controller forms another system. The following two definitions define the closed loop system [49]:

Definition 1.3 (Control System) *A control system is a system in which a desired effect (or: objective) is achieved by operating on the various inputs to the plant until the output, which is a measure of the desired effect, falls within an acceptable range of values.*

Definition 1.4 (Closed Loop Control System) *A closed loop control system is a control system in which the controlled quantity is measured and compared with a standard representing the desired performance.* Note: *Any deviation from the standard is fed back into the control system in such a way that it will reduce the deviation of the controlled quantity from the standard.*

In thesis the term feedback system is also used to indicate an closed loop control system.

The fundamental reason that control is an enabling feedback for so many processes is that in real life the process is always disturbed by its environment. In [49] a disturbance is defined as:

Definition 1.5 (Disturbance) *A disturbance is an undesired variable applied to a system that tends to affect adversely the value of a controlled variable.*

The more the performance of a machine depends on feedback, the more the performance is limited by the disturbances acting on the system.

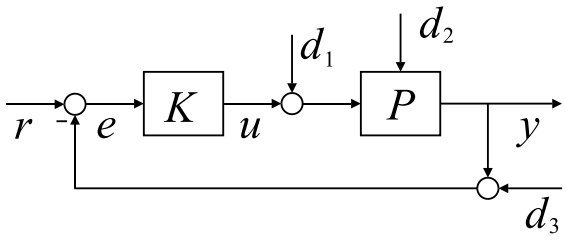

Figure 1.2. *An illustration of a closed loop control system, with the plant denoted by P and the controller with K. The output of the plant y is compared to the reference r and fed back to the controller. To close the loop the calculated corrective action u is applied to the plant. In the control system, various disturbances act on different places of the loop (d).*

No unambiguous definition exists for the term "mechatronic". As a result it is used for a very wide variety of electrical systems. In this thesis the following definition is used:

Definition 1.6 (Mechatronic) *Refers to a closed loop control system with an electromechanical plant.*

1.4.3 System Design

A typical feedback system is sketched in Figure 1.2. The plant P is controlled by the controller K, which calculates the corrective action u by comparing the output feedback y with the desired value (reference) r. In the control system disturbances d act on different places of the loop. Some disturbances act on the input of the plant, some on the measured output signal, while others interact somewhere in the plant. The error e is commonly taken as a performance measure; the smaller the error the better the performance.

A feedback loop consists of many components, such as: sensors to measure the process, electronics to readout the sensors, actuators to make the corrective action, amplifiers to provide the power for the actuators, and a controller to calculate the corrective action required. Furthermore, the properties of the loop are largely determined by the mechanical structure that houses the process and the components.

In the design of the total closed loop control system the design effort must be distributed over all the components. Traditionally, this is done via *error budgeting*, i.e. each component is allowed to contribute only a part of the allowed error, see [89]. At the start of the design, each component is typically allowed to contribute an equal part. During the design iterations, when it turns out that some

components are more critical than others, these components are allowed a larger part of the error budget. This procedure tries to balance the design effort over the components, while optimizing the performance in a minimal of design iterations.

Traditional error budgeting, as described in [89], does not take into account the dynamic behaviour of the closed loop control system and the disturbances. To optimize the system design a frequency dynamic budgeting of the error over the components, would provide increased additional value. This thesis will develop such a budgeting method, which will be denoted as Dynamic Error Budgeting (DEB).

1.4.4 Development Approach

As was explained in Subsection 1.2.3, there is an interest in the optical disk mastering industry to use magnetic bearing technology in future mastering technologies. In a mastering machine there are two critical moving parts that needs accurate bearing. One part is the linear motion of the laser[4] and the other part is the rotation of the platform that holds the glass master. The project consisting of developing the rotating platform started in September 2000 and is funded by IOP[5]. The goal of this project is to develop technology to be used for a magnetically suspended and actuated rotor with six DOFs, which fulfills the anticipated specifications for the mastering of modern optical disks.

The project is multi-disciplinary, each having its own challenges. Here, the project is roughly divided in the following fields:

Control design Actuation using magnetic bearings results in an unstable and non-linear plant and must be linearized and stabilized with feedback,

Mechanical Design Design of the rotor and the frame, of which the internal resonances should be as high as possible, not to limit the bandwidth of the closed loop control system.

Sensor Technology The position of the rotor must be monitored for the feedback. The sensing technology must cope with the specific performance demands measuring on a rotating object.

Rotor Dynamics The rotation of the rotor generates gyroscopic forces, which makes the dynamics of the plant dependent on the rotation speed,

Electromagnetic Design The rotor needs to be magnetically actuated. Especially for the motor design, the challenge is to minimize disturbing elements, while generating a torque to the rotor.

[4] Another project, not described in this thesis, focussed on the design of a linear bearing for the laser.

[5] IOP is the Dutch acronym for Innovatiegerichte OnderzoeksProgramma and is an initiative from the Dutch Ministry of Economic Affairs to stimulate innovation-oriented research.

This thesis has the emphasis on the mechanical and feedback control design of the rotating platform. Another PhD-project dealt with the sensor technology combined with the rotor dynamics, while the electromagnetic design was subject of a postdoctoral research project.

Of course, a successful design cannot be made without taking into account the interaction that exists between the different disciplines. The main contribution of this thesis is the development of a methodology to cope with these interactions such that the design effort is balanced over the disciplines while optimizing the performance.

The final goal of the project is the design of a magnetically suspended rotor that fulfills the anticipated specifications for modern optical disks. The anticipated specifications are such, that it cannot be expected that a machine can be designed and successfully constructed in one iteration. Because of the complexity that is involved, it is simply not feasible to take into account all the disturbing effects that act on the final machine and all the interactions between the components involved. For this reason, a first step will be the design of a prototype.

The prototype described in this thesis has been made operational up to standstill, leaving the rotation for further research.

1.5 Problem Statement

The problem that is addressed in this thesis is summarized as follows:

> Design a magnetically actuated rotating platform with an accuracy that fulfills the anticipated specifications for modern optical disk mastering. Develop a method using systems and control knowledge which balance the design efforts over all the disciplines involved, while optimizing the performance and reducing the design iterations. Validate these methods by building a demonstrator and comparing the realized performance with the predicted performance.

1.6 Outline

In the next chapter a *concept design* for the rotor (spindle) in a new optical disk mastering system will be developed. The first step in arriving at a concept design for such a mechatronic system is to gain insight in the requirements. Since the specifications for Blu-ray mastering are not publicly available, these are derived from DVD specifications. Achieving these specifications is thwarted by disturbances acting on the system. Hence, the second step is to assess the main disturbances which will act on the system. Based on the estimated requirements and disturbances, several fundamental design choices can be made concerning the working principle of the system.

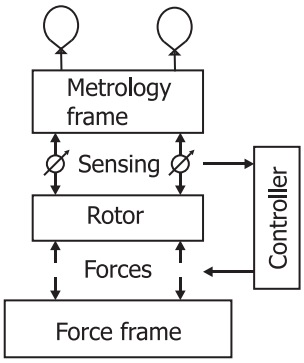

To evolve the concept design to the final design, a tool is needed to predict the influence of design choices on the performance. In Chapter 3 a procedure is developed to analyse the performance of a closed loop system on which stochastic disturbances act. Using the superposition principle, the contribution from each disturbance source to the error can be analysed separately. This procedure, denoted *Dynamic Error Budgeting* (DEB), provides the necessary information in the design phase on how to improve the controller design and/or the plant design, and by indicating which disturbances are dominant. This procedure can be applied to many mechatronic systems, hence it is described in a general sense.

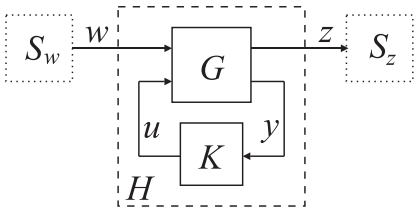

Starting point for the design of the rotor is the use of active magnetic bearing technology. Active magnetic bearings use Reluctance Type Actuators (RTAs) which have a strong nonlinear behaviour with respect to the current and the air gap. The technology that is commonly applied to linearize these RTAs results in constant power dissipation and a strong mechanical coupling. Especially the latter effect conflicts with the requirement of low stiffness actuators which stems from the concept of separating the force and the metrology frame (this is discussed Chapter 2). Chapter 4 proposes *Non-Linear Compensation* (NLC) to minimize these effects. The sensitivity of NLC to parameter changes is analysed and the approach is validated on two experimental setups.

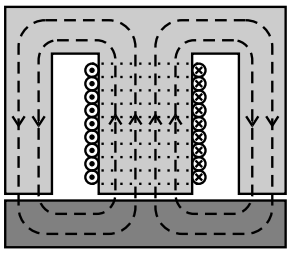

Chapter 5 discusses the design of the rotating demonstrator. First the conceptional design choices as discussed in Chapter 2 are further worked out into an initial design. This initial design is the starting point of an *iterative design process* in which DEB is used to evaluate the design choices. This design process is illustrated with a few examples. The chapter ends with the description of the realized setup and the encountered fabrication difficulties.

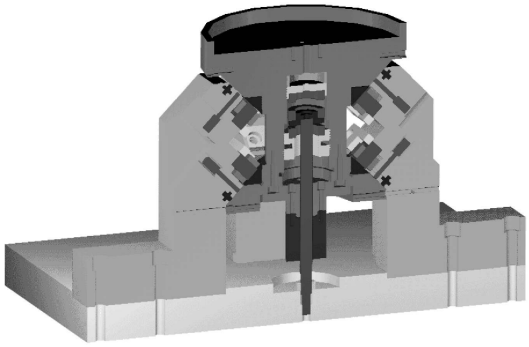

In Chapter 6 the experimental results obtained with the demonstrator at standstill are first described. The best achieved servo positioning error is less than 0.5 nm (RMS). Next, the functioning of the non-linear compensation is validated, after which the measured transfer functions are discussed. With the use of the measured transfer functions, the initial controller design is further tuned. The chapter ends with a discussion on the obtained results.

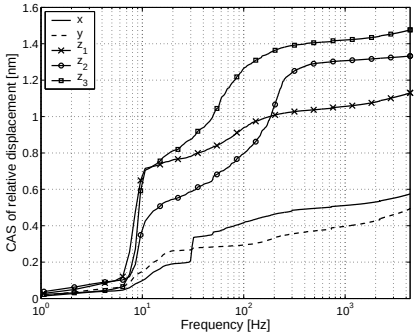

This thesis ends with the conclusions and recommendations.

2

Development of a Concept Design

In this chapter a concept design for the demonstrator is developed. The first step in arriving at a concept design for a (mechatronic) machine is to gain insight in the requirements. Since the specifications for Blu-ray mastering are not publicly available, these are derived from DVD specifications. The second step in developing the concept design, is to assess the main disturbances which will act on the system. Based on the estimated requirements and disturbances, several fundamental choices are made concerning the working principle of the system.

2.1 Design Methodology

This research deals with the design of a mechatronic systems. As was stated in Chapter 1, such a system consists of electrical actuators, a mechanical structure, motion sensors and a controller. In such a system three parts determine the final performance; the plant, the controller and the disturbances acting on the mechatronic system. In general the design of a mechatronic system is an iterative process between:

1. assessment of requirements and disturbances,
2. design and modelling of the plant,
3. controller design and
4. verification of the performance in the face of disturbances.

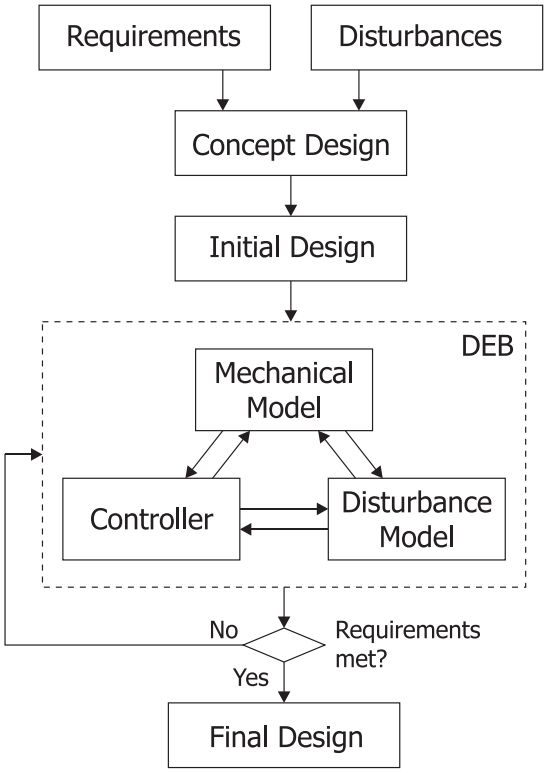

Figure 2.1. *Simplified scheme of a design process to illustrate the application of the Dynamic Error Budgeting (DEB) methodology during the design. The scheme is simplified in the sense that many design iteration arrows are not shown for the sake of clarity.*

First step is the assessment of the requirements and disturbances. Based on this assessment a concept design can be made. In the conceptual and initial design phase, a model is derived using first-principles. This model is then used for the design of the preliminary controller. Having derived a model of the design and a controller, the closed loop performance of the design can be estimated. Using this estimation the design is improved in an iterative process, until it satisfies the specifications. Then a prototype is usually built in order to confront the design with phenomena of the real world. In this phase the prototype can be modelled by means of identification of the transfer function. Based on this more accurate model, the controller design can then be improved. Now the performance of the prototype facing real-life disturbances can be directly measured. If the performance is unsatisfactory, the cause should be identified. The more fundamental the cause, the more radical the system should be redesigned.

In the past the four mentioned steps were often taken sequentially. The mechanical system was designed and then fixed, limiting the potential of control design. In recent years the effort has been focussed towards an integral design of plant and the controller using predictive modelling. Still surprises occurred due the underestimated influence of disturbances on the performance. Hence, an improved methodology to integrate the disturbances into the design process seems advantageous.

Stimulated by methods used to describe disturbances and their influence on the system performance the Dynamic Error Budgeting (DEB) methodology used in this research was developed. In this research the DEB methodology to integrate the above mentioned three steps has been further developed and applied. The DEB method is extensively described in Chapter 3 on page 31.

Application of the DEB method during the design is illustrated in the (simplified) design process flow scheme shown in Figure 2.1. Based upon assessment of the requirements and disturbances, a concept design is developed and further matured to the initial design. This initial design is the input to the DEB process, in which the influence of the plant, controller and disturbances on the performance are evaluated concurrently. These iterations are done in the design phase at relatively low cost and throughput time. When successful, the design effort of all the relevant components are well balanced. This approach has the potential benefit of a significant reduction of experimental iterations.

2.2 Derivation of Specifications

2.2.1 Specifications on Blu-Ray Disks

As stated in Chapter 1 the two possible follow-ups for DVD are the Blu-ray Disk (BD) and the High Definition DVD (HD-DVD). The specifications for the BD are more tight than for the HD-DVD, hence this chapter focusses on the derivation of the specifications for BD mastering. Although the specifications for the Blu-ray Disk (BD) have recently been laid down, not all relevant specs were publicly available at the time of starting this design (2001). The relevant values for the various properties of the DVD and BD are given in Table 2.1.

Track Pitch Variation

An important specification is the limitation of the variation of the distance between two adjacent tracks, called Track Pitch Variation (TPV). If two tracks are too close to each other, the reflected laser light will contain information of both tracks. This will lead to cross-talk, and, in the worst case, loss of tracking.

Table 2.1. *Comparison of the properties of the DVD and the BD. Unless stated differently the values for DVD are from [25], while those of BD are from [9].*

Property	symbol	unit	DVD	Blu-Ray
Wavelength	λ_{laser}	nm	650	405
Numerical Aperture	NA	-	0.6	0.85
Track pitch	d_{track}	nm	740	320
Linear velocity	v_{scan}	m/s	3.49	4.92
Pit length	l_{pit}	nm	400[a]	150
Pit width	w_{pit}	nm	350[a]	250[a]
Radii information layer	$r_{\text{min,max}}$	mm	24, 58	24, 58

[a] From [63]

Table 2.2. *Official specifications on the DVD (from [25]) and white paper specifications on the BD (from [9]). The questions marks indicate the unknown specifications which are be derived.*

Property	symbol	unit	DVD	Blu-Ray
Tracking error	e_{track}	nm	$\pm$22	$\pm$9
Focus error	e_{focus}	nm	$\pm$230	$\pm$45
Birefringence	d_{biref}	nm	100	30
Track pitch variation	d_{tpv}	nm	$\pm$30	?
Radial track runout	d_{runout}	μm	100[a]	75[a]
Radial acceleration	a_{rad}	m/s^2	1.65	?

[a] peak-to-valley

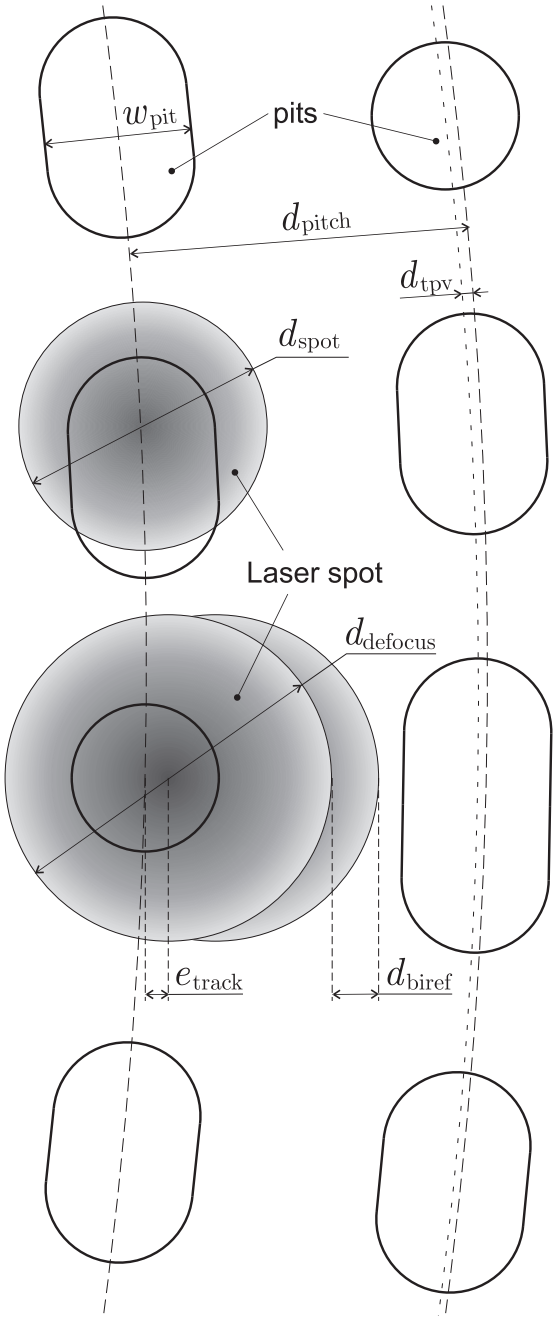

Figure 2.2. *Illustration of track pitch tolerances for an OD (with exaggerated curvatures of the tracks). The upper laser spot illustrates the nominal situation, while the lower spot illustrates the worst case tolerated situation.*

In Figure 2.2 two adjacent tracks are shown in which the parameters involved are indicated. The values of some of these parameters are given in Table 2.2. To derive the diameter of the focus spot when the spot is slightly defocussed, the laser light is described by a *Gaussian beam*, see [104]. For a Gaussian beam the beam radius r_G is given by:

$$r_G = r_0 \sqrt{1 + \left(\frac{\lambda_{\text{laser}}\, e_{\text{focus}}}{\pi r_0^2} \right)^2}, \tag{2.1}$$

in which r_0 is the minimal radius of the focussed spot. At the radius r_G the intensity of the light is $1/e^2$ times the intensity at the centre of the beam (e being Napier's number). The minimum beam diameter is given by:

$$r_0 = \frac{\lambda}{\pi \arcsin(NA)}. \tag{2.2}$$

Using the values of Table 2.1, the above equation gives a spot diameter of 643 nm for the DVD and 254 nm for BD.

Due to the movement of the disk and the limited bandwidth of the Pick Up Head (PUH), there will be a certain amount of defocusing. The allowed focussed error is given in Table 2.2. At a distance equal to the maximum allowed focus error the spot size becomes 708 nm for the DVD and 270 nm for the BD.

The optical layer of an Optical Disk (OD) is made of polycarbonate. Because polycarbonate consists of long molecules, the index of refraction differs for light polarized in different directions. This phenomenon is called birefringence. As a result, the laser light will divide into two beams (the ordinary beam and the extraordinary beam) having opposite polarization, propagating in different directions. The maximum allowed distance between the centres of the two beams d_{biref} is specified in Table 2.2.

With the above given and calculated values, the distance between the focus spot and the adjacent track can be calculated. This distance acts as a safety against other optical abberations that have an increasing effect on the focus spot size, such as coma (due to tilting of the disk) and spherical abberations.

In the worst case position the distance between the laser spot and the adjacent track, the safety region d_{sr}, is given by:

$$d_{sr} = d_{\text{pitch}} - \tfrac{1}{2} w_{\text{pit}} - \tfrac{1}{2} d_{\text{defocus}} - d_{\text{biref}} - e_{\text{track}} - 2 d_{\text{tpv}}. \tag{2.3}$$

For the DVD the safety region is then 29 nm. Hence the safety region is about equal to the allowed peak track pitch variation; $d_{sr} \approx d_{\text{tpv}}$. Assuming that this relation is also valid for the BD, than the TPV for the BD can be calculated as

follows:

$$\begin{aligned} d_{sr} &= d_{\text{pitch}} - \tfrac{1}{2}w_{\text{pit}} - \tfrac{1}{2}d_{\text{defocus}} - d_{\text{biref}} - e_{\text{track}} - 2d_{\text{tpv}} \Leftrightarrow \\ 3d_{tpv} &= d_{\text{pitch}} - \tfrac{1}{2}w_{\text{pit}} - \tfrac{1}{2}d_{\text{defocus}} - d_{\text{biref}} - e_{\text{track}} \Leftrightarrow \\ d_{\text{tpv}} &= \tfrac{1}{3}(320 - \tfrac{1}{2}250 - \tfrac{1}{2}270 - 30 - 9) = 7.0. \end{aligned} \tag{2.4}$$

Hence, the track pitch variation of a BD must be within ± 7 nm.

Radial Acceleration

Besides the focussing of the laser, the PUH also performs radial tracking. Because the bandwidth of this control system is limited, the allowed radial acceleration of the track, as seen from the PUH system, must be bounded in order for the PUH to follow the track, see [25].

For the DVD the maximum allowed radial acceleration of the track is 1.5 times the expected maximum radial acceleration of 1.1 m/s^2. The expected maximum acceleration can be calculated assuming that the allowed track runout of 100 μm is due to an eccentricity d_{ecc} of 50 μm. At maximum rotating velocity, the radial acceleration a_{rad} of the track is then:

$$a_{\text{rad}} = e_{\text{ecc}} \cdot \Omega_{\text{max}}^2, \tag{2.5}$$

where Ω_{max} is the maximum rotation speed in rad/s. The maximum rotation speed in Hz is derived by dividing the linear scanning speed of the OD by the minimum track circumference, which has a radius r_{min} of 24 mm for both the DVD and BD. The maximum expected radial track acceleration for the BD is then:

$$\begin{aligned} a_{\text{rad}} &= e_{\text{ecc}} \cdot \Omega_{max}^2 \\ &= e_{\text{ecc}} \cdot \left(\frac{v_{\text{scan}}}{2\pi r_{\text{min}}} 2\pi \right)^2 \\ &= \frac{75 \cdot 10^{-6}}{2} \cdot \left(\frac{4.92}{24 \cdot 10^{-3}} \right)^2 = 1.58 \text{ m/s}^2. \end{aligned} \tag{2.6}$$

Assuming the same safety factor of 1.5, the maximum radial track acceleration for the BD is then 2.4 m/s^2.

2.2.2 Definitions of Rotor Movement

The OD-master is mounted on the top of the rotating platform (rotor), hence radial movement (of the top) of the rotor directly contributes to the shape of the spiral. To derive the specifications for the rotor from the specifications of ODs, first the various definitions relating to radial movement of the rotor are defined. The

movement of a rotating plane is usually specified according to ANSI (see [5]) and can also be found in Slocum [89] and IDEMA [47].

Following [89] the most relevant definitions to quantify the rotation of a rotor are given below. Their mutual relationships are illustrated in Figure 2.3.

Definition 2.1 (Radial Runout) *The radial runout is the total displacement measured by a displacement indicator sensing against the rotor surface in a direction normal to the reference rotation axis.*

The measured radial runout includes two error sources, which are the out-of-roundness of the rotor and the radial error motion. The radial error motion is defined as:

Definition 2.2 (Radial Error Motion) *The radial error motion is the change of position in a direction normal to the reference rotation axis, of a perfect rotor with its centre line coincident with the axis of rotation.*

In which a perfect rotor is defined as:

Definition 2.3 (Perfect Rotor) *A perfect rotor is a rigid body having a perfect surface of revolution around a centre line.*

Hence, perfect measurement of the radial runout on a perfect rotor equals the radial error motion. The radial error motion is divided into a synchronous part and an asynchronous part:

Definition 2.4 (Synchronous Radial Error Motion) *The synchronous error motion is the portion of the radial error motion that occurs at integer multiples of the rotation frequency.*

Definition 2.5 (Asynchronous Radial Error Motion) *The asynchronous error motion is the portion of the radial error motion that occurs at frequencies other than integer multiples of the rotation frequency.*

The Asynchronous Radial Error Motion (AREM) comprises those components of error motion that are: a) not periodic, b) periodic but occur at frequencies other than the spindle rotational frequency and its integer multiples and c) periodic at frequencies that are sub-harmonics of the spindle rotational frequency.

Various measurements must be made in order to evaluate these error motions. The measured data is typically represented in polar plots, in which the error motion is plotted in synchronization with the rotation of the spindle. In Figure 2.4 an example of a radial error motion polar plot is given, together with its averaged radial error motion plot. The averaged radial error motion plot is the mean contour of the radial error motion polar plot, averaged over a number of revolutions. When

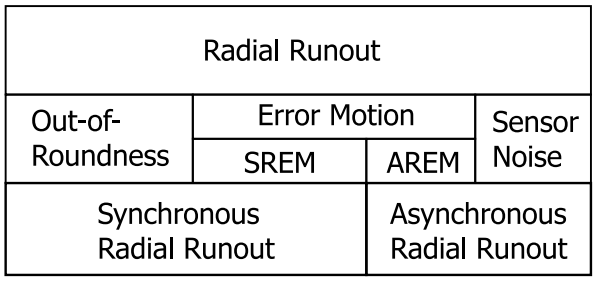

Figure 2.3. *The mutual relationships between the various error motions and measured radial runout depicted in one figure.*

the radial error motion plot is averaged over a very large number of rotations, the AREM averages to zero, and the averaged error motion plot equals the SREM.

The difficulty in practise is how to separate the SREM from the synchronous signal resulting from the out-of-roundness of the rotor. This will not be further discussed in this thesis. The interested reader is referred to [89] and [34].

Finally, the Face Error Motion (FEM) relates to the movement of the rotor in axial direction and is defined as:

Definition 2.6 (Face Error Motion) *The face error motion is the change of position in a direction parallel to the reference rotation axis, of a perfect rotor with its centre line coincident with the axis of rotation.*

2.2.3 Specifications for Optical Disk Mastering

During mastering the master disk is mounted on a rotor, which makes it natural to specify the movement of the rotor at the top surface. It is assumed that the rotor is perfect with a flat top surface (perpendicular to the centre line of the rotor).

Radial Specifications

The radial error motion of the rotor contributes to the radial runout and the allowed radial acceleration of the tracks and the Track Pitch Variation (TPV). Suppose that the only error movement of the rotor is a Synchronous Radial Error Motion (SREM) and that this is the only error source in the whole mastering system. Then the tracks written by the laser on the master will have a "potato" shape of which an example is shown by the averaged radial error motion plot in Figure 2.4. However, the track pitch will still be exactly 320 nm, with a TPV equal to zero. Only the Asynchronous Radial Error Motion (AREM) of the rotor contributes to the TPV.

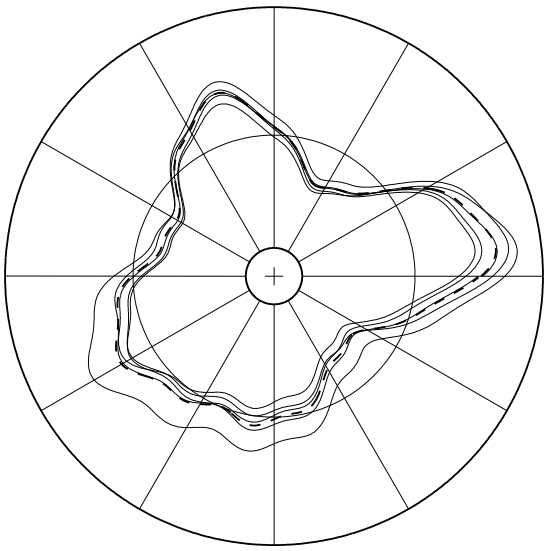

Figure 2.4. *Example of a radial error motion plot. To keep the separate lines visible only five revolutions are shown. The dashed line indicates the averaged error motion polar plot, which is the mean contour of the radial error motion plot averaged over the revolutions. The asynchronous error motion plot is approximated by the deviation of the total error motion plot from the average error motion polar plot.*

Because of the asynchronous character, the movement can be considered as being stochastic. Approximating the specification on the TPV of ± 7 nm with six times (± 3) the STandard Deviation (STD)[1], gives a STD of 2.3 nm. The AREM of the rotor is one four contributors to the TPV within an optical disk mastering machine. These contributors are:Four sources that contribute to the TPV can be distinguished :

1. Translation of the laser alignment optics, which carry the light from the laser (often on a fixed world) to the moving focussing optics,
2. Movement linear slider, which carries the focussing optics,
3. Tilt of the focussing optics,
4. The AREM of the rotor at the position of the disc.

It is good practise to allow each disturbance source an equal contribution to the TPV. Each source is then considered as being stochastic and independent (see

[1] This has a confidence interval of 99.7%, see Chapter 3.

Chapter 3) with a STD of σ. This results in a total STD of the track pitch variation of:

$$\sigma_{tpv} = \sqrt{\sigma^2 + \sigma^2 + \sigma^2 + \sigma^2} = 2\sigma. \tag{2.7}$$

Thus the maximum allowed AREM of the rotor is 1.2 nm STD. This research project strives to achieve a maximum AREM of 1 nm STD.

Since the maximum allowed runout of the BD of ± 50 μm is much bigger than the allowed TPV of 7 nm, the contribution of the AREM to the allowed radial acceleration of the tracks is expected to be much smaller than that of the SREM.

Other Specifications

To achieve an acceptable throughput of master disks, it is anticipated that the mastering process takes place with a rotating velocity of the master of 100 Hz.

In the final application, the translations of the focussed laser beam relative to the master, must be controlled. In the direction of the axis of rotation, this control is done by the focussing of the optical system. Given the present performance of the focus control system, it is assumed that this system will correct for the resulting axial motion of the master disk.

Tipping and tilting of the rotor results in an axial movement of the master disk at the position of the laser spot. Since the focussing system will compensate for this, there are no specifications placed on the tipping and tilting of the rotor.

The tangential movement is determined by the rotational speed of the rotor and the synchronization with the switching of the laser light. In this research focus will be on controlling the radial motion of the master disk relative to a reference. The issue of controlling the rotational speed is covered by the research of P. Overschie, see [71].

2.3 Disturbances

Contrary to the existing air bearing spindles for mastering equipment, the aim of this research is to realize an actively controlled positioning of the rotor. In such a system the performance is limited by disturbances that act on the system. A disturbance is defined in [49] as:

Definition 2.7 (Disturbance) *A disturbance is an undesired variable applied to a system that tends to affect adversely the value of a controlled variable.*

This basically means that any change in some physical quantity, in or outside the system, which deteriorates the performance is a disturbance.

In the following, the disturbances are classified in disturbances resulting from the operation of the rotor and disturbances which originate from the environment.

2.3.1 Environmental Disturbances

The disturbances that originate from the environment that will be discussed here are floor vibrations, temperature changes, acoustics and electro-magnetic waves. Many more disturbance sources can be thought of e.g. acceleration forces due to earth rotation, light changes, random movement of air molecules, etc. These effects have not been investigated.

Floor Vibrations

Any floor is subject to vibrations, which results in movement of the machine frame. The rotor needs to follow this movement to avoid the occurrence of tracking errors. In high precision applications, floor vibrations are usually a major disturbance source, see [93]. To illustrate this, Figure 2.5 shows an example of a typical specification that ASM Lithography (ASML) poses to the floor of customers for the PAS5500 wafer stepper. In the same graph an actual measured floor vibration level in a laboratory at the Delft University of Technology is given (in the direction perpendicular to the floor). The total area of the measured PSD results in a RMS of 1.4 mm/s^2. It can be seen that in between 9 to 13 Hz, the vibrations are higher than would be allowed at ASML.

To isolate the system from the disturbing floor, vibration isolation tables are commonly used. The table top of such a vibration isolation table is supported by compliant springs, usually air mounts. Typically, the resulting eigenfrequency of such a table is in the range 1—2 Hz. Above the eigenfrequency of the table, the transfer function from floor movement to table movement has a -2 slope, thus isolating the table top from high frequency floor vibrations.

Temperature Changes

High precision machines are usually operated in temperature controlled rooms. These rooms usually also condition the humidity, since components, like e.g. capacitive sensors, can be sensitive for this as well.

The direct effect of changes in temperature on systems, are usually of low frequency nature, i.e. less than 0.1 Hz. At these frequencies the closed loop system will be very well capable to correct for these disturbances, thus these changes have little influence on the performance. Still other effects might occur, which are not measured and are not corrected for by the control loop. These effects should be accounted for.

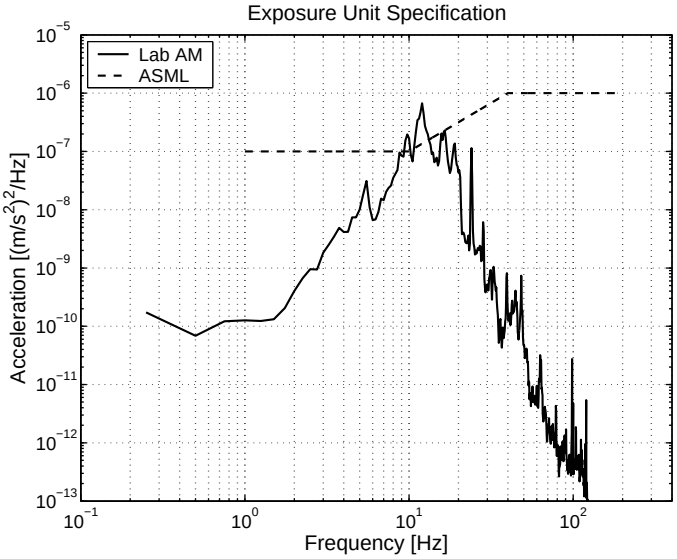

Figure 2.5. *Measured Power Spectrum Density (PSD) of the floor vibrations in the laboratory of Advanced Mechatronics (solid). Also indicated is the specification from ASML on the allowed floor vibrations for the exposure unit. In the range 9 to 13 Hz the measured vibrations exceed the ASML specification.*

An indirect effect of temperature changes on the system is that properties of the system determining the dynamic behaviour might change. In the new rotor system model based control will be used and large variations of the modelled parameters might influence the performance, although this is not likely.

Acoustics

Acoustic noise will introduce pressure waves, which gives disturbing forces on the system. A big source of acoustic noise in clean-rooms are the air-conditioning machines.

Electro-magnetics

Modern society uses technology with many sources of electro-magnetic fields. These will introduce disturbance currents in any electric conducting loop. In well designed electric components, these loops are usually made as small as possible. In [62, Section 4.10.2] these are referred to as cable noise. For example, sensor cables should not be laid close to power cables. The large alternating current of the power cable is a source of electro-magnetic fields and can easily perturb the small signals from the sensors.

Ground loops are also contributors to cable noise. If two electric components are connected to two grounding point with different potential, a current will flow through the cable's shield.

Another source of cable noise are *Triboelelectric* effects. These can occur in damaged cables, when either the centre core wire or shield wire "rubs" against the common electrical insulation material.

2.3.2 Operational Disturbances

Having the system in closed loop operation inevitably introduces disturbances. These are disturbances from electronic components used in the control loop, actuator non-linearities and disturbance caused by rotation of the rotor.

Electronic Components

Electronic components that are used in the control loop are: sensors, amplifiers, filters and analogue to digital and digital to analogue converters. Each component introduces disturbances stemming from the electronics in the components. The nature of these disturbances is often stochastic.

Non-Linearities

One of the fundamental design choices mentioned in Chapter 1, was the use of Active Magnetic Bearing (AMB) technology. In AMBs Reluctance Type Actuators (RTAs) are used, which inherently have a non-linear behaviour; the force is proportional to the current squared and inversely proportional to the air gap squared. Using non-linear compensation in the controller can compensate much, however, non-linear effects will always remain due to modelling uncertainties. This is extensively covered in Chapter 4 on page 67.

Rotation

The rotation will introduce disturbances to the closed loop system. Due to unbalance of the rotor forces will be exerted on the bearing system. Additional effects occur due to inhomogeneities in the materials that are used in the rotor that are part of the actuators and sensors. These disturbances are synchronous with the rotation of the rotor and do not contribute to the AREM.

The rotation of the spindle causes an air flow. Due to the shape of the rotor and stator, some degree of turbulence will likely occur, which would generate noisy forces on the rotor.

The influence of disturbances resulting from rotation and the methods to minimize their negative effect on the performance are addressed in the research of P. Overschie, see [71].

2.4 Concept Design Choices

Having addressed the relevant specifications and disturbances, the concept design choices can now be made. In a series of brainstorm meetings with experts from industry and universities a number of potential concepts have been derived. The main building elements and design considerations are described here.

2.4.1 Low Sensitivity for Slow System Variations

The maximum rotation velocity that is aimed for is 100 Hz. Because the radius at which the data is written varies (see Table 2.1), the minimum rotation velocity is 41 Hz. This means that slow variations in the system, which are not corrected for by the control loop, are averaged over many written tracks. Hence, the slower the system varies, the lower the sensitivity for these variations.

This practically takes care of the sensitivity for temperature changes, since these are typically slow (sub-Hertz).

2.4.2 Separation of Force and Metrology Frame

One of the fundamental starting points was the decision to separate the force frame from the metrology frame. This decision was based on the estimation that floor vibrations would be a big disturbance source in the final setup. In this concept the position of the rotor with respect to the metrology frame is sensed and controlled, while the reaction forces of the controller act on a separate force frame. The concept is illustrated in Figure 2.6. This approach gives three big advantages. Firstly, the reaction forces do not deform the metrology frame, such that the metrology frame acts as an accurate reference. Secondly, by mechanically isolating the metrology frame from the environment, a quiet reference world is created. This implies that the rotor should also be quiet and hence only small forces are required to let the rotor follow the metrology frame. These can be generated by the controller with (very) small servo errors. Thirdly, the dynamics of the force frame is decoupled from the rotor and do not have at destabilizing effect on the control loop.

The main consequence of this concept principle is that the actuators of the rotor and the motor should have a minimal mechanical coupling (low stiffness) to prevent vibrations of the force frame to enter the rotor.

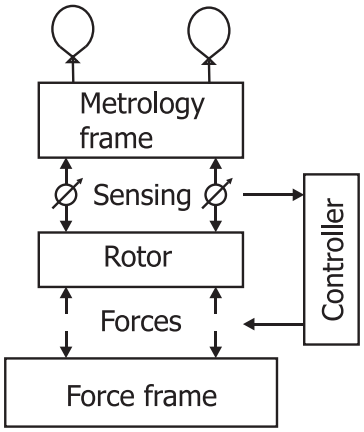

Figure 2.6. *Illustration of the concept principle to separate the force frame from the metrology frame. In this concept the position of the rotor with respect to the metrology frame is sensed and controlled, while the reaction forces of the controller act on a separate force frame. A still reference is created by mechanically isolating the metrology frame from the environment (here illustrated with two balloons).*

2.4.3 Reluctance Type Actuators

A starting point of the project was the use of AMB technology, for the reasons discussed in Chapter 1. In AMBs Reluctance Type Actuators (RTAs) are used to generate the forces required for control. These forces are proportional to the current squared and inversely proportional to the position squared, i.e. $f \propto i^2/x^2$, see Section A.1. In standard active magnetic bearings the force relation is linearized around a working point by pre-loading the RTAs with a bias current. Linearization by pre-loading has two major disadvantages in a system with separated force and metrology frames. Firstly, the working range is very small, which implies that the relative movement of the metrology frame and the force force must be limited to this range in order for the rotor to follow the metrology frame. However, this is contradicting since the two frames are fundamentally decoupled. Secondly, because of the pre-loading the RTAs create a strong coupling between the rotor and the force frame, which will translate movements of the force frame into disturbing forces to the rotor.

Another approach to linearize the RTAs is using Non-Linear Compensation (NLC) in the controller, see [96, 48]. Using NLC allows operation of the RTAs with (very) low bias current, minimizing the power consumption. More important however, is that NLC can be used to reduce the position dependency of a RTA, such that it ideally behaves as an actuator with zero mechanical stiffness. This topic is

extensively covered in Chapter 4.

2.4.4 Gravity Compensation

The mass of the rotor is compensated with a passive Gravity Compensator (GC) to relieve the actuators from a constant effort, which has two advantages. Firstly, constant power dissipation of power inherently introduces actuator stiffness when using RTAs. Because of the frame separation this should be minimized. Secondly, heating of stator and/or rotor, which could introduce deformations, is prevented. Thirdly, it allows the actuators to be smaller, which reduces the disturbances, since the noise sources in the current supply chain in general scale proportionally with the range of the actuator.

Because of the separated frames principle the weight of the mass should be compensated with an as low as possible mechanical stiffness.

2.4.5 Rotation around Principal Axis of Inertia

The hole that is made in the stamper after the mastering process, is centred with respect to the tracks that are written. Hence, the rotation axis of the rotor need not to be aligned with the geometrical centre of the rotor (and the master). Rotating the rotor around one of its Principal Axis of Inertia (PAI), instead of its geometrical axis, gives the advantage that the actuators can be reduced in size, since no bearing forces are required to rotate a body around its PAI.

In order to achieve rotation around the PAI of the rotor, an algorithm is required that minimizes the periodic components in the bearing forces by generating feed-forward signals for the sensors. Since rotation of the rotor is not included in this research, such an algorithm is not further discussed here. However, since powerful algorithms[2] exist which minimize periodic signals in a closed loop system by adjusting a feed-forward signal, solving this issue is not considered too problematic.

2.4.6 One DoF with Tight Specification

Considering the optical disk mastering process as discussed in Section 1.2, it is noted that there is only one direction at which the highest accuracy is needed. Only if the disk moves in the translation direction of the laser, the track pitch will change. Hence only one DoF of rotor needs accurate positioning.

[2] An example of such an algorithm is *lifted iterative learning control*, see [22].

2.4.7 Vacuum Compatible

As discussed in Subsection 1.2.3, future mastering techniques are likely to require vacuum conditions. Hence, the technical solutions should allow operation under vacuum conditions. Differently put, since it is not required for the demonstrator to work in vacuum, the components that fulfill the functions of the concept design should not fundamentally exclude operation in vacuum.

2.5 Conclusions

In this chapter a concept design has been developed. To arrive at this concept design, the anticipated specifications for modern optical disk mastering have been derived. Next step encompassed a categorization of the disturbances that will act on a mastering system. The ground vibrations have been identified as being one of the most dominant disturbances. For this reason it was decided to separate the metrology and force frame, which has a profound impact on the concept design.

To evolve the concept design to the final design, a tool is needed to predict the influence of design choices on the performance. This tool is developed in the next chapter.

3
Dynamic Error Budgeting

The previous chapter focussed on the concept design, which was based on an assessment of the specifications and the disturbances. In this chapter a procedure is developed to analyse the performance of a closed loop system on which stochastic disturbances act. This procedure, denoted Dynamic Error Budgeting (DEB)*, provides useful information on how to improve the controller or plant design, by indicating which disturbances are dominant and how they propagate through the closed loop system. The DEB approach is used in the design of the rotating demonstrator, as described in Chapter 5. The procedure can be applied to many mechatronic systems, hence it is described in a general sense.*

3.1 Introduction

3.1.1 Motivation

In the design and analysis of mechatronic machines, the use of Bode diagrams is widely spread to assess stability and performance. The reason for its widespread use, also outside the control community, is its easy and clear interpretation of performance when dealing with systems which perform periodic tasks. However, a large class of mechatronic machines have specifications based on their standstill (or constant velocity) performance, e.g. step (or scan) machines for lithography, positioning stages (for example in microscopes) and active vibration isolation. The standstill performance is then limited by the disturbances acting on the closed loop. Many, if not all, disturbances are stochastic of nature, resulting in a performance measure with stochastic properties.

The difficulty in calculating with stochastic signals and Bode plots, is that, instead of calculating with the complex response at one frequency, the *area* over

a frequency range should be taken into account. For this reason, stochastic calculation tools are not commonly used outside the control community.

In the design of precision machines, *error budgeting* is often used to allocate how much each component is allowed to contribute to the total error, see e.g. [89, p.61]. For the design and analysis of mechatronic systems one would like to incorporate the influences of the disturbances acting on the closed loop system in the error budget. Since many of these disturbances have a stochastic nature, they can often be modelled with their *Power Spectral Densities* (PSD). Then the PSD of the performance measure in the closed loop system is the weighted sum of PSDs of the contributions of each disturbance to the performance channel. This approach allows frequency dependent error budgeting, which is why it is referred to as *Dynamic Error Budgeting* (DEB).

In the design phase of mechatronic machines the added value of DEB is that it enables the designer to better assess the quality of the components in the loop. As such, the design effort can be more effectively spent on the most limiting components. The ratio performance over cost would be increased by either speeding up the design process, improving the achievable performance or allowing the use of cheaper components.

In the performance analysis of a mechatronic machine, DEB facilitates the identification of performance limiting disturbances or the recognition of the limiting component in the plant.

3.1.2 Literature Overview

In [2, 46, 1] the authors use the philosophy behind DEB to find the biggest disturbance for the position error in a disk drive. Calculation with PSDs has been used in [8, 81], to determine the optimal pre-amplifier in a geophone. Noise analysis of electronic devices using PSDs of various electronic components is extensively covered in [29, 66]. The approach of [29] is applied in [94] to analyse the total noise in an operational amplifier. The same approach has been used in [97] to analyse the vibration levels on the international space station. Manufacturers of step and repeat (scan) machines for lithography usually specify the allowed floor disturbance by a PSD [93]. The shape of these PSDs suggests that a similar approach is used for error analysis.

Much of the theory of this chapter is covered in [65], in which the theory applied to vibration isolation.

3.2 Disturbance Modelling

In the DEB framework disturbances are considered as realizations of stationary, stochastic processes. In order to make the reader aware of the implications of the assumptions which are made, a short introduction to the theory of stochastic variables is given here. The assumptions are further discussed in Section 3.7. For more complete introductions refer to [100, 6]. A more complete coverage of the theory is given in [76] and [73].

3.2.1 Stochastic Variables

Consider a (measured) continuous random variable x_m. The signal $x_m(t)$ is one of many possible realizations of a stochastic process. The stochastic process is characterized by the complete set of possible realizations, called an *ensemble*. For each given time, t_1 there exists a set of (infinite) ensemble values; $x_1(t_1)$, $x_2(t_1)$, $x_3(t_1)$, etc. The set of ensembles can then be described by *ensemble averages*, e.g. *mean* and *variance*. Calculation of ensemble averages is done via the *expectation operator*. A stochastic process whose ensemble averages does not change with time, is a stationary process. If the time average of a realization converges to the corresponding ensemble average as time goes to infinite, the process is called *ergodic*. For a process to be ergodic it must be stationary.

In the DEB framework it is assumed that all disturbances are realizations of ergodic stochastic processes. Hence, from here on only time averages are considered.

Mean, Power and Variance

The mean, power and variance of a signal are defined in the following way:

$$\begin{aligned}
&\text{mean :} && \bar{x} = \lim_{T\to\infty} \frac{1}{2T} \int_{-T}^{T} x(t)\mathrm{d}t \\
&\text{power :} && \|x\|_{\text{rms}}^2 = \lim_{T\to\infty} \frac{1}{2T} \int_{-T}^{T} x(t)^2\mathrm{d}t \\
&\text{variance :} && \sigma_x^2 = \lim_{T\to\infty} \frac{1}{2T} \int_{-T}^{T} \left(x(t)-\bar{x}\right)^2\mathrm{d}t = \|x-\bar{x}\|_{\text{rms}}^2 ,
\end{aligned} \tag{3.1}$$

where RMS refers to Root Mean Square. Note that $\|\cdot\|_{\text{rms}}$ in the definition above is a semi-norm since $\|x\|_{\text{rms}} = 0$ does not imply that $x(t) = 0$, $\forall t$ (the RMS-norm for any time limited signal is zero). The term power is sometimes also referred to as *mean square*, while the square root of the variance is called the STandard Deviation (STD).

Useful to realize is that the variance can be written as:

$$\sigma_x^2 = \|x-\bar{x}\|_{\text{rms}}^2 = \|x\|_{\text{rms}}^2 - \bar{x}^2 \tag{3.2}$$

Hence, for signals with zero mean, variance equals the power (and the STD value equals the RMS-norm) of a signal.

Probability Density Function

The mean and the variance give information on the shape of the *Probability Density Function* (PDF). The PDF f_{pdf} gives us the means to calculate the probability that a stochastic variable x is in a certain interval (a,b):

$$\text{Prob}\,(a < x < b) = \int_a^b f_{\text{pdf}}(z)\text{d}z \tag{3.3}$$

In addition, $f_{\text{pdf}}(z) \geq 0\ \forall z$ and $\int_{-\infty}^{\infty} f_{\text{pdf}}(z)\text{d}z = 1$. Although there are many PDFs being used in the analysis of stochastic processes, here only the two most common encountered distributions for continuous stochastic variables are considered.

First is the *uniform* or *rectangular* distribution, which is defined as:

$$f_{\mathcal{U}}(z) = \begin{cases} \dfrac{1}{b-a}, & a \leq z \leq b \\ 0, & \text{otherwise} \end{cases} \tag{3.4}$$

The second is the *normal* or *Gaussian* distribution. This distribution function is valid for many stochastic processes encountered in practice. The reason behind this is explained by the *Central Limit Theorem*, see Subsection 3.7.1. The normal distribution has a PDF described by:

$$f_{\mathcal{N}}(z) = \frac{1}{\sigma_z\sqrt{2\pi}} e^{-(z-\bar{z})^2/(2\sigma_z^2)} \tag{3.5}$$

If the PDF of a stochastic variable is unknown, the Tchebycheff inequality ([76, p.51]) can be used to obtain a rough indication on the deviation of x from its mean value. For any positive constant n it gives:

$$\text{Prob}\,(|x-\bar{x}| \geq n\sigma_x) \leq 1/n^2 \tag{3.6}$$

Table 3.1 compares the two distribution functions together with the lower bound from the Tchebycheff inequality. The table gives the probability that the deviation of the stochastic variable x from its mean is less than n times the STD: Prob $(|x-\bar{x}| \leq n\sigma_x)$, which is calculated with (3.3). From the table it can be seen

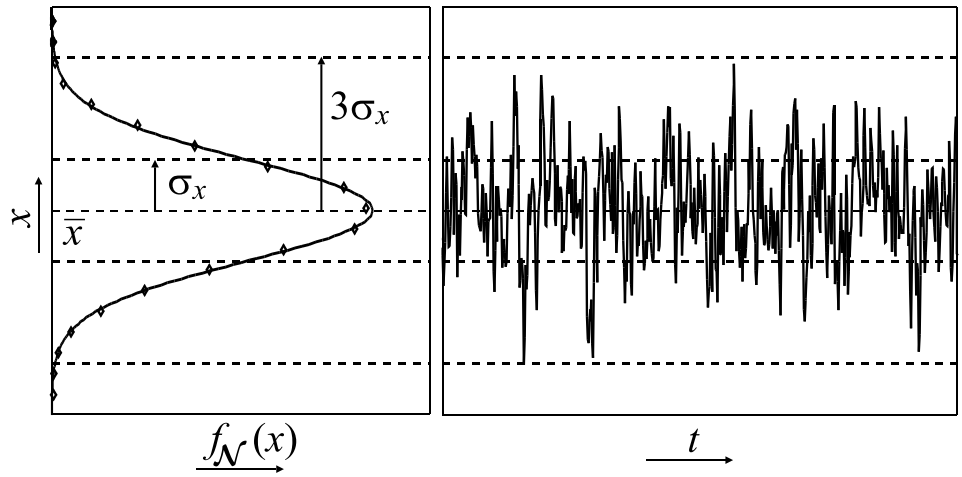

Figure 3.1. *A time trace (right) of a realization of a stochastic variable with a normal distribution. On the left the normal Probability Distribution Function (PDF) is shown, together with the PDF estimated from the time trace data.*

that with a uniform PDF a stochastic variable has a probability that it is within two times the STD of one. The table shows further that this probability very rapidly increases with the interval range when having a normal PDF as compared to the Tchebycheff lower bound.

When a stochastic variable has a normal distribution the probability that the Peak-to-Valley (PtV) value of a realization is smaller than 3σ is 99.73%. This is illustrated in Figure 3.1, where a simulated realization of the stochastic process is plotted together with its one and three sigma bounds. Also shown is the PDF estimated from the time trace data and the normal PDF of the stochastic process. The three sigma bound is often used in the engineering community to estimate the PtV value of a stochastic process.

Table 3.1. *This table gives the probability that the deviation of a stochastic variable* x *from its mean is less than* n *times the* STD*. The table gives the values for the normal and uniform Probability Density Functions (PDF) and the Tchebycheff lower bound.*

	Prob $(\lvert x-\overline{x}\rvert \leq n\sigma_x)$		
n	uniform	normal	Tchebycheff
1	0.58	0.6827	>0.00
2	1.00	0.9545	>0.75
3	1.00	0.9973	>0.89
4	1.00	0.9999	>0.98

3.2.2 Spectral Analysis

First the autocorrelation function R_{xx} is defined as:

$$R_{xx}(\tau) = \lim_{T\to\infty} \frac{1}{2T} \int_{-T}^{+T} x(t-\tau)x(t)\mathrm{d}t. \tag{3.7}$$

Since only real valued processes are considered in this thesis, $R(\tau)$ is an *even function*. Note that for $\tau = 0$ the autocorrelation function equals the definition of power:

$$R_{xx}(0) = \|x\|_{\text{rms}}^2 = \sigma_x^2 + \bar{x}^2. \tag{3.8}$$

The PSD function $S_x(f)$ of x is then defined as the Fourier transformation of the autocorrelation:

$$S_x(f) = \int_{-\infty}^{+\infty} R_{xx}(\tau)e^{-j2\pi f\tau}\mathrm{d}\tau. \tag{3.9}$$

in which f denotes the frequency in Hz. With the inverse Fourier transformation, the autocorrelation becomes:

$$R_{xx}(\tau) = \int_{-\infty}^{+\infty} S_x(f)e^{j2\pi f\tau}\mathrm{d}f. \tag{3.10}$$

From (3.10), it follows that the power of a stochastic variable equals the integral of the PSD:

$$\|x\|_{\text{rms}}^2 = R_{xx}(0) = \int_{-\infty}^{+\infty} S_x(f)\mathrm{d}f. \tag{3.11}$$

Equation (3.11) actually relates the definition of power in the time domain to the frequency domain. This relation is referred to as *Parseval's relation*.

Since the autocorrelation is even, the PSD function is also even (two-sided). This allows us to redefine the PSD for only positive frequencies (one-sided):

$$S_x^+(f) = \begin{cases} S_x(0), & f = 0, \\ 2S_x(f), & f > 0. \end{cases} \tag{3.12}$$

Parseval's relation makes the following function very convenient:

$$\text{CPS}_x(f) = \int_0^f S_x^+(\nu)\mathrm{d}\nu, \qquad f \geq 0, \tag{3.13}$$

which gives for the frequency f the power of the signal from zero up to that frequency and is denoted Cumulative Power Spectrum (CPS)[1]. Finally, Cumulative Amplitude Spectrum (CAS) is defined as:

$$C_x(f) = \sqrt{\text{CPS}_x(f)}, \tag{3.14}$$

which has the following properties:

[1] In [76] this function is simply called integrated spectrum, but the name CPS is more precise.

1. $C_x(f)$ is a non-decreasing function, i.e.
   $f_2 > f_1 \Rightarrow C_x(f_2) \geq C_x(f_1)$, with
2. $C_x(0) = 0$ and
3. $C_x(\infty) = \sqrt{\overline{x^2}}$

Examples of estimating spectral models of common disturbances in mechatronic systems are given in Section 3.3.

3.3 Common Mechatronic Disturbances

Here the modelling of some commonly encountered disturbances in mechatronic systems is discussed.

3.3.1 Ground Vibrations

In many mechatronic machines, the performance is limited due to internal deformation of the machine caused by floor vibrations. Floor vibrations have many sources. Waves crashing on the shorelines, constant grind of tectonic plates and blowing wind are examples of sources induced by nature. Plant activities can excite the floor as well; rotating machinery, impact acting machines, material handling and persons walking. A statistical analysis of an ensemble of floor vibrations measured at various locations on a plant floor showed these vibrations constitute a non-stationary and non-ergodic random process ([80]). Furthermore, rotating machinery introduce periodic components resulting in mixed spectra. Altogether the factors make floor vibrations rather difficult to model. One way of dealing with the non-stationary property is by applying some kind of time averaging to the periodogram measurements, e.g. taking the maximum envelope over twenty four hours. In [67] suggestions are given on how to measure floors with mixed spectra.

In spite of these difficulties, standards exist that characterize floor vibrations, see [93] for an excellent overview. Most well known are the BBN *criteria*[2]. The BBN criteria are specified as *one-third octave* spectra[3] on velocity and were proposed by Gordon in [33]. The BBN Vibration Criteria (VC) curves are defined by a $1/f$ line from 4 to 8 Hz, and are constant from 8 to 80 Hz. These are obtained by filtering the noise with a one third octave band-pass filter[4] and taking the rms

[2] BBN stands for Bolt, Beranek & Newman Inc.

[3] One-third octave analysis is an example of *broad (proportional) band* analysis. This in contrast to *narrow (constant) band* analysis, for example FFT analysis.

[4] The pass-band, defined by the -3dB frequencies, is 23.2% of the centre frequency.

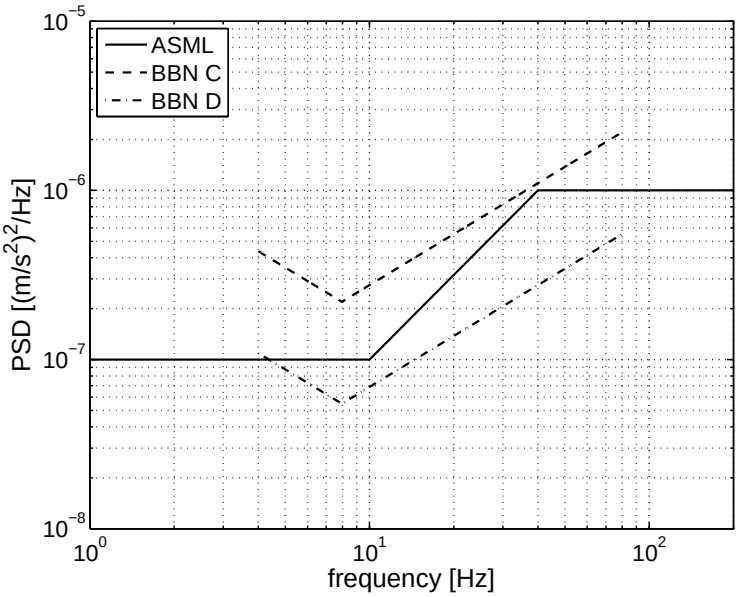

Figure 3.2. *Power spectral density of floor vibration specifications from ASML and BBN.*

value. A one-third octave spectra can be approximated from a PSD using:

$$V_{\mathrm{BBN}}(f) = \sqrt{\int_{-\sqrt[6]{2}f}^{\sqrt[6]{2}f} S_x(\nu)\mathrm{d}\nu}. \tag{3.15}$$

To give an impression of these criteria, two BBN curves (VC-C and VC-D from [33]) are compared to a specification for the exposure unit from ASM Lithography (ASML, taken from [93]) in Figure 3.2. The VC-C curve has a constant part of 12.7 μm/s, and the VC-D half of that (in one-third octave). The RMS velocity values of the BBN specifications are 51 μm/s (VC-C) and 26 μm/s (VC-D). The BBN curves were converted to a PSD using (3.15) and then differentiated (multiplied with $(2\pi f)^2$). The corresponding RMS acceleration values of the BBN specifications are 9.4 mm/s^2 and 4.7 mm/s^2.

The PSD specified by ASML refers to accelerations and is characterized by 0.1 $(\mathrm{mm/s^2})^2/\mathrm{Hz}$ from 1 to 10 Hz and 1 $(\mathrm{mm/s^2})^2/\mathrm{Hz}$ from 40 to 200 Hz. Integrating the PSD from ASML gives a RMS value for acceleration of 13.2 mm/s^2 (and in velocity 57.8 μm/s (RMS)).

In order to estimate the vibration levels below the 1 Hz threshold, the New High Noise Model from the Albuquerque Seismological Lab can be used, see [74]. The model is a spectrum of *average* high background noise power, reconstructed using data obtained from seismological sites around the world.

3.3.2 Electronic Noise

Electronic noise enters the closed loop system at many points, since many electronic components are used in sensors, amplifiers and other devices. Electronic noise has many origins, which are named after their behaviour, e.g. thermal, shot, excess, burst and avalanche noise. Here, only the most relevant will be discussed, refer to [29] and [11] for a complete coverage of electronic noise.

Thermal Noise

Any resistor will have a fluctuating potential difference across its ends, caused by the thermally induced, random motion of charge carriers (electrons or holes). Thermal noise (also known as *Johnson* or *Nyquist* noise[5]) can be modelled as a voltage source in series or as a current source parallel with a noiseless conductor. A model for thermal noise can be derived using the *fluctuation dissipation theorem*, first described in [20].

Consider any system in thermal equilibrium with its surroundings. If there is a mechanism for energy in a particular mode to leak out of that mode to the surroundings in the form of heat, then energy can leak back into that mode from the surrounding heat by the same mechanism. The fluctuation dissipation theorem of quantum mechanics states that the average energy flow in each direction is the same if the system is in thermal equilibrium. Thermal noise has a normal PDF and its spectral density is white. It can be modelled with a noise source in series with the impedance of the system. This noise source then has a PSD given by:

$$S_T(f) = 4kT\mathrm{Re}\,(Z(f)), \tag{3.16}$$

with k the Boltzmann's constant ($1.38{\cdot}10^{-23}$ J/K), T the temperature [K] and $Z(f)$ the frequency dependent impedance of the system. For a mechanical system the impedance is force divided by velocity, for an electric system the impedance is the ratio of voltage over current.

In electric systems the energy is dissipated in the resistors. With the theory described above, the noise from a resistor can now be described as a voltage source in series with the resistor, with a PSD of:

$$S_T = 4kTR \qquad [\mathrm{V}^2/\mathrm{Hz}], \tag{3.17}$$

with R the resistance [Ω]. To give an example, a kilo Ohm resistor, at 20° Celsius will show noise with an STD of 0.13 μV from zero up to one kHz.

[5]The effect was experimentally demonstrated by Johnson, and the theoretical analysis was given by Nyquist, both in 1928.

Shot Noise

Shot noise results from the random passage of individual charge carriers across a potential barrier. This is often seen with junctions in a transistor. The noise has a normal PDF and has a white spectral density:

$$S_S = 2q_e i_{\mathrm{dc}} \qquad [\mathrm{A}^2/\mathrm{Hz}], \tag{3.18}$$

with q_e the electronic charge ($1.6{\cdot}10^{-19}$ C), i_{dc} the average current [A]. An average current of 1 A will introduce noise with a STD of $18{\cdot}10^{-9}$ A from zero up to one kHz.

Excess Noise

The noise in excess of the thermal and shot noise when a current passes through a resistor or a semiconductor, is called excess noise (other names are *flicker* or $1/f$ noise). It results from fluctuating conductivity due to imperfect contact between two materials. This is why carbon composition resistors, which are made up of many tiny particles molded together, show more excess noise than wire wound resistors. The power spectral density of excess noise increases when the frequency decreases:

$$S_E = K_f / f^{\alpha} \qquad [\mathrm{V}^2/\mathrm{Hz}], \tag{3.19}$$

where K_f is dependent on the average (DC) voltage drop over the resistor and the index α is usually between 0.8 and 1.4, and often set to unity for approximate calculation. For resistors the excess noise is proportional to the average voltage drop $\overline{u}$ over the resistor, which is why manufacturers typically specify the excess noise as a noise index C_R [μV/V] for one frequency decade:

$$C_R = \frac{\sigma_u^* \cdot 10^6}{\overline{u}} \tag{3.20}$$

with σ_u^* the STD over one decade frequency range of the voltage and $\overline{u}$ the average voltage drop over the resistor. For standard resistors the noise index C_R typically ranges from 1 to 10. For example, if the noise index equals 10, an average voltage drop of one volt introduces noise with a STD of 17 μV in a frequency range from 1 up to 1000 Hz. Note that the frequency range 1 mHz up to 1 Hz also introduces noise with a STD of 17 μV!

The relation between K_f and C_R can be found by equalling σ_u^* from (3.20) to

the value calculated by integrating (3.19) over one decade:

$$\begin{aligned}\sigma_u^* &= C_R \bar{u} \cdot 10^{-6} \\ &= \sqrt{\int_{f_0}^{10 f_0} \frac{K_f}{f} \mathrm{d}f} \\ &= \sqrt{K_f \ln(10)}.\end{aligned} \tag{3.21}$$

Hence:

$$K_f = \frac{C_R^2 \bar{u}^2 \cdot 10^{-12}}{\ln(10)} \tag{3.22}$$

Signal to Noise Ratio

Electronic equipment does most often not come with detailed electric schemes, in which case the PSD should be determined from measurements. In the design phase however, one has to rely on information provided by specification sheets from the manufacturer. The noise performance of components like sensors, amplifiers, converters, etc., is often specified in terms of a Signal to Noise Ratio (SNR). The SNR gives the ratio the RMS value of a sine that covers the full range of the channel through which the signal is propagating over the RMS value of the electrical noise. Usually, the SNR is specified up to a certain cut-off frequency. If no information on the colouring of the noise is available, then the corresponding PSD can be assumed to be white up to the cut-off frequency F_c:

$$S_{\text{snr}} = \frac{x_{\text{fr}}^2}{8 F_c C_{\text{snr}}^2}, \tag{3.23}$$

with x_{fr} the full range of x, and C_{snr} the SNR. The SNR for electronic components is typically around 80 dB.

3.3.3 AD and DA Converters

More and more mechatronic systems utilize digital control. This introduces Analogue to Digital Converters (ADC) and Digital to Analogue Converters in the loop. Besides the electronic noise, it brings another type of noise source: quantization.

In literature the quantization errors from sampling are thought of as an additional noise signal $e(t_k)$ at each time sample t_k, see [70, 11]. For the statistical representation of the quantization error, the following assumptions are made:

- The error is a stationary random process.
- The error is uncorrelated with the signal sequence.

- The PDF of the error process is uniform over the quantization range.

According to [70] the assumptions appear to be valid if the signal is sufficiently complex and the quantization steps are sufficiently small so that the amplitude of the signal is likely to traverse many quantization steps from sample to sample.

Based on the above assumptions, the variance can be calculated to be:

$$\sigma^2 = \frac{q^2}{12}, \tag{3.24}$$

with q the quantization interval. The corresponding PSD is white up to the Nyquist frequency:

$$S_Q = \frac{q^2}{12 f_N}, \tag{3.25}$$

with f_N the Nyquist frequency [Hz].

It should be noted that quantization is fundamentally a non-linear process. For this reason it is advisable to verify the performance with time domain simulations, if quantization noise is one of the dominant disturbances.

3.3.4 Acoustic Noise

Acoustic excitation can be a big error source in high precision machines, especially when the surface is big compared to the mass (e.g. hollow structures). This section describes a way to estimate the disturbance caused by a certain sound intensity level, assuming the sound to be stochastic. The formulas presented here are from [13].

The sound intensity level L_i (in dB) is defined as:

$$L_i := 10 \log(I/I_0), \tag{3.26}$$

with I the sound intensity [$\mathrm{W/m^2}$] and $I_0 = 10 \cdot 10^{-12}$ $\mathrm{W/m^2}$. The sound intensity is defined as the expectation (considering the sound to be stochastic) of sound pressure p [$\mathrm{N/m^2}$] times the sound velocity v [m/s]:

$$I = \mathrm{E}(pv). \tag{3.27}$$

For free travelling waves, the velocity equals:

$$v = \frac{p}{\rho_a c}. \tag{3.28}$$

By substituting the above equation into (3.27), and using $\mathrm{E}(p^2) = \|p\|^2_{\mathrm{rms}}$, the following equation is found:

$$I = \frac{\|p\|^2_{\mathrm{rms}}}{\rho_a c}. \tag{3.29}$$

Now the intensity level can be related with the sound pressure level:

$$\begin{aligned} L_i &= 10\log\left(\frac{\|p\|^2_{\text{rms}}}{\rho_a c I_0}\right) \\ &= 10\log\left(\frac{\|p\|^2_{\text{rms}}}{p_0^2}\right) + 10\log\left(\frac{p_0^2}{\rho_a c I_0}\right) \\ &= L_p + 10\log C, \end{aligned} \tag{3.30}$$

where p_0 equals $2 \cdot 10^{-5}$ N/m^2 and C is a constant. For room temperature and atmospheric pressure of 1 bar, C equals approximately unity ([13, Sec.2.2.6]), thus $L_i \approx L_p$.

Given the sound intensity level and assuming that the acoustic noise is equally distributed over a certain frequency range f_Δ, the following PSD is found:

$$S_A = \begin{cases} \dfrac{p_0^2 \cdot 10^{L_i/5}}{f_\Delta}, & f \in f_\Delta \\ 0, & \text{otherwise.} \end{cases} \tag{3.31}$$

Now the disturbance force acting on a body, is the difference of pressure between the front and the back times the surface. To have a pressure difference, the body must have a certain minimum dimension, depending on the wave length of the sound. By setting the dimension d_b to a quarter of the wave length, one can calculate the frequency f_{th} below which the pressure is not fully felt by the body:

$$f_{\text{th}} = \frac{c_s}{4 d_b}. \tag{3.32}$$

So for a body of typical dimensions of 100 mm, only frequencies above 800 Hz have a significant disturbance contribution.

For example, consider a cube with a rib size of 100 mm located in a room with a sound level of 80 dB, distributed between one and ten kHz, then the force disturbance PSD equals $2.2 \cdot 10^{-2}$ N^2/Hz.

3.3.5 Brownian Noise

In mechatronic systems where a small mass needs positioning (e.g. in MEMS applications), the motion due to thermal effects becomes notable. This effect has been taken in account for geophone analysis, see [78, 81]. A derivation of the spectrum of a mechanical mass-spring system is given in [4]. The spectrum can be easily found using the fluctuation dissipation theorem (3.16), in which the impedance of a mechanical system is the dampening.

3.3.6 Turbulence

Rotation of the spindle introduces an air flow in which turbulence is caused by sharp angles on the rotor and stator. Due to this turbulence, noisy forces will act on the rotor. Calculating this turbulence for the relative complex shapes of the rotor and especially the stator was considered to be too complex to solve. Hence, turbulence is a disturbance source whose influence is left to be measured on the demonstrator.

A field in which turbulence plays an important role is adaptive optics. Turbulence in the atmosphere deforms the flat wave front of light coming from distant stars, which results in a shimmering blur for large-diameter telescopes, see [40]. In many modern telescopes the deformed wave front is corrected with an adaptive mirror, whose mirror surface can be deformed.

Various models describing the turbulence of the atmosphere have been developed, see [39]. These models show that the effect of turbulence is mainly at frequencies below one Hertz. Since the bandwidth of such systems is usually much higher, the use of DEB in the design of such systems is beneficial.

In new, very big telescopes to be build, the main mirror is so big that it is broken up into several segments. For example, in the European Extremely Large Telescope (E-ELT) design the main mirror has a diameter of 42 metres! These segments keep their mutual positions with nanometre accuracy by means of control. Because of the size of the mirror, an enclosure to protect the mirror from the wind would be very expensive. Hence, the control system must also deal with turbulent wind disturbances.

3.4 System Noise Propagation

Now that the disturbances can be modelled, next step is to consider how they propagate through the closed loop system. In this section the Single Input, Single Output (SISO) case is discussed, in Subsection 3.6.2 the formulas are repeated for the Multi Input, Multi Output (MIMO) case. Consider the system displayed in Figure 3.3. The stochastic signal $x(t)$ is the sum of two uncorrelated stochastic variables $x_1(t), x_2(t)$. Two signals are uncorrelated if their cross correlation, defined as:

$$R_{x_1x_2}(\tau) = \lim_{T\to\infty} \frac{1}{2T} \int_{-T}^{+T} x_1(t-\tau)x_2(t)\mathrm{d}t, \tag{3.33}$$

is zero. It can then be shown [76, 73] that the PSD of x is the sum of the PSDs of x_1, x_2:

$$S_x = S_{x_1} + S_{x_2}. \tag{3.34}$$

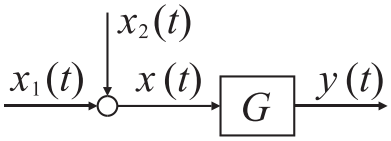

Figure 3.3. *Block scheme of a simple system.*

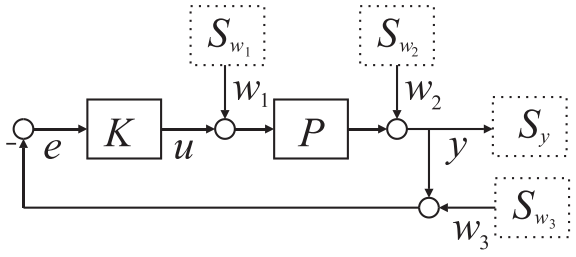

Figure 3.4. *Closed loop system with disturbances being described by their PSDs.*

Taking the integral over (3.34), leads to:

$$\sigma_x^2 = \sigma_{x_1}^2 + \sigma_{x_2}^2 \tag{3.35}$$

The signal $x(t)$ is filtered through a Linear Time Invariant (LTI) stable system G, such that $y(s) = G(s)x(s)$, with s the Laplace operator. Then the PSD of y is given by ([73, 105]):

$$S_y(j\omega) = |G(j\omega)|^2 S_x(j\omega), \tag{3.36}$$

with $\omega = 2\pi f$. So the PSD of the output signal is simply the PSD of the input signal times the Bode magnitude of the corresponding transfer function squared.

Now consider the SISO closed loop system depicted in Figure 3.4. The plant is indicated with $P(s)$ and the controller with $K(s)$. On the system disturbances act, modelled by their PSDs (indicated with the dashed blocks). If the disturbances are uncorrelated, the PSD of the positioning error output y of the system can be calculated using the equation given above[6]:

$$S_y = |SP|^2 S_{w_1} + |S|^2 S_{w_2} + |SPK|^2 S_{w_3}, \tag{3.37}$$

where $S(s) = (1 + P(s)K(s))^{-1}$ is the sensitivity function.

Taking the cumulative integral on both sides of (3.37), gives the CPS of the positioning error as well as the CPS of the contributions to the positioning error. Plotting these CPS in one graph, the designer has immediate insight into which is

[6]The the propagation of correlated signals through a system is discussed in Subsection 3.6.2

the most performance limiting disturbance and at which frequencies this disturbance is most dominant. This provides valuable information to the designer for deciding where to direct the design effort.

For the DEB approach, it is assumed that the (sub-)system can be accurately described with a linear time invariant model. This assumption is not expected to cause many problems, for the following reasons: First of all, in today's high precision mechatronic systems a lot of effort is put in to make these systems behave as linear as possible. Secondly, the mechatronic system comprises a feedback loop, which has a linearizing effect on the closed loop behaviour. Finally, many machines have a relatively small working range, which makes it more likely that the system behaves in a linear way.

3.5 Illustrative Example

To illustrate the working principle of the theory of the previous sections, it is here applied to a single directional positioning system. Since DEB can be applied to a broad range of mechatronic systems, an example not related to the design of the rotor is discussed here.

3.5.1 Description of the System

In the system a tool tip is to be positioned with respect to a stator, see Figure 3.5, with a positioning error smaller than 40 nm (RMS). The tool tip is attached to a rotor of which the remaining 5 DoFs are restrained by spring blades. The position of the rotor is measured with a sensor and is fed back to a digital controller. The controller commands the actuator, which acts between the rotor and the stator.

The total moving mass (rotor and tool tip) is 2.5 kg, of which the tool tip has a mass of 0.2 kg. The eigenfrequency of the total moving mass with the spring blades is 5 Hz. The tool tip is mounted with limited stiffness to the rotor, which results in a resonance frequency of 150 Hz. The relative damping of the spring blades and the tool tip are respectively 0.01 and $5{\cdot}10^{-3}$. The whole setup is fixed to a vibration isolation table of 500 kg supported by air mounts, with an eigenfrequency of 2 Hz and a relative damping of 0.2.

The total positioning range of the system is 1 mm, and the maximum force of the actuator is 5 N. The command for the actuator is generated by a controller running at 2000 Hz. The controller has a 16 bit Analogue to Digital Converter (ADC) which has electronic noise with a SNR of 80 dB, and a low resolution Digital to Analogue Converter (DAC) with 10 bits. The sensor shows noise with peak-to-valley noise of 0.1 μm up to the Nyquist frequency. It is assumed that the ranges of the converters matches with the ranges of the sensor and actuator. The noise

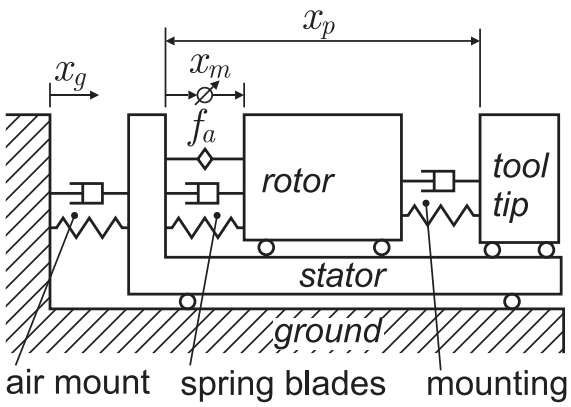

Figure 3.5. *Simplified representation of the positioning problem example. The tool tip is to be positioned with an error smaller than 40 nm (RMS) with respect to the stator.*

introduced by the electronics of the DAC and amplifier are negligible. For simplicity's sake it is further assumed that the controller has physical signals as input ([μm]) and output ([N]).

The difficulty in this case is that the allowed positioning error is specified at the tool tip which has limited stiffness, while the controller controls the position of the rotor.

In Figure 3.6 the Bode plots of the transfer function from actuator force input to the measured position (x_m) and relative position of the tool tip to the stator, the performance measure (x_p), are given for the resulting plant. The resonance frequency of the tool tip appears at 156 Hz.

3.5.2 Disturbance Modelling

In the positioning case disturbances can enter the closed loop system as sensor noise, floor vibrations and force disturbances. The details of the spectral modelling of these disturbances have been discussed in Section 3.3.

Sensor Noise

Sources that contribute to the total sensor noise are electronic noise of the sensor itself, and noise from the ADC.

Sensor electronic noise The peak-to-valley specification on the electronic sensor noise can be approximated with $\pm 3\sigma$, the standard deviation of the sensor is: $\sigma_{\text{sn}} = 17$ nm.

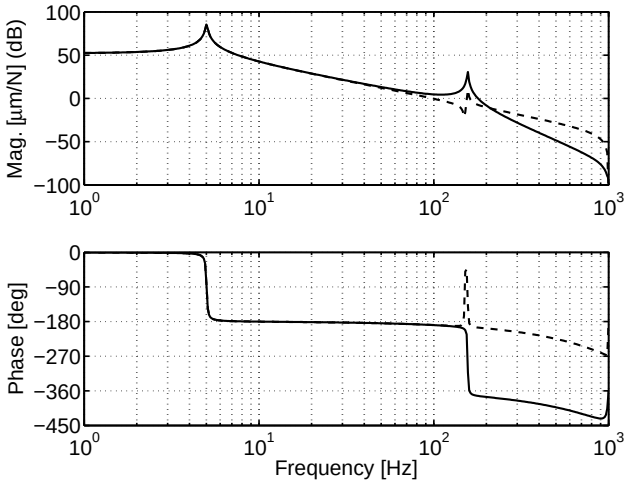

Figure 3.6. *Bode plots of the plant, from actuator force input to the position of the tool tip with respect to the stator x_p (solid), which is the performance measure and to the measured position x_m (dashed).*

ADC quantization noise The quantization noise is calculated with (3.24), where the quantization level equals the size of the Least Significant Bit (LSB). Having 16 bits over the range of 1 mm, the standard deviation from the quantization becomes $\sigma_{\text{ADq}} = 1 \cdot 10^6/2^{16}/\sqrt{12} = 4.4$ nm.

ADC electronic noise If the full range of the ADC is 1 mm, then the RMS value of a sine that covers the full range equals: $\frac{1}{4}\sqrt{2} \cdot 1 \cdot 10^3 = 354$ μm. With a SNR of 80 dB, the electronic noise from the ADC becomes: $\sigma_{\text{ADn}} = 35$ nm.

Since the three sources that contribute to the sensor noise are assumed to be white and uncorrelated to each other, they can be considered stemming from one noise source. The STD of this sensor noise can be found as follows:

$$\sigma_s = \sqrt{\sigma_{\text{sn}}^2 + \sigma_{\text{ADq}}^2 + \sigma_{\text{ADn}}^2} = 39 \quad \text{nm}, \tag{3.38}$$

from which the PSD of the total sensor noise S_s is calculated :

$$S_s = \frac{\sigma_s^2}{f_N} = 1.55 \quad \text{nm}^2/\text{Hz}, \tag{3.39}$$

in which f_N is the Nyquist frequency of 1000 Hz.

Floor Disturbances

The floor is assumed to have a PSD of 10^{-5} $[(\text{m/s}^2)^2/\text{Hz}]$ from 1 up to 200 Hz with fourth order roll-up and roll-off before 1 Hz and after 200 Hz. This spectrum

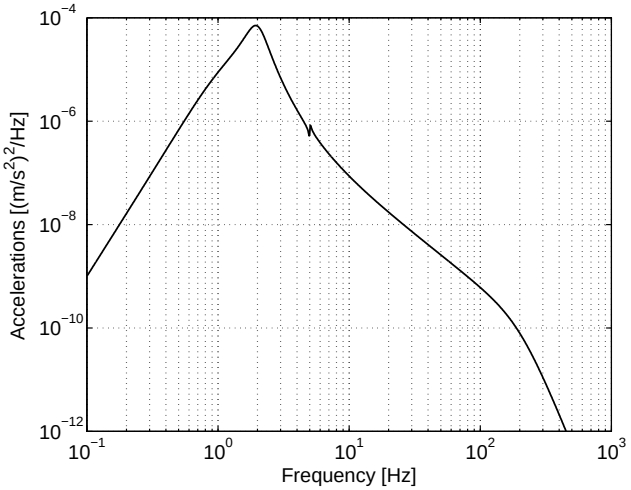

Figure 3.7. *PSD of the accelerations of the stator resulting from the floor vibrations with the system in open loop. The area corresponds to a RMS value of 8.6 mm/s*

is based on the specifications given by ASML for the excimer laser, [93], which is less demanding than the specification for the exposure unit as was given in Subsection 3.2 on page 38. Taking the cumulative integral of this floor spectrum, results in a RMS value of the accelerations of 47 $\mathrm{mm/s^2}$. Due to the vibration isolation table, the acceleration level of the stator is reduced to 8.6 $\mathrm{mm/s^2}$.

To keep the position error between the stator and tool tip close to zero, they should have the same accelerations. Assuming that the tool tip is infinitely stiff connected to the rotor, the force required to give the tool tip the same accelerations as the stator, is the accelerations of the stator multiplied by the mass of the rotor and tool tip combined. Hence, the vibrations of the stator can be interpreted as a force disturbance on the rotor. In Figure 3.7 the PSD of the accelerations of the stator is given.

Force Disturbances

Finally, the controller output with a range of ± 5 N is converted to an analogue signal by the ten bit DAC. This results in a quantization noise of 2.8 mN (RMS). Doing the calculations similarly as with the ADC, the PSD resulting from the quantization in the DAC becomes:

$$S_{\mathrm{DAq}} = \frac{\left(\frac{a_{\mathrm{PP}}}{2^{\mathrm{bits}}}\right)^2}{12 \cdot F_N} = \frac{\left(\frac{10}{2^{10}}\right)^2}{12 \cdot 1000} = 3.2 \cdot 10^{-8} \quad [\mathrm{N^2/Hz}] \tag{3.40}$$

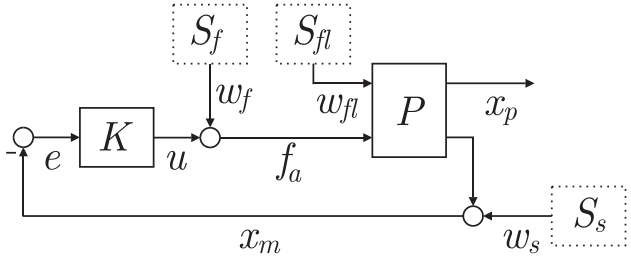

Figure 3.8. *The closed loop configuration for the one directional example, in which is indicated where the disturbances act on the loop. The subscripts* f, fl, *and* s *refer to force, floor and sensor, respectively.*

3.5.3 Controller Design and Performance Analysis

Now that the models of the system and the disturbances are known, the Dynamic Error Budgeting (DEB) approach can be applied. Figure 3.8 indicates where the disturbances enter the closed loop system. The performance is first evaluated with an initial controller, and then improved by tuning.

Initial Controller

First a standard PID-controller with a maximum phase lead of 40° at the bandwidth frequency[7] of 70 Hz is tried. The bandwidth was found by varying the bandwidth in such a way that the positioning error x_p is minimized. The Bode plot of this controller is given in Figure 3.9a. In Figure 3.9b the resulting closed loop transfer functions from the force, floor and sensor disturbances, w_f, w_{fl}, w_s, to the positioning error x_p are shown.

In Figure 3.10 the PSD and CAS of the positioning error are given. The standard deviation of the positioning error of the tool tip is 91 nm and that of the controller output (not shown) is 73 mN. From the figure it is seen that, despite the low resolution of the DAC, the contribution of the force disturbance to the positioning error is only 7.2 nm and much lower than the contributions of the floor (35 nm) and the sensor noise (84 nm). Note that the end value of the CAS equals the RMS of the signal, as was explained in Subsection 3.2.2. The CAS of the performance in Figure 3.10 is the square root of the sum of the squared CAS of the contributors, see (3.35) on page 45.

[7] The bandwidth is defined as the 0-dB crossing of the open loop gain.

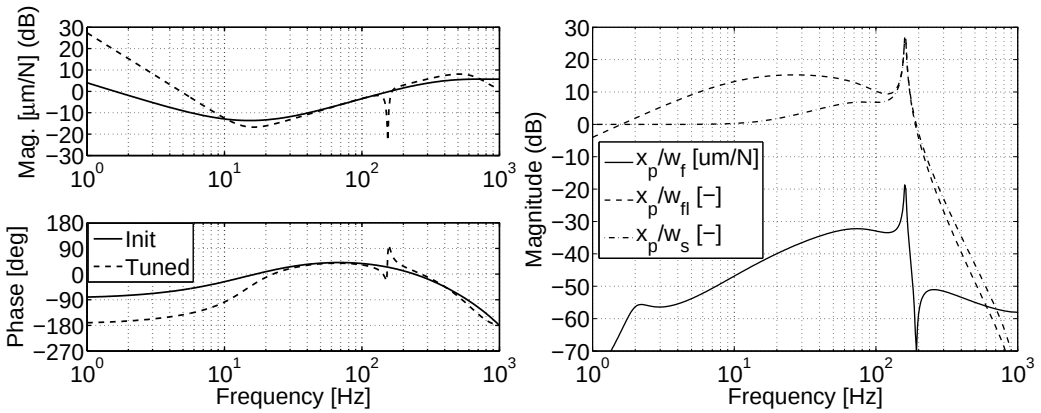

a b

Figure 3.9. *a) Bode magnitude plots of the initial and tuned controller. b) Bode magnitude plots the closed loop transfer functions from the force, floor and sensor disturbances to the positioning error with the initial controller.*

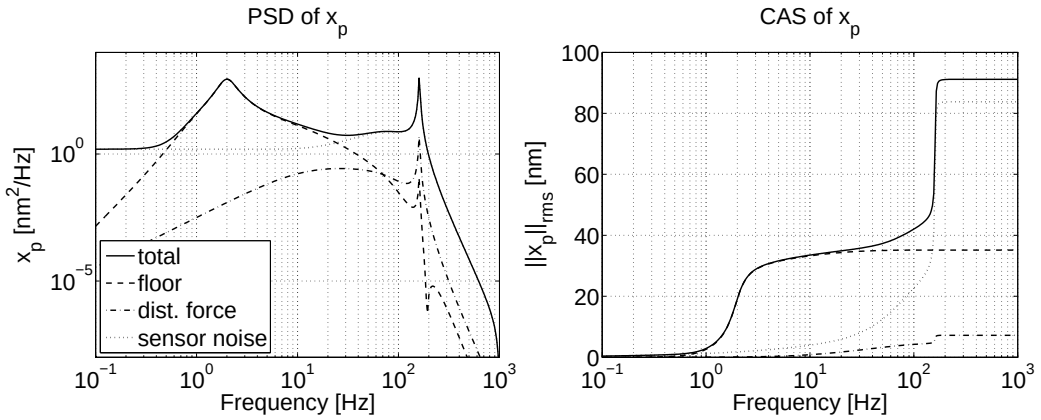

Figure 3.10. *The PSD and CAS of the positioning error of the tool tip with the initial controller implemented. The resulting positioning error is 91 nm (RMS). The STD-values of the contributions of the disturbances sources are 35 nm, 7.2 nm and 84 nm, for the floor, force and sensor, respectively.*

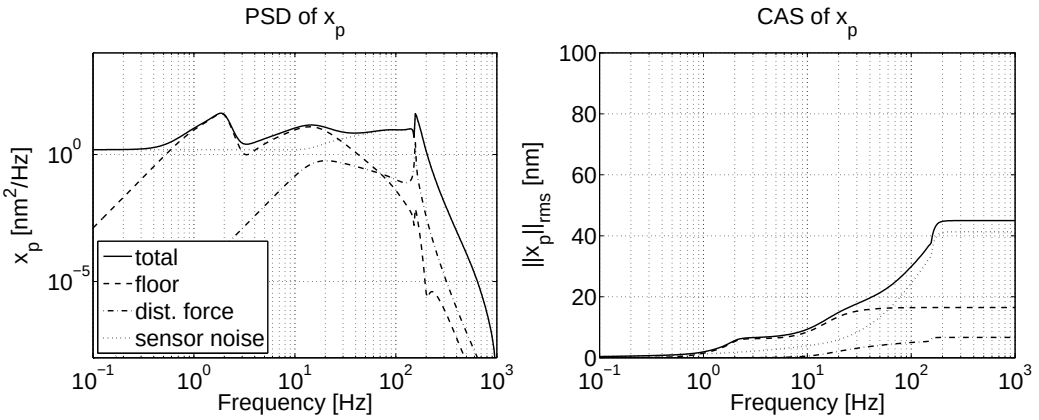

Figure 3.11. *The PSD and the CAS of the tool tip movement with the tuned controller. The resulting positioning error has improved to 45 nm (rms). The STD-values of the contributions of the disturbances sources are 17 nm, 1.7 nm and 41 nm, for the floor, force and sensor, respectively.*

Tuned Controller

From the CAS of the positioning error with the initial controller it becomes clear, that there are two major contributors: from ground vibrations up to 3 Hz and from sensor noise, mostly caused by the resonance of the tool tip at 156 Hz. Since the ground vibrations only contribute at low frequencies, an effective way of dealing with this is to add integral action to the controller, which increases the controller gain at low frequencies. The excitation of the tool tip is reduced by adding a notch filter at 156 Hz to the controller. The resulting controller is compared to the initial controller in Figure 3.9a.

Figure 3.11 gives the PSD and the CAS of the positioning error of the tool tip x_p achieved with the tuned controller. From the figure, it can be seen that the performance has improved with a factor two: $\left\|x_p\right\|_{\text{rms}} = 45$ nm. This at the cost of a slightly increased controller effort (not shown) of 79 mN. Although the contribution of the floor vibration to the positioning error has been reduced to 17 nm, the bulk of the performance improvement is achieved by a reduction of the sensor noise contribution to 41 nm.

Concluding

With an positioning error of 45 nm the target of 40 nm is almost achieved. Assuming that the tuned controller achieves the best performance possible with this system, the system must be improved to achieve the specification. Here, the DEB analysis can be used to asses the component of the system most profitable to improve.

From Figure 3.11 it is clear that the sensor noise is still the biggest contributor. Since the sensor noise was mostly due to the electric noise in the ADC, the best investment would be to improve the ADC. Other measures to improve the performance would be to lower the eigenfrequency of the vibration isolation table or to increase the stiffness of the tool tip mounting. However, an improved ADC might prove considerably cheaper than a redesign of the mechanical system.

Important to realize is that in a real system the positioning error of the tool tip can be only derived using the DEB analysis. The first reason for this is obvious, since only the relative position of the rotor and not the tool tip is measured. However, even if the sensor would be placed between the tool tip and the stator, the measured positioning error would be corrupted with noise from the sensor and associated electronics (analogue filters, ADC). For instance, if an additional identical sensor is placed between the stator and the tool tip in the example above, the measured RMS values with the initial and tuned controllers would respectively be 99 and 60 nm.

Hence, in a mechatronic system the measured servo error is an *indication* of the real servo error, valid only if the sensor noise is significantly smaller than the servo error. If this is not the case the real servo error can only be measured with an additional sensor with (much) higher resolution.

The application of DEB is shown in a relative simple example of a mechatronic system. The results indicated how to change elements in the mechatronic design in order to meet the required specifications.

3.6 Optimal Control

3.6.1 The use of Optimal Control in DEB

In the closed loop configuration of Figure 3.4, three factors influence the performance: the disturbances, the plant, and the controller. The external disturbances are often a given, and reduction of the disturbances induced by the components in the loop might only be realized with more expensive components. Also, a redesign of the plant can be costly, especially if the design is in a mature stage.

The controller on the other hand might have much freedom in design. Before pinpointing one disturbance as the source of performance limiting factor, and concentrating plant design effort on this source, it should be investigated if the controller can deal with this disturbance.

The modelling of the disturbance as stochastic variables, is par excellence suitable for the optimal stochastic control framework. In Figure 3.12 the closed loop setting of Figure 3.4 is redrawn in a so-called *generalized plant* setting. The

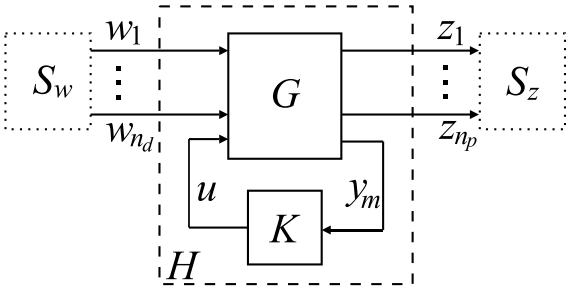

Figure 3.12. *Control system with the generalized plant G. The performance channels are stacked in z, while the controller input is denoted with y.*

generalized plant maps the disturbances to the performance channels, such as the tracking error and controller output. By minimizing the $\mathcal{H}_2$-system norm of the generalized plant, the variance of the performance channels is minimized.

The theory on optimal control has been extensively studied in the 1960's and 1970's. Optimality was based on minimizing an integral quadratic cost function in time domain, with white noise disturbances. This is called Linear Quadratic Gaussian (LQG) control, see [54], and is closely related to $\mathcal{H}_2$-optimal control (any LQG control problem can be formulated as a $\mathcal{H}_2$-control problem). The main limitation of $\mathcal{H}_2$-optimal control, namely that it lacks the formal treatment of uncertainty in the plant, caused a shift of research attention towards $\mathcal{H}_\infty$-control and μ-synthesis in the 1980's and 1990's. For a good introduction in the subject, refer to [88]. An advanced and thorough coverage of $\mathcal{H}_2$- and $\mathcal{H}_\infty$-control can be found in [105]. With the availability of solvers for so-called Linear Matrix Inequalities (LMIs), multi-objective control, which allows the use of mixed $\mathcal{H}_2$- and $\mathcal{H}_\infty$-norms on a system, has recently received a lot attention, see e.g. [85] and the references therein. The main difficulty with μ-synthesis and LMI-solvers, is the numerical conditioning for large problems (state dimension > 50).

In this thesis only $\mathcal{H}_2$-optimal control is considered.

3.6.2 MIMO Formulation of DEB

Here, the relevant equations of Sections 3.2 and 3.4 are repeated for MIMO systems.

First the autocorrelation function is redefined:

$$R_{xx}(\tau) = \lim_{T\to\infty} \frac{1}{2T} \int_{-T}^{+T} x(t-\tau)x^{\mathrm{T}}(t)\mathrm{d}t, \tag{3.41}$$

where $x(t)$ is a vector of n time signals. The non-diagonal term of the autocorrelation function thus contains the cross correlation terms. It follows that

$R_{ij}(\tau) = R_{ji}(-\tau)$ (where R_{ij} denotes the i-th row and j-th column element of R_{xx}). The PSD matrix $S_x(f)$ is then the Fourier transform of (3.41). It can be shown that S_x is *self adjoint* (or *Hermitian*), i.e. $S_x = S_x^*$, where the asterisk denotes the complex conjugate transpose operation. Next, the power norm is redefined for vectors:

$$\|x(t)\|_{\text{rms}}^2 = \left\| \begin{bmatrix} x_1(t) \\ \vdots \\ x_n(t) \end{bmatrix} \right\|_{\text{rms}}^2 = \sum_{i=1}^{n} \|x_i(t)\|_{\text{rms}}^2 . \tag{3.42}$$

Then the power (mean square) of x is given by:

$$\begin{aligned} \|x(t)\|_{\text{rms}}^2 &= \lim_{t\to\infty} \frac{1}{2T} \int_{-T}^{+T} x(t)x(t)^{\mathrm{T}} \mathrm{d}t \\ &= \text{Tr}\left(R_{xx}(0)\right) \\ &= \int_{-\infty}^{\infty} \text{Tr}\left(S_x(f)\right) \mathrm{d}f \end{aligned} \tag{3.43}$$

For multivariate signals the propagation rule (3.36) becomes:

$$S_y(f) = G(j2\pi f) S_x(f) G^*(j2\pi f). \tag{3.44}$$

3.6.3 Optimal Control Formulation

The $\mathcal{H}_2$-norm of a system G, $\|G\|_2$, is defined as the RMS norm of the output y, when a white input x with unit spectral density, i.e. $S_x = I$ is applied. Thus:

$$\|G\|_2^2 = \|y\|_{\text{rms}}^2 = \int_{-\infty}^{\infty} \text{Tr}\left(G(j2\pi f) G^*(j2\pi f)\right) \mathrm{d}f \tag{3.45}$$

To put it in words, for a SISO system the $\mathcal{H}_2$-norm is the area of Bode magnitude squared. It is clear that the $\mathcal{H}_2$-norm is only bounded if and only if G is strictly proper and asymptotically stable.
The optimal controller minimizes the $\mathcal{H}_2$-norm of the closed loop system of Figure 3.12, assuming white noise disturbances:

$$K \in \arg\min_K \|G(j2\pi f)\|_2 , \tag{3.46}$$

where the notation *arg min* denotes a minimizer of the objective function. The solution of (3.46) is computational effectively found through solving two Ricatti equations, see [23, 105], which result in a unique optimal controller.

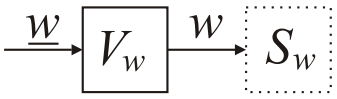

Figure 3.13. *The use of a weighting filter V_w to colour the white noise input $\underline{w}(t)$ such that the output $w(t)$ has a desired PSD S_w.*

3.6.4 Using Weighting Filters for Disturbance Modelling

Since many real life disturbances are not white, but coloured, the system of Figure 3.12 needs to be augmented with so-called disturbance weighting filters. A disturbance weighting filter gives the disturbance PSD when white noise as input is applied. This is illustrated in Figure 3.13. A vector of white noise time signals $\underline{w}(t)$ is filtered through a weighting filter to obtain the coloured physical disturbances, stacked in vector $w(t)$, with the desired PSD matrix S_w. The normalized disturbances are denoted by $\underline{w}(t)$[8]. The normalized signals are dimensionless, so the weighting filter has the unit of the physical signal.

The generalized plant framework also allows to include weighting filters for the performance channels, which is especially useful in multi-variable systems. First of all, the performance channels might have different dimensions, which require scaling in order to compare. Secondly, some performance channels may be of more importance than others and, thirdly, by using dynamic weighting filters, one can emphasize the performance in a certain frequency range.

The weighting filters should be stable transfer functions, otherwise the generalized plant is not stabilizable (in case of unstable disturbance weighting filters) or undetectable (in case of unstable performance weighting filters).

With the use of the weighting filters Figure 3.12 becomes Figure 3.14.

Obtaining the Weighting Filters

If the PSD is given as a function, $S_x(j\omega)$, the disturbance filter can be found using *spectral factorization*. The SISO spectral factorization problem can be stated as (from [73, p.402]):

> Given a positive even function $S_x(f)$ of finite area, find a minimum-phase stable function L(s), such that $|L(j2\pi f)|^2 = S(f)$[9].

[8] This notation deviates from literature on modern control, where $\underline{w}(t)$ usually denotes the unscaled (physical) disturbance.

[9] If the PSD is diagonal (uncorrelated signals), a more pragmatic approach is to take the square root of the data, and fit a stable function.

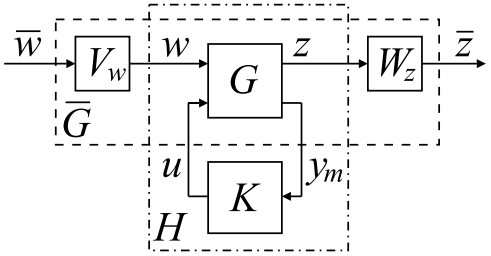

Figure 3.14. *Control system with the generalized plant G and weighting functions. The performance channels are stacked in z, while the controller input (the measured outputs) is denoted with y_m.*

A MIMO formulation of the spectral factorization problem can be found in [105, Section 13.4].

Several methods have been developed for the computation of spectral factorizations. An overview of such methods in given in [84], which focusses on scalar spectra, but some of the discussed methods can be extended to vector-valued spectra.

The weighting filters can be directly found by using parametric time models for spectral analysis, see Subsection 3.7.2.

Harmonic Signal Modelling

Harmonic signals can be approximately modelled by filtering white noise with a badly damped second order system, having a +1 slope below the resonance frequency and a -1 slope above the resonance frequency:

$$V_h = \frac{s}{s^2 + 2\zeta\omega_h + \omega_h^2}, \tag{3.47}$$

with ζ the relative damping and ω_h the resonance frequency [rad/s]. By choosing ζ small (10^{-3}–10^{-2}), the resulting PSD will show a (very) sharp peak[10]. By making the $\mathcal{H}_2$-norm of V_h equal to the RMS-value of the sinus, the propagation of the disturbance to the performance channel can be well approximated.

3.6.5 Balancing Control Effort vs Performance

If only the output(s) y of Figure 3.4 are considered in the performance channel z, the resulting optimal controller might result in very large actuator signals. So, to

[10]Note that ζ cannot be made arbitrary small, since this will lead to numerical problems in the $\mathcal{H}_2$-controller synthesis.

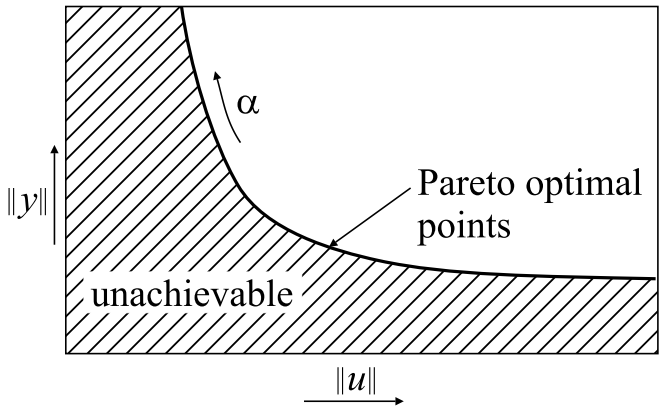

Figure 3.15. *An illustration of a Pareto curve. Each point of the curve represents the performance obtained with an optimal controller. The hatched area is not achievable and the area above the curve is not optimal. The curve is obtained by varying the scaling parameter* α *and calculating an* $\mathcal{H}_2$ *-optimal controller for each* α*.*

obtain feasible controllers, the performance channel is a combination of controller output(s) u, and the system output y. By choosing suitable weighting filters for y and u, the performance can be optimized while keeping the controller effort limited.

The performance and controller effort can be balanced systematically, as described in [18, Sec.12.1] and [59, Sec.7.4]. By augmenting the controller output u in the generalized plant (Figure 3.14) with an additional weighting scalar α, the norm that is minimized becomes:

$$\|z\|_{\text{rms}}^2 = \left\| \begin{bmatrix} y \\ \alpha u \end{bmatrix} \right\|_{\text{rms}}^2 = \|y\|_{\text{rms}}^2 + \alpha \|u\|_{\text{rms}}^2 . \tag{3.48}$$

By calculating $\mathcal{H}_2$-optimal controllers for increasing α and plotting the performance $\|y\|$ vs. the controller effort $\|u\|$, the curve as depicted in Figure 3.15 is obtained. Each point on this curve is Pareto optimal, i.e. demanding less controller effort with the same performance or more performance with the same controller effort is not feasible. Hence, choosing a controller on the Pareto curve with $\|u\|_{\text{rms}} = a$, equals the controller found by:

$$K \in \arg \min_{\substack{K \\ \|u\|_{\text{rms}} \leq a}} \|y\|_{\text{rms}} . \tag{3.49}$$

3.6.6 Practical Considerations

Discrete Time Optimal Control

For the calculation of the optimal controller for DEB, discrete time synthesis is recommended for the following reasons. Firstly, today many mechatronic systems make use of digital control. Direct discrete time synthesis would omit the transformation from continuous to a discrete time controller.

A second reason is based on the Bode-sensitivity integral. The Bode-sensitivity integral states that the integral from zero to infinite frequency of the log of the sensitivity magnitude equals zero (in case of a stable system or equals π times the sum of the real parts of the unstable poles), see [92, 31, 88]. In his excellent Bode lecture ([92]), Stein calls the quantity $\ln|S(j\omega)|$ "dirt", that can be moved around, but is conserved no matter how good the controller is. Hence, disturbance suppression in one frequency region results in an equal amount of disturbance magnification at another frequency region. This phenomenon is also referred to as the "waterbed" effect.

The continuous time $\mathcal{H}_2$-controller might achieve very good disturbance rejection by distributing the dirt over an infinite frequency range. With discrete time synthesis the dirt can only be distributed up to the Nyquist frequency.

The third reason is for the designer's convenience. In case a disturbance is white (which is often the assumption in the design phase), for continuous synthesis the disturbance filter should be made strictly proper by adding a cut-off filter. The choice of the cut-off frequency is arbitrary but has rather a large influence of the modelled power in the disturbance. Furthermore, adding cut-off filters to the models results in an increased order of the controller. Discrete time synthesis allows to use filters with a direct feed-through (non-zero D-matrix in the state space realization).

Order Reduction

The optimal controller will have the same order as the generalized plant, i.e. the order of the plant plus the orders of the weighting filters. This might easily be too high for practical implementation. Order reduction techniques are discussed in [88, Chapter 11] and [105, Chapter 7&8]. In [101, Chapter 7] the author motivates that closed loop controller reduction is preferable, since only the input/output behaviour of the closed loop system is relevant. Closed loop order reduction is the subject of [102], and the tools resulting from this research are available in a MATLAB® toolbox. Refer also to [103] and the references therein for closed loop order reduction.

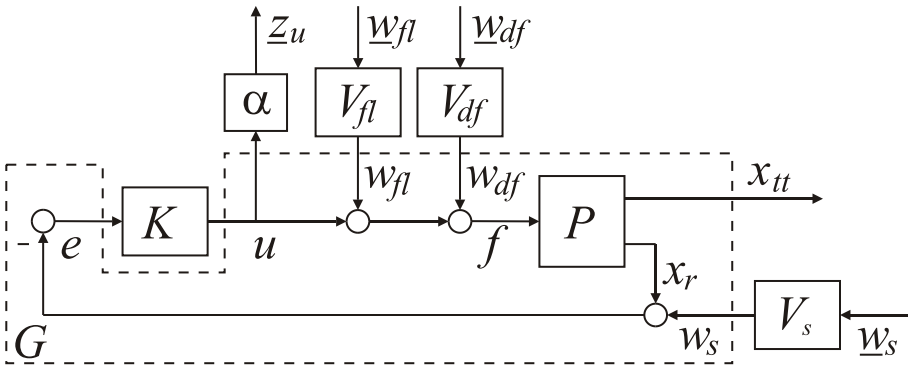

Figure 3.16. *The generalized plant configuration for the example of Section 3.5.*

Standard Assumptions

Synthesis of the optimal controller is only possible when the generalized plant fulfills the standard assumptions, which are extensively discussed in [88, Section 9.3] and [105, Sections 17.1 and 21.7] and are therefore not repeated here.

3.6.7 Optimal Control Applied to the Positioning Example

In the one directional positioning example of Section 3.5 it was assumed that the performance achieved with the tuned controller could only be improved by using better components. With the theory of optimal control this assumption can be validated.

First the system is put in the generalized plant configuration, as shown in Figure 3.16. The generation of the weighting filters is relatively straightforward in this example; except for the floor vibrations, all disturbances are assumed to be white noise and the weighting filter can be modelled with a gain:

$$V_d = \sigma_d \sqrt{T_s}, \tag{3.50}$$

in which V_d is the weighting filter of the disturbance, σ_d the STD of the concerning disturbance and T_s the sampling time. The weighting filter of the floor vibrations has second order roll-off before 1 Hz and after 200 Hz.

The discrete $\mathcal{H}_2$-controllers used here are calculated with the SLICOT-package, see [35], using the function `dishin.m`. The algorithm is based on the formulas from [105, Chapter 21].

In Figure 3.17 the Pareto curve for this system is given. A sharp improvement of the performance is seen at a controller effort of 22 mN. This makes sense, since the RMS of the accelerations of the stator multiplied by the combined mass of the rotor and tool tip, equals 22 mN. It appears that the $\mathcal{H}_2$-controller is very

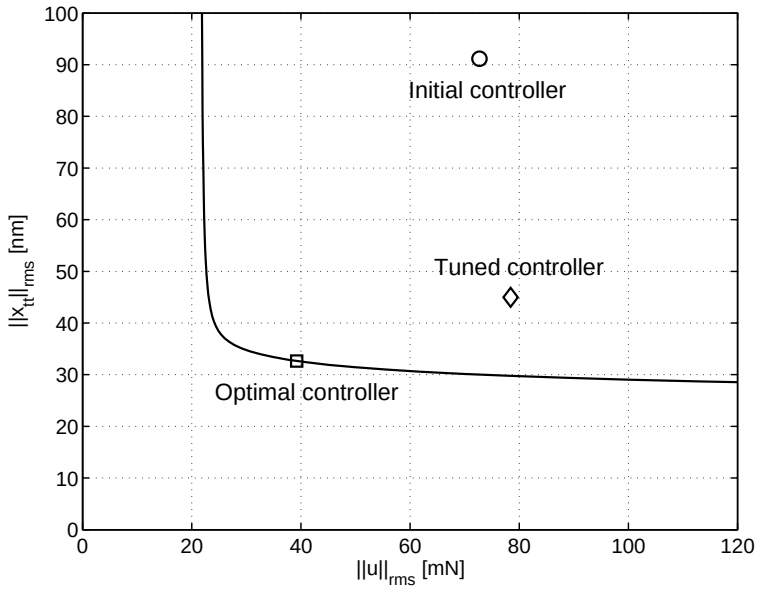

Figure 3.17. *The Pareto curve for the example of Section 3.5. The circle, diamond and square indicate respectively the performance with the initial controller, the tuned and the optimal controller.*

efficient in dealing with the floor disturbances. In the figure the initial and tuned controllers of the previous section are also given. To select a controller from the Pareto-curve, a controller with an effort of 39 mN is chosen (half the effort of the tuned controller).

In Figure 3.18 the PSD and CAS of the performance achieved with the optimal controller is given. It is seen that the optimal controller achieves a positioning error of 33 nm (RMS), with contribution of the floor of 19 nm, the DAC of 8.6 nm and the sensor of 25 nm. Note that the contribution of the sensor noise to the positioning error is smaller than the sensor noise itself, which was 39 nm (RMS). Hence, the achieved performance is better than one would suspect from the sensor signal. To obtain a better estimation of the performance, the measured performance should be filtered with the complementary sensitivity function of the closed loop system.

In Figure 3.19 the tuned controller of the previous section is compared with the optimal controller. It can be seen that the optimal controller has a lower gain for all frequencies, which results in a bandwidth of only 53 Hz, compared to the bandwidth with the tuned controller of 70 Hz. Because of the lower bandwidth achieved, less power of the sensor noise is propagated to the performance channel. Hence, increasing the bandwidth does not necessarily lead to a better performance!

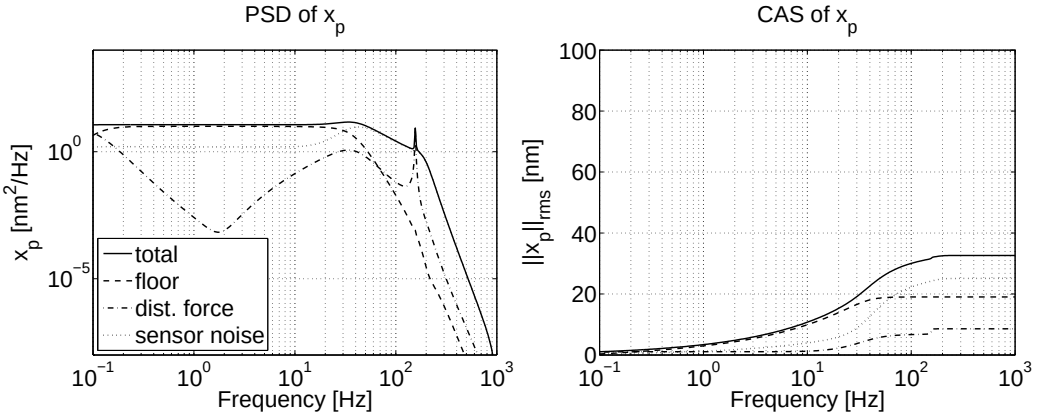

Figure 3.18. *The PSD and the CAS of the tool tip movement with the optimal controller.*

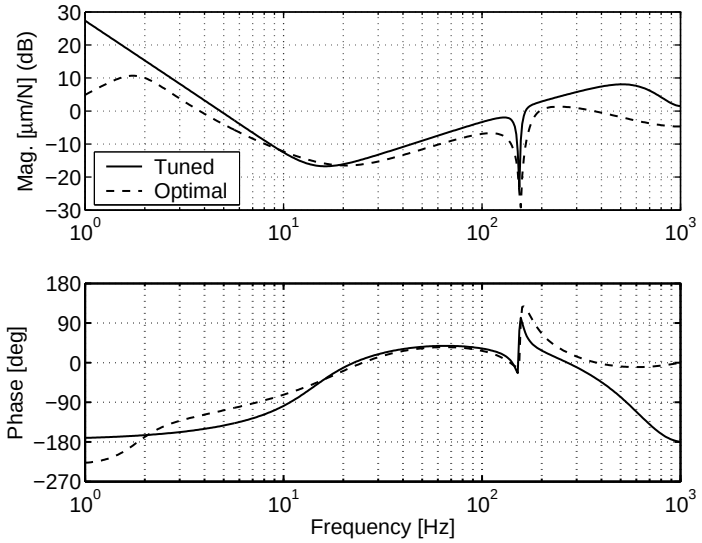

Figure 3.19. *Comparison of the tuned controller and the optimal controller.*

3.7 DEB in Practice

3.7.1 On Stochastic Assumptions

Stationarity

In practise the assumption that the PSDs are stationary with respect to time, can be dealt with by applying some sort of averaging of the measured PSDs over longer periods of time. For example, when ground vibrations are modelled, it is customary to measure the worst case PSD over a few hours, sometimes even a whole day, see [32, Chapter 5].

Probability Distribution

It should be noted that the calculation method makes no assumption on the distribution of the probability distribution functions of the disturbances. In practise, many (stochastic) disturbances will have a normal-like distribution. Although not all disturbances have a normal distribution, the performance output channel is most likely characterized accurately with a normal distribution; the performance channel is the sum of contributions by many disturbances, the *Central Limit Theorem*, see e.g. Priestley [76, p95] and Papoulis [73, p266] then states that the output will approach a normal distribution as the number of disturbances goes to infinity.

Correlation Between Signals

Especially for a MIMO systems it is likely that disturbances, like e.g. ground vibrations are correlated. This means that in practice much effort should be put in to make accurate modelling of the disturbance environment in which the mechatronic system operates.

3.7.2 On Power Spectrum Density Analysis

Mixed Spectra

When considering signals with a non-zero mean (DC-component), the PSD function will show an infinite peak (which can be represented with a Dirac pulse[11]) at $f = 0$. The same thing happens when periodic signals are present; the (two sided) PSD of a sinusoidal signal with frequency f_0 will consist of Dirac pulses at $-f_0$ and f_0. Periodic disturbances are introduced into the system, e.g. by electrical pick-up noise of the power grid (typically at 50 or 60 Hz, and higher harmonics),

[11] The Dirac function $\delta(x)$ has the fundamental property that: $\int_{-\infty}^{\infty} f(x)\delta(x-a)\mathrm{d}x = f(a)$

vibrations (through ground) from rotary or other vibrating machines and acoustic pick-up.

A simple way to avoid the Dirac pulse stemming from analysing a signal with a non-zero mean, is to only consider the AC part of the signal (subtracting the mean)[12]. The impact of DC signals on the closed loop performance is easily calculated with the static gain of the system. Furthermore, since often an integrator is used in the controller of mechatronic systems, the presence of DC-signals have very limited influence on the performance.

In practise the PSD is calculated discretely and the Dirac pulse will not be infinite because the energy content is distributed over a (small) frequency bin. There is no difficulty in using these "mixed" PSDs for analysing the performance using DEB.

If the designer wants to use optimal control for the DEB, the disturbances should be modelled. On way to model the periodic disturbances is to use a badly damped second order system, as discussed in Subsection 3.6.4. Another approach is to discard the contributions of the periodic parts of the signals in the DEB analysis and only model the stochastic part of the disturbances. The impact of the periodic parts on the performance can then be easily evaluated using more conventional methods.

Spectral Estimation

The modelling of disturbances is called spectral estimation. There are two main methods for spectral analysis, 1) non-parametric using periodograms and 2) parametric using time series models.

The periodogram, see [76], is best to be used for analysing periodic signals, as motivated by [19]. Due to the extreme computational efficiency of the Fast Fourier Transform (FFT), the periodogram is often used for estimating the PSD of stochastic processes. Because the FFT algorithm considers the data to be periodic (treating the first and last observation as neighbours), averaging over multiple periodograms and data tapering or multiplication of the data with a window, are measures required to improve the quality of the estimation. The selection of the appropriate windows is extensively covered in [62, Ch.5],[76, Ch.7] and [73].

Parametric spectral analysis assumes the measured data is the result of filtering through a linear filter. The filter may be of one of the following types: 1) autoregressive, 2) moving average, or 3) both. Looking at the $\mathcal{Z}$-transformation of the filters, an autoregressive filter only has poles and a moving average filter only has

[12]This is identical as defining the PSD by the Fourier transformation of the autocovariance $C_{xx}(\tau)$: $C_{xx}(\tau) = R_{xx}(\tau) - \bar{x}^2$

zeros. Any stationary stochastic process can be written as an unique autoregressive or moving average filter of infinite order [76]. Main difficulty in using this identification method is the selection of the order. It is motivated in [19] that parametric analysis is the preferred method for pure stochastic processes. However, in practice periodic components are often present, in which case FFT analysis might prove more reliable.

3.8 Conclusions

In the mechatronic design procedure suggested in Chapter 2 on page 13 the integral evaluation of plant, controller and disturbances is suggested, here denoted as Dynamic Error Budgeting (DEB). To enable DEB a quantitative description of disturbances is introduced. For disturbance sources that often occur in mechatronic systems practical examples of describing models are given.

The use of these models is shown in the analysis of a simplified system for positioning. From this example the potential benefit of DEB during the design phase can be understood.

Finally, the DEB approach is coupled to the field of $\mathcal{H}_2$-optimal control. The quantitative description of the disturbance prove to be a powerful method to select proper weighting filters of the inputs to the system. Applying $\mathcal{H}_2$-optimal control to the case of the simplified system helped to derive a controller that achieves increased performance at low controller effort. This allows to make more systematic design decisions, since it eliminates a degree of freedom over which the performance can be optimized.

The DEB approach, which was extensively treated here, shall be applied to the design of the rotating prototype in Chapter 5 on page 95.

4

Non-Linear Active Magnetic Bearing Technology

Starting point for the design of the rotor is the use of active magnetic bearing technology, as was stated in Chapter 1. Active magnetic bearings use Reluctance Type Actuators (RTAs) which have a strong non-linear behaviour with respect to the current and the air gap. The technology that is commonly applied to linearize these RTAs results in constant power dissipation and a strong mechanical coupling. Especially the latter effect is contradicting the concept choice to separate the force and the metrology frame, which require low stiffness actuators, as discussed in Chapter 2. In this chapter a Non-Linear Compensation (NLCs) scheme is proposed which minimizes these effects. The sensitivity of NLC to parameter changes is analysed and the approach is validated on two experimental setups.

4.1 Introduction

One of the starting points in the design of the rotating demonstrator, as were discussed in Section 2.4, is the use of an active magnetic bearing system with Reluctance Type Actuators (RTAs). Another starting point discussed in the same section is the concept of separation of the force and metrology frame. Hence, the reaction forces of the RTAs are exerted to a different frame as to which the position of the rotor is measured. This concept works better when the mechanical stiffness of the actuators are reduced. In this section the difficulties in using RTAs in a system with separated force and metrology frame are discussed.

The forces in Active Magnetic Bearings (AMBs) are (usually) generated by Reluctance Type Actuators (RTAs). An RTA consists of an electro-magnet, gener-

ating the magnetic flux, and a target on which the force is exerted. The core of the electro-magnet and the target is usually made of some ferromagnetic material to increase the magnetic flux density.

In Appendix A on page 159 it is shown that the force of a reluctance type actuator (Figure A.1) is approximated by:

$$f_{\text{rta}} \approx k_{\text{rta}} \frac{i^2}{x_g^2}, \tag{4.1}$$

with f_{rta} the force exerted by the RTA acting to decrease the air gap, k_{rta} a constant dependent on the geometry and material properties of the RTA, i the current through the coil, and x_g the air gap. In literature the term AMB is often used without a clear definition. Throughout this report the following definition will be used:

Definition 4.1 (Active Magnetic Bearing) *An active magnetic bearing is a system in closed loop which restricts at least one degree of freedom of a moving body in a mechanical system with respect to a reference coordinate frame, using reluctance type actuators.*

In the above definition the reference coordinate frame need not to coincide with the force frame on which the reaction forces of the RTAs act. This is the case for the rotating demonstrator, where the reference coordinate frame coincides with the metrology frame. With the rotor following the metrology frame, movement of this frame leads to varying air gaps at the RTAs.

4.1.1 Important Criteria

As can be seen by (4.1), an RTA has fundamentally a non-linear behaviour. As such standard control techniques cannot be used, since they require linear systems. Hence, the behaviour of the RTA should be linearized. In high precision mechatronic machines, the following points are important for the linearization.

Linearity

The linearity of a system is an important property for three reasons. Firstly, if the gain of the actuator varies too much within the operating range, the stability of the feedback loop is endangered.

Secondly, in machines in which feedforward is crucial for the performance the allowed gain variation is much smaller. Since feedforward is based on open loop compensation, a gain variation would directly result in an error, which needs to be compensated for by the feedback loop.

Finally, a non-linearity in the system tends to distort the input signal, such that higher harmonics are introduced. The higher harmonics are disturbances, which also need to be suppressed by the feedback loop.

Mechanical Stiffness

In machines in which the metrology frame is separated from the force frame, the mechanical stiffness between the rotor and the force frame should be minimized, as has been discussed in Section 2.4.

By taking the partial derivative of (4.1) with respect to the air gap, gives the mechanical stiffness introduced by a single RTA:

$$k_x = \frac{\partial f_{\text{rta}}}{\partial x_g} = 2k_{\text{rta}}\frac{i^2}{x_g^3} = 2\frac{f_{\text{rta}}}{x_g}. \tag{4.2}$$

Hence, reducing the current with a factor three would reduce the stiffness nine times.

Force Slew Rate

In machines which need to follow a certain trajectory, the force slew rate needs to be considered. The *force slew rate* (FSR) of an actuator is defined as the maximum change in force over time. Now the time derivative of the RTA force is given by:

$$\frac{\mathrm{d}f_{\text{rta}}}{\mathrm{d}t} = \frac{\partial f_{\text{rta}}}{\partial i}\frac{\mathrm{d}i}{\mathrm{d}t} + \frac{\partial f_{\text{rta}}}{\partial x_g}\frac{\mathrm{d}x_g}{\mathrm{d}t} \tag{4.3}$$

Neglecting the last velocity dependent term, the worst case force slew rate as function of the current is given by:

$$\text{FSR} = \min_x \frac{\mathrm{d}f_{\text{rta}}}{\mathrm{d}t} = \min_x \left(\frac{\partial f_{\text{rta}}}{\partial i}\right) \max\left(\frac{\mathrm{d}i}{\mathrm{d}t}\right) = 2k_{\text{rta}}\frac{i}{x_{max}^2}\frac{u_{max}}{L}, \tag{4.4}$$

where x_{max} is the maximum air gap [mm] for which the RTA is designed to operate, L is the inductance [H] of the coil and u_{max} the maximum driving voltage [V] of the current amplifier. Thus, the FSR becomes zero when no bias current is applied, see also [98].

Dynamic Properties

Equation (4.1) does not take into account dynamic behaviour due to magnetic effects such as eddy currents and hysteresis. To justify this simplification, effort

must be made to reduce these effects. For example, lamination or the use of materials with a low conductivity can be used to reduce the eddy currents and special materials should be selected to minimize the hysteresis effects.

The inductance of the coil can also have severe dynamic implications for the current amplifier. The maximum supply voltage limits the frequency at which the amplifiers works linearly for big amplitude signals, while the inductance usually limits the achievable current loop bandwidth in terms of phase loss. The latter is of more importance, since at higher frequencies the demanded control currents (forces) are small due to the inertia of the mass controlled. Hence, the amplifier should be selected or designed such that the current bandwidth does not limit the bandwidth of the system.

Linearization techniques can be divided into two main groups; *Bias Current Linearization* and *Non-Linear Control*. These two techniques will be discussed in the following two sections.

4.2 Bias Current Linearization

Since an RTA can only provide attracting forces, additional RTAs (or gravity) are used in an AMB, a possible configuration is shown in Figure 4.1. Common practise to linearize the system is to use a bias current i_b and linearize around the nominal operating point x_{nom}. Usually, the bias current is half the maximum current, which pre-loads the system with a quarter of the maximum force. The control current i is added to the bias current of the RTA acting in the positive force direction and subtracted from the bias current of the RTA acting in negative direction. For the configuration of Figure 4.1, the force acting on the rotor then becomes:

$$f(i,x) = f_1 + f_2 = k_{\text{rta}} \left(\frac{(i_b+i)^2}{(x_{\text{nom}}-x)^2} - \frac{(i_b-i)^2}{(x_{\text{nom}}+x)^2} \right), \tag{4.5}$$

in which f_1 and f_2 are the forces generated by the upper and lower RTA, respectively. This equation is linearized by truncating the Taylor's series expansion after the first order term:

$$\begin{aligned} f(i,x) &\approx f(0,0) + \frac{\partial f}{\partial i} i + \frac{\partial f}{\partial x} x \\ &\approx 4k_{\text{rta}} \frac{i_b}{x_{\text{nom}}^2} i + 4k_{\text{rta}} \frac{i_b^2}{x_{\text{nom}}^3} x = k_i i + k_x x \end{aligned} \tag{4.6}$$

An important property of linearization via current biasing is the stiffness term k_x. The term is corresponds to a mechanical spring with a negative stiffness, which

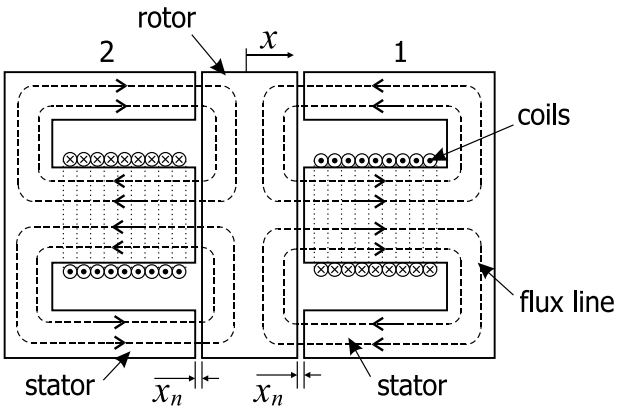

Figure 4.1. *An Active Magnetic Bearing (AMB) configuration with two Reluctance Type Actuators (RTAs) for actuation of one Degree of Freedom (DoF).*

implies that the bearing system is unstable. Hence, to stabilize the bearing system, active control should be applied to add positive stiffness.

Note that (4.6) is exact when the rotor is at the nominal position ($x = 0$). When moving away from the nominal position, (4.6) quickly loses its validity, which is why the working range with bias current linearization is only a fraction of the air gap.

For application in ultra high precision machines, linearizing RTAs with a bias current brings about three major disadvantages, namely continuous energy dissipation, a negative stiffness and a small working range.

Small working range

The approximation given by (4.6) is accurate when the rotor is at the nominal position, but quickly looses accuracy when the rotor moves away from the nominal position. As a result, the tracking performance of linear control strategies deteriorate rapidly with increasing deviations from the nominal operating point, potentially making the system unstable, see [95, 55].

Continuous energy dissipation

Due to the resistance of the coil in the RTA, a bias current results in a continuous dissipation of energy in the system. Temperature gradients in the system results, which leads to mechanical deformations of the system due to non-zero temperature expansion coefficients of the materials used. When the system operates under vacuum conditions, these temperature gradients increase, since then there is no more heat transport through air and the transport of heat is limited to radiation

and conduction through solid material. Hence, the generation of heat in high precision machines should be minimized.

The flux generated by the bias current, can also be generated by using permanent magnets. This has been used in magnetic bearing design by many researchers, see e.g. [60, 64].

Negative stiffness

In many ultra high precision machines, such as the rotating demonstrator, the accuracy is achieved with respect to a metrology frame, while the reaction forces of the actuators act on a separate force frame. In these kind of machines, mechanical stiffness of an actuator introduces disturbance forces due to the coupling of vibrations in the force frame.

Another drawback is the fact that this stiffness is negative. This makes the open loop system unstable and inherently more difficult to control, see [92].

These undesirable factors lead to the demand for other linearization techniques in ultra high precision machines. Instead of making the system linear by physical means, the non-linear behaviour of the RTAs can also be linearized by the controller, resulting in non-linear controllers.

4.3 Overview of Non-linear Control

In literature four methods based on non-linear control have been encountered to linearize RTAs. These are:

- gain scheduling,
- sliding mode control,
- integrator backstepping and
- feedback linearization.

Gain scheduling relies on successive linearization at various operating points with a suitable controller designed for each of these operating points [52]. In [14], the authors apply the approach to a high speed AMB spindle. In order to have longer ranges of travel, the operating range needs to be broken up into (very) fine intervals, and the corresponding controller gains stored in (possibly large) lookup tables.

With *sliding mode control* (also called *variable structure control*) the system is stabilized by a controller which switches between two unstable modes. This method has been successfully applied to experimental setups, see [37]. In [21] the method is compared to *input-output linearization* applied to an inertial flywheel

with two AMBs. It is questionable, whether a switching approach is suitable in high precision applications.

A quite recent approach is *integrator backstepping*. The key idea of integrator backstepping, is to start with a system which is stabilizable with a known feedback law for a known Lyapunov function and then to apply integrators to the input to increase the complexity [53]. This approach has been applied to simulated AMB systems in [77, 98].

Most of the above mentioned literature focusses on reducing the power loss resulting from the bias linearization. The need for a bigger working range and the reduction of mechanical stiffness receives much less attention in the above methods. To take into account these factors, the non-linear controller should have information on the air gap. *Feedback linearization* provides a frame work that is very suitable for using air gap information, which is why this point is more extensively elaborated.

4.3.1 Feedback Linearization

The goal of feedback linearization is to transform the original control inputs of the system into virtual control inputs, using an *inner loop*, in order to linearize the dynamic relation between these new control inputs and the outputs of the system to be controlled. The theory of feedback linearization is extensively covered in [91] (which also describes variable structure (sliding mode) and adaptive control), and [68]. A nice introduction is given in [32].

The advantage of feedback linearization is that it inherently takes into account the position information to linearize the system, making it a suitable frame work increase the working range and to reduce the mechanical stiffness. Disadvantages of feedback linearization are that the non-linear feedback can be very complicated [68] and that it can be quite sensitive to parameter variations and unmodelled dynamics, see [36, 7, 95].

Feedback linearization has been developed for systems with voltage control [55] and current control. Linearization feedback using voltage control involves dynamic compensation (frequency dependent) and is generally more complex than when current control is used, which allows static compensation, see [45]. In [95] the authors apply feedback linearization to a one DoF AMB. They show that a much larger operating range is possible without stability problems. The same approach is applied to a six DoF stage in [57], where sub-nanometre accuracy was achieved.

In [96] the authors refer to (static) feedback linearization with current control as Non-Linear Compensation (NLC), a term which is adapted in this thesis.

The literature on feedback linearization that has been discussed here, rely on a Digital Signal Processor (DSP) for the computations. Since digital control is more and more utilized in mechatronic systems and DSPs are becoming more and more cost effective, digital control will be used in this research.

4.4 Working Principle of NLC

In this section the application of NLC for a single RTA, two RTAs with one DoF and and active magnetic bearing system with multiple DoFs and RTAs will be discussed.

The working principle of NLC is sketched in Figure 4.2. With an inner feedback loop the NLC linearizes the RTA, such that the outer loop (with controller K) controls a Linearized Reluctance Type Actuator (LRTA).

4.4.1 Single Reluctance Type Actuator

First consider an actuator consisting of a single RTA (see Figure 4.3). Since an RTA only generates an attracting force, applying a preload force is necessary. A single RTA can be preloaded using for example the gravity or a spring. Assuming that the behaviour of the RTA is accurately described by (4.1);

$$f_{\text{rta}}(i, x_g) = k_{\text{rta}} \frac{i^2}{x_g^2}, \tag{4.7}$$

than the Non-Linear Compensation (NLC) function of Figure 4.2 simply becomes:

$$i_{\text{nlc}}(f_r, x_g) = x_g \sqrt{\frac{f_r}{k_{\text{rta}}}}, \tag{4.8}$$

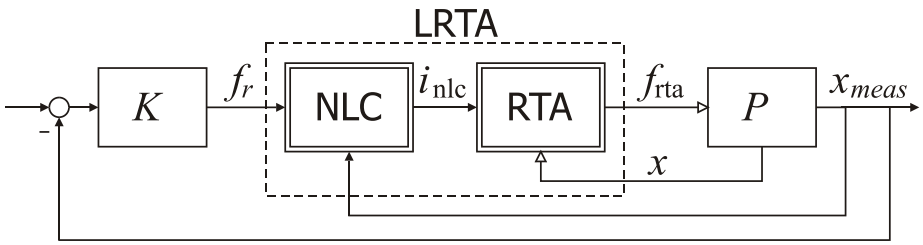

Figure 4.2. *Block diagram which shows the basic working principle of Non-Linear Compensation (NLC), in which the open arrows indicate physical relations. With an (static) inner feedback loop the NLC linearizes the RTA, such that the outer loop controls the plant P through a Linearized Reluctance Type Actuator (LRTA).*

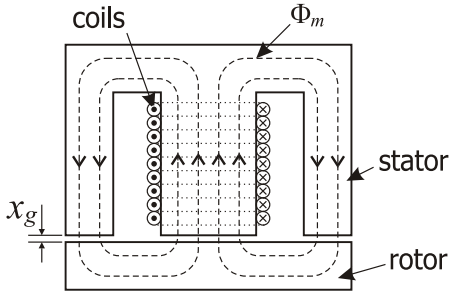

Figure 4.3. *An magnetic bearing with one RTA for actuation of one DoF.*

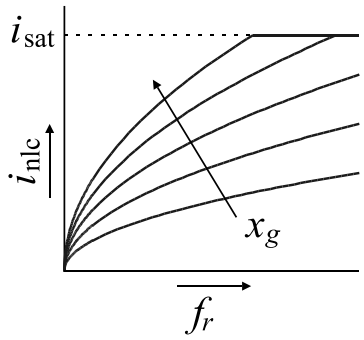

Figure 4.4. *The non-linear compensation function for a single RTA. With increasing air gap x_g the required current increase. Saturation of the RTA at i_{sat} limits both the force and the maximum air gap.*

where i_{nlc} is the set-point to the current amplifier and f_r the positive force set-point to the NLC. Applying (4.8) to (4.1), and assuming that the amplifier exactly provides the coil with a current i_{nlc}, then results in $f_{\text{rta}} = f_r$. The NLC function is shown in Figure 4.4.

One of the assumptions leading to (4.1) is that all flux flows through the iron and the gap. In reality, there will be leakage flux; flux lines that do not cross the air gap and thus do not contribute to the change of magnetic energy with position. It has been found that the amount of stray flux depends on the air gap, see [55, 51]. Hence, for accurate description of the behaviour of an RTA, a more complex function than (4.1) might be required. On the other hand, inversion of the function must still be possible in order to calculate the NLC function.

Suppose the force as function of the air gap and the current of an RTA is more complex than (4.1) and is described with $f_{\text{rta}}(i, x_g)$. An inverse function $i_{\text{nlc}}(f_r, x_g)$ of $f_{\text{rta}}(i, x_g)$ can only be found if and only if $f_{\text{rta}}(i, x_g)$ is bijective. Since theory predicts that the function is fundamentally quadratic with current, the inverse function is double-valued and general inverse function cannot be found. However,

only positive currents and positive forces need be considered, hence any function in the form of:

$$f_{\text{rta}}(i,x_g) = g_2(x_g)\,i^2 + g_1(x_g)\,i + g_0(x_g), \tag{4.9}$$

can be solved for i using the quadratic formula, giving i_{nlc}. The functions g_0, g_1 and g_2 are allowed to be quite complex. To solve (4.9) the functions g_0, g_1 and g_2 need to be evaluated each time sample using the measured air gap.

4.4.2 Two RTAs with One Degree of Freedom

With the configuration as depicted in Figure 4.1 using two RTAs, a positive force can be generated with RTA 1 and a negative force with RTA 2. Using NLC as given by (4.8) for each actuator would than result in a force slew rate (FSR) of zero when the reference force is zero, as discussed in the previous section. This can also be seen in Figure 4.4, where an infinite gain is required at $f_r = 0$. As a result, there will a disturbing transition (switching) whenever the force changes sign.

This can be solved by applying a small bias current through both coils. With a bias current of 10% to 20% of the current used with bias current linearization (i.e. half the maximum current), the dissipated energy is reduced with a factor 100 to 25.

When operating outside the bias region, the set-point current is calculated using (4.8) (or a more complex inverse function). In the bias region the force for the configuration of Figure 4.1 is given by:

$$\begin{aligned} f(i,x) &= f_1(i_b + i, x_n - x) + f_2(i_b - i, x_n + x) \\ &= k_{rta}\left(\frac{(i_b+i)^2}{(x_n-x)^2} - \frac{(i_b-i)^2}{(x_n+x)^2}\right) \end{aligned} \tag{4.10}$$

where f_1 and f_2 denote the forces from the two RTAs of Figure 4.1, i_b the bias current and x_n the nominal air gap. Note that by choosing the direction in which f_1 works positive, f_2 is always negative. Equation (4.10) can be expanded, by which it can be reduced to the form of (4.9), and an inverse can be found.

Each time sample the NLC needs to determine whether the reference force set-point f_r is within the biasing regime:

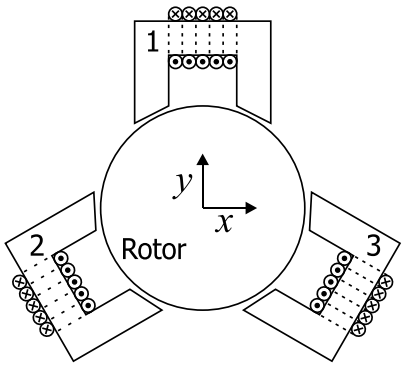

Figure 4.5. *An AMB configuration with coupled degrees of freedom; three RTAs are used to control two DoFs.*

- The reference force is bigger than the upper bound of the preload range, i.e. $f_r \geq f_1(2i_b, x_n - x)$. Then RTA 1 should generate all the required force, and the required current i_1 can be calculated using (4.8), the NLC for a single RTA. The current for RTA 2 is set to zero.

- The reference force is smaller than the lower bound of the preload range, i.e. $f_r \leq f_2(2i_b, x_n + x)$. Then RTA 2 should generate the required force, and the required current i_2 can be calculated using (4.8). The current for RTA 1 is set to zero.

- The reference force is in the preload range. Then both RTAs generate a force. The control current i is then calculated using (4.10). The current for RTA 1 is then set to: $i_1 = i_b + i$ and for RTA 2 to: $i_2 = i_b - i$

4.4.3 AMBs with Coupled Degrees of Freedom

The above approach does not work for coupled AMB systems. A coupled AMB system is a system where the RTAs generate forces in more degrees of freedom and cannot be decoupled. An example of such a system is given in Figure 4.5. The linearization strategy as described above requires superposition of the currents for the RTAs calculated in one direction with those calculated for the other direction. Superposition of the currents is not possible since the force of an RTA is proportional to the current squared.

In order to linearize the case of the coupled AMB the rotor is preloaded with a force. For each DoF a bias force is demanded of the RTAs involved in both

directions of the DoF. The forces required from the RTAs $\vec{f}_a$ can be written as:

$$\vec{f}_a = Q \begin{bmatrix} \vec{f}^{+}_{\text{dof}} \\ \vec{f}^{-}_{\text{dof}} \end{bmatrix}, \tag{4.11}$$

where Q is a matrix with positive entries dependent on the geometry, and $\vec{f}^{+}_{\text{dof}}$ and $\vec{f}^{-}_{\text{dof}}$ are defined for each entry i as:

$$f^{i+}_{\text{dof}} = \begin{cases} f^{i}_{\text{dof}}, & f^{i}_{\text{dof}} \geq 0 \\ 0, & \text{otherwise} \end{cases} \tag{4.12}$$

and

$$f^{i-}_{\text{dof}} = \begin{cases} -f^{i}_{\text{dof}}, & f^{i}_{\text{dof}} \leq 0 \\ 0, & \text{otherwise} \end{cases} \tag{4.13}$$

This way the entries of $\begin{bmatrix} \vec{f}^{+}_{\text{dof}} & \vec{f}^{-}_{\text{dof}} \end{bmatrix}^{\text{T}}$ are always positive, and since the entries of Q are also positive, the required forces from the RTAs are always positive. To preload the RTAs simply a positive constant vector is added to $\begin{bmatrix} \vec{f}^{+}_{\text{dof}} & \vec{f}^{-}_{\text{dof}} \end{bmatrix}^{\text{T}}$. The current for each RTA is then calculated using (4.8). This approach is easy to implement on a real-time environment.

For example, for the system of Figure 4.5, preloading with a constant force f_c is done as follows:

$$\begin{bmatrix} f_1 \\ f_2 \\ f_3 \end{bmatrix} = \begin{bmatrix} \frac{1}{\sqrt{3}} & 1 & \frac{1}{\sqrt{3}} & 0 \\ 0 & \frac{2}{\sqrt{3}} & 0 & 1 \\ \frac{2}{\sqrt{3}} & 0 & 0 & 1 \end{bmatrix} \left(\begin{bmatrix} f^{+}_{x} \\ f^{+}_{y} \\ f^{-}_{x} \\ f^{-}_{y} \end{bmatrix} + \begin{bmatrix} 1 \\ 1 \\ 1 \\ 1 \end{bmatrix} f_c \right). \tag{4.14}$$

A drawback of this solution is that the maximum deliverable force is reduced by the bias force, which is a trade-off to increase the force slew rate and reduce the switching effect.

4.5 NLC Parameter Sensitivity Analysis

With the assumption that (4.1) or (4.9) accurately describes the behaviour of an RTA, the methods for NLC discussed in the previous section results in a perfect Linearized RTA (LRTA) with no mechanical stiffness. In reality, the functioning of NLC is endangered by four factors. Firstly, there is uncertainty in the model of the RTA. Secondly, the current amplifier might not be correctly modelled, and as a result the current in the RTA coil would deviate from the desired current calculated by the NLC. Thirdly, due to measurement inaccuracy the measured air gap can be

different than the actual mechanical air gap. Lastly, the mechanical air gap can be different from the magnetic air gap, due to flux stray and lamination.

This section analyses the consequences of the above mentioned factors in the relative simple case of a single RTA, as shown in Figure 4.3 in which the RTA is modelled by (4.1) and the accompanying NLC is described by (4.8). The analysis focusses on the effect on the resulting gain and mechanical stiffness. Although reality is more complex, the analysis presented here provides a good insight in the fundamental behaviour of NLC.

A factor that can destabilize the loop is when the modelled gain of the plant differs from the actual gain. Common practise is to design a controller which establishes a gain margin bigger than two. When a gain margin bigger than two is realized, a gain variation of the plant of less than 20% does not have a big influence on the feedback performance[1].

4.5.1 RTA Constant Modelling Error

Suppose the RTA constant of (4.1) k_{rta} is modelled as $k_{\text{mod}} = a\,k_{\text{rta}}$. Using k_{mod} for the NLC law (4.8), leads to:

$$f_{\text{rta}} = \frac{1}{a} f_r. \tag{4.15}$$

Hence, a modelling error in the RTA constant leads to a gain error of the LRTA. With a modelling error of 20%, the gain can vary between 0.83 and 1.25.

4.5.2 Current Amplifier Modelling Error

Suppose that due to a modelling error of the amplifier, that the current i to the coil equals $i = a\,i_{ref} + b$. Then the force generated by the RTA is given by:

$$f_{\text{rta}} = a^2 f_r + 2k_{\text{rta}} \frac{ab}{x_g} \sqrt{\frac{f_r}{k_{\text{rta}}}} + k_{\text{rta}} \frac{b^2}{x_g^2}. \tag{4.16}$$

Here, the result is a gain error dependent of a, a constant force which depends on b and varies with position, and a non-linear term. The nonlinearity introduced by the square root function might deteriorate the stability performance. The influence of this nonlinearity is kept small if the off-set current b is small, and the air gap not too small. These are also good measures to decrease the resulting bias force and gain variation.

[1] If the performance of the system is mostly achieved by feedforward, then the allowed gain variation of the plant should be much smaller!

The latter two terms of (4.16) are position dependent, hence the linearized actuator exhibits a behaviour comparable to a mechanical stiffness. This stiffness can be found by taking the partial derivative of (4.16) with respect to the air gap:

$$\frac{\partial f_{\text{rta}}}{\partial x_g} = -2\frac{ab}{x_g^2}\sqrt{\frac{f_r}{k_{\text{rta}}}} - 2k_{\text{rta}}\frac{b^2}{x_g^3}. \tag{4.17}$$

To interpret the above result, the gain variation is assumed to be zero, while the offset current equals $b = c\,i_{\max}$. Realizing that $\sqrt{\frac{f_r}{k_{\text{rta}}}} = \frac{i_r}{x_g}$, the above equation can be simplified to:

$$\frac{\partial f_{\text{rta}}}{\partial x_g} = -2\,c\frac{i_r}{i_{\max}}\frac{f_{\max}}{x_g} - 2\,c^2\frac{f_{\max}}{x_g}, \tag{4.18}$$

in which $f_{\max} = k_{\text{rta}}\frac{i_{\max}}{x_g}$. For reference currents bigger than $c\,i_{\max}$ the first term dominates the second. Despite the fact that c is usually quite small (e.g. less than 1%), the resulting stiffness at small air gaps and big forces can limit the performance as vibrations become mechanically coupled over the RTA.

4.5.3 Position Measurement Error

The difficulty in measuring the air gap is that the mechanical air gap differs from the air gap experienced by the magnetic flux. This is due to the magnetization of the flux guiding material (see (A.27) on page 165) and manufactory inaccuracies of the shape of the RTA.

Suppose the measured gap x_m equals $x_m = a\,x_g + b$. Using x_m for the NLC law (4.8), gives:

$$f_{\text{rta}} = \left(a + \frac{b}{x_g}\right)^2 f_r. \tag{4.19}$$

Hence, an affine position measurement error leads to a position dependent gain error of the LRTA. As the air gap goes to zero this gain quickly blows up, hence very small air gaps should be avoided. Suppose an offset b of 10% of the nominal air gap, then the resulting gain at an air gap 20% of the nominal air gap, is already 2.25! This clearly shows than the closed loop stability is endangered at small air gaps.

From (4.19) the stiffness resulting from the measurement error can be derived to be:

$$\frac{\partial f_{\text{rta}}}{\partial x_g} = -2\left(\frac{ab}{x_g^2} + \frac{b^2}{x_g^3}\right) f_r. \tag{4.20}$$

It can be seen that a zero position off-set error, would decrease the resulting stiffness to zero. Again, small air gaps are disadvantageous, as the stiffness blows up with position measurement errors.

4.5.4 Position Measurement Noise

If the measured position x_m is corrupted with sensor noise n, hence $x_m = x_g + n$, the resulting noise amplification can be calculated to be:

$$\frac{\partial f_{\text{rta}}}{\partial n} = 2\left(\frac{x_g + n}{x_g^2}\right) f_r \approx 2\left(\frac{f_r}{x_g}\right), \tag{4.21}$$

where the last approximation can be made because the sensor noise is usually much smaller than the air gap. Hence, the generated force at a certain position equals approximately:

$$f_{\text{rta}} \approx f_r + 2\frac{f_r}{x_g} n. \tag{4.22}$$

The last term of (4.22) is the force noise resulting from the sensor noise. To give an idea of the sensitivity, suppose a maximum force of 10 N is required and that the force noise should be less then 10 mN (RMS). With a minimum air gap of 0.5 mm, the sensor noise should be less than 0.25 μm (RMS).

4.6 NLC Functioning Tests

The objective of NLC is to create linear behaviour for the controller and to reduce the stiffness of the RTA. Different experiments were done to assess the performance of the proposed NLC solutions.

4.6.1 Stiffness and Gain Measurement

To analyse the performance of NLC to reduce the stiffness of the RTA different tests can be done. Two such methods have been used and are introduced here. Results from experiments are presented in the next section.

Dynamic Stiffness and Gain Assessment

The first method encompasses the measurement of the Frequency Response Data (FRD) of the plant with the linearized RTA (LRTA) in the closed loop system as shown in Figure 4.2. A model can that be fitted on the FRD, from which the stiffness and gain can be extracted. A drawback of this method, is that it measures

only the stiffness around one operating point. To asses the stiffness over the whole working range, the same experiment must be repeated for several positions and currents.

Static Stiffness Assessment

A quick method to obtain an indication of the stiffness and gain over the whole working range is possible if the setup allows the compensation of constant force while travelling over the full position range. For example, if a DoF is in the direction of the gravity, the constant force is the weight of the supported mass. Any change in effort by the controller to keep the system in a certain position, is then the result of the mechanical stiffness in the system *and* a compensation mismatch of the NLC. By stepping through the position range and repeating the experiment for various weights, the whole working range of the AMB is quickly covered. Plotting the controller effort f_u versus the position x travelled through, gives then an indication of the stiffness present in the system, which includes the stiffness introduced by the LRTA.

However, this test quantifies a combination of the stiffness and the LRTA gain, which is shown here. The force generated by the LRTA of Figure 4.2, only depends on the reference input f_r to the NLC and the air gap x_g, hence the force around a nominal point can be written as:

$$f_{\text{rta}}(f_r, x_g) = f_{\text{rta}}(f_r^n, x_n) + \frac{\partial f_{\text{rta}}}{\partial f_r}\delta f_r + \frac{\partial f_{\text{rta}}}{\partial x_g}\delta x_g, \tag{4.23}$$

where f_r^n is the nominal reference set-point and x_n the nominal air gap. Now suppose that the LRTA is preloaded with a constant force, e.g. from lifting a mass, hence $f_{\text{rta}}(f_r, x_g) = f_{\text{mass}}$. The reference force is then equal to $f_r = f_u + f_{\text{mass}}$, where f_u is the force from the controller required to keep the mass at a certain position. Now the position is chosen positive in the direction of the force, hence $x = x_n - x_g$. Omitting the deltas in (4.23) then gives:

$$f_{\text{mass}} = f_{\text{rta}}(f_r^n, x_n) + \frac{\partial f_{\text{rta}}}{\partial f_r} f_u - \frac{\partial f_{\text{rta}}}{\partial x_g} x, \tag{4.24}$$

The term $f_{\text{rta}}(f_r^n, x_n)$ is constant, hence (4.24) can be written as:

$$f_{\text{mass}} = f_{\text{rta}}(f_r^n, x_n) + k_f f_u - k_x x \iff f_u = \frac{k_x}{k_f} x + c, \tag{4.25}$$

with c some constant. Hence, the slope of f_u versus x depends on the position dependency of the linearized system, as well as the linearity of the LRTA. Henceforth, the quantity $\partial f_u / \partial x$ is referred to as *apparent stiffness*.

Another property of the test is that when the position range is traversed in up and downward direction, the effect of magnetic hysteresis will become visible as a hysteresis loop in the control effort.

4.6.2 Frequency Dependent Measurement of the Linearity

Many methods exist to assess the linearity in a system. An overview of such methods are given in [10, 38]. Here, two methods are explained, which give an frequency dependent analysis.

Harmonic Distortions

When a nonlinear system is excited with a sinusoid signal $u = a_u \sin(2\pi f t)$, the resulting stationary output will contain higher harmonics of the base frequency, see [38]:

$$y = a_0 + \sum_{k=1}^{n} a_k \sin(k2\pi f t + \varphi_k). \tag{4.26}$$

Hence the quantity:

$$\nu_{\text{thd}}(f) = \frac{1}{a_1^2} \sum_{k=2}^{n} a_k^2 \tag{4.27}$$

is a measure of the nonlinearity at frequency f and is denoted Total Harmonic Distortion (THD) index.

Validation by Coherence

The coherence function γ_{xy} is defined as:

$$\gamma_{xy}^2(f) = \frac{|S_{xy}(f)|^2}{S_{xx}(f)S_{yy}(f)}, \tag{4.28}$$

where $S_{xy}(f)$ the spectral function as defined in Subsection 3.6.2. If the relation between x and y is 100% linear at a certain frequency, the coherence γ_{xy} will be equal to unity at that frequency. According to [10], there are four main reasons why the coherence will differ from a value that was expected to be close to unity:

1. Extraneous noise in the input and output measurements.
2. Bias and random errors in spectral density function estimates.
3. The output $y(t)$ depends on more inputs than the measured $x(t)$.
4. Nonlinear system operations between $x(t)$ and $y(t)$.

If the first three possibilities are ruled out by good data acquisition, proper data processing, and physical understanding, it is reasonable to conclude that low coherence at particular frequencies is due to nonlinear systems effects at these frequencies.

Following [38], the noise nonlinearity index is defined as:

$$\nu_{\text{noise}} = 1 - \gamma_{xy}^2 \tag{4.29}$$

By injecting a white noise signal to the LRTA, the FRD can be estimated by the fourier transforms of the input and output.

4.7 Experimental Dynamic Results Two RTAs

4.7.1 Experimental Setup Description

The developed NLC approach and qualification methods were applied to the setup shown in Figure 4.6. The setup consists of a mass of 2.5 kg which is supported by spring blades (blocking five DOFs), and actuated by two RTAs. The two RTAs work in opposite direction of each other in the direction of the remaining DOF. The position of the rotor was measured by a Philtec D63 optical sensor[2]. The currents through the RTAs are provided by linear amplifiers controlled by a dSpace 1104 controller board. When the system is in closed loop, according to the definition given in Section 4.1, a one DoF active magnetic bearing results. The air gap at the two RTAs was mechanically set to 0.5 mm. However due to mechanical imperfections in the alignment of the target material, the magnetic gap was tuned to 0.66 mm.

The measurement of the force-position-current relationship was done with a separate setup, as described in Appendix A.2 on page 167. For the NLC used in this setup, the function in which the RTA constant k_{rta} is made position dependent: $k_{\text{rta}} = n_2 x_g^2 + n_1 x_g + n_0$.

The NLC was tested with the bias strategy as explained in Subsection 4.4.2, with two bias current levels, 50 and 200 mA. The NLC is compared with the standard bias linearization, as was described in Subsection 4.2, using a bias current of 500 mA (half the maximum current of the amplifiers).

[2]The sensor on the photo is actually an inductive sensor. The setup was changed for experiments using the optic fiber sensor (see also www.philtec.com).

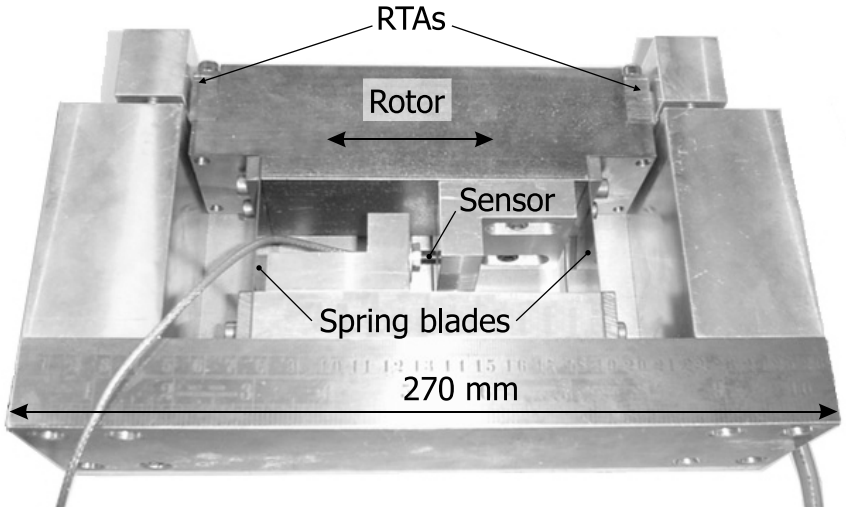

Figure 4.6. *Active magnetic bearing setup, with one Degree of Freedom (DoF) , using two RTAs. The remaining DoFs are restrained by means of spring blades.*

4.7.2 Measurement of Linear Properties

Dynamic Linearity

First the linearity of the system was assessed with the sinusoidal method as described in Subsection 4.6.2. The test was applied to the measured accelerations[3] while injecting an excitation force at f_r of 0.5 N in closed loop. During the experiments, the bandwidth of the controller (0-dB crossing of the open loop) was set to 20 Hz. The bandwidth is a compromise between on the one hand being able to stabilize the system, especially for the system with bias current linearization, and on the other hand, minimizing the linearizing effect of feedback. In Figure 4.7 the results of the linearity test is shown. The linearity was measured at seven positions; $+250$, $+200$, $+100$, 0, -100, -200, -250 μm from the centre position of the two RTAs. At each position the Total Harmonic Distortion (THD) was measured for the three linearization methods. For clarity, for each method only the envelope of the worst and best measured THD at each frequency is shown in the figure. Typically, the lowest THD (best result) was measured at middle position, while the highest THD was measured at one of the two extreme positions.

Up to 150 Hz the NLC with 200 mA works more linear than the NLC with 50 mA. In this frequency range the harmonic power is a factor 500 less than the power in the base frequency, while for the bias linearization and the NLC with 200 mA the factor is even better than $2{\cdot}10^4$ at zero position. Above 150 Hz the performance of the linearization techniques deteriorates, especially for the

[3]Measured with PCB 357B33 accelerometer, see www.pcb.com.

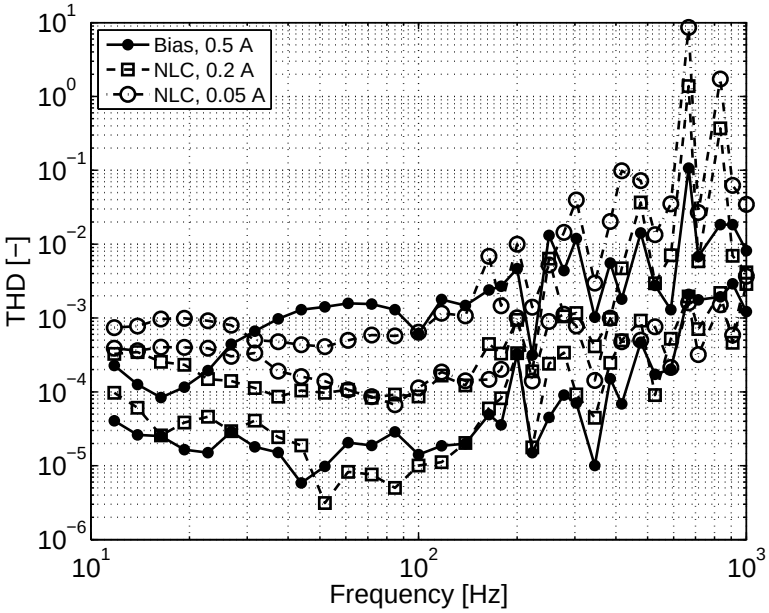

Figure 4.7. *The Total Harmonic Distortion (THD) for each frequency of the measured accelerations. The THD was measured at five positions of the rotor, however only the best and worst THD at each frequency is given. This results in two lines for each linearization method giving the envelope of THDs. It can be seen that at the outer positions up to 200* Hz *the linearization using NLC with 0.2* A *preloading is much better than biasing with 0.5* A.

NLC methods. Around 670 Hz, where the system has mechanical resonances (see Figure 4.8), the NLC methods show a ratio bigger than one!

Measurement of Gain and Stiffness Variation

The gain and stiffness variation of the plant was evaluated by measuring the FRD from reference force f_r to measured position and accelerations $\ddot{x}_{meas}$ at the seven different positions as before. In Figure 4.8a the Bode plot of the measured FRD from reference force to position is given, in Figure 4.8b the Bode magnitude of the FRD from force input to accelerations multiplied by the mass of the rotor is shown from 1 to 10 Hz.

From the change of resonance frequency it is clear that the stiffness introduced by the LRTA changes with position. To increase the accuracy of estimating the resonance frequency at each frequency, transfer functions was fitted on the measured FRD, which are also shown in Figure 4.8. The stiffness of the spring blades is known[4] (from open loop measurement of the resonance frequency), hence the

[4]It is assumed that the displacement of the rotor does not change the stiffness of the spring

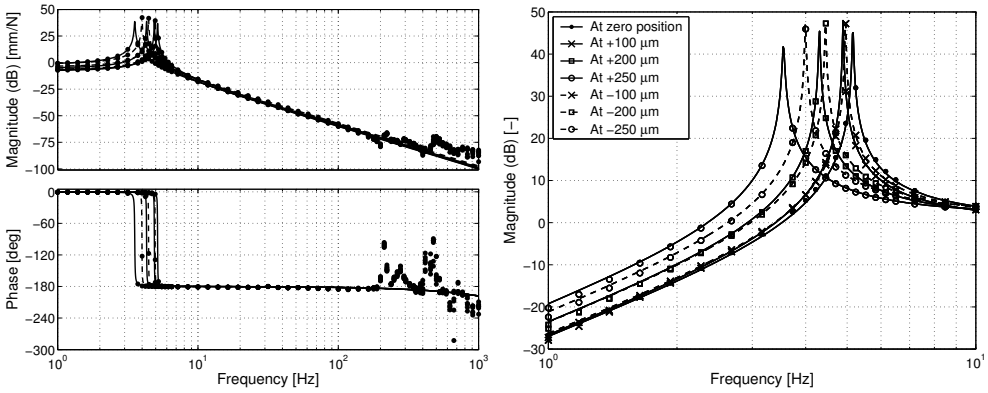

a b

Figure 4.8. *a) Bode plot of the reference force input of the NLC to measured position of the rotor. b) Bode magnitude of the reference force input of the NLC to accelerations of the rotor multiplied with the mass of the rotor. The marks represent the measured data, the lines gives the fitted transfer functions.*

stiffness introduced by the LRTA can be calculated from the change in resonance frequency. In Table 4.1 the result for standard bias current linearization, NLC with 200 mA bias current and NLC with 50 mA bias current is shown.

From the fitted transfer function of the FRD from force to measured acceleration multiplied by the mass, the variation in the gain is assessed. In Table 4.2 the result is given. The very low value for the standard bias linearization is due to the fact that the nominal air gap was tuned such that the gain was close to one. This resulted in an estimated air gap of 0.66 mm. For the experiments with NLC the estimated air gap was not tuned, which could explain the relatively high gain variations at the zero positions. If so, it shows that NLC is quite sensitive to errors in the estimated air gap, as also came apparent from the sensitivity analysis in Subsection 4.5.3.

4.7.3 Discussion of Results

The peaking in the non-linearity index of Figure 4.7 might be explained by the fact that the sensor is not co-located with line of work of the RTAs. From the measured bode plot, shown in Figure 4.8b, it is seen that the phase at this frequency drops below -180 deg, indicating the behaviour of non co-located position information.

After conducting the experiments with the one DoF setup, it was found that the fitting accuracy of the force-current-position relationship could be greatly improved by adding a constant l_i to the air gap x_g in (4.1), see Section A.2. Hence

blades.

Table 4.1. *Introduced stiffness [N/m] by the NLC compared to bias linearization.*

Position [μm]	Stiffness [N/m]		
	bias	NLC	
	0.5 A	0.2 A	50 mA
250	$-10.26 \cdot 10^3$	$-1.58 \cdot 10^3$	$-1.38 \cdot 10^3$
200	$-8.51 \cdot 10^3$	$-0.86 \cdot 10^3$	$-0.77 \cdot 10^3$
100	$-6.84 \cdot 10^3$	$-0.30 \cdot 10^3$	$-0.22 \cdot 10^3$
0	$-6.00 \cdot 10^3$	$-0.05 \cdot 10^3$	$0.06 \cdot 10^3$
-100	$-6.85 \cdot 10^3$	$-0.22 \cdot 10^3$	$-0.15 \cdot 10^3$
-200	$-8.74 \cdot 10^3$	$-0.75 \cdot 10^3$	$-0.64 \cdot 10^3$
-250	$-10.31 \cdot 10^3$	$-1.15 \cdot 10^3$	$-1.04 \cdot 10^3$

the force of the RTA becomes:

$$f_{\text{rta}} = k_{\text{rta}} \frac{i^2}{(x_g + l_i)^2}. \tag{4.30}$$

Such an additional term is consistent with analytical modelling, see (A.27) on page 165 and accounts for the magnetic resistance of the iron. Using NLC based on (4.8) to calculate the current (see also Section 4.5), the generated force becomes:

$$f_{\text{rta}} = \left(\frac{x_g}{x_g + l_i} \right)^2 f_r. \tag{4.31}$$

With a minimal air gap of 250 μm and fitted constant of $l_i = 48$ μm (see Table A.2 on page 171), the maximum gain variation is 30%. This effect could explain the gain variation of Table 4.2.

Taking the partial derivative of (4.31) with respect to the air gap gives:

$$\frac{\partial f_{\text{rta}}}{\partial x_g} = 2 \frac{l_i x_g}{(x_g + l_i)^3} f_r. \tag{4.32}$$

Using the same values as before, and with a force of 1 N (which is roughly the preload force with an air gap of 250 μm using NLC with 0.2 A biasing), gives a stiffness about 907 N/m. This would explain the stiffness as found in Table 4.1.

The values found for the stiffness and gain variation engendered by neglecting the additional constant magnetic flux path l_i, are of the same magnitude as were measured. Two conclusion can be drawn here. Firstly, when characterizing the RTAs on measured data, a parameter l_i for the additional flux path should be taken

Table 4.2. *The experimental force gain error (% [-]) at various positions with NLC and bias linearization.*

Position [μm]	Gain variation (%) [$-$]		
	bias	NLC	
	0.5 A	0.2 A	50 mA
250	34	25	26
200	19	15	17
100	3	6	7
0	-1	6	15
-100	4	10	14
-200	19	22	24
-250	33	26	31

into account. Secondly, if the RTAs are to be used in a different setup than that they were measured on, a calibration step should be made to optimize this value l_i.

4.8 Experimental Static Results Single RTA

To validate whether improved modelling of the RTA would indeed result in a better performance, another experiment was conducted with a setup using a single RTA. Here, the more quick method of statically measuring the apparent stiffness, as explained in Subsection 4.6.1, was used.

4.8.1 Experimental Setup Description

The setup consists of a rotating arm, actuator with one RTA. The arm leaves one DoF free (rotation), which is approximately a linear motion at the position of the RTA over the range of interest. The RTA needs to lift the mass of the arm and the additional mass on top of the arm. An inductive sensor[5] measures the position of the arm with respect to the table.

The RTA used is an standard E-core with a typical dimension of 20 mm (see Figure A.4 on page 168) and a thickness of 30 mm made of transformer steel. The RTA coil has 670 turns, capable of carrying maximally 6 A[6]. The RTA was designed to deliver a maximum force of 1000 N at an air gap of 1.5 ± 0.5 mm.

[5] Baluff BAW-M18ME

[6] Delivered by a Kepco 72-6M amplifier

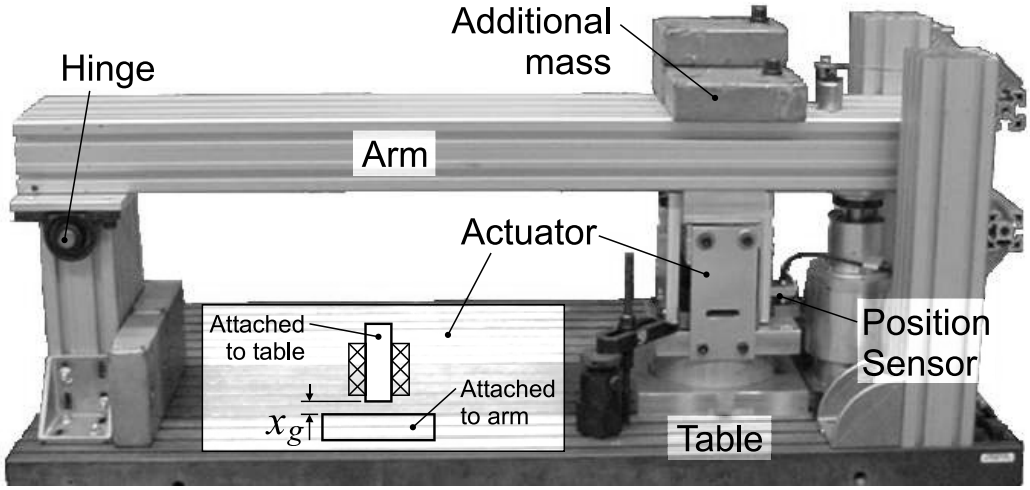

Figure 4.9. *Photo of the setup with one RTA. The arm can rotate around the hinge and is lifted by the RTA. On the arm additional masses can be placed to increase the weight that needs to be lifted by the RTA.*

4.8.2 Force-Current-Position Relationship

To measure the force-position-current relationship $f_{\text{rta}}(x_g, i)$, the arm of the setup is moved ± 0.5 mm with various loads in closed loop. To bring the system in closed loop, the theoretical relationship (4.1) is used for the NLC. From (A.28) on page 165 it is seen that the RTA constant is given by:

$$k_{\text{rta}} = \tfrac{1}{4}\mu_0\mu_a n_c^2 A = 161 \text{ N}\,\text{mm}^2/\text{A}^2. \tag{4.33}$$

To compare the resulting stiffness with NLC applied, the stiffness resulting from standard biasing is calculated, see (4.2) on page 69:

$$k_x = 2k_{\text{rta}}\frac{i^2}{x_g^3} = 2 \cdot 161\frac{3^2}{1.5^3} = 859 \text{ N/mm} \tag{4.34}$$

With no additional weights on the arm, the RTA needs to exert a force[7] of 170 N. The arm was moved up to 0.5 mm, then down to -0.5 mm and back up to the zero position in steps of 0.1 mm. For each position the current was measured, providing data on a (curved) line for a constant force, $f_{\text{rta}}(i_k, x_k) = \text{constant}$. This experiment was repeated for additional weights of 10, 20 , 30, 40 and 50 kg. On the collected data the following function was fitted:

$$f_{\text{rta}} = k_{\text{rta}}\frac{i^2}{(x_g + l_i)^2}, \tag{4.35}$$

[7] Measured with an Aikoh 9820 push/pull force gauge

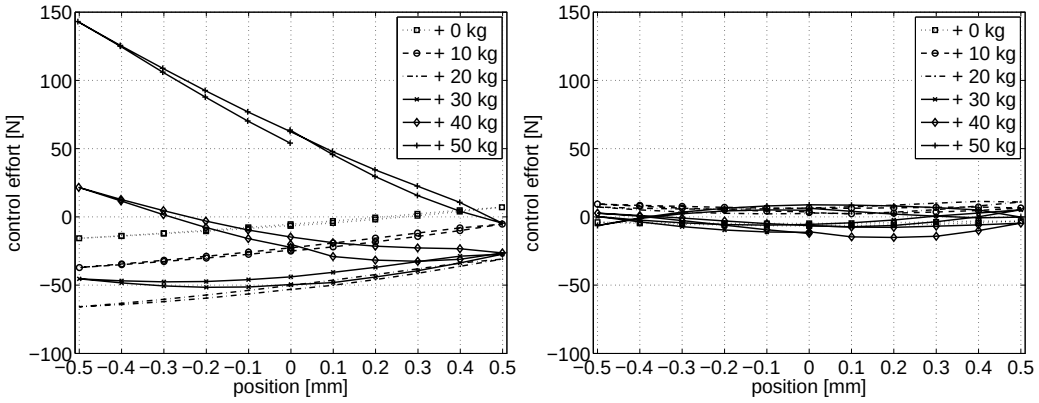

Figure 4.10. *Plot of the position vs. control effort. The slope of the plot gives an indication for the stiffness introduced by the NLC. a) NLC with a fitted RTA constant, b) NLC using the more complex model with five additional terms. Especially with a load of 50* kg*, the more complex model compensates the non-linearity of the RTA much better.*

where l_i represents the length of the flux path through the iron and the remaining air gap when rotor touches the E-core, due to uneven lamination. The parameter k_{rta} was found through linear regression, as explained in Subsection A.2.2, while the constant l_i was simply found by a search over a range. The optimal values were found to be 0.41 mm for l_i and for k_{rta} to be 218 $\text{N}\,\text{mm}^2/\text{A}$, differing 35% with the theoretically found value. Assuming that this fitted value for k_{rta} is more representative than the value found theoretically, the resulting stiffness from standard biasing is even higher: 1163 N/mm.

4.8.3 Static Stiffness Measurement

In Figure 4.10a the control effort for each additional weight is plotted versus the position, using NLC based on the fitted RTA constant. For each weight the feedforward was adjusted to compensate for the different weights, such that the control effort really results from a non-perfect compensation of the RTA. From the figure it is clear that the feedback loop needs to compensate for relative large force errors. The worst case being at an air gap of 2 mm at which the feedback compensates for 140 N to lift the arm with a total weight of 660 N.

To improve the performance of the NLC, a more complex model was fitted:

$$f_{\text{rta}} = k_{\text{rta}}\frac{i^2}{x_g^2} + k_1\frac{i^2}{x_g} + k_2\frac{i}{x_g} + k_3 i + k_4 x_g + k_5, \tag{4.36}$$

Table 4.3. *Optimal fitted parameters of the advanced RTA model.*

Parameter	Value	Unit
k_{rta}	232	$\text{N}\,\text{mm}^2/\text{A}^2$
k_1	-181	$\text{N}\,\text{mm}/\text{A}^2$
k_2	159	$\text{N}\,\text{mm}/\text{A}$
k_3	357	N/A
k_4	-130	N/mm
k_5	-237	N

in which the air gap x_g is adjusted with the value of l_i as found with (4.35). The optimal found parameters are given in Table 4.3. From the values of the parameters it is clear that the validity of the NLC is limited outside the range over which it has been fitted; for zero current the model predicts a negative (repelling) force, which clearly cannot be.

Figure 4.11 gives the NLC function for the advanced RTA model with the air gap and reference force as inputs and current as output. It can be seen that the maximum force of 1000 N can only be delivered with an air gap of 1.5 mm, instead of the designed 2.25 mm.

The function (4.36) was found with the following argumentation. From Figure 4.10a it is observed that compensating the feedback force for each weight with affine approximations would provide a large improvement. Thus for each compensated weight, a function $k_1 x_g + k_0$ should be found, in which the coefficients k_1 and k_0 are dependent on the compensated weight. However, the RTA model should be a function of position and current. According to (4.1) the ratio i/x_g should remain approximately constant over the position range for each compensated weight, so the coefficients k_1 and k_0 are similarly dependent on the ratio i/x_g. It was found that these coefficients are quadratic functions of the ratio i/x_g, which leads to the function of (4.36).

In Figure 4.10b the control effort for each additional weight is plotted versus the position, using NLC based on the fitted advanced RTA model (4.36). In Subsection 4.6.1 it was argued that the slope of the plot is a measure of the stiffness in the system and the gain variation of the LRTA. From the figure it is clear that the stiffness and gain variation is greatly reduced. The maximum absolute feedback force that was used was less than 15 N.

Interpreting the slope of the plots in Figure 4.10 as a stiffness, Table 4.4 gives the maximum (positive or negative) apparent stiffness for each additional weight along the position range using standard NLC and advanced NLC.

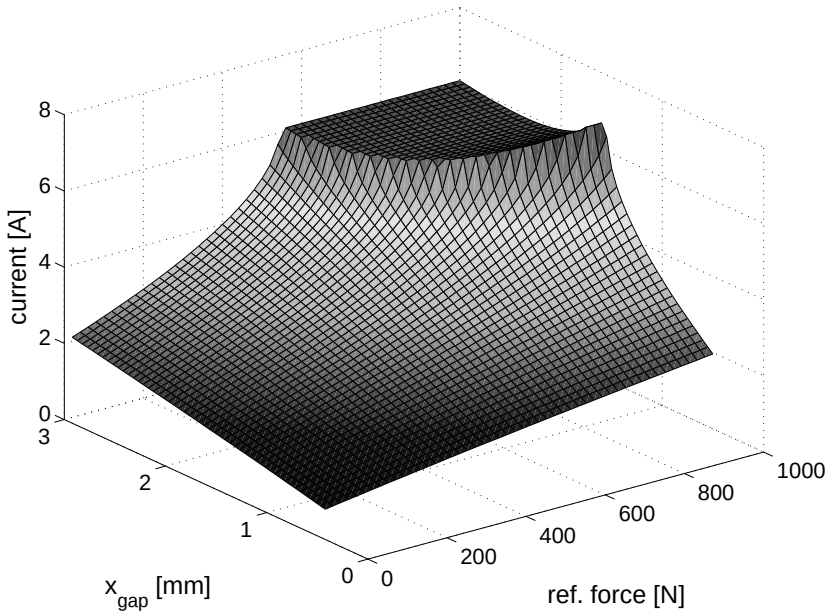

Figure 4.11. *The NLC function based on the advanced RTA model of equation (4.36) with air gap and reference force as inputs and the current as output. The maximum force of 1000* N *can only be delivered with an maximum air gap of 1.5* mm*, instead of the the designed 2.25* mm*.*

Table 4.4. *Comparison of the apparent stiffness introduced by standard NLC based on the simple model of the RTA, and advanced NLC based on the more complex model. The minimum and maximum values over the travel range are given. To compare with, the stiffness resulting from standard biasing with half the maximum current is* $1160{\cdot}10^3$ N/m.

Add. weight [kg]	Standard NLC [N/m]		Advanced NLC [N/m]	
	min	max	min	max
0	$16.8{\cdot}10^3$	$31.8{\cdot}10^3$	$-7.7\cdot10^3$	$13.3{\cdot}10^3$
10	$21.7{\cdot}10^3$	$47.2{\cdot}10^3$	$-16.0{\cdot}10^3$	$17.7{\cdot}10^3$
20	$16.2{\cdot}10^3$	$52.8{\cdot}10^3$	$-20.9{\cdot}10^3$	$28.3{\cdot}10^3$
30	$-30.3{\cdot}10^3$	$64.2{\cdot}10^3$	$-39.5{\cdot}10^3$	$51.6{\cdot}10^3$
40	$-100.0{\cdot}10^3$	$47.1{\cdot}10^3$	$-37.9{\cdot}10^3$	$54.1{\cdot}10^3$
50	$-189.0{\cdot}10^3$	$-88.1{\cdot}10^3$	$-51.7{\cdot}10^3$	$56.1{\cdot}10^3$

4.9 Conclusions

The functioning of the non-linear compensation (NLC) depends on accuracy of the model of the Reluctance Type Actuator (RTA). In this chapter the functioning of NLC has been quantified for parameter changes in a simple model of the RTA. The inner feedback loop (Figure 4.2 on page 74) brings the risk of destabilizing the system if the modelling error is big. It has been found that the theoretical values of the RTA constant in (4.1) on page 68 and the experimental determined values can differ up to 35%. With the experiments described in this chapter, however, the system could always be made operational using the theoretical values, indicating that the destabilizing effect of non-ideal NLC is small and easily corrected with the outer control loop.

Although NLC enables the use of RTA within a certain working range, instead of a working point, the possible range is practically limited. Operating an RTA at a big air gap, greatly limits the maximum force, while operation at a small air gap, greatly increases the influence of parameter modelling errors. A modelling error in the magnetic flux path of 5% of the smallest working air gap, gives a gain error of 10%. For this reason the use of NLC is less suitable in mechatronic machines in which accuracy performance is achieved through feed-forward.

The experiments conducted with the setup with two RTAs showed that the stiffness at the extreme positions could be decreased with a factor 6.5 compared to the stiffness when the setup was linearized with current pre-loading. At nominal position the reduction has increased to a factor 100, resulting in a stiffness of only 60 $\mathrm{N/m}$.

The setup with the single RTA has shown a reduction of the stiffness with a factor 6.2 over the full travel range using the model based NLC. Using the more complex NLC algorithm, a reduction with a factor 21 was achieved, resulting in a stiffness of $56{\cdot}10^3$ $\mathrm{N/m}$.

Based on the experiments, it is concluded that the performance of NLC can be greatly increased if the machine allows for calibration of the critical parameters after assembly. In the ideal situation the data on which the NLC function is fitted, is measured on the machine itself.

5

Design of the Rotating Demonstrator

In this chapter the design of the rotating demonstrator is discussed. First the conceptional design choices as discussed in Chapter 2 are further worked out into an initial design. This initial design is used for Dynamic Error Budgeting (DEB) procedure, developed in Chapter 3. Using the DEB procedure the initial design is developed further into the final design. This process is illustrated with a few design examples. Finally, the realized setup is discussed.

5.1 Introduction

In Section 2.1 the design procedure was explained. In this chapter, the procedure will be followed for the design of the five DoF (rotating) demonstrator. In accordance with Figure 2.1 on page 14, the initial design will be discussed first.

Secondly, the mechanical and disturbance modelling and initial controller design will be discussed. In the third part the design process will be illustrated with a few examples. Next, the final design will described and the chapter ends with a discussion of the realized demonstrator.

5.2 Description of the Initial Design

The specifications and the conceptual design choices have been discussed in Chapter 2. In this section the conceptional design is further developed into the initial design, the second step in the design process as illustrated in Figure 2.1 on page 14.

The conceptional design is a functional design; only choices in functions were made. The following parts will perform the various functions:

Rotor The part that has to rotate within specifications with respect to the metrology frame.

Gravity compensator To generate a force in z-direction, such that it compensates the weight of the rotor.

Actuators To generate the forces needed to control the rotor in five degrees of freedom.

Motor To drive the rotor in the rotation direction and acts between the force frame and the rotor.

Sensors are needed to sense the position of the rotor with respect to the metrology frame such that in closed loop the rotor follows the metrology frame. Additional sensors are needed for sensing of the rotor position with respect to the force frame, necessary for the non-linear compensation of the actuators and to start up the system.

Force frame The body on which the reaction forces of the actuators, motor and gravity compensator act. It also holds the sensors to measure the position of the rotor with respect to the force frame.

Metrology frame To hold the high precision sensors which measure the position of the rotor with respect to the metrology frame.

Amplifiers To provide the actuators and motor with the currents.

Control hardware To read the sensors signals, calculate the control currents, and to set the voltage set-points to the amplifiers.

The step in Figure 2.1 from conceptual design to initial design, is an iterative process in itself. For example, from the size of the support of the master disk (180 mm), approximate sizing of the rotor can be estimated. The dimensions of the rotor and the choice of material[1] gives an initial estimation of the weight of the rotor. Starting value of the weight for the design process was 4 kg. This number allows estimation of the dimensions of gravity compensator and the forces that are required for control, thus the physical sizes of the actuators. In its turn, more accurate estimation of the physical sizes, allows more accurate estimation of the weight of the rotor.

[1] Since a magnetic inert material is needed, aluminium was the logical design choice.

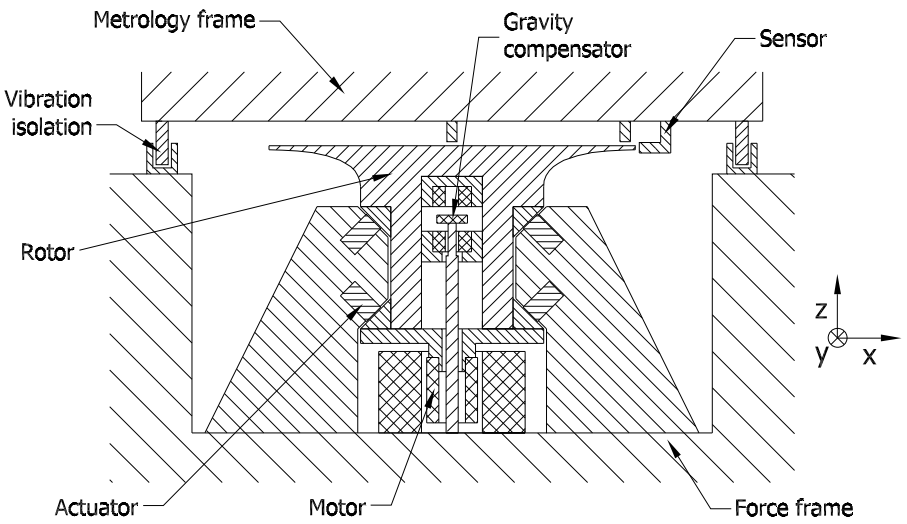

Figure 5.1. *Initial design at the start of the DEB process.*

In Figure 5.1 a drawing of the initial design is given. In the following subsections the individual parts are further elaborated on. To determine the shape of the rotor, the heart of the design, first the parts related to it are discussed. For the design of the individual parts, the bandwidth criteria to be achieved by the total system is crucial.

5.2.1 Initial Bandwidth Estimation

In Section 2.3 it was assessed that the ground vibrations are likely a critical disturbance. Assuming for the moment that these vibrations are the only disturbance, an estimation of the minimum required bandwidth can be made the following way. Suppose in worst case that the metrology frame has the same vibration level as the force frame, hence $a_{vib} = 1.4$ mm/s^2 (see Figure 2.5 on page 25). If the rotor would perfectly follow the metrology frame, the required control forces are $f_{control} = m_r a_{\text{vib}}$. Assuming the controller to be a simple spring with stiffness k_{control}, the control forces equal $f_{\text{control}} = k_{\text{control}}\varepsilon$, in which ε is the tracking error. These assumptions lead to the following estimation for the bandwidth frequency:

$$f_{\text{bw}} = \frac{1}{2\pi}\sqrt{\frac{k_{\text{control}}}{m_r}} = \frac{1}{2\pi}\sqrt{\frac{a_{\text{vib}}}{\varepsilon}} = \frac{1}{2\pi}\sqrt{\frac{1.4\cdot 10^{-3}}{1\cdot 10^{-9}}} = 190 \text{ Hz} \qquad (5.1)$$

For the initial design, the target bandwidth was rounded off towards 200 Hz. To achieve this bandwidth means that the mechanics much be designed such that

resonances which appear in the plant, should be at least above 600 Hz and preferably above 1000 Hz.

Just as important is that the components in the chain that closes the loop may only give a limited phase delay at the target bandwidth frequency. The amount of allowed phase delay is budgeted as follows. The behaviour of the plant to be controlled is mainly determined by the inertia of the rotor. Hence, the phase delay of the plant will be at least 180° at the target bandwidth. Closed loop stability is then achieved by adding a controller in the loop with sufficient phase lead. Assuming a maximum phase lead of the controller of 60° and that the loop should have a minimum phase margin (see [88]) of 30°, leaves a phase delay of 30° for the loop at the target bandwidth of 200Hz. The chain of components forming the loop can be divided in a sensor chain (sensors, sensor electronics and anti-aliasing filters) and actuator chain (amplifier and RTA). Furthermore the system is digitally controlled, which adds to the phase delay due to the limited sampling frequency. Distributing the phase delay budget to these three contributors, leaves a phase delay of 10° to each contributor at the bandwidth frequency.

This specification which should be taken into account when selecting the components of the actuator chain and the sensor chain.

5.2.2 Control Hardware

Flexible control architecture is required due to the experimental nature of the demonstrator. For this purpose the multi-board solution from dSPACE® was chosen. To minimize the phase delay due to sampling, the sampling frequency should be as high as possible. Based on earlier experiences with the system it was estimated that a full controller with additional safety software, can run at a sampling frequency of 10 kHz. This would introduce a phase delay of 3.6° at 200 Hz. The computational time should than remain below 90 μs in order to stay within the assigned budget of 10°. The allowed computation time allows for quite a computational load.

5.2.3 Gravity Compensator

Working Principle

The requirement of vacuum operation led to the decision to compensate the weight of the rotor with magnetic forces. To minimize the energy dissipation in the Gravity Compensator (GC), a solution using permanent magnets was sought. In [69] a solution is proposed using two pairs of permanent magnets, one pair that gives a positive stiffness and another pair that generates a negative stiffness. This is illustrated in Figure 5.2. The force resulting from the centre and the upper magnet,

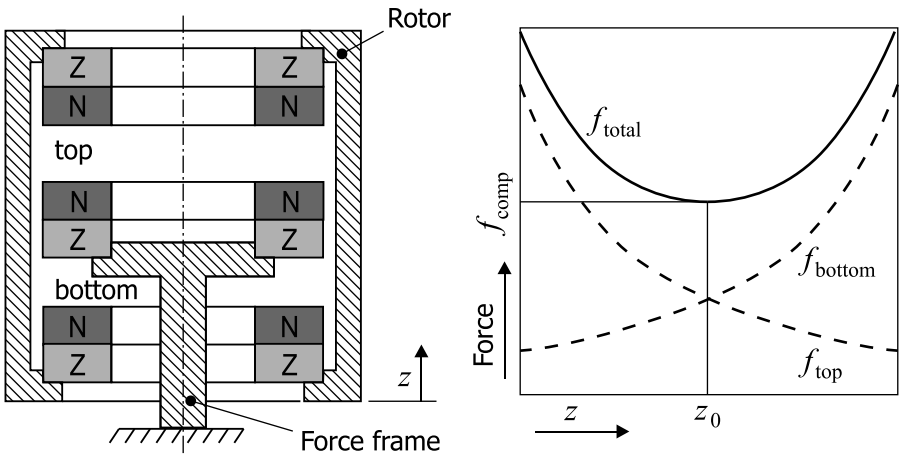

Figure 5.2. *Working principle of the gravity compensator. The force resulting from the centre and the upper magnet, is denoted f_{top}, while f_{bottom} indicates the force resulting from the centre and the lower magnet. The sum of these two force (f_{total}) has a small stiffness around working point z_0.*

is denoted f_{top}, while f_{bottom} indicates the force resulting from the centre and the lower magnet. The sum of these two force, denoted by f_{total}, is position dependent, except at certain position z_0 where a nett compensation force f_{comp} results. Hence, around z_0 a working range can be defined where the stiffness remains under a certain (low) value.

It can be shown that a low stiffness can be achieved in all directions [56]. The author of latter also developed the software for the configuration above with the use of Neodymium-Iron-Boron (NdFeB) magnets. This program was used in the design process to finalize the dimensions of the magnets.

In [43] another interesting solution is presented. The main difference is that the magnetization of the permanent magnets is in radial direction instead of axial. An advantage of this approach is that a coil can be added to generate Lorentz forces in z-direction. A disadvantage is that the compensated weight cannot be adjusted. At the time the design decision was made, this concept was still under development.

Note that the configuration as sketched in Figure 5.2 is unstable. Earnshaw ([24]) showed that it is not possible to have a stable stationary equilibrium of point charges that interact through position inverse-square forces, as is the case with permanent magnets.

The resulting compensation force acts on the rotor with its attachment point close to the centre of the middle magnet. Placing the middle magnet above the Centre of Gravity (CoG) of the rotor would result in a mechanical coupling due to

the pendulum effect. Placing the middle magnet below the CoG of the rotor would not only give mechanical coupling, but also increase the instability of the system. In this case the gravity force and the compensation forces have the same working line, but they are pointed towards the attachment point of the other force[2]. It is easily seen that a slight displacement of the rotor yields instability. In order to minimize these effects, it was decided to place the middle magnet of the GC close to the CoG of the rotor.

Disturbance Generating Mechanisms

The disturbances that could originate from the GC are due to inhomogeneous magnetization of the magnets or misalignment with respect to the central axis. Both mechanisms would result in synchronous disturbances.

Only at one exact point the stiffness in z-direction will be zero. Also, some stiffness in the other directions will remain. Hence, through these residual couplings vibrations in the force frame introduce force disturbances to the rotor.

5.2.4 Motor

The requirement of contact free operation and a low torque ripple leads to using brushless permanent magnet motors. These motors have permanent magnets on the rotor and three phase coils on the stator. The information of the position of the rotor, needed for the electric commutation of the coils, is provided by Hall-sensors or a separate encoder mounted on the motor's shaft.

The main consequence of the separation of the metrology and force frame is the requirement to have low stiffness between the rotor and the force frame. Commercially available brushless motors have (laminated) back iron on the stator, to increase the efficiency. Unfortunately, this inherently brings about a large stiffness, due to the attraction forces between the permanent magnets on the rotor and the back iron on the stator.

To decrease the stiffness the use of an ironless motor is therefore preferred. A drawback of an ironless motor is that the efficiency will decrease. For the demonstrator this is not a critical issue however, for the following reasoning. When the rotor is at stationary rotation speed, the coupling that the motor needs to provide is quite low; it only needs to overcome the drag resulting from air friction, eddy currents and hysteresis effects. Also the spinning up time is not critical, hence the motor efficiency is not a critical parameter.

Although an ironless motor was preferred, it was decided to use a motor with back iron that was available for this project, and then use the DEB approach to

[2] An extensive stability analysis of forces acting on a rigid body is given in [41].

evaluate its influence. It was also decided to start a separate project within the group of Advanced Mechatronics to find and/or design an ironless motor.

With the gravity compensator placed at the CoG of the rotor, the motor was designed to be under the gravity compensator.

Disturbance Generating Mechanism

The disturbances the motor can introduce are mainly torque ripples. These ripples can be caused by inhomogeneous magnetization of the magnets, cogging effects when slotted back-iron is used, and errors in commutation. Other disturbance are introduced by misalignment of the rotor axis with respect to the magnets of the motor.

All the disturbance generating mechanisms stated here, principally have a synchronous character. Indeed, it is unlikely the motor will generate asynchronous disturbances, hence in the Dynamic Error Budgeting (DEB) design process, the disturbances introduced by the motor are not considered.

5.2.5 Actuators

As was discussed in Section 2.4, reluctance Type Actuators (RTAs) are used for actuation of the rotor in all DoFs except for rotation. To minimize the stiffness of these actuators, Non-Linear Compensation (NLC) in the control law is used, as discussed in the previous chapter.

Geometrical Placing

Since the actuators only generate attracting forces, more than one actuator is needed per DoF. In Figure 5.3 the possible actuation configurations, with the number of RTAs, are given to control the five DoFs. The amount of space (for actuation surface and cables) is limited, which makes it desirable to minimize the number of actuators. This would lead to solutions with six actuators. On the other hand, since the high accuracy is only required in one plane, it is beneficial to have physical decoupling of the x-z and y-z planes. This would leave solutions c_1 and d_1. Rotors with shape c brings the risk of reduced controllability of the rotations around the x- and y-axis. Hence, actuator configuration d_1 is chosen.

Material Selection

For low phase delay, the flux damping due to eddy currents should be made as small as possible (see Subsection A.1.5). A disadvantage of the configurations c and d is that lamination is mechanically difficult to make. Another solution to

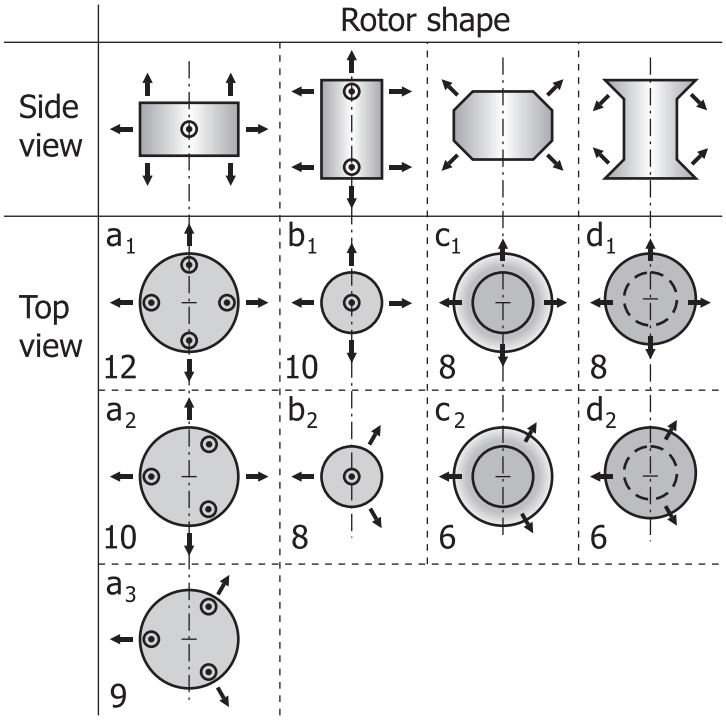

Figure 5.3. *Nine basic configurations for placing the Reluctance Type Actuators (RTAs), such that five DoF of the rotor are actuated. The arrows indicate the forces of the RTAs and the numbers indicate the amount of RTAs used in each configuration. Compromising between minimization of the number of RTAs and decoupling in the planes through the rotation axis, configuration* d_1 *was chosen.*

minimize the eddy currets is to chose a material with a sufficiently high relative permeability ($\mu_r > 1000$) and a electrical resistivity much higher than that of iron ($130{\cdot}10^{-9}$ Ωm). The resistivity is increased by adding elements of silicon or chromium to low-carbon iron. With these elements it is possible to make alloys with increased resistivity of about $700{\cdot}10^{-9}$ Ωm, while retaining good magnetic properties. However the increase of resistivity is not high enough for such alloys to have similar eddy current rejection compared to laminated iron.

A completely different type of soft magnetic material is ferrite. Ferrite is a ceramic material, composed out oxidized iron (Fe_2O_4) and one or several divalent transition metals, such as zinc (Zn), manganese (Mn) or nickel (Ni). These components do not mix by melting; the material is formed through a sintering process. Through the sintering process the material remains granular, which results in a high resistivity: 0.1 to 10 Ωm for MnZn ferrites and 10^4 to 10^6 Ωm for NiZn ferrites. Because the resistivity is high, the effects of eddy current damping are nearly eliminated, which removes the need for lamination. For this reason it was decided to use ferrite as the target material for the rotor. A disadvantage of ferrite is that it is very hard and brittle, making it difficult to machine.

Although NiZn ferrites have a higher resistivity, a MnZn ferrite was chosen because the material saturates at a much higher magnetic flux. The selected material has a resistivity of 2 Ωm, a saturation flux of 440 mT and a relative permeability of 2000.

Dimensioning

The initial estimation of the actuator force required, was based on four considerations. The first consideration is based on the fact that the gravity compensator will not perfectly compensate the weight of the rotor. With a rotor mass of 4 kg and assuming that the gravity compensator only compensates 80% of the rotor weight at startup and 90% around the working point, then a force of 8 N is required for starting up the system and 4 N when operational. This force is generated by four actuators which work under 45 degrees, hence starting up requires a force 2.8 N after which a force of 1.4 N per actuator is needed for operation.

One of the fundamental design choices, as discussed in Section 2.4, is that the rotor is to rotate around its Principal Axis of Inertia (PAI). The sensors measure on the surface of the rotor and hence measure not only the movement of the PAI, but also the roundness error of the rotor and the misalignment of the PAI with the geometrical rotation axis. These effects can be compensated by a feedforward table for each sensor, such that only the PAI is measured. The principle used to identify these feedforward tables is based on the fact that when the rotor is spinning around the PAI, no actuator force would be required.

To find the actuator forces required to maintain the rotor position when the PAI is not perfectly identified, it was assumed that the misidentified PAI axis is parallel to the real PAI with a distance of maximal 5 μm. With a maximum rotation velocity of 100 Hz, this would result in centrifugal forces of $m_r \Omega^2 \Delta r = 4 \cdot (2\pi 100)^2 \cdot 5 \cdot 10^{-6} = 7.9$ N. Forces in the x,y-directions are generated by two actuators under 45 degrees, hence a force of 5.6 N is required per actuator.

Non-Linear Compensation (NLC) requires current or force preloading, as discussed in Section 4.4. At this stage it was assumed that the force resulting from preloading would be maximally 1.0 N.

Finally, the estimated maximum peak acceleration level of the metrology frame is 10 mm/s^2. This would require a force of 40 mN for the rotor to follow the metrology frame and is negligible compared to the other considerations.

Using Equation (A.30) on page 165 the pole surface of the RTA can be calculated. The maximum force with the contributions discussed above is 9.0 N. The ferrite material saturates at 0.44 T, however to keep a safety margin to the ferrite that will be used, a saturation level of 0.35 T is taken. This leads to a surface of:

$$A_{flux} = \frac{\mu_0 \mu_a f_{max}}{B^2} = \frac{4\pi \cdot 10^{-7} \cdot 1 \cdot 8.0}{0.35^2} = 82 \text{ mm}^2. \tag{5.2}$$

A laminated E-core with standard dimensions (see Figure A.4 on page 168) was chosen for the RTA. The centre pole surface is 10×10 mm^2 and the thickness of the sheets are 0.35 mm.

From the analysis of parameter sensitivity of non-linear compensation, see Section 4.5, it follows that the air gap should not be too small compared to the dimensions of the actuator. On the other hand, a big air gap leads to a less efficient actuator. To compromise between these two effects an air gap of 0.5 mm was chosen.

Using (A.14) on page 162 and choosing a maximum current of 1 A, leads to an RTA with 280 windings, which is round off towards 300 turns. With a maximum current density of 10 A/mm^2 in the copper wires, the required copper surface is 30 mm^2. Although the required surface increases due to insulation of the wire and the fact that round wires do not fill a surface without leaving spaces, the required surface easily fits into the available surface (75 mm^2).

Disturbance Generating Mechanism

The main contributor to force disturbances is the current noise through the coil. The current noise is generated by the amplifier and by voltage noise on the input of the amplifier caused by the digital-to-analogue converter. These disturbance have an asynchronous character.

To linearize the RTAs NLC will be applied. As discussed in Chapter 4 on page 67, the NLC will not compensate perfectly, hence position couplings and non-linear effects will remain. As a result, force frame vibrations introduces force disturbances to the rotor. These position couplings are modelled with a spring stiffness of 1000 N/m at each actuator.

Furthermore, NLC uses measured position which will not be noise free. This sensor noise also translates to a current noise.

5.2.6 Sensors

Force Frame Sensors

The NLC requires position information of the rotor relative to the force frame. Two contactless sensing principles were considered; inductive and optic reflection. Optic reflection was preferred, since it reduces the risk of cross-talk between sensors and actuators to zero. Fiber-optic sensors from Philtec (see www.philtec.com, sensor type D63) were initially chosen, with a working range of 0.8 mm and a resolution of 80 nm (RMS) up to 100 Hz and 600 nm (RMS) up to 20 kHz.

Since eight RTAs are used, eight sensors are used, to be placed as close as possible to the RTAs.

Metrology Frame Sensors

The high precision sensors are used to measure the five DoFs of the rotor with respect to the metrology frame, hence five sensors are needed. Since the sensors need to have a very high accuracy, only two sensing principles appeared to be suitable; laser interferometry and capacitive. A parallel research project, focussing on the sensing challenges with the demonstrator, found a capacitive solution from ADE Technologies. According to the manufacturer, the 2805 sensor has a RMS-resolution of 0.2 nm at 1 kHz and 0.8 nm at 10 kHz, over a range of 50 μm.

The master disk (see Section 1.2) is placed on the top of the rotor. Hence, to minimize the Abbe-errors (see [89]), it is desirable to place the sensors as close as possible to the surface of the rotor, where the precision is needed.

Disturbance Generating Mechanism

Asynchronous disturbances are introduced by the electronic noise of the sensor and associated electronics.

5.2.7 Rotor

Now that the actuator configuration and the position of the motor and the gravity compensator is determined, the shape of the rotor is mostly determined. Other considerations that

effect the shape, are given here.

- The top surface should have a diameter of at least 150 mm to support the optical disk. The optical disks have a diameter of 180 mm, however it is not required to support the whole disk.
- The rotor should be as stiff as possible, in order to prevent that resonances in the rotor will limit the closed loop bandwidth. This consideration favours rotor designs in which the rotor diameter is roughly equal to the height.
- Considering that rotation at high speeds greatly influences the rotor dynamics, one might conclude that rotor dynamics might prefer a different shape than "square". However, at this stage of the design, it was concluded that the need for a high closed loop bandwidth, and thus rotor stiffness, outweighs the possible disadvantageous effects of rotor dynamics.

Taking in account the above points led to a shape of the rotor as shown in Figure 5.1. The diameter of the top surface is 180 mm and the total weight is 1.6 kg. This mass is a factor three lower than was considered for the actuator dimensioning. Since the design is only in the initial stage, the mass can still vary considerably. Hence, the actuator size was not reconsidered at this stage.

5.2.8 Force frame

Since the main function of the force frame is to hold the actuators and sensors, its shape is determined by the shape of the rotor and actuator placement.

Vibrations in the force frame result in disturbances to the rotor, due to the residual (position) couplings between rotor and force frame. To prevent excessive displacement due to vibrations in the force frame, it should be reasonably stiff.

The shape of the frame was not considered at this stage of the design. Main focus at this stage was to finalize the design of the rotor. Hence, during the DEB design process of the rotor, the force frame was not further considered.

5.2.9 Metrology Frame

The metrology frame was initially estimated at 100 kg, with the suspension frequencies in the five DoF at 1.5 Hz and a relative damping of 0.4.

The shape of the frame was not considered at this stage of the design. Again, the main focus at this stage was to finalize the design of the rotor, so the metrology frame was not further considered at this point.

Disturbance Generating Mechanism

The rotor is to follow the metrology frame, hence any movements of the metrology frame acts as a disturbance for the accuracy to be achieved. Movements of the metrology frame are induced by vibrations on the force frame and acoustic noise.

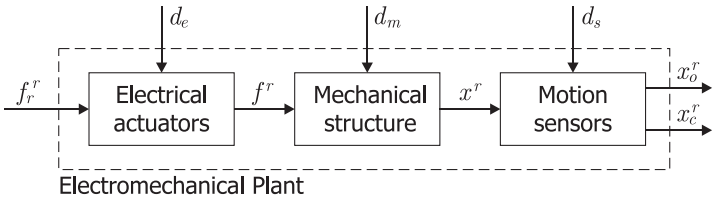

Figure 5.4. *The electromechanical plant divided into three subsystems. Electrical actuators convert the reference force input to NLC f_r^r into the force f^r that acts on the mechanical structure. The motion sensors detect the movement of the rotor with respect to the force frame (x_o^r) and metrology frame (x_c^r).*

5.3 Modelling and Controller Design

5.3.1 Introduction

Following the design approach as indicated by Figure 2.1 on page 14, once the initial design choices are made, the Dynamic Error Budgeting (DEB) design process is started. This requires models of the system and the disturbances.

The goal of the system model is twofold. Firstly, it is to be used for the design of the controller. Hence the model should be able to predict the behaviour of the movements of the rotor with respect to the Force Frame (FF) and the Metrology Frame (MF), as function of the actuator forces. Secondly, the model is used for DEB. This implies that the model should not only predict the behaviour of the movement of the rotor as function of the actuator forces, but as function of the ground vibrations as well.

Following [83], an electromechanical plant can be divided into electrical actuators, a mechanical structure and motion sensors, as indicated in Figure 5.4. The electrical actuators transform the reference input force f_r^r into the force acting on the mechanical structure (in this case the rotor), f^r. Here, it encompasses the Non-Linear Compensator (NLC), the Digital-to-Analogue-Converters (ADCs), the amplifiers and the Reluctance Actuators (RTAs). It is assumed that the NLC perfectly linearizes the RTAs and that the remaining position dependency can be modelled as a linear stiffness (see next section). By linearizing around a working point the disturbances that act on the NLC, ADCs, amplifiers and RTAs can be converted to the input of the plant as a disturbance force f_d^r. It is also assumed that the electrical actuators have no relevant dynamics below 1000 Hz, ignoring the effect of eddy currents (see Subsection A.1.5).

The mechanical structure transforms the input force f_r^r into a physical position of the rotor x^r. The mechanical structure is composes of the rotor, the metrology frame and the force frame. The disturbances that act on the mechanical structure are floor vibrations and acoustic noise. The modelling approach for the mechanical structure is discussed in the next section.

The motion sensors measure the position of the rotor with respect to the force frame x_o^r, and with respect to the metrology frame x_c^r. Here, the block motion sensors encom-

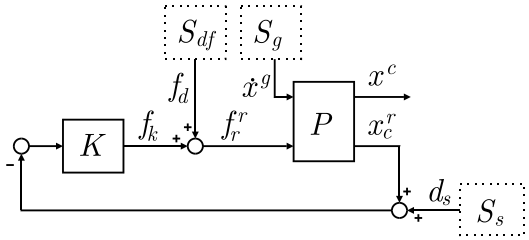

Figure 5.5. *The closed loop system for the rotating demonstrator with its disturbance sources.*

pass the physical motion sensors, as well as the Analogue to Digital Converters (ADCs). Disturbances such as sensor and ADC noise can be converted to the output of the physical plant, as position noise. It is here assumed that the dynamics of the sensors can be neglected up to 1000 Hz.

Except for the floor vibrations, all the disturbances acting on the plant can be converted to force disturbance acting on the input or sensors disturbance acting on the output of the plant. Hence, the closed loop configuration for the Dynamic Error Budgeting (DEB) analysis takes the form of Figure 5.5. Since the electric actuators and motion sensor are assumed not to have any dynamic behaviour, only the mechanical modelling is of importance for the DEB analysis.

5.3.2 Modelling of the Plant

Steps in Modelling Complexity

In the DEB design process, the complexity of the model (and disturbance) was increased in several steps. Of the initial design of Figure 5.1, first a two dimensional model (with three DoFs of the rotor) was made, and then a three dimensional model (with five DoFs of the rotor), including rotor dynamics. Also, in an early stage, the force frame was considered to have infinite mass, such that reaction forces of the actuators did not contribute to the movement of the metrology frame.

This section describes the model of the final design, and the DEB process is illustrated with examples using this model.

Assumptions

For the modelling of the rotor only five DoFs are considered, since the rotation around the z-axis has, inherently to the design, very low couplings with the other DoFs. Also, the moment around the z-axis will be very small during operation (except when the rotor spins up or down, but then the specifications need not be achieved). Similar reasoning applies to the metrology frame. Since, rotation around the z-axis are not visible for the capacitive sensors, this DoF is not considered. Now for the force frame it is assumed that

rotations around the z-axis can be neglected. Assuming further that the rotor, the force and metrology frame are infinitely stiff, the total model will compass fifteen DoFs. The mechanical modelling of the system is extensively covered in Appendix B.

The most salient assumptions made for mechanical model are:

- The rotor, force frame and metrology frame are rigid bodies.
- Rotation around the z-axis can be neglected for all three rigid bodies.
- All the mass and inertia of the force frame are determined by the granite block.
- The damping in the system is viscous, i.e. the forces due to damping are proportional to the velocity.
- The remaining position dependency of the NLC in combination with the actuators are modelled with a stiffness of 1000 N/m at each actuator.
- The gravity compensator is modelled with a negative stiffness couplings of 250 N/m in z-direction and 125 N/m in x- and y-direction.

Modelling of the Rotor

With the above assumptions, the motion equations can be shortly written in matrix form. For example, the motion equation for the rotor becomes:

$$M_r \ddot{x}^r + D_r \dot{x}^r + K_r x^r = D_{fr} \dot{x}^f + K_{fr} x^f + F_r f^r, \tag{5.3}$$

where $x_r = [x\ y\ z\ r_x\ r_y]_r^{\mathrm{T}}$, the displacement vector at the Centre of Gravity (CoG) of the rotor, $M_r = [m_r\ m_r\ m_r\ I_r\ I_r]^{\mathrm{T}}$ the mass matrix, in which m_r the mass and I_r the inertia of the rotor, D^r the damping matrix and K^r the stiffness matrix, D_{fr} the damping matrix representing the forces that act on the rotor caused by the velocity of the force frame, K_{fr} the stiffness matrix representing the forces that act on the rotor caused by the displacement of the force frame and $f^r = [f_x\ f_y\ f_z\ m_x\ m_y]^{\mathrm{T}}$ the force vector acting on the CoG of the rotor.

Due to rotation, additional coupling between the DoFs is introduced. The coupling can be modelled by skew-symmetric matrix, which is dependent on the rotation velocity. This matrix adds to the dampening term D_r of (5.3), see [3, 87]. The force on the rotor due to rotation is given by:

$$f^r = -\Omega \begin{bmatrix} 0 & 0 & 0 & 0 & 0 \\ 0 & 0 & 0 & 0 & 0 \\ 0 & 0 & 0 & 0 & 0 \\ 0 & 0 & 0 & 0 & I_z \\ 0 & 0 & 0 & -I_z & 0 \end{bmatrix} \dot{x}^r, \tag{5.4}$$

with Ω the rotation velocity of the rotor in rad/s.

Total Mechanical Model

The motion equations of the force and metrology frame can be written in the same form of (5.3). Stacking the three matrix equations gives:

$$\begin{bmatrix} M_r & 0 & 0 \\ 0 & M_f & 0 \\ 0 & 0 & M_m \end{bmatrix} \begin{bmatrix} \ddot{x}^r \\ \ddot{x}^f \\ \ddot{x}^m \end{bmatrix} + \begin{bmatrix} D_r & -D_{fr} & 0 \\ -D_{rf} & D_f & -D_{mf} \\ 0 & -D_{fm} & D_m \end{bmatrix} \begin{bmatrix} \dot{x}^r \\ \dot{x}^f \\ \dot{x}^m \end{bmatrix} + \begin{bmatrix} K_r & -K_{fr} & 0 \\ -K_{rf} & K_f & -K_{mf} \\ 0 & -K_{fm} & K_m \end{bmatrix} \begin{bmatrix} x^r \\ x^f \\ x^m \end{bmatrix} = \begin{bmatrix} 0 \\ D_{gf} \\ 0 \end{bmatrix} \dot{x}^g + \begin{bmatrix} 0 \\ K_{gf} \\ 0 \end{bmatrix} x^g + \begin{bmatrix} I \\ -T^a_{vf} T^a_{rv} \\ 0 \end{bmatrix} f^k + \begin{bmatrix} f^r \\ f^f \\ f^m \end{bmatrix}, \quad (5.5)$$

where x^m, x^f and x^g are the displacements vectors of the metrology frame, the force frame and the ground, respectively, f^k is the control force from the controller and D_{gf} and K_{gf} represent the coupling from ground vibrations to forces on the CoG of the force frame. The matrix $T^a_{vf} T^a_{rv}$ converts the reaction force of the control force f^k to the CoG of the force frame. Equation (5.5) can be easily written into state space form. More details on the modelling can be found in Appendix B.

The Bode magnitude of the resulting plant is given in Figure 5.6. The diagonal terms shows a stiff behaviour for low frequencies (< 6 Hz) and an inertia behaviour for higher frequencies (-2 slope). The anti-diagonal terms show relative high couplings for low frequencies, but they drop off with -4 slopes. The remaining terms inhibit small couplings in between 2 and 30 Hz. Rotation of the rotor introduces more dynamics and coupling. The rotation diagonal terms show an well-known phenomenon of rotor dynamics; a single rigid body resonance frequency will break down into two resonance frequencies when rotating. The corresponding modes are denoted nutation or forward whirl and precession or backward whirl, see [3, 87]. The nutation frequency increases with increasing rotation velocity, while the precession frequency decreases. Above the highest eigenfrequency (at 60 Hz), the rotation diagonal quickly dominates the cross-diagonal terms, as the latter drop off with -3 or -4 slopes.

5.3.3 Initial Controller Design

For the design of the controller it is assumed that the NLC (see Subsection 4.4.3) perfectly linearizes the RTAs. If this is the case, the input of the plant are forces and moments acting on the CoG of the rotor in the five DoFs.

For the initial controller design, controllers were designed for each DoF independently, neglecting the couplings in the transfer function. The controllers used for the DEB

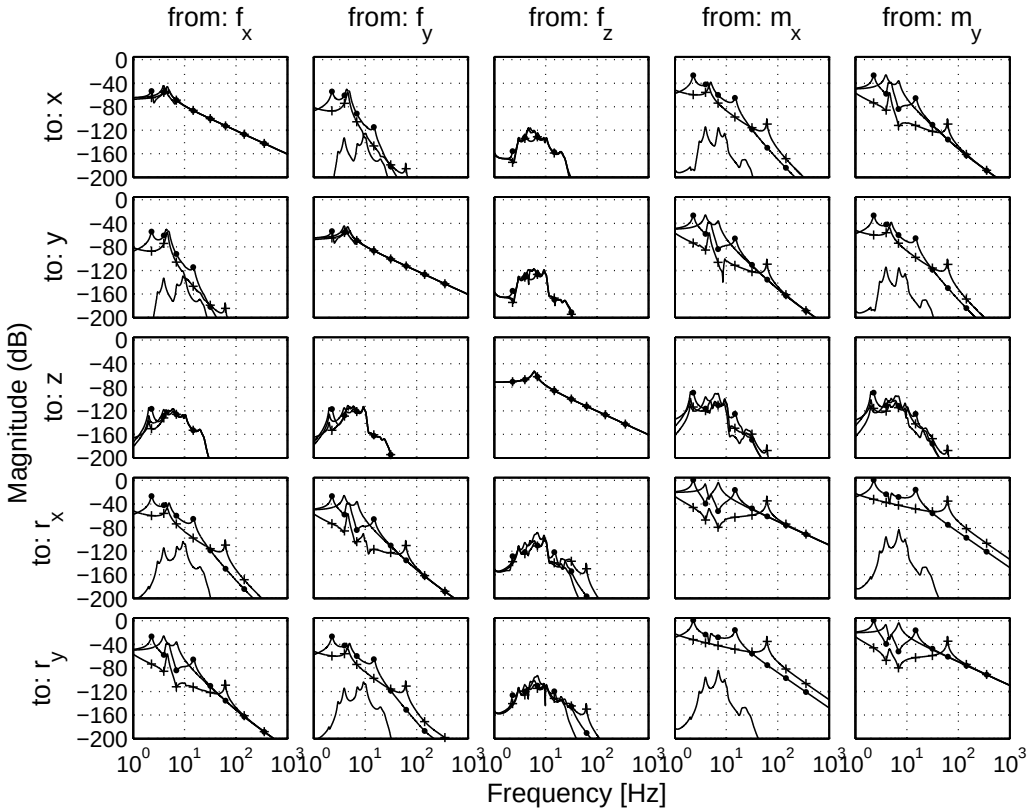

Figure 5.6. *The Bode magnitude of the modelled plant for different rotation velocities: 0 Hz (solid), 20 Hz (solid-dot) and 100 Hz (solid-plus). For 0 Hz, the diagonal terms shows a stiff behaviour for low frequencies (<6 Hz) and an inertia behaviour for higher frequencies (-2 slope). The anti-diagonal terms show relative high couplings for low frequencies, but they drop off with -3 slopes. With rotation the system shows (much) more dynamics and coupling.*

Table 5.1. *Parameters of the controller used to show the influence of the design on the performance.*

Parameter	Value	Unit	Parameter	Value
ω_{bw}	$2\pi f_{\text{bw}}$	rad/s	α_d	15
ω_i	$\omega_{\text{bw}}/(\alpha_i\sqrt{\alpha_d})$	rad/s	α_i	1
ω_{ro}	$\omega_{\text{bw}}\cdot\alpha_{\text{ro}}\sqrt{\alpha_d}$	rad/s	α_{ro}	2

analysis are standard PID-based controllers:

$$K(s) = k_p \underbrace{\left(\frac{s+\omega_i}{s}\right)}_{K_i} \underbrace{\left(\frac{s+\omega_{\text{bw}}/\sqrt{\alpha_d}}{s+\omega_{\text{bw}}\sqrt{\alpha_d}}\right)}_{K_d} \underbrace{\left(\frac{\omega_{\text{ro}}}{s+\omega_{\text{ro}}}\right)}_{K_{\text{ro}}}, \tag{5.6}$$

in which $\omega_{\text{bw}} = 2\pi\cdot f_{\text{bw}}$ is the bandwidth frequency, α_d determines the maximum phase lead, ω_i the cut off frequency of the integration action and ω_{ro} the frequency where the roll-off starts. The parameters of (5.6) are given in Table 5.1. With these parameters a controller with a maximum phase lead of 40 degrees at the bandwidth frequency is realized. The controller gain k_p is chosen in such a way that $|L_{\text{dof}}(\omega_{\text{bw}})| = 1$, in which L_{dof} is the loop gain of the concerning DOF.

From Figure 5.6 it is seen that rotation introduces additional dynamics in the transfer functions with inputs m_x and m_y and with outputs r_x and r_y. When the rotor makes 100 revolutions per second, the rotation diagonal terms shows resonances at 60 Hz and only above this frequency the rotor reacts as an inertia on the diagonal terms. This implies that the bandwidth frequency should be higher than this resonance frequency for the rotation directions. Indeed, a bandwidth frequency of at least 130 Hz is required in these directions to stabilize the system when rotating at 100 Hz.

In the next section controllers with double integrating action are used in some cases. Such controllers gives better disturbance suppression for frequencies less than the bandwidth divided by roughly a factor ten. This at the cost of more amplification of disturbances around the bandwidth frequency (the "dirt" that is moved around, see Subsection 3.6.6). In these cases the controller is given by:

$$K(s) = k_p K_i^2 K_d K_{\text{ro}} \tag{5.7}$$

In Section 3.6 it was shown that the performance could be significantly improved by designing an $\mathcal{H}_2$-optimal controller. For the design of the rotor this was not done, because no weighting filters were available. Obtaining these weighting filters would require spectral factorization (see Subsection 3.6.4) of the measured PSDs, which was not attempted due to time constraints. As a result, the design tends to be more conservative[3].

[3] Which is actually good practise; (slight) conservatism during the design gives some additional safety margin.

5.3.4 Disturbance Modelling

Synchronous Disturbances

In the previous section, several disturbance generating mechanisms that would result in synchronous errors were discussed. In the design process the following synchronous disturbances were modelled.

Firstly, a misalignment of the Gravity Compensator (GC) with respect to the rotor z-axis causes a moment around the r_x- and r_y-axis with a frequency equal to the rotation frequency. This disturbance torque equals the compensation force times the misalignment. With an initial estimated mass of 5 kg and assuming a worst case misalignment of 0.1 mm, results in a moment of $m_{\text{mis}} = 2.54 \cdot 9.8 \cdot 0.2 = 5$ Nmm.

Another disturbance caused by the GC is the inhomogeneity in the magnetic field density of the magnets in the GC. This is estimated to be 1%, which results in a force variation of 2% (see (A.30) on page 165) of the GC force. It is further assumed that the variation of the inhomogeneity around the circumference is smooth such that it can be approximated by the sum of sine waves up to 10 periods, with each sine having an equal contribution to the variation. The centre diameter of the magnets is 22 mm[3], so the amplitude of the sines of the resulting disturbing moments is $m_{\text{inh}} = 0.02 \cdot 22 \cdot 10^{-3} \cdot 25/10 = 1.1$ Nmm.

A third disturbance source is the unbalance in the rotor. Two types of unbalance are distinguished, see [87]. When the CoG is not on the axis of rotation, a static unbalance results, while dynamic unbalance refers to when the PAI is not aligned with the rotation axis. In the previous section, when the actuators were dimensioned, it was assumed that the PAI could be identified with an accuracy of 5 μm. This is in fact very conservative, since machining with a turning lathe has about the same accuracy. As a still conservative estimation, it is assumed that the identification algorithm will be able to determine the PAI with an inaccuracy of 1 μm. Hence, the resulting static unbalance creates a disturbing force in the x- and y-direction of $m_{\text{stat}} = m_r \Omega^2 \Delta r = 2.54 \cdot (2\pi \cdot 100)^2 \cdot 1 \cdot 10^{-6} = 1.0$ N at the rotation frequency.

The disturbance force resulting from a dynamic unbalance is given by the following equation (from [87]):

$$m_{\text{dyn}} = I_{xy} \Omega_z^2 = \tfrac{1}{2} (I_{xx} - I_{zz}) \tan(2\alpha_{\text{pai}}) \, \Omega_z^2, \tag{5.8}$$

in which I_{xy}, I_{xx} and I_{zz} are moments of inertia and α_{pai} the inclination of the PAI. With a height of the rotor of 155 mm, the worst case inclination is estimated at: $\tan \alpha_{\text{pai}} = 2 \cdot 10^{-6}/0.155$. Filling in the values in the above equation give a disturbing moment of:

$$m_{\text{dyn}} \approx \tfrac{1}{2} (6.03 \cdot 10^{-3} - 4.55 \cdot 10^{-3}) \, 2 \frac{2 \cdot 10^{-6}}{155 \cdot 10^{-3}} \, (100 \cdot 2\pi)^2 = 7.5 \text{ Nmm} \tag{5.9}$$

The impact of these synchronous disturbances on the performance is discussed in Subsection 5.4.6.

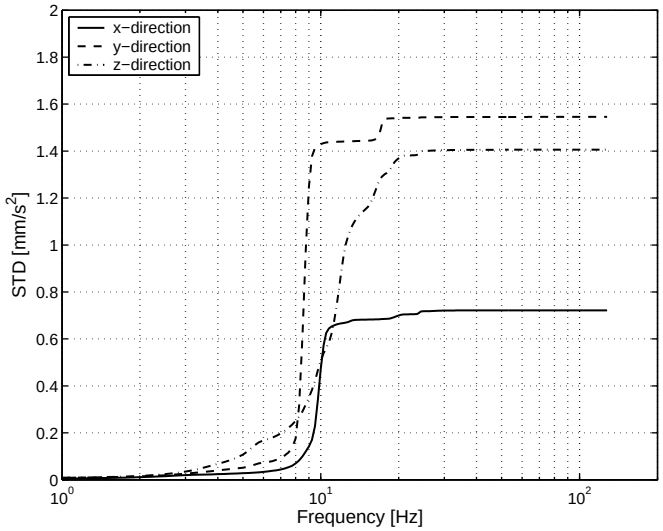

Figure 5.7. *Measured Cumulative Amplitude Spectra (CAS) of the vibration levels at the granite table (not shown are the CAS for the rotations). The end-values are 0.72, 1.5 and 1.4 mm/s², for the* x, y *and* z*-direction, respectively.*

Ground Vibrations

The ground vibrations were measured at the granite table. This to ensure that the vibration level on the table is correctly modelled and does not depend on the model accuracy of the force frame (granite table). Figure 5.7 shows the measured CAS of the vibration levels at the granite table. Since the force frame is included in the model, the measured acceleration spectra on the table are filtered with the inverse transfer function from floor to table. To calculate the inverse of a transfer function, it must be proper[4] and must not contain right half plane zeros (non-minimum phase system). The transfer function $\ddot{x}_f/\dot{x}_g$ can be made with the techniques described in Appendix B.1 on page 173 and is invertible with the described model. With the transfer function $\ddot{x}_f/\dot{x}_g$ the measured acceleration are transformed into a velocity spectrum at the ground input.

Using relation (3.44), the velocity spectra of the floor can be calculated:

$$S_g = G_{g2f}\, S_f\, G_{g2f}^* \tag{5.10}$$

with S_f the measured acceleration PSD of the force frame, G_{g2f} the transfer function $\ddot{q}_f/\dot{q}_g$, and S_g the velocity PSD of the ground.

[4]The D matrix of the state space realization must be invertible, see [83, p.87]

Force Disturbances

The force disturbances to the rotor are due to the current noise caused by the amplifier and the Digital-to-Analogue Converter (DAC). The noise from the position sensors used for NLC also translates to disturbance forces but these were neglected in the design phase. Whether this assumption is justified is discussed in the next section.

The current noise of the amplifier is measured to be 60 μA (PtV), see [27]. Assuming the noise has a normal distribution and approximating the peak-to-valley value with the six sigma value (99.7% confidence interval), the STD becomes 10 μA. The DAC from dSPACE® has sixteen bits over a range from 0 to 10 V, whereas 10 V corresponds to 1 A, the STD of the quantization noise is: 4.4 μA.

The generated currents drive the RTAs, which are non-linear. Hence, to translate the current noise as an force disturbance on the input of the plant of Figure 5.5, the RTAs are linearized around a working point. It is assumed that the applied NLC strategy (see Subsection 4.4.3) results in a bias force of 1 N, and that the gravity compensator is not perfectly balanced, resulting in a constant force of 1.4 N for some of the actuators (see Subsection 5.2.5).

With the chosen RTA, a DC force of 2.4 N is realized with a DC current of 0.46 A. The linearized gain of the RTA then becomes:

$$k_i = \left.\frac{\partial f_{\text{rta}}(i, x_{\text{nom}})}{\partial i}\right|_{i_{\text{dc}}} = 2k_{\text{rta}}\frac{i_{\text{dc}}}{x_{\text{nom}}^2} = 10.4 \text{ N/A}. \tag{5.11}$$

With the linearized, worst case scenario gain, the PSD of the disturbance force per actuator becomes:

$$\begin{aligned} S_{act} &= \frac{(k_i \sigma_i)^2}{f_N} \cdot I^{8\times 8} \\ &= \frac{(10.4 \cdot \sqrt{4.4^2 + 10^2} \cdot 10^{-6})^2}{5000} \cdot I^{8\times 8} = 2.6 \cdot 10^{-12} \cdot I^{8\times 8} \end{aligned} \tag{5.12}$$

This 8×8 PSD is easily converted to a 5×5 PSD acting at the CoG of the rotor using (3.44) on page 55:

$$S_f = (T_{vr}^a T_{av}^a) S_{act} (T_{vr}^a T_{av}^a)^{-1}, \tag{5.13}$$

where $(T_{vr}^a T_{av}^a)$ is the transformation matrix from actuator force to forces at the CoG of the rotor.

Sensor Noise

There are three contributors that add disturbances in the sensor chain; noise from the sensor itself, quantization noise from the ADC and electronic noise of the ADC.

The noise of the sensors have been measured to have an RMS value of 0.25 nm up to 5000 Hz. The ADCs from dSPACE® are specified to have 16 bits and a SNR due to electronic noise better than 80 dB. The PSDs from these two disturbances can be calculated using the formulas given in Section 3.3.

5.4 Design Process Examples

5.4.1 Elaboration on the Design Process

The design of the demonstrator was carried out in a iterative process, during which the design gradually matured to its final design. In this process design decisions were taken using the Dynamic Error Budgeting (DEB) approach. The complexity of the models used for DEB increased during the design process, starting with a relative simple two dimensional model with three DoFs for the rigid bodies, and ending with the full three dimensional five DoF model.

The implications of the design examples here discussed are evaluated though with the final five DoF model. This is done to prevent describing the various subsequent models. The details of this design process is described in [42].

For the design examples discussed in this section the performance is evaluated in y-direction only. The reason for this is that because the modelled disturbances are biggest in this direction, as shown in Figure 5.7 on page 114. The examples are evaluated with the system rotating at 100 Hz.

In Subsection 2.2.3 it was derived that the AREM should be smaller than 1 nm (STD). To account for unknown disturbances which might occur in the real system, a margin of two is taken for the design, resulting in a target performance of 0.5 nm (STD).

5.4.2 On the Motor

The motor function is a fundamental element in the design, and one of the first design issues that was addressed. As discussed in Subsection 2.4.2, the stiffness of the motor should be minimized in order to prevent that movements of the force frame introduce disturbing forces to the rotor. At an early stage in the design a brushless Direct Current (DC) motor was available. In a brushless DC motor the magnets are attached to the rotor, and the coils to the stator. The motor was optimized for low cogging, but had iron on the stator for flux guiding to increase the efficiency. Because of the iron the motor has a large negative stiffness, which was estimated at $-230 \cdot 10^3$ N/m in x- and y-direction at the centre of the motor. The couplings in the rotation directions were unknown.

Figure 5.8 shows the CAS of the performance with the motor. The performance is 60 nm (STD), completely dominated by floor vibrations. This was achieved with a closed loop bandwidth of 200 Hz. Even if a controller with double integration action would be used, the best performance is 1.2 nm, requiring a bandwidth of 350 Hz. Even worse, the stiffness of the motor quickly increases when not in the centre position (exactly as with the RTAs in Chapter 4, which show an increasing stiffness with decreasing air gap), making the coupling effects very likely to be stronger.

All in all, it was abundantly clear that the back iron motor was not suitable. At this point in the design it was decided to look for a brushless DC motor without iron in the stator to minimize the position coupling between the force frame and rotor. In anticipation

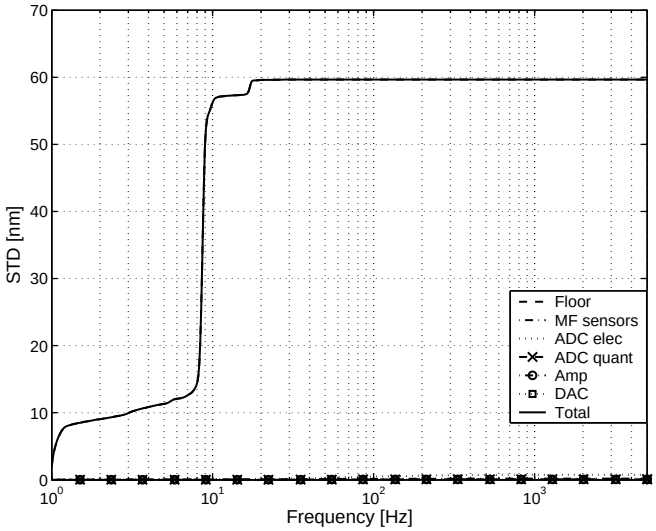

Figure 5.8. *Cumulative Amplitude Spectrum (CAS) of the predicted performance using of a motor with back iron in the design. The back iron in the motor results in a high stiffness, which couples the force frame with the rotor. This coupling explains why the performance is completely dominated by the floor vibrations.*

of such a motor, a dummy mass at the position of the motor was incorporated in the design with a stiffness of 500 N/m in x- and y-direction.

The performance of the design without the high stiffness motor is given in Figure 5.9. From the figure it becomes clear that the performance increases dramatically to a STD of 0.82 nm.

5.4.3 On the Analogue to Digital Converter

Figure 5.9 shows that the biggest contributor to the position error is the electronic noise of the Analogue to Digital Converters (ADCs) used to read the analogue voltage outputs of the capacitive sensors. The STD of the performance is 0.82 nm of which the ADCs contribute 0.72 nm, which is already close to the goal of 0.5 nm.

Note that the servo error as measured differs from the performance. The measured servo error is 1.8 nm (rms), of which 76% comes from the electronic noise of the ADC. This makes it difficult to judge whether the specifications are met in reality when considering the sensors signals. Hence for this reason it is useful to keep the noise of the complete sensor chain amply below the target performance (in this case half a nanometre).

To have a noise contribution of the ADC comparable to that of the sensor, the ADC should have a SNR better than 97 dB. Hence, a separate research project[5] was started to

[5]This was part of another PhD project, see the division of the total project, described in Subsection 1.4.4.

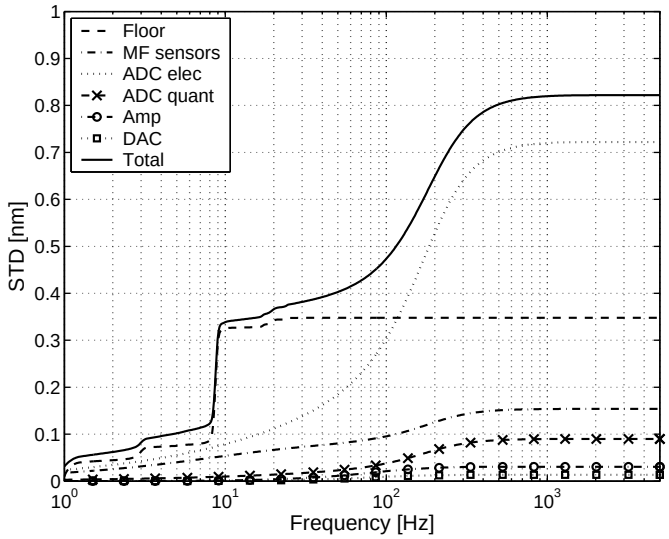

Figure 5.9. *CAS of the predicted performance of the design without the high stiffness motor. The biggest contribution to the error now comes from the analogue-to-digital converters.*

find/build a "true" 16 bit converter (a true 16 bit converter has a SNR of 98 dB). Figure 5.10 shows the result with such an ADC. The design goal to achieve a performance of 0.5 nm (RMS) is now achieved with a STD of 0.40 nm. At this stage it was decided to finalize the design of the rotor and continue the design of the metrology frame.

5.4.4 On the Resolution of the Metrology Frame Sensors

One of the design choices (see Section 2.4) is that the AREM specification need only to be met in the x- or y-direction. So, from a cost prize point of view, it can be beneficial to have lower quality components for the servo loops in the other directions. Expensive components in the system are the high resolution Metrology Frame (MF) sensors and associated high quality ADCs.

To gain insight in the sensitivity of the system to using MF sensors of lower quality in the z-direction, these sensors are made 50 times more noisy than in the x- or y-direction. Hence, the RMS value of the sensors in the z-direction are now 10 nm.

The DEB analysis showed that the contribution from the MF sensors increased from 0.15 nm (as was shown in Figure 5.10) to 0.40 nm. However, the total performance only decreased from 0.40 nm to 0.55 nm, which is only very slightly more than the design target. Although this knowledge was not used any further, it should be considered when redesigning the system.

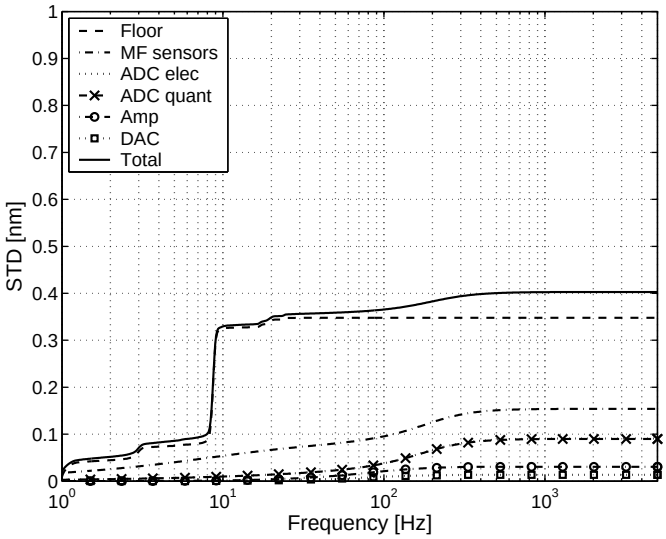

Figure 5.10. *CAS of the performance with a true 16 bit ADC. The design goal to achieve a performance of 0.5 nm (RMS) is now achieved.*

5.4.5 On the Influence of the Force Frame Sensors

The design of the rotor was finalized assuming that the noise stemming from the Force Frame (FF) sensors used for Non-Linear Compensation (NLC) would not be critical. In this subsection that assumption is investigated.

The NLC uses the relative position of the rotor with respect to the FF measured by the optical fiber optic sensors. As a result, the noise of the FF sensors translate into a current noise. In Section 4.5 it was derived that the force disturbance from measurement noise equals:

$$d_f = 2\left(\frac{f_r}{x_g}\right) d_s, \tag{5.14}$$

in which d_f is the disturbance force, f_r the reference force input to the NLC, x_g the air gap, and d_s the measurement noise. The optical sensors have a noise of 0.33 μm (RMS) up to 5000 Hz.

In the previous section, to analyse the current noise propagation, the total worst case bias force was estimated to be 1 N for NLC and 1.4 N because of that the gravity compensator would only compensate 90% of the weight of the rotor. The 1.4 N is only delivered for four actuators, hence in average 0.7 N can be taken for all eight actuators. In Figure 5.11 the performance of the system with a bias force of 1.7 N is shown. It can be seen that the performance has deteriorated to 1.2 nm. To reduce the deteriorating effect of the FF sensors, the bias force should be reduced. If the bias force required by the NLC is reduced to 0.2 N and the gravity compensator is better adjusted such that only 0.35 N on average is required from the actuators, the performance can be improved to 0.54 nm.

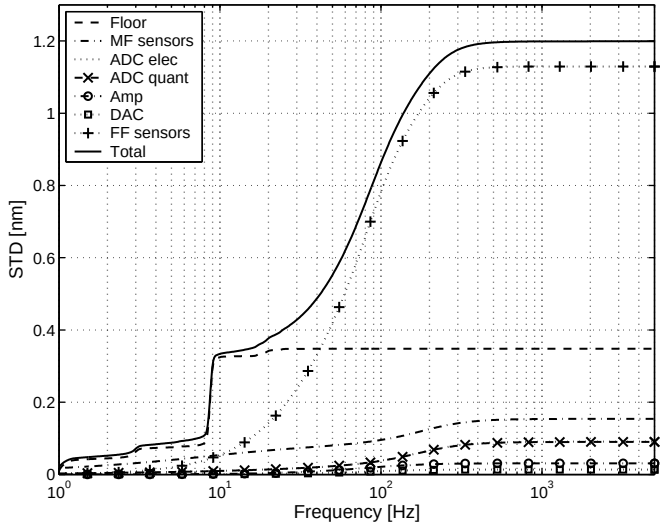

Figure 5.11. *CAS of the performance with taking into account a worst case estimation of the noise from the force frame sensors. The noise of the force frame sensors translate to current noise due the NLC. The performance has deteriorated to 1.2 nm. With pre-cautions this can be improved to 0.55 nm.*

The DEB analysis clearly showed that the noise from the FF sensors cannot be neglected. Care must be taken to minimize the effect.

5.4.6 On the Synchronous disturbances

With the synchronous disturbances as modelled in the previous section, the calculation of the resulting synchronous displacement of the rotor is rather straightforward. Representing the disturbances for the five DoFs as complex entries of a vector, the response is easily calculated by multiplying this vector with the process sensitivity function of the closed loop system evaluated at the rotating frequency (and the higher harmonics for the disturbances introduced by the inhomogeneity of the magnets in the gravity compensator). The resulting displacement, evaluated at the rim of the rotor, is shown in Figure 5.12a in a polar plot. It can be seen that the rotor shows a movement with an amplitude of 650 nm, which is much lower than the specification of 50 μm (see Section 2.2).

Section 2.2 also specified that the allowed accelerations in x- and y-directions should be lower than 2.4 $\mathrm{m/s^2}$. Figure 5.12b gives the resulting accelerations in a polar plot. The maximum acceleration level is 0.31 $\mathrm{m/s^2}$, which is indeed well within the specification.

With the safe margins on the synchronous disturbances to the performance, it can be assumed that synchronous disturbances are no serious difficulty for the system.

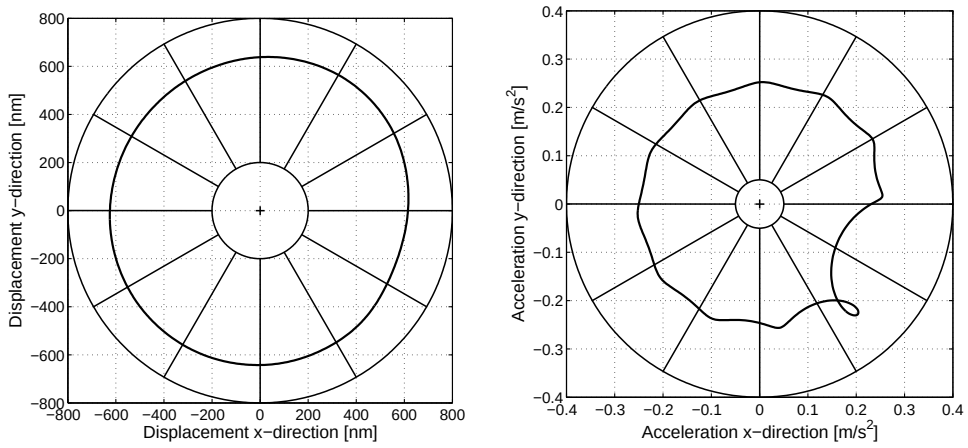

a b

Figure 5.12. *Analysis of the simulated influence of the synchronous disturbances on the performance. a) Polar plot of the synchronous radial error motion. b) Polar plot of the accelerations in radial directions. Both are well within specifications.*

5.5 Discussion Final Design

In Figure 5.13 the final design of the rotor is given. The several parts are discussed in the subsections below.

5.5.1 Rotor

Comparing the shape of the rotor of the final design to that of the initial design of Figure 5.1 on page 97, the rotor has become more "solid". The outer diameter has been decreased to 150 mm, while the mass has increased to 2.54 kg. In addition a rim has been added to the rotor, to provide a target surface for the capacitive sensors measuring in x- and y-direction.

To verify whether or not the internal resonances should be taken into account for the controller design, a Finite Element Model (FEM) of the rotor was made using Ansys[6]. Because of the actuators the rotor is not cylindrical symmetric and one quarter of the model was modelled. The six rigid body modes predicted by the FEM corresponded nicely with the analytical model.

Ten internal resonances below 10 kHz were found. Not taking into account modes around the z-axis (the lowest of which is at 4.3 kHz), the lowest resonance frequency relevant for the control is at 4.4 kHz. The corresponding mode of this resonance is shown in Figure 5.14a, while Figure 5.14b shows an eigenmode with a frequency of 8.3 kHz.

It can be concluded that the rotor is abundantly stiff designed, and that internal eigenfrequencies are much higher (a factor 20) than the foreseen bandwidth frequency.

[6] Ansys version 5.7.1 was used, see www.ansys.com.

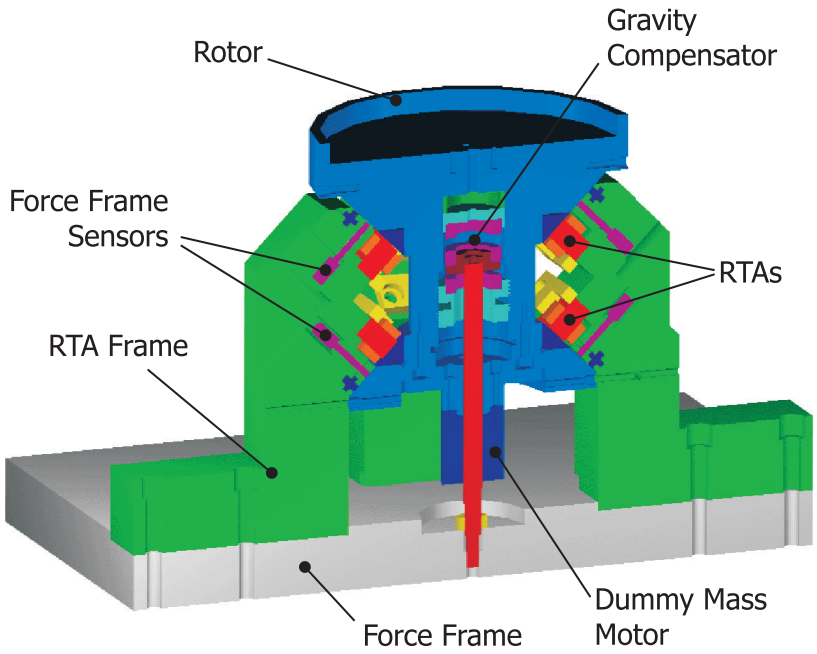

Figure 5.13. *Final design of the rotor.*

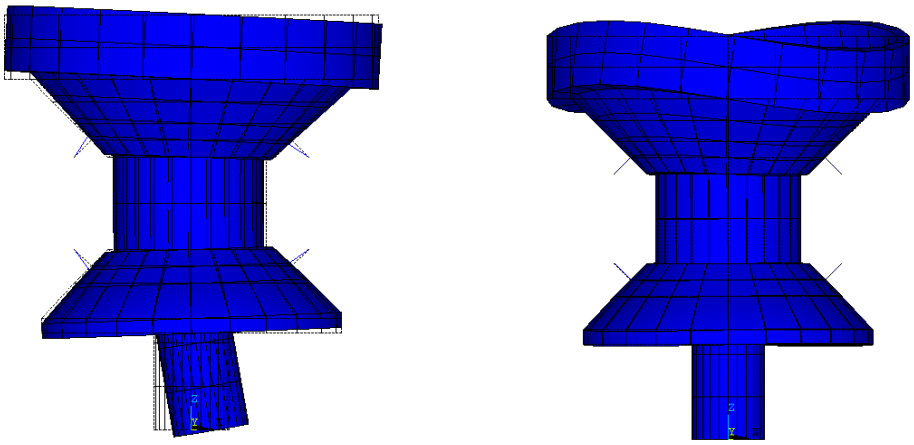

a b

Figure 5.14. *a) The lowest eigenmode (except for rigid body and torsion modes) at a frequency of 4.4 kHz found by finite element analysis. b) An example of an eigenmode at 8.3 kHz.*

5.5.2 Metrology Frame

In Figure 5.15 a sketch of the total system including metrology frame is given. In Section 2.4 the motivations for using a separate metrology frame were discussed. The design of the metrology frame was actually done after the design of the rotor was finished. The designed metrology frame has a mass of 22.2 kg and is supported by three springs of 200 mm, see Figure 5.16 on page 126. Five DoFs of the rotor (the sixth being the rotation of the rotor around the z-axis) are measured with respect to the metrology frame with five metrology sensors. These sensors are mounted on a sensor disk, which can be positioned in six DoF with respect to the metrology frame using micro-screws. This allows fine adjustment of the sensors with respect to the rotor when the rotor is in nominal position with respect to the force frame. The metrology frame has two eigenfrequencies at 0.92 Hz, two at 3.0 Hz and one at 2.0 Hz. The eigenmode corresponding to a rotation around the z-axis (at 1.1 Hz) was removed from the model, since this mode is not observable with the metrology frame sensors.

One of the functions of the metrology frame is to create a reference with a low acceleration level. The acceleration level of the metrology frame caused by floor vibrations will decrease with decreasing suspension frequency and damping. On the other hand, the movement of the frame should be within ± 100 μm (limited range of linearity of the actuators), which limits the lower bound of the suspension frequency and damping.

For this reason three dampers were included in the design; one below each spring, see Figure 5.16. Each damper consists of a nylon cylinder submerged in liquid with high viscosity. To predict the movement of the metrology frame resulting from the ground vibrations, the calculation method as discussed in Section 3.4, was used. It was found that the peak-to-valley movement was minimal with a relative damping of 0.2, see [90]. This was achieved by using pure glycerin in the dampers.

5.5.3 Gravity Compensator

The Gravity Compensator (GC) consists of three identical magnets made of Neodymium-Iron-Boron (NdFeB). The magnets have a toroid shape with a square cross section with an inner diameter of 17 mm, an outer diameter of 27 mm and a thickness of 7 mm. The position of the middle and lower magnet are made adjustable, so that (slight) variations in mass of the rotor and magnet field variations can be compensated for. The stick supporting the middle magnet goes through a hole in the rotor of the motor. The diameter of this hole was estimated to be 10 mm. The diameter of the stick holding the magnet is a compromise between making it stiff to increase the eigenfrequency and making it thin in order to allow easy assembling. A diameter of 9 mm was chosen, which results in an estimated eigenfrequency of the first bending mode of approximately 800 Hz.

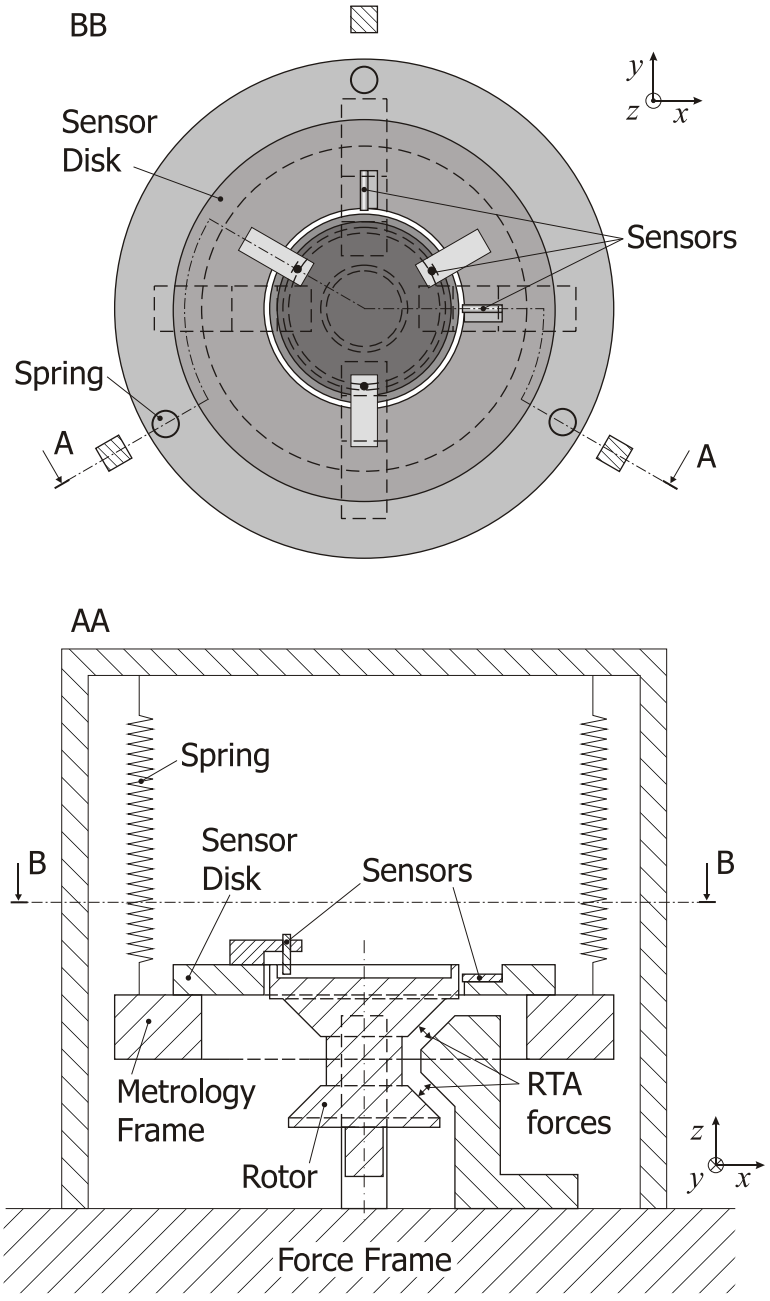

Figure 5.15. *Schematic drawing of the complete mechanical design of the rotating demonstrator.*

5.5.4 Actuators

For the dimensioning of the actuators, a mass of 5 kg was taken for the rotor. In the final design the mass of the rotor is only 2.54 kg, which would allow the actuators to be scaled down with a factor two. Scaling down the actuators would be advantageous, since it would also reduce the disturbances related to the amplifier chain. It was chosen not to do so, as the DEB analysis showed that the force disturbances from the amplifier and the digital-to-analogue converter are not critical. As a result, there is more safety margin for unbalance forces and gravity compensation mismatch.

5.6 Realized Setup

Figure 5.16 shows the realized demonstrator with the metrology frame in upper position. In this section the various difficulties during the fabrication and assembly of the setup are discussed.

5.6.1 Rotor

The target material of the actuators, MnZn ferrite, was delivered by Ferroxcube in the form of a toroid. These ferrite rings proved very difficult to machine. First attempts to machine the rings resulted in cracks in the material. In order to prevent undesired delays in the manufacturing of the setup, it was decided at this time to make two rotors. In the first rotor the ferrite rings are replaced with soft iron rings. The realization of the second rotor was postponed to a later stage to solve the machining of the ferrite rings (and other issues such as virtual grounding of the capacitive sensors, see [72]).

The force frame sensors, which work by means of reflection (see Subsection 5.2.6), showed too much variation in reflectivity when reflecting on aluminium. This proved a major difficulty in making the system operational. To reduce this variation, two strokes on the rotor were painted white. Still, it proved very difficult to verify the exact position of the rotor with respect to the force frame based on the sensor information.

The mass of the rotor was weighted to be 2.69 kg, slightly more than the designed 2.54 kg.

5.6.2 Motor

The project that was started to find a low stiffness (ironless) brushless permanent magnet motor was successful, see [26]. In collaboration with Aerotech[7], an ironless low-stiffness motor has been built, in which the laminated iron is replaced with epoxy resin. The motor has a lower efficiency, with a stall torque[8] of 0.12 Nm vs. 0.42 Nm for the same

[7] www.aerotech.com (last accessed: August 2005).

[8] The maximum torque without over heating the motor.

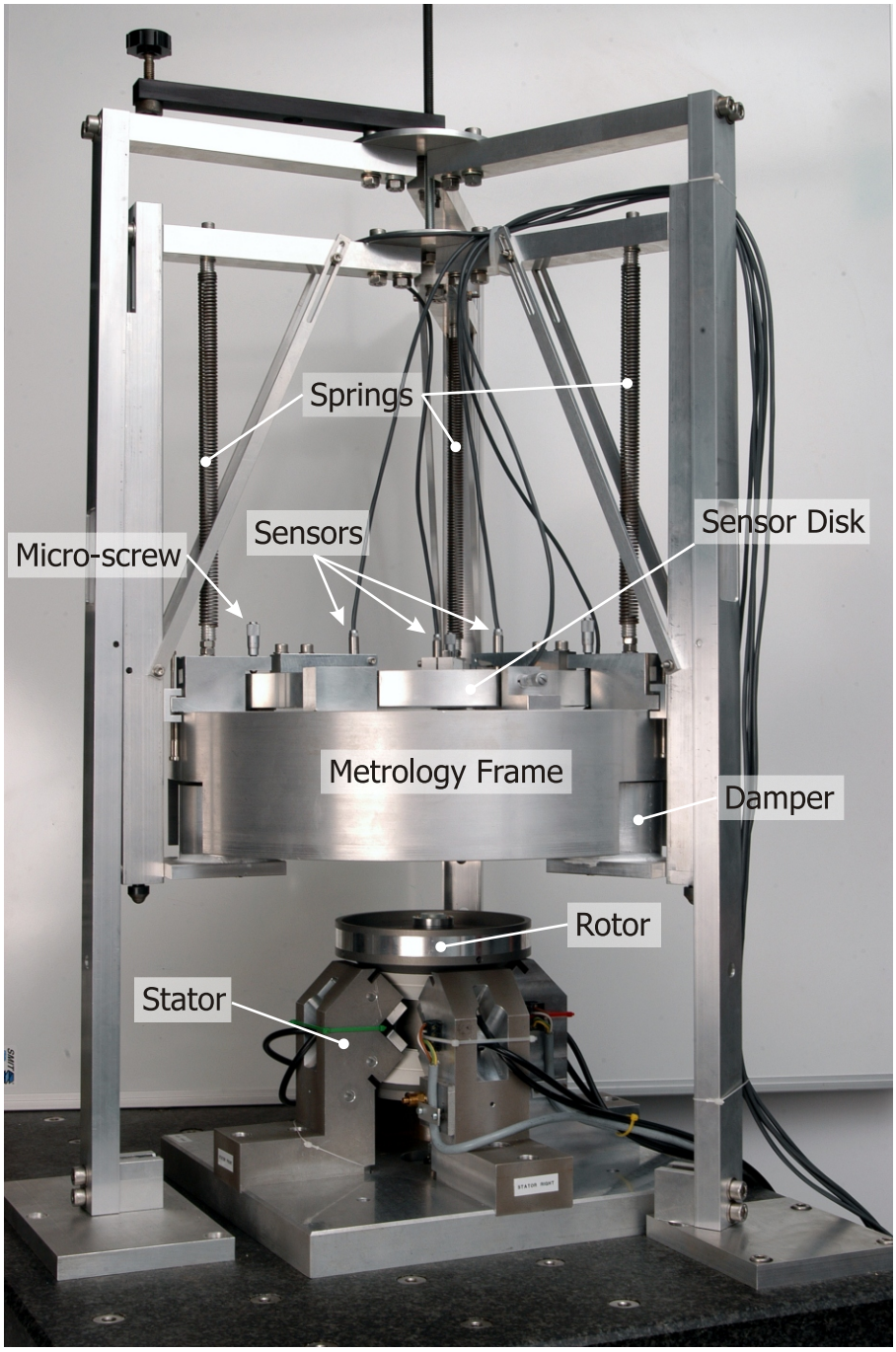

Figure 5.16. *The realized demonstrator with the metrology frame in lifted position so that the rotor is visible. When operational, the metrology frame is lowered such that the indicated sensors are in range with the rotor.*

motor with back iron. The stiffness (resulting from currents in the coils) of the motor was measured to be less than 500 $\mathrm{N/m}$.

Unfortunately, the availability of the motor was too late to incorporate in the design of the rotor and the rotor was made with a dummy mass to represent the mass of the magnets.

5.6.3 Amplifiers

Based on the schematics as were published in [44], special amplifiers were designed and build, see [27]. Since the amplifiers need only to provide positive currents, a relatively simple design is possible. The amplifiers are modified class-A, MOSFET-based, linear power amplifiers, and have been specially designed to have a very high negative current slew rate. The amplifiers achieve a current (small signal) bandwidth higher than 10 kHz.

Note that in Chapter 4 it was discussed that the proposed NLC requires a high bandwidth of the currents amplifiers in order to realize the demanded reference currents. With the bandwidths that are achieved with the amplifiers, it is safe to assume that the current loop will not limit the functioning of the NLC up to several hundreds Hertz.

5.6.4 Analogue to Digital Converter

As was shown in Section 5.4, the ADC from dSPACE® is the biggest disturbance source. Special ADCs were designed and build, which meet the requirement of a SNR better than 96 dB, see [86]. This was achieved by using a principle known as over-sampling. Over-sampling is based on the fact that the quantization and electronic noise of an ADC is the same for each sample. Thus sampling twice as fast does not change the RMS-value of the time record. But because this energy is now distributed over a twice as big frequency range, the resulting PSD is twice as low. By digital low pass filtering, for example averaging, the noise on the signal is effectively reduced and then passed through to a system working at a lower sampling frequency, see [57, 58, 79]. For this purpose the ADC is equipped with a Digital Signal Processor (DSP) which takes eight samples during one time sample of the dSPACE® system, and sends the averaged result to dSPACE®.

In general, the RMS of the noise from the ADC is reduced with a factor $1/\sqrt{N}$, in which N is the number of samples used for over-sampling. With an over-sampling of a factor eight, the noise is reduced with almost a factor three.

5.7 Conclusions

In this chapter the design of the rotating demonstrator is discussed. Starting from the concept design, as discussed in Chapter 2 on page 13, the design was further developed. First the shape and the dimensions of the rotor were determined, after which the actuator size could be estimated. After this, the initial design was modelled, such that the design could be further matured with the Dynamic Error Budgeting (DEB) analysis as discussed in Chapter 3 on page 31.

The most far-reaching design choices was the choice for an iron-less motor and the decision to start the development of an improved analogue to digital converter.

With the final design the asynchronous radial error motion was predicted to less than 0.5 nm (STD), which gives a margin of two compared to the specification.

During fabrication the machining of the ferrite rings proved more difficult than was estimated. It was decided to make two rotors, one with soft iron, which could be manufactured without further delay, and one with the ferrite rings.

6

Experimental Results of the Demonstrator

In this chapter the experimental results obtained with a non-rotating demonstrator are described. The best achieved servo positioning error is less than 0.5 nm *(rms). First the start-up procedure is discussed. Next, the functioning of the non-linear compensation is validated, after which the transfer functions are measured. With the measured transfer functions, the initial controller design is further tuned. At the end the results are discussed.*

6.1 Summary of Performance

The performance measurement of the demonstrator was done with a non-rotating rotor. This because the implementation of the motor was not finished at the time of writing of this thesis. Important to realize is that the Asynchronous Radial Error Motion (AREM) as defined in Section 2.2, principally equals the positioning error at standstill. Theoretically, rotating will only add errors with a synchronous character. Of course, in practise the rotating rotor will probably introduce asynchronous disturbances, due to e.g. air turbulence, but the standstill performance gives a good idea of the best rotating performance attainable with the demonstrator.

In Figure 6.1 the best measured performance at standstill is given. The figure shows the Cumulative Amplitude Spectrum (CAS) of the readouts from the five capacitive sensors. These sensors measure the relative movement of the rotor with respect to the metrology frame (MF). The one-sigma values for the x- and y-direction are 0.58 nm and 0.49 nm, respectively. The one-sigma values for the three sensors in z-direction are 1.13 nm, 1.33 nm and 1.47 nm. The performance was achieved with PID-type controllers acting on a system which is decoupled around the Centre of Gravity (CoG) (see also Section B.6).

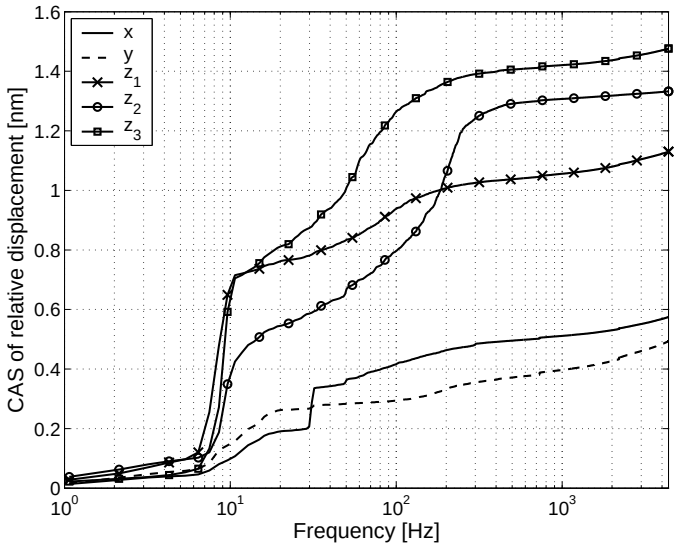

Figure 6.1. *The best result obtained with the demonstrator (non-rotating). Shown is the Cumulative Amplitude Spectra (CAS) of the servo errors as measured with the five capacitive sensors of the metrology frame. The end values of the CAS in* x- *and* y*-direction are 0.58 nm and 0.49 nm, respectively.*

Double integration action was used to suppress the low frequency disturbances from the floor. The controller design used to achieve this performance, is discussed in Section 6.4.

Note that the CAS of the sensor readouts differs from the actual movement of the rotor relative to the MF. The sensor readouts consist of the positioning error and the noise stemming from the sensor and the converter, hence the real performance is always better than what the sensors show. This is also explained in the positioning example in Section 3.5.

6.2 Validation of Eight DoF NLC

6.2.1 Closed Loop Experiment Description

Since the plant is open loop instable, frequency response measurements must be performed in closed loop. The block scheme for the closed loop situation is given in Figure 6.2. If the Reluctance Type Actuators (RTAs) are perfectly linearized by the Non-Linear Compensator (NLC), the combination of the two (indicated by the dashed block) has unity gain. Then the input force vector f_r^r consisting of f_x, f_y, f_z, m_x, m_y around the CoG of the rotor, is the same as the real generated forces on the rotor f^r. Hence, to measure the transfer function of the plant P, the one-to-one relation between f_r^r and f_r must first be established.

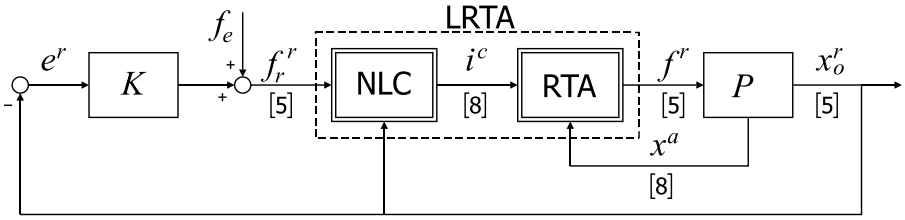

Figure 6.2. *Block scheme indicating how the frequency response was measured. If the NLC achieves perfect compensation of the nonlinear RTAs, the dashed block has unity gain. The numbers in the straight brackets indicate the width of the signal lines.*

Table 6.1. *The measured mean force and apparent stiffness for each direction.*

Direction	Bias force	Stiffness
x	0.23 N	-0.27 N/mm
y	0.60 N	1.17 N/mm
z	2.92 N	0.18 N/mm
r_x	41.2 mNm	5.32 Nm/rad
r_y	38.1 mNm	-3.60 Nm/rad

6.2.2 Measurement of Apparent Static Stiffness

The apparent static stiffness of the Linearized RTA (LRTA) was measured with the method described in Subsection 4.6.1. The rotor was moved in closed loop with respect to the force frame over a range of 50 μm in a certain direction and the reference force f_r to the NLC in the same direction was measured. In Figure 6.3 the measured forces are plotted. On the measured data an affine function (of the form $ax+b$) in each direction was fitted, giving the apparent residual static stiffness of system and the (bias) force at zero position. The results are summarized in Table 6.1.

Comparing the bias force in z-direction and the weight of the rotor (2.7 kg) shows that the gravity compensator has a compensation mismatch of about 11%. In all directions a small hysteresis effect is visible, which is due to the used weak-iron target material on the rotor and the permanent magnets in the gravity compensator. In the z-direction the hysteresis is about 70 mN, which is 0.26% of the nominal force. The off-set force in y-direction is about three times as much as in the x-direction, and the stiffness about four times as much. Still, the stiffness is only 17% higher than the value used in the design.

6.2.3 Measurement of Linearity

To measure the linearity the approach as described in Subsection 4.6.2 is used. As with the experiment of Subsection 4.7.2, the accelerations of the rotor were measured to assess the

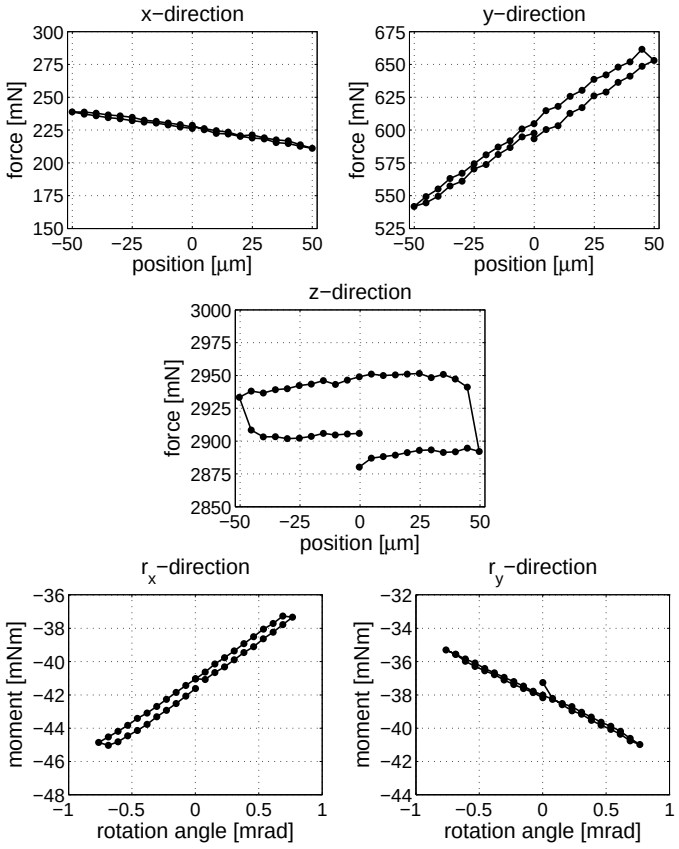

Figure 6.3. *Measurements of the apparent static stiffness in the five directions. In all directions a small hysteresis effect is visible, which is due to the used weak-iron target material in the rotor and the permanent magnets in the gravity compensator. In the z-direction the hysteresis is about 70 mN, which is about 0.3% of the nominal force.*

forces f^r. The generated force, for frequencies above the rigid body resonances, is found by multiplying the accelerations with the mass matrix M_r. This approach is only valid under the assumption that the rotor acts as a rigid body in the frequency range of interest (10–1000 Hz). As was shown by Finite Element Modelling (FEM) in Subsection 5.5.1, the internal resonances of the rotor are not to be expected below 4000 Hz.

Experiment Description

Due to the limited accessibility of the rotor, the accelerometers[1] could only be placed on the top surface of the rotor. By using two accelerometers at the same time (each

[1] These were Bruël & Kjær deltatron type 4508B accelerometers.

measuring in the z-direction), the acceleration in z-direction, as well as one rotation could be measured. So three DoFs can be measured this way: $\ddot{z}^r$, $\ddot{r}_x^r$, $\ddot{r}_y^r$.

The force in the z-direction is calculated via:

$$f_z = m^r \frac{a_1 + a_2}{2}. \tag{6.1}$$

In which a_1 and a_2 are the measured accelerations of the sensors. The moment around the y-axis m_y is found by subtracting the two measurements:

$$m_y = I_{xy}^r \frac{a_2 - a_1}{d_a}. \tag{6.2}$$

In which d_a is the distance between the two accelerometers.

For the excitation signal f_e two type of signals were used; white noise excitation with excitations levels of 0.25, 0.5 and 0.75 N (RMS) and stepped sinusoids with excitations levels of 0.25 and 0.5 N (RMS). For the coherence test, the force f^r and accelerations were measured during five seconds. For the harmonic ratio test, the signals were measured during at least five periods and with a minimum of one second, for fifty logarithmically spaced frequencies over a range of 1 to 1000 Hz.

The controller used is the same controller that is used to start up the system, i.e. a PID controller with a bandwidth of 30 Hz.

Results

Here, only the results in z-direction are shown, the results for the two rotational directions r_x and r_y are given in Section C.2. In Figure 6.4 the result for the test with white noise excitation in z-direction is given. On top the gain of the estimated transfer function (using the MATLAB® function `tfe`) of the Linearized RTA (LRTA) is given. Below, the non-linearity index (one minus the coherence) of the measured accelerations is given.

In the frequency range 10 to 100 Hz the gain is about 10% higher than was expected. Below 10 Hz the estimate of the gain becomes unreliable because the relation between accelerations and force becomes dominated by the residual stiffness in the system. At higher frequencies, above 100 Hz, the gain starts to abate. This is probably due to dynamic effects such as eddy currents. Up to 500 Hz the decrease in gain is still acceptable, considering the robustness of the controller for gain variations less than $\pm$20%.

The result of the test with sinusoidal excitation in z-direction is given in Figure 6.5. The estimation of the LRTA gain shows the same results as for the noise excitation, except for that the gain is about 20% higher than was expected. From the ratio of power above 10 Hz it can be concluded that the distortion level is less than -70 dB. Taking the square root of this value, gives a non-linearity of less than 2%.

6.2.4 Discussion

The apparent static stiffness measurement showed that the Gravity Compensator (GC) does not fully compensate the weight of the rotor. This can be corrected by bringing the

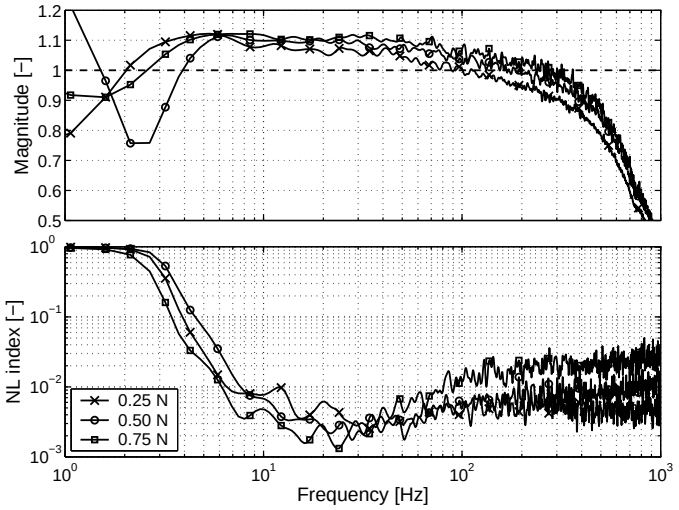

Figure 6.4. *Figure giving the result of the non-linearity test with white noise excitation in the z-direction. The figure on the top give the gain between the input to the NLC and the estimated output of the RTAs. The figure below gives the function one minus the coherence plotted on a logarithmic scale.*

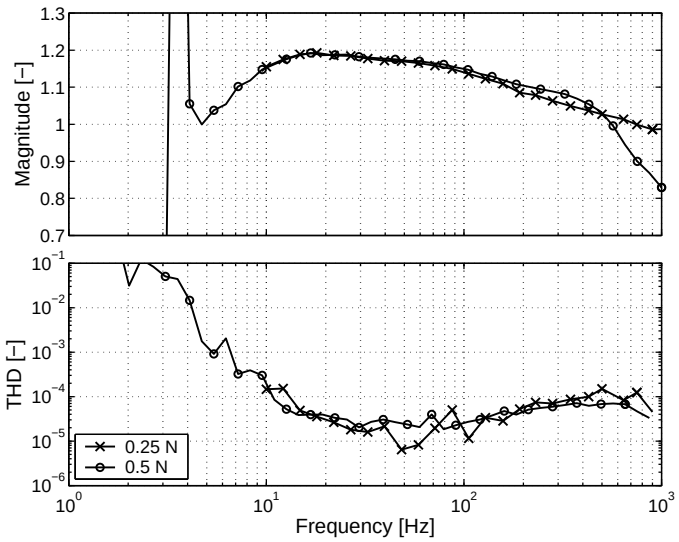

Figure 6.5. *Figure giving the result of the non-linearity test with sinusoid excitation in the z-direction. On the top the gain between the input to the NLC and the estimated output of the RTAs is given. The figure below gives the total harmonic distortion, as defined by (4.27), of the estimation of the generated force.*

two permanent ring magnets of the GC closer to each other (see Figure 5.2 on page 99). However, to do so would require disassembly of the force frame, which was preferred to be delayed until the new rotor with ferrite rings was ready.

In the experiments a gain variation of 10% up to 20%, depending on which method of measuring, was found. In Section 4.7 it was motivated that a gain variation of 30% found in a one DoF setup could be explained by an uncertainty of about 50 μm in the magnetic air gap (with a nominal air gap of 0.66 mm). The uncertainty in the magnetic air gaps in the demonstrator is likely to be in same order of magnitude. This is due to the difference between the magnetic air gap and the mechanical air gap, and the measurement uncertainty of the air gaps with the optical reflection sensors. The measured harmonic non-linearity index at zero position of the one DoF setup (Figure 4.7) is roughly equal to the index of the demonstrator (Figure 6.5) in the frequency range from 20 to 100 Hz.

Concluding from both tests, is that NLC compensates the non-linearity of the RTAs well. Assuming a gain margin of the closed loop system bigger than two, the gain variation up to 500 Hz will not cause stability problems.

6.3 Frequency Response Measurements

6.3.1 Experiment Description

Within dSPACE® the five by five transfer function matrix was measured by the stepped sinus method. A sinusoidal external force f_e with an amplitude of 0.5 N was injected in one direction and the signals f^r and x^r were recorded in all five directions. By fitting a sinusoidal signal on the measured data, the gain and the phase of the signals could be determined. By stepping through the frequency range of interest, the sensitivity and process sensitivity was measured, from which the Frequency Response Data (FRD) of the five by five transfer function of the plant P can be calculated. Repeating the experiment in the other directions, gives the FRD of the full five by five transfer function matrix.

The experiments were performed with the rotor in closed loop with respect to the force frame and to the metrology frame, using a decentralized (multiple SISO) controller achieving a 60 Hz bandwidth.

6.3.2 Measurement Results and Discussion

The Measured Bode Magnitude

For clarity's sake only a three by three subset of the full transfer function matrix is presented here. The phenomena shown by this subset is representative for the behaviour of the full system. The full transfer function matrix measurement is given in Appendix C on page 191.

From the three by three Bode magnitude of the FRD, as shown in Figure 6.6, several observation can be made. First observation is the cross-coupling terms are much higher

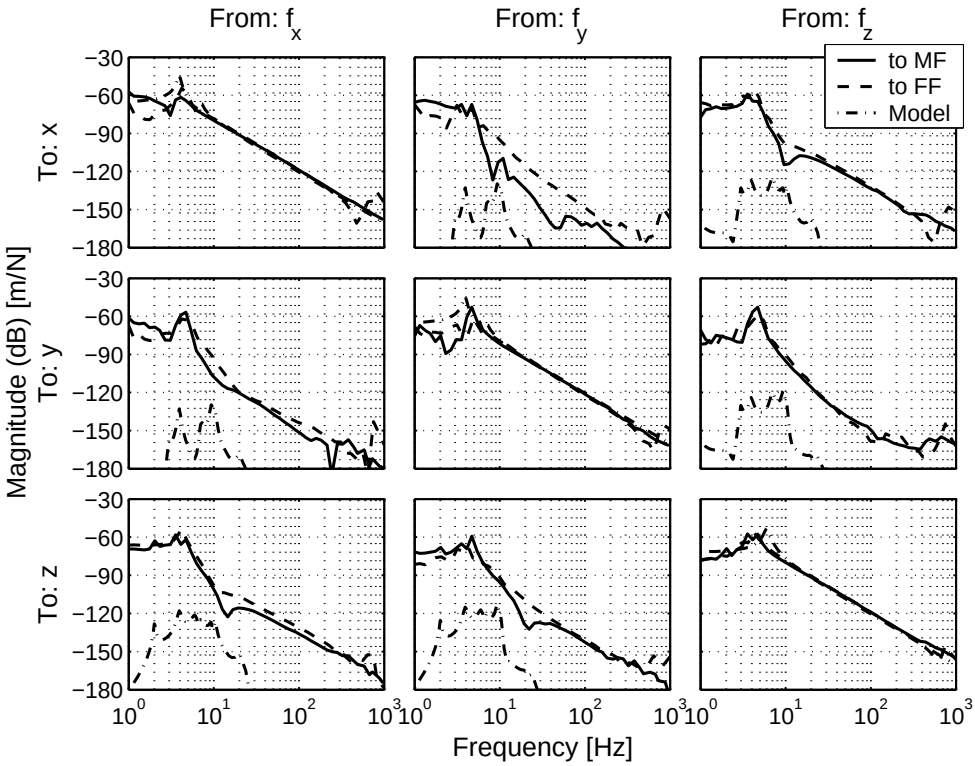

Figure 6.6. *Bode magnitude of the frequency response data from force to metrology frame sensors (solid) and to the force frame sensors (dashed). It can be seen that the cross-couplings are much higher than predicted by the model (dash-dotted). Another observation is that the resonances in the force frame around 800 Hz are not present in the transfer function relative to the metrology frame, which proves that the frame are effectively decoupled for these frequencies.*

than was expected from the model (see Section 5.3).

Another observation is that the rigid body resonances appear around 4 to 5 Hz. Considering the mass of the rotor, this would correspond to a stiffness of around 1.7 up to 2.6 N/mm, which is higher than expected from the static stiffness measurement in Subsection 6.2.2.

The third observation is that the transfer functions relative to the force frame, show a resonance around 820 Hz for the x-direction, and around 750 Hz for the y- and z-direction. These resonances disappear in the transfer functions relative to the metrology frame, confirming the concept design strategy, as discussed in Section 2.4.

Discussion of the Cross-Couplings

From the fact that the couplings in the transfer functions measured with the force frame and metrology frame sensors hardly differ, it can be concluded that the couplings are due to the actuation system.

One possible mechanism which would introduce couplings is a mismatch in position of the actuators between what has been modelled and the real setup. However, assuming a worst case mismatch of 0.5 mm, and comparing this to the minimum distance between the actuators of about 50 mm, would lead to couplings which are negligible to the measured couplings.

Another source of couplings is the uncertainty in the air gaps at the RTAs. Any discrepancy between the measured air gap and the real gap in one of the RTAs would result in disturbance forces in the other directions. In the previous section, it was measured that the gain of the linearized RTAs differs in between 10 to 20% with the intended unity gain. This difference was explained by the uncertainty in the air gaps. Realizing that a force in one direction is generated with four or eight (in the z-direction) RTAs, a 10% (or -20 dB) cross coupling to the outer directions seems very plausible.

The next question is how bad are these couplings? In the ideal case the couplings are zero, and each direction can be controlled independently of the other directions. This is called decentralized control. As a result of couplings the stability of the closed loop system is endangered when decentralized control is used. This is illustrated in Figure 6.7, where decentralized control for a two by two plant is depicted. The couplings introduce additional dynamics of the other loop to each main loop, which can destabilize the total closed loop system.

Another effect of couplings is that disturbances in the loops of other directions are coupled in.

To evaluate the couplings, the Relative Gain Array (RGA) is introduced. The RGA, denoted by Λ, is defined as (from [88]):

$$\Lambda(s) = P(s) \times \left(P(s)^{-1}\right)^{\mathrm{T}}, \tag{6.3}$$

where $\times$ denotes element by element multiplication. The closer the RGA is to the identity matrix, the more decoupled the system is. More properties of RGA are given in [88]. To give an idea of how the couplings are quantified by the RGA, the following example is considered. Given a plant defined as:

$$P(s) = \frac{1}{s^2}\begin{bmatrix} 1 & a \\ b & c \end{bmatrix}, \tag{6.4}$$

then the RGA equals:

$$\Lambda = \frac{1}{1-\frac{ab}{c}}\begin{bmatrix} 1 & -\frac{ab}{c} \\ -\frac{ab}{c} & 1 \end{bmatrix}. \tag{6.5}$$

Indeed, if either a or b becomes zero, the RGA becomes the identity matrix and there is no instability threat. This can also be seen in Figure 6.7 where there is no additional dynamics

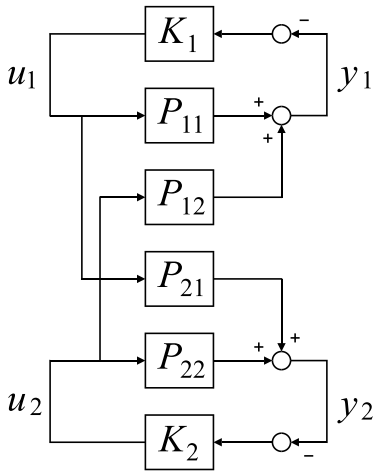

Figure 6.7. *Decentralized control for a two by two plant with couplings. The couplings introduce additional dynamics of the other loop to each main loop. This can destabilize the total closed loop system.*

if either P_{12} or P_{21} is zero. Controlling the plant (6.4) with standard PD-type[2] decentralized controllers, yields an unstable closed loop system when the product ab becomes bigger than c.

Specifying the maximum peaking of the magnitude of the sensitivity function, gives a robustness margin. The maximum sensitivity is the inverse of the minimum distance to the point -1 in the Nyquist curve. For the MIMO case, one should consider the inverse of the distance of the characteristic loci[3] to the point -1 for the maximum peaking of the sensitivity. Setting a or b to zero and using PD controllers with a maximum phase lead of 53°, leads to a maximum peak in the sensitivity of 1.3. If the product ab is less than one tenth of c, the sensitivity has increased to 1.35, which is a reasonable small increase. Hence, if the off-diagonal terms of the RGA are smaller than one tenth of the diagonal terms, no stability problems should be expected. Of course, this guideline gives only a rough idea and loses its validity as the dynamics of a system becomes less and less comparable to that of the example.

Note that the RGA of the plant (6.4) in this example is frequency independent. If this is not the case, the authors of [88] claim that the RGA is especially important around the bandwidth frequencies.

Figure 6.8 shows the three by three Relative Gain Array (RGA) of the measured FRD of the demonstrator (the full RGA is given in Figure C.5 on page 196). From the figure it is seen that the system below 5 Hz is strongly coupled, due to the mechanical couplings present in system. From 20 to 200 Hz the system is reasonably well decoupled

[2]The term PD is explained in the next section.

[3]This is also explained in the next section, for now one can read "Nyquist plot" instead.

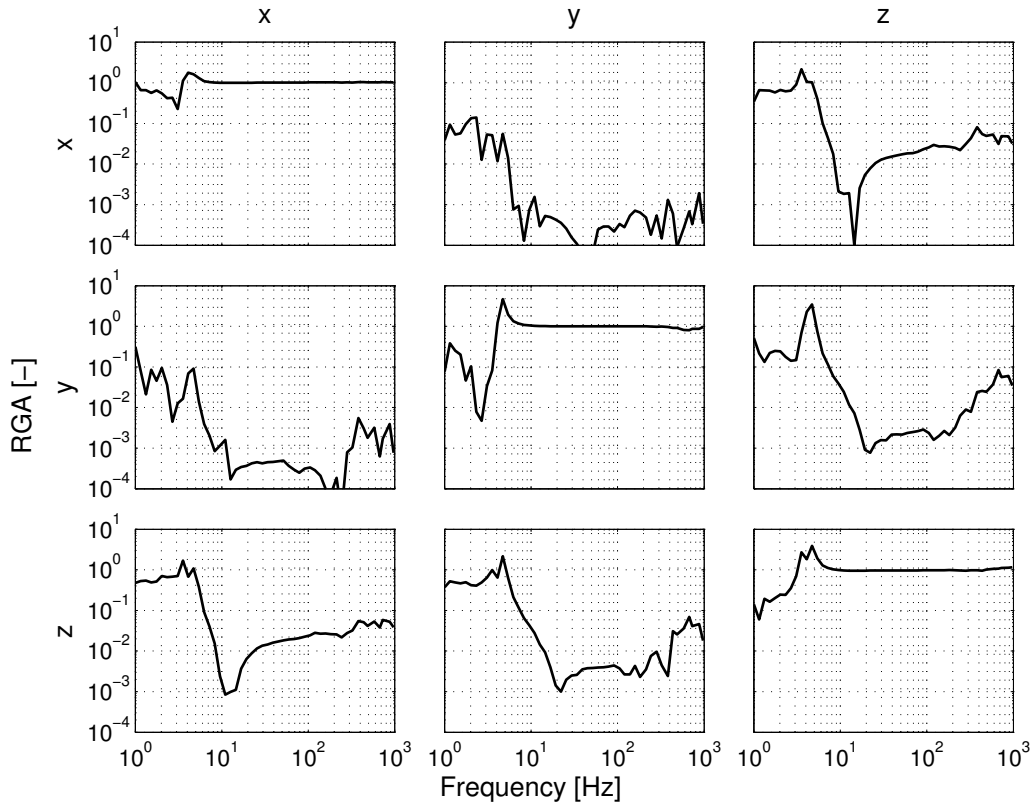

Figure 6.8. *Relative Gain Array (RGA) of the frequency response data. The closer the RGA is to the identity matrix, the more decoupled the system. From 10 to 300* Hz *the system is reasonably well decoupled and becomes slowly more coupled after 300* Hz*. Hence, decentralized control should be possible in this frequency range without too much effect of the couplings on the robustness.*

and becomes slowly more coupled after 300 Hz. Hence, decentralized control with the bandwidth of the controllers between 20 and 200 Hz should be possible without too much effect of the couplings on the robustness.

Discussion of the Phase Lag Due to Eddy Currents

Figure 6.9 shows the phase of the FRD of the transfer function from force to displacement in x-direction measured with the force frame sensors and with the metrology frame sensors. The phase of the transfer function measured with the force frame sensors shows a jump at 500 Hz. This is due to a mechanical resonance in the force frame, see also Figure 6.6. The phase of the transfer functions in the other directions are given in Figure C.7 on page 198.

The phase of the plant for frequencies above the rigid body resonances and below the

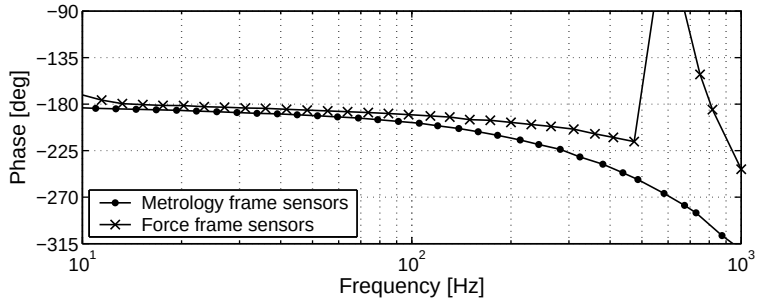

Figure 6.9. *Bode phase of the transfer function from force to metrology frame sensors and to force frame sensors in the* x*-direction. The jump in phase in the transfer function measured with the force frame sensors is due to a mechanical resonance. The phase responses of the two transfer functions are matched when an additional 1.8 time sample delay is added to the force frame sensors. This additional delay is due to the analogue-to-digital converters used for the metrology frame sensors.*

internal rotor resonances should be -180°, stemming from the double integrating action of the inertia. From the figure it is seen that both transfer functions have additional phase loss. First the phase response of the transfer function measured with the force frame sensors is analysed.

By accounting for the phase lag introduced by the various components, the phase lag due to the magnetic bearings can be derived. The phase of the transfer function measured with the force frame sensors reads -197.7° at 200 Hz. The additional phase loss of 17.7° have the following causes:

- The plant is digitally controlled, which gives a time delay due to the sample and hold of the DAC and the computation time. The sample and hold action gives an average delay of half the sample time. At a sample frequency of 8650 Hz this gives 58 μs time delay. The computation (including the conversion times for the ADC and DAC) takes 40 μs. The total time delay of 98 μs accounts for -7.1° at 200 Hz.
- The force frame sensors have a bandwidth of 20 kHz, hence at 200 Hz this gives a phase loss of 0.5° at most.
- The anti-aliasing filters are hourglass-type (see [12]) with a cut-off frequency of 3.8 kHz and have a phase loss of 4.6° at 200 Hz.
- The amplifiers generating the current for the RTAs have a bandwidth higher than 10 kHz, see [27]. This results in an additional phase loss at 200 Hz of less than one degree.
- Eddy currents in the target material of the RTA and magnetic hysteresis have an additional damping effect.

Adding the phase loss contributions, leads to the conclusion that the phase loss due to

eddy currents and hysteresis at 200 Hz is between 5° and 6°. Applying the same analysis to the other directions, gives a variation of phase loss between 4° and 7°, with an average of 5°.

Discussion of the Phase Due to the ADC

From Figure 6.9 it can be seen that the phase lag in the transfer function measured with the metrology frame sensors is significantly more than the phase lag measured with the force metrology sensors. At 200 Hz, the phase difference of the FRD measured with the force frame and metrology frame sensors, is 15.2°. Both sensor channels have the same components which add to the phase loss. These are the sensors themselves, analogue filters and the ADCs. The phase contributions for the force frame channel of these components have been discussed above. Here, the additional phase loss of the components in the metrology frame sensor channels is analysed.

The working principle of the custom made ADC is based on over-sampling to reduce the electronic noise in the converter, see also Subsection 5.6.4. The over-sampling results in an additional delay of half a time sample (58 μs), so the total delay of the discrete system (sampling and calculation) should be 154 μs, accounting for 11.1° phase delay.

The excitation frequency of the capacitive sensors used in the metrology frame is 25 kHz. How the capacitance is measured is kept secret by the manufacturer. So, as a worst case, it is assumed that this gives a time delay of $1/(25{\cdot}10^3)$ s. At 200 Hz, this gives a phase delay of 2.9°. The metrology frame sensors have built-in analogue filters to suppress the frequency component at the excitation frequency. According to the manufacturer, these are a second order butterworth filter at 10 kHz and fifth order butterworth filter at 14 kHz, which give a phase lag of 4.3° at 200 Hz.

The custom designed ADCs used for the metrology frame sensors have analogue anti-aliasing filters (Butterworth-type, 2^{nd} order), with a cut-off frequency at 5 kHz. At 200 Hz they give a phase loss of 3.5°.

Adding the phase losses of the components in metrology frame sensor chain gives 2.9+4.3+3.5+11.1=21.8°. For the same components in the force frame sensor chain the phase loss is 0.5+4.6+7.1=12.2°. Comparing the two chains gives a phase difference of 9.6°, which is 5.6° less than the measured difference of 15.2°. Doing the same analysis to the other directions leads to an averaged additional phase loss of 5.5°. After investigation it was concluded that the synchronization between the custom designed ADC and dSPACE® is the most probable cause for the additional phase delay. Solving this problem, would add 4.1° to the phase margin at the bandwidth frequency in y-direction (150 Hz).

6.4 Controller Design

6.4.1 Controller Design Considerations

For Multi-Input, Multi-Output (MIMO) plants advanced design methods exists, such as $\mathcal{H}_2$- and $\mathcal{H}_\infty$-controller design, see [105, 88, 59]. All these methods have as a starting

point that a model of the plant (and disturbances) is available. Hence, the problem is to identify a MIMO model of the plant. Since the rotor will not remain in the operating range in open loop, identification must be done in closed loop. Furthermore, due to the uncertainty in the sign of the stiffness introduced by the NLC, the plant might be open loop unstable. With direct (closed loop) identification, the algorithm used must be capable of identifying MIMO open loop unstable systems. With indirect (closed loop) identification, two stable MIMO transfer function must be identified. In [30] an overview of closed loop identification techniques is given.

At the start of the research described in this report, an indirect approach based on coprime factorization was applied to the MIMO magnetic bearing of [64], described in [82]. Although the approach led to a good model of the plant, the procedure itself is, all by all, quite time consuming and given the time constraint on this project, could not be applied to the demonstrator.

Without a model of the demonstrator, for the design of the controller the measured frequency response data (FRD) should be used. Fortunately, as shown in the previous section, the effect of the measured cross-couplings on the stability is quite small. This means that decentralized controllers can be designed for each direction independently using the main diagonal of the FRD matrix. The stability can then be judged by closing the loops with the full FRD matrix.

Because of the decentralized control design, it makes sense to use the term bandwidth. The bandwidth in a direction is defined as the lowest frequency where the corresponding main diagonal entry of the loop gain has unit gain.

6.4.2 Performance with PID-Controller

First the performance using controllers of the PID-type, as defined by (5.6) on page 112, was measured. The maximum phase lead of each controller is 60 deg. After a few trials, the best performance was measured with a bandwidth of 150 Hz in each direction. Figure 6.10 gives the CAS of the performance measured with the five capacitive sensors. The end values are 2.2 and 3.1 nm for the x- and y-direction and 9.6, 9.9 and 5.1 nm for the three sensors in z-direction.

6.4.3 Additional Integrator Action

From the CAS of the performance, as given in Figure 6.10, it is clear that the main source of error contribution is due to disturbance below 5 Hz. To increase the disturbance suppression at low frequencies, additional integrating action was added. In Figure 6.11 the two controllers are compared.

This controller finally led to the performance as was shown in Figure 6.1 on page 130. the CAS of the performance of the five capacitive sensors with the additional integrator is given.

The controller used is given by (5.7) on page 112, with the parameters as given in Table 6.2.

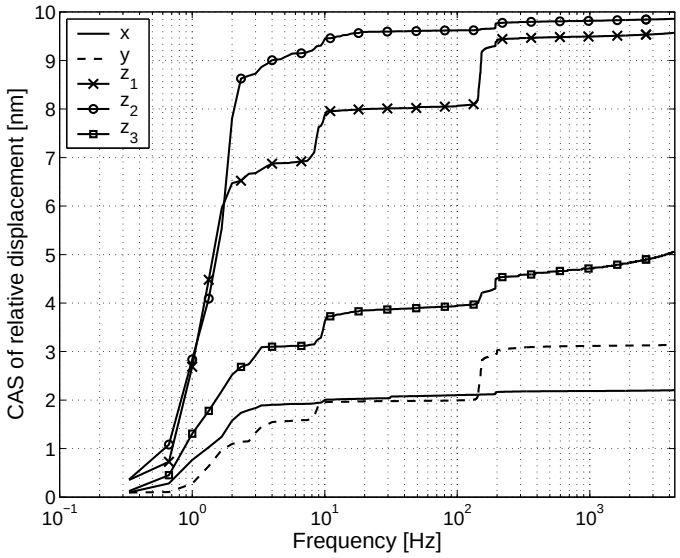

Figure 6.10. *The CAS of the metrology frame sensors, achieved with the PID controller acting on the main diagonal terms with a bandwidth of 150 Hz.*

To judge the stability margins of the designed closed loop system, the generalized Nyquist plot is used, see [59]. The generalized Nyquist plot are the graphs of the eigenvalues of the loop gain $L(s)$, as s goes once round the Nyquist contour. The graphs of the eigenvalues are called *characteristic loci*. As with the Nyquist plot for SISO systems, the stability criterion for MIMO systems becomes:

> If the loop gain $L(s)$ has n_P unstable poles, then the closed-loop system is stable if and only if the characteristic loci of $L(s)$, taken together, have n_P anticlockwise encirclements of the point -1.

An advantage of the generalized Nyquist stability criterion is that it is judged exactly as with SISO systems. A drawback is that the individual loci cannot be traced to a physical

Table 6.2. *Parameters of the controller used to achieve the performance as shown in Figure 6.1.*

Parameter	Value	Direction	Bandwidth
ω_{bw}	$2\pi f_{\text{bw}}$	x	120
ω_i	$\omega_{\text{bw}}/\sqrt{\alpha_d}/\alpha_i$	y	150
ω_{ro}	$\omega_{\text{bw}}\sqrt{\alpha_d}\alpha_{ro}$	z	100
α_d	20	r_x	150
α_i	1	r_y	100
α_{ro}	10		

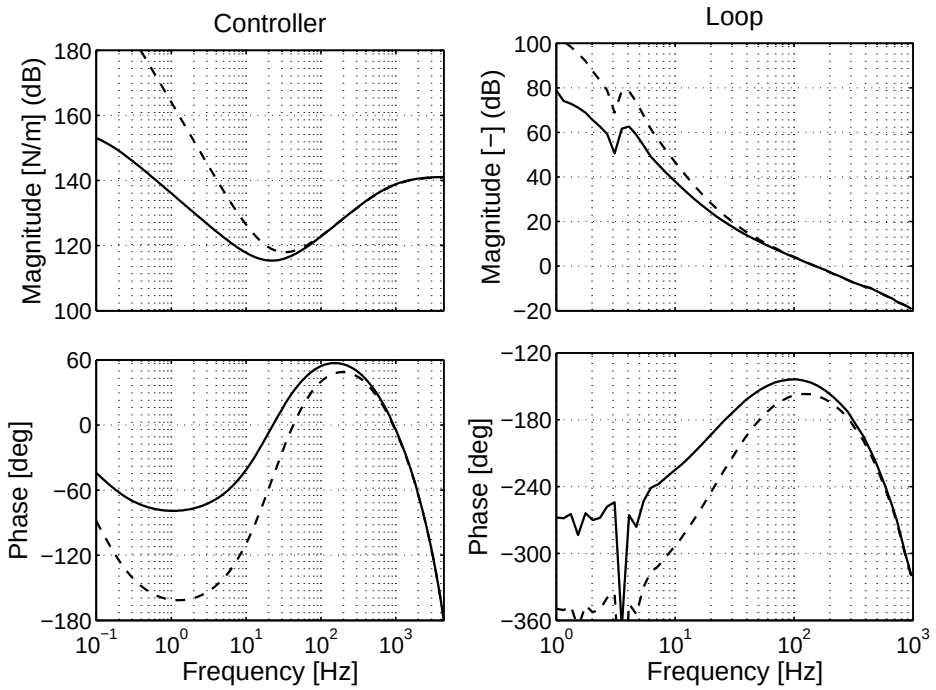

Figure 6.11. *On the left the Bode-diagram of the PID (solid) and PI²D (dashed) controller. On the right, the resulting loop gains in the* x*-direction. The measured performance with this controller is shown in Figure 6.1 on page 130.*

meaning, such as a DoF.

In Figure 6.12 the characteristic loci of the loop gain, with the designed controller and measured FRD is given. It can be seen that the gain margin is approximately 2, and the phase margin of about 30 deg.

6.4.4 Static Decoupling

To improve the performance of the decentralized controller, the off-diagonal terms of the plant can be decreased by using static transformation matrices on the input T_u and on the output T_y, as shown in Figure 6.13.

For example, choosing $T_u = P_o^{-1}$ and $T_y = I$, where P_o is a real approximation of $P(j\omega_o)$, leads to a decoupled plant $P_d = T_y P T_u$, which is approximately diagonal for a certain frequency ω_o. Usually, the bandwidth frequency is a good selection for ω_o because the effect on performance of reducing coupling is normally the greatest at this frequency, as claimed in [88]. A decentralized controller K_d can then be designed for the decoupled plant P_d. Finally, the controller that is implemented, $K = T_u K_d T_y$, is no longer decentralized.

Four techniques for decoupling were compared. Two methods use pre- and post-

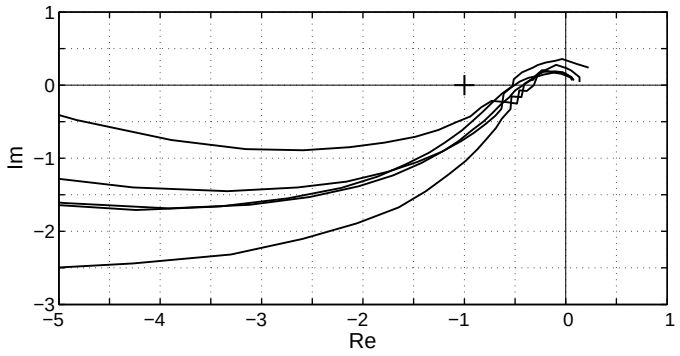

Figure 6.12. *Plot of the characteristic loci of the loop gain using the measured frequency response data.*

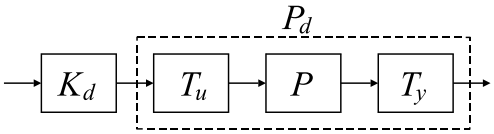

Figure 6.13. *Block scheme illustrating the static decoupling strategy; the plant P is pre-multiplied with T_u and post-multiplied with T_y, such that the compensated plant $P_d = T_y P T_u$ becomes less coupled than the plant P.*

multiplication and two use only pre-compensation. The results are shown in Figure 6.14.

The first method uses the magnitude of the transfer function at the bandwidth frequency as approximation, hence $T_u = P_o^{-1} = \left(|P(j\omega_o)|\right)^{-1}$.

A drawback of using the magnitude for the real plant approximation is that it neglects the phase information. The *align* procedure, as described in [59] does take into account the phase. This procedure also results in a pre-compensator.

The third technique is based on a Singular Value Decomposition (SVD) of a real approximation P_o, see [88]. With the SVD, the approximation P_o can then be written as $P_o = U\Sigma V^{\mathrm{T}}$. The matrices U and V are real, if P_o is real. By setting $T_y = U^{-1}$ and $T_u = \left(V^{\mathrm{T}}\right)^{-1}$, the plant is approximately decoupled at w_o. Here the magnitude of the transfer function at the bandwidth frequency is again used as real approximation of the plant.

The last decoupling method which was tested assumes that the system is dyadic, in which case the plant can be written as:

$$P(j\omega) = U\Sigma(j\omega)V^{\mathrm{T}}, \tag{6.6}$$

in which $\Sigma(j\omega)$ is a diagonal transfer function matrix. Choosing the transformation matrices T_u and T_y as with the SVD method, then decouples the system for all frequencies. This method is described in [99, 15]. The columns of U are the eigenvectors of

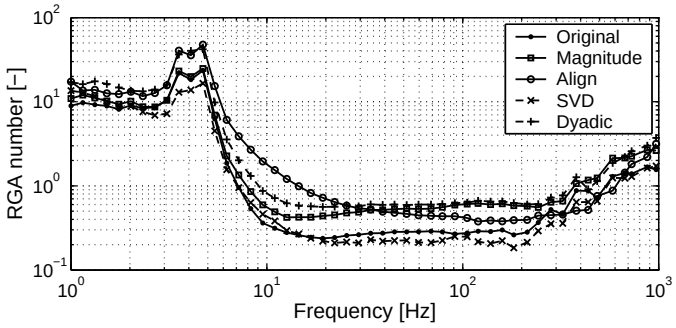

Figure 6.14. *The RGA-number for various decoupling strategies. Except for the SVD method, the methods do not improve the decoupling in the frequency range of interest.*

$P(j\omega_2)P(j\omega_1)^{-1}$ and the rows of V are the eigenvectors of $P(j\omega_1)^{-1}P(j\omega_2)$, in which ω_1 and ω_2 are two frequencies in the frequency range of interest. For the demonstrator two frequencies of the FRD around the target bandwidth were chosen in a trial and error process such that the decoupling performance was optimal. The resulting frequencies were 105 and 213 Hz.

To compare the four decoupling strategies, the RGA-number $\rho(f)$ is used instead of the full RGA. The RGA-number is defined as:

$$\rho(f) = \sum_{i,j} \left| \left\{ \Lambda(f) - I \right\}_{ij} \right|, \tag{6.7}$$

in which $\left\{\Lambda(f) - I\right\}_{ij}$ denotes the element in the i^{th} row and j^{th} column of $(\Lambda(f) - I)$.

In Figure 6.14 the results for the various decoupling strategies are given. Except for the SVD method, the methods do not improve the decoupling in the frequency range of interest. The SVD method gives a slight improvement from 20 up to 200 Hz.

6.4.5 Control at the Sensor Locations

One of the fundamental design concepts, as discussed in Section 2.4, is that for mastering only one DoF is of real importance, namely the direction in which the laser moves. In the realized setup this DoF is directly measured by the capacitive sensors sensing in either the x-direction or the y-direction. From this point of view, decoupling the rotor at the sensor locations for decentralized control design might increase the performance, since the performance measure is directly controlled.

The plant with force inputs and position outputs at the capacitive sensor locations, is given by: $P^c = T_{cr}^{-1} P T_{cr}^a$, in which the transformation matrixes T_{cr} and T_{cr}^a are discussed in Appendix B on page 173. The followed approach did not lead to a performance improvement. When implemented, a bandwidth for the decentralized controllers of 100 Hz could be achieved, which resulted in an standstill performance of 7.9 nm. Attempts to

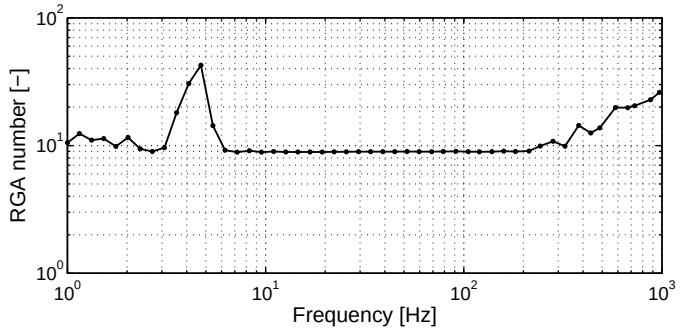

Figure 6.15. *The RGA-number for the plant with inputs and outputs at the capacitive sensor locations.*

increase the bandwidth were unsuccessful due to resulting instability of the setup. This can be explained by looking at the RGA-number given in Figure 6.15. From 7 to 200 Hz the RGA-number is about nine, meaning that the *average* terms of the RGA are approximately 0.4. Closer inspection learns that the RGA has off-diagonal terms which dominate the diagonal terms, indicating bad input/output pairing.

Although the analysis and experiment show that the plant decoupled at the capacitive sensors is difficult to control with a decentralized controller, for mathematical design MIMO methods this framework can be beneficial, since the performance would be directly optimized. These mathematical design methods, such as $\mathcal{H}_\infty$ and $\mathcal{H}_2$ -control design, generally yield full-block controllers, which can compensate the deficient input/output pairing. Indeed, implementing a controller $(T_{cr}^a)^{-1}KT_{cr}$, in which K is the controller of Subsection 6.4.3, yields an almost full block controller with the best performance obtained.

6.5 Conclusions

The demonstrator has been successfully built and made operational, although the motor function has not been incorporated due to time constraints. The performance at standstill as measured with the capacitive sensors is better than 0.6 nm (RMS, up to 1000 Hz)! Since the measurements are corrupted with sensor and ADC noise, it is expected that the real performance is even better. This implies that the system has a budget for non-synchronous disturbances introduced by rotation of about 0.5 nm (RMS), which is a promising result.

The linearity of the Reluctance Type of Actuator (RTA) linearized with the Non-Linear Compensation (NLC) has been shown to function reasonably well up to 400 Hz. Although the measured gain of the linearized RTA has a variation in the range 10–20%, feedback can compensate. The variation in gain can be explained by the uncertainty in the measured air gaps of the RTAs.

The measured Frequency Response Data (FRD) demonstrated that resonances in the

force frame do not appear in the FRD measured with respect to the metrology frame, which demonstrates that the two frames are decoupled for higher frequencies.

The system has more cross-coupling between the Degrees of Freedom (DoF) than was expected from the model. Analysis showed that the cross-couplings have limited effect on the closed loop stability. How much influence they have on the performance was not analysed.

The use of soft iron rings in the RTAs, much phase loss was expected due to the dampening caused by the eddy-currents. The phase of the Bode-diagrams of the FRD measured with the optical sensors showed that this effect resulted in about 5° phase loss at 200 Hz. Although the phase loss is less severe than expected, implementation of ferrite rings in the RTAs is still beneficial, since reduction of phase loss directly adds to the phase margin. An increased phase margin will increase both robustness and performance. Another advantage of having low eddy-current damping is that less motor power is required for rotation.

The phase difference in the Bode-diagrams measured with the two sensors types showed that the capacitive sensor channel has more phase loss than was expected. It was shown that the phase loss is due to an additional time delay of 76 μs in the custom designed Analogue to Digital Converters (ADCs). Improving the ADCs can reduce this additional time delay to zero, which would add 4.1° to the phase margin at the bandwidth frequency in y-direction (150 Hz).

A rigourous control design would require several accurate models; a model which describes the measured dynamics, a model which takes the uncertainties into account, and a model of the disturbances acting on the system. Such rigourous control design is not done here, instead the performances was optimized using the measured FRD and using aspects of the dynamic error budgeting approach. The best performance obtained was achieved with a decentralized controller with PID-type controllers in each direction. The controllers have double integrating action, to suppress the low frequency disturbances in the metrology frame.

Attempts to further increase the performance by using (static) decoupling techniques to decrease the cross-couplings, did not gave significant improvements. Using accurate models to (dynamically) decouple the system could improve the performance further.

7

Conclusions and Recommendations

7.1 Conclusions

The general conclusions resulting from this research are the following:

- A magnetically levitated platform has been realized, with a performance around 0.5 nm (RMS up to 1000 Hz) when not rotating. Because a suitable motor was not yet available during the realization of the system, the performance could not be evaluated with a rotating system. Since the specification for the Asynchronous Radial Error Motion (AREM) is 1 nm (RMS), the system has a budget for non-synchronous disturbances introduced by rotation of about 0.5 nm (RMS), which is a promising result. The fundamental working principles that led to this performance are the separation of a force and metrology frame and minimizing the positional couplings between the rotor and the force frame to reduce the influence of ground vibrations.
- The Reluctance Type Actuators (RTAs) used for suspension of the rotor are non-linear; the generated force is proportional to the current squared and to the inverse of the air gap squared. A method for linearization of these RTAs, in literature known as Non-Linear Compensation (NLC), was applied. With NLC the stiffness (positional coupling) between the rotor and the force frame could be significantly reduced.
- During the design of the system a method, here denoted as Dynamic Error Budgeting (DEB), has been developed and successfully used. With DEB, dynamic spectral models of the disturbances are used to evaluate the final performance, as well as the contribution of each disturbance to the performance measure. Using DEB during the design process greatly helped to identify the performance limiting components and disturbances. The DEB approach can be used to a wide variety of mechatronic systems.

7.1.1 Non-Linear Compensation

The experiments described in Chapter 4 showed that with a relatively simple NLC the stiffness can be reduced with at least a factor five compared to the stiffness resulting from linearization with a bias current of half the maximum current. This reduction was achieved over a travel range twice the minimal air gap. Using more a complex NLC resulted in a stiffness reduction of a factor more than twenty. The reduction quickly increases when limiting the travel range, up to a factor hundred at the nominal position.

From the experiments in chapters four and six it can be concluded that the linearization of the RTAs with NLC works well up to 400–500 Hz. The gain variation in this frequency range of the linearized RTAs was measured in between 10–20%. This gain variation can be explained by the uncertainty in the measured air gaps of the RTAs.

Differences in the force constant up to 35% between the value predicted by analytical modelling and experimentally fitted values were found. Another source of modelling error is the uncertainty in measuring the magnetic air gap. It was shown that this uncertainty could be significantly reduced by fitting this parameter to experimental data.

Non-linear compensation was applied to three different setups of different sizes. With these setups it was found that the non-perfect compensation resulting from modelling uncertainties were easily compensated for with the outer feedback loop. Because of the gain variation in the linearized RTA, resulting from the modelling uncertainties, NLC is less suitable to be used in mechatronic machines which achieve performance through feed-forward.

7.1.2 Related to System Design Aspects

Dynamic Error Budgeting (DEB) is a mechatronic design procedure in which the plant, the controller and disturbances are integrally evaluated. The DEB procedure requires a quantitative description of the disturbances, which is introduced here. This thesis gives practical examples of such models for disturbance sources that often occur in mechatronic systems.

The use of these models is shown in the analysis of a simplified system for positioning. From this example the potential benefit of DEB during the design phase can be understood.

The DEB approach is coupled to the field of $\mathcal{H}_2$-optimal control. The quantitative description of the disturbance proves to be a powerful method to select proper weighting filters of the inputs to the system. Applying $\mathcal{H}_2$-optimal control to the case of the simplified system helped to derive a controller that achieves increased performance with low controller effort.

Using the DEB analysis during the design helped to formulate the specifications of the several subcomponents, such as:

- The target bandwidth of the decentralized closed loops, which is very important for the mechanical design, as mechanical resonances can severely limit the bandwidth.

This value was also used to specify the current loop bandwidth of the custom designed power amplifiers for the RTAs and other components such as sensors and filters.

- The target value of the stiffness of the actuators was derived at 1000 $\mathrm{N/m}$. It was shown that the stiffness of a motor with back-iron is too much for the separated frame concept.
- The analysis pinpointed the most limiting component in the final design to be the Analogue-to-Digital Converter (ADC). An ADC was custom made to be able to fulfill the requirements set by the DEB analysis.

7.1.3 Control Aspects

The best performance was achieved with PID-type controllers decentralized around the CoG in each direction. The controllers achieved bandwidths in between 100 and 150 Hz. The controllers have double integrating action, to suppress the low frequency disturbances in the metrology frame. The controllers were tuned with the measured Frequency Response Data (FRD) and using aspects of the dynamic error budgeting approach.

Besides robustness against the uncertainties due to the NLC, the feedback controller also showed robustness against cross-couplings. Further attempts to decrease these cross-couplings by using static decoupling techniques, did not result in significant improvements. Best results were obtained when the Degrees of Freedom (DoFs) of the sensors and actuators were decoupled around the centre of gravity of the rotor.

7.1.4 Experimental Results

The measured FRD demonstrated that resonances in the force frame do not appear in the FRD measured with respect to the metrology frame, which proves the effectiveness of the separated frame principle.

The system has more cross-coupling between the DoF than was expected from the model. Analysis showed that the cross-couplings have limited effect on the closed loop stability. How much influence they have on the performance was not analysed.

Because the electric resistivity of soft iron, used as target material for the RTAs, is much smaller than of that of ferrite, the eddy-currents resulting from changing magnetic flux is much higher. These eddy currents result in additional phase loss of the plant. From the phase plot of the FRD measured with the optical sensors, it was derived that this effect resulted in about 5° phase loss at 200 Hz. Implementation of ferrite rings in the RTAs would decimate this effect, resulting in an increased phase margin and thus improved robustness and performance.

The phase difference in the Bode-diagrams measured with the metrology and force frame sensors showed that the metrology frame sensors introduce more phase lag than was expected. It was shown that the phase loss is due to time delay of 230 μs in the custom

designed Analogue to Digital Converters (ADC). Improving the ADC would reduce this delay to 154 μs, which would add 4.1° to the phase margin (at 150 Hz).

7.2 Recommendations

7.2.1 The Current System

The first step in the continuation of the project is the implementation of the motor. A suitable motor has been found and can be implemented with the new rotor. As was stated in Chapter 2, rotation of the rotor will introduce mainly synchronous disturbances, which are of less importance since synchronous movements of the rotor does not change the track distance on the master disk. However it is likely that the rotation also induces asynchronous disturbances. One could think of air turbulence around the rotor, or non-linear effects as hysteresis in the magnetic bearings as phenomena that can lead to an asynchronous character of the induced disturbances. Of course, nature may still have more surprises in store.

With the new rotor it is recommended to include the ferrite rings as target material for the RTAs. This will help to improve the phase margin due to the reduced eddy currents, as well as reducing hysteresis effects. Furthermore, dSPACE® recently added a new ADC board to their catalogue, capable of over-sampling. Since this board is easily integrated into the current control hardware, it is expected that this will solve the problems pertaining to the additional time delay.

7.2.2 Dynamic Error Budgeting

To speed up the use of DEB early in the design process, it would be beneficial to have a library available which contains disturbance models of the most used components and most common disturbances. Examples are sensors and associated electronics, amplifiers, ADCs and DACs that are often used in mechatronic machines. Measuring and modelling these components is relatively simple, since it involves single variate signals. Multi-variate disturbances such as floor disturbances and acoustic noise takes more effort to measure and model. This is because these disturbances are correlated in the various directions and these directions should be measured simultaneously in order to calculate their cross-spectra.

In the DEB-framework there are three distinct factors which determine the performance. These are the plant, the controller and the disturbances. Synthesizing optimal controllers, such as $\mathcal{H}_2$-control, in the design helps to eliminate the controller out of the equation. If the performance specifications are not met with an optimal controller, it is certain that a redesign of the system is required.

To use the measured PSDs in an optimal control design, such as $\mathcal{H}_2$-control, the disturbances must be modelled using linear time invariant models with multiple white noise input. To derive such models, spectral factorization is used. It is recommended to in-

vestigate which methods for spectral factorization are currently available and numerically robust.

7.2.3 Non-Linear Compensation

Although this thesis has proved the functionality of compensating the non-linear behaviour of Reluctance Type Actuators (RTAs), some important issues should be considered when applying Non-Linear Compensation (NLC).

Analytical derivation of the behaviour of the RTAs does not result in an accurate model. An important aspect which is not considered in an analytical derivation is the leakage flux, which is position dependent. An improvement might be to use finite element modelling of the RTA, which does take into account the leakage flux. More ideal would be to characterize the RTAs on a separate test setup, measuring the generated force as function of air gap and current. Based on the measured data, a model (of limited complexity) can be fitted. In this case, the RTAs should be calibrated in the setup of the application to compensate for the differences in the current supply chain and position measurement chain between the test setup and the setup of the application. Best results would be obtained if the RTAs can be characterized in the setup of the application itself.

Calibration of the RTAs in a setup is much facilitated if the Degrees of Freedom (DoF), that are controlled by the RTAs, are decoupled from each other. Although this might require more RTAs than the minimum number of RTAs that is necessary, the benefits of being able to do a good calibration and thus achieving a better performing NLC probably outweighs the additional costs.

The experiments described in this thesis showed that NLC was able to linearize the RTAs up to several hundreds Hertz. This frequency range is limited by eddy currents, magnetic hysteresis and the bandwidth of the current amplifier. In the experiments laminated RTAs were used, with a sheet thickness of 0.35 mm. It would be interesting to investigate if the linearization frequency range can be increased by using thinner sheets or better materials.

7.2.4 On the Design Process

The design of a mechatronic setup is optimized if the various disciplines involved closely work together in an as early possible phase of the design. Because of the variety of disciplines, usually many experts of various fields are involved. In case of the demonstrator, the work was distributed over the fields of sensing and rotation, electromagnetic and control. Many of the difficulties encountered in the realization of the setup were due to mechanical aspects, which probably could have been avoided if a good constructor would have been constantly involved during the design process.

7.2.5 On a New Design

At the moment of writing the implementation of the motor is underway. Clearly, the design for a new rotating system should wait until results obtained with the current setup are available. However, already with the experience obtained sofar, the following considerations for a new design of a rotating platform can be made.

Concept Design

To start with, the concept of the system as discussed in Chapter 2 can be maintained, with the possible exception of the gravity compensator. Especially the separation of the force and metrology frame, and the non-linear compensation of the RTAs have shown to be successful. Starting with this concept system the following improvements can be made for the development of a new system.

Actuators

It is strongly advised to have the RTAs work under straight angles and to have such a geometry that each Degrees of Freedom (DoFs) can be individually actuated. The first advantage that this approach brings, is that the calibration of the NLC in combination with the RTAs is much less complicated and of higher quality. Another advantage is that a rotor with straight angles is much easier to manufacture within tight tolerances, especially if hard and brittle materials, such as ferrite, are used. A third advantage is that the required force of the RTAs in lateral directions would decrease, since they do not need to compensate for the gravity compensator if it does not not compensate 100%.

A drawback of having independent actuation of DoFs is that the numbers of RTAs increase. This can be circumvented by realizing that when the rotor is rotating around its principle axis of rotation, the accelerations of the rotor required to follow the metrology frame are small compared to the free fall acceleration. Then gravity can be used to preload the rotor, which allows to reduce the number of RTAs.

It was shown that the soft iron, used as target material for the RTAs, was responsible for an average phase lag of 5° at 200 Hz. Using ferrite as target material would help to achieve higher bandwidths.

Gravity Compensator

The Gravity Compensator (GC) compensates for the bulk of the weight of the rotor, such that the RTAs can be kept small in terms of power consumption. This can also be achieved by including permanent magnets in the RTAs used for the z-direction. Because this direction requires a relative large force, the resulting stiffness of such an RTA is quite big. Since NLC can only compensate a part of this stiffness, more disturbing forces resulting from vibrations of the force frame can be expected to work on the rotor in this direction. On the other hand, this direction is less critical, and since the x- and y-direction are now

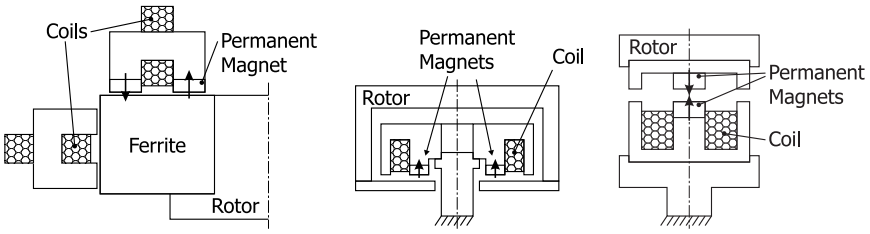

Figure 7.1. *Three options for an actuator in* z*-direction including compensator.*

better decoupled with the RTAs working under straight angles, a high performance in the writing direction might still be achievable.

There are many realizations possible of an actuator in z-direction (in which the gravity acts), which combines gravity compensation. First option, already mentioned in the text, is the gravity compensator by Hol, see [43]. This solution consists of 4 magnet rings and a coil ring with different diameter so that they fit into each other. With a total diameter of 97 mm, a force of 85 N in z-direction is realized. This is too big for the rotor, but since the force is three times too large as well, scaling down should be possible. A drawback in the realization of the GC that is described is that separate magnets are used, which can introduce disturbances when the setup is rotating.

Another possibility is to have an RTA work on a target ring on the rotor. Adding an additional ring to the two rings already on the rotor for the remaining four DoFs, is probably not preferred since it adds to the weight of the rotor. This would make it more difficult to make a stiff rotor, with internal resonances above 1000 Hz. A practical solution could be to have the RTAs for z-direction work on the same lower target ring as the RTAs working in lateral directions. This is sketched in Figure 7.1a. By having the two (or four) RTAs acting in z-direction rotated over 45°, as seen from above, in comparison with the four (or three) RTAs working in lateral directions, the coupling between the RTAs can be minimized.

In Figures 7.1b and c two other options of a combined gravity compensator and actuator are given. These are options which work on the rotation axis of the rotor, thus consisting of a single RTA. The pulling option (b) has the disadvantage of difficult assembly, hence option (c) is preferred.

For the design of the GC the use of finite element methods to predict the stiffness in the various directions is compulsory.

Since the RTA in z-direction has a relative big constant force ($\approx$ 300 N), the placing of this actuator should be close to the centre of gravity, in order to prevent disturbing moments when not perfectly aligned.

Motor

Because the separation of force and metrology frame is maintained, a low stiffness motor is required. The ironless motor that was specially constructed by Aerotech, fulfills this specification. However, the currently made available motor has a very small centre hole (9.5 mm, which is not convenient since the pole supporting the z-direction RTA goes through it.

From the same series as the currently made available motor (S-series) other motors are available which have much bigger centre holes. For instance, the S-130 has an outside diameter of 130 mm and a centre hole with a diameter of 50 mm. If the outer diameter of the GC is smaller than the centre hole of the motor, the rotor can be machined as one piece which greatly improves the alignment of the PAI with the geometrical axis. A drawback is that the rotation frequency for these motors are limited to 66 Hz. It should be investigated if this rotation speed limitation is due to the electronics or the mechanics. If the rotation speed cannot be increased for these type of motors, a motor with a smaller centre hole must be used, but this results in a rotor which is made of two parts.

Sensor Selection

The metrology frame sensors in the current prototype are capacitive sensors. These sensors have two disadvantages. The first disadvantage is that they need grounding. The sensors currently used proved to be quite sensitive to 50 Hz pick up when not perfectly grounded. At standstill this is easily done with a wire, but when rotating only virtual grounding can be employed. Virtual grounding is done by a creating a big capacitance between the rotor and the ground. This requires a large surface available on the rotor, which limits the design of the rotor. Another disadvantage is the limited Signal to Noise Ratio (SNR) of these sensors. Due to the out-of-roundness of rotor and because the rotor rotates around its PAI, a certain minimum stroke of the sensor is required. This limits the sensing resolution because of the limited SNR.

Both disadvantages disappear when interferometry is used as sensing principle. Interferometry has unlimited SNR and resolutions up to 40 pm available, resulting in that quantization noise is no longer relevant. Another advantage is that no ADC is required, avoiding the associated electronic noise.

To use interferometry, reflective surface areas around the glass master and on the side of the rotor should be made. Interference on the sides of the rotor can be obtained by using a cylinder shaped lens, with its focus at the rotor centre, such that the wave-front of the light returning from the rotor can interfere with the wave-front returning from the reference path.

A disadvantage of using an interferometry system is that it is relatively expensive. The cost can be reduced by using interferometry only in the x- and y-direction. Since DEB analysis showed that the performance is much less sensitive to the resolution (see Subsection 5.4.4), less expensive sensors (such as eddy current sensors) can be used for the three sensors in z-direction.

Besides the metrology frame sensors, sensors measuring the displacement of the rotor

with respect to the force frame are required for the functioning of NLC. The force frame sensors in the current setup, which measure distance by the amount of reflected light (see Subsection 5.2.6), gave difficulties with the current rotor because of variations in the optical reflectivity of the rotor. This variation, in combination with the redundant sensor information (eight sensors are used to measure five DoFs), makes calibration difficult. It was also shown by simulation that the noise of the force frame sensors resulted in a force disturbance source to the rotor, which can easily be dominant when bias forces are used in the NLC. Especially when rotating, small variations in reflectivity will translate into relatively big disturbing forces.

With the new proposed shape of the rotor, only five sensors should be used to measure each DoFs independently. With a SNR of 82 dB up to 100 Hz the noisy influence of the FF sensors is four times less. This specification is met with eddy current sensors. This sensing principle was first not selected because of the risk of cross-coupling with the actuators. However, eddy current sensors work at much higher frequencies (up to 80 kHz), so that sensors and actuators are decoupled in the frequency domain.

Metrology Frame

A redesign of the metrology frame is not worked out further here. An important aspect that should be considered in a redesign is the accessability of the OD-master on top of the rotor. One could design the metrology frame in such a way that it can be quickly removed after the mastering process and quickly be replaced. However, given the weight of the metrology frame, it is probably more simple to design the system with a free top.

A New Design

Figure 7.2 summarizes the above recommendations in a new design. Of course, this preliminary design should be further optimized with a team of experts in the fields involved.

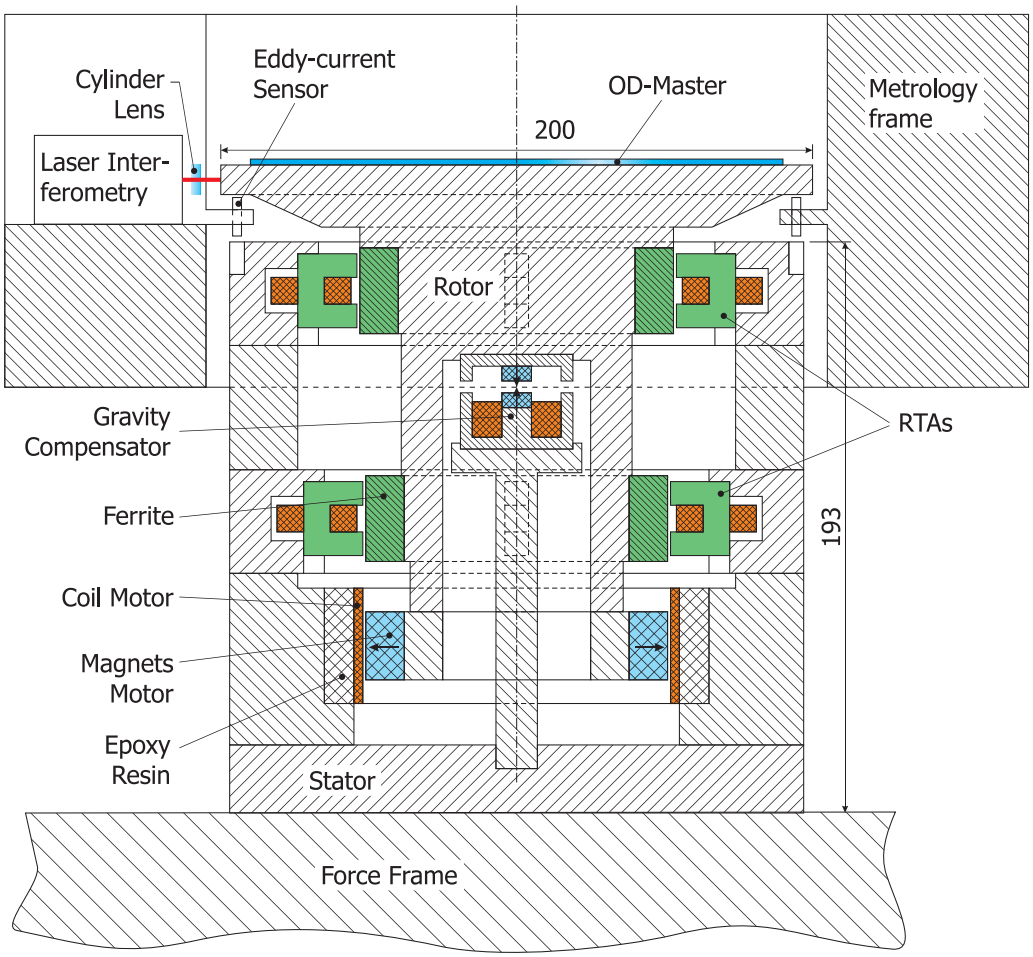

Figure 7.2. *A new conceptual design for the rotor system.*

A

Derivation of Reluctance Type Actuator

A.1 Modelling of a Reluctance Type Actuator

A.1.1 Magnetic Theory

This section gives a somewhat mathematical summary of the derivation to come to a model for a Reluctance Type Actuator (RTA). In [28], Feynman gives a more detailed and very well written introduction to the magnetic theory.

Gauss' Law, one of Maxwell's famous four equations, states that the divergence of the magnetic flux density B [T] is zero:

$$\nabla \cdot \vec{B} = 0. \tag{A.1}$$

In integral form, it reads:

$$\iint_S \vec{B} \cdot \mathrm{d}\vec{a} = 0 \tag{A.2}$$

where $\mathrm{d}\vec{a}$ is the area of a differential square on the closed surface S with an outward facing surface normal defining its direction. In other words; an arbitrary volume (space or material) cannot generate flux. This is the connection to the analogy with electricity; for steady currents the divergence is also zero. Thus magnetic flux could be thought of as thin closed "wires" transporting the flux. These wires are called *flux lines*[1]. Where the flux density is high, the flux line density is high and vise versa.

[1]The representation of a magnetic flux field with flux lines should be used with caution. A fundamental property of magnetism is that the resulting flux fields of two sources, can be simply found by adding the two vector fields. In a representation with flux lines this summation is less trivial.

Continuing with the current analogy, what is then the battery that drives the flux? This is explained by another one of Maxwell's equations. For slowly varying electric fields[2], it equals Ampere's Law for magnetism and reads:

$$\nabla \times \vec{B} = \mu_0 \vec{\rho}_i, \tag{A.3}$$

where μ_0 is the permeability of vacuum ($\mu_0 = 4\pi \cdot 10^{-6}$ N/A^2) and $\vec{\rho}_i$ the current density [A/m^2]. When materials are involved, the current density in (A.3) consists of a free current density ρ_f and a current density due to magnetization of the material ρ_m[3]. Since the divergence of a rotation is always zero ($\nabla \cdot \nabla \times \vec{B} = 0$) the divergence of the current density must also be zero. Hence, the magnetization current can be written as: $\rho_m = \nabla \times \vec{M}$, where $\vec{M}$ is called the *magnetization*[4]. Now (A.3) is rewritten as follows:

$$\nabla \times \left(\frac{\vec{B}}{\mu_0} - \vec{M} \right) = \nabla \times \vec{H} = \vec{\rho}_f. \tag{A.4}$$

Here a new (auxiliary) quantity $\vec{H}$ is introduced, which is denoted the magnetic field (intensity)[5] [A/m][6].

If the material is isotropic the magnetization will be in the same direction as the external applied magnetic field density:

$$\vec{M} = \chi(x, y, z, H)\vec{H}, \tag{A.5}$$

with χ the magnetic susceptibility, which is a scalar. If the material is linear ($\frac{\partial \chi}{\partial H} = 0$) as well as homogeneous ($\frac{\partial \chi}{\partial (x,y,z)} = 0$) then the magnetic flux density can be written as:

$$\vec{B} = \mu_0(1 + \chi)\vec{H} = \mu_0 \mu_r \vec{H}, \tag{A.6}$$

where the quantity $1 + \chi$ is called the relative permeability of a material, denoted by μ_r.

---

[2] An electric field varies slowly if $\frac{\partial \vec{E}}{\partial t} \ll \rho_i / \varepsilon_0$. This is the case for frequency below 1 MHz, see [75, p.447].

[3] And a third component due to polarization of dielectric material, which is outside the scope of this derivation.

[4] Magnetization is the effect that magnetic domains of the material tends to align with an external applied field H. A magnetic domain is a region where the material in which the magnetic fields, generated by the electrons circling the atoms, exhibit coherence, producing a net magnetic field, see [75, 28].

[5] The concept magnetic field (in analogue with electric field strength) is useful in calculating with magnetism, however one should bear in mind that the magnetic flux density is the fundamental physical field.

[6] In many books dealing with magnetism, the centimeter-gram-second (cgs) unit convention is used, in which permeability of free space equals unity. The magnetic field using cgs units is defined as $\vec{H} = \vec{B} - 4\pi\vec{M}$, and its unit is Gauss!

From (A.6) it follows that for materials with $\mu_r > 1$ (called paramagnetic) the magnetization intensifies the flux resulting from an external magnetic field. In some paramagnetic materials the magnetic fields generated by the magnetic domains are very high. These materials are called ferromagnetic, after the most well known material showing this effect: iron. Pure iron has a relative permeability of $2{\cdot}10^5$, while that of 99.8% pure iron typically is around 6000, from [75].

Integrating both sides of (A.4) over an open surface A, gives:

$$\iint_A \nabla \times \vec{H} \cdot \mathrm{d}\vec{a} = \iint_A \vec{\rho}_f \cdot \mathrm{d}\vec{a}, \tag{A.7}$$

The left side of (A.7) can be transformed to a line integral over de boundary of A (∂A) using Green's theorem:

$$\iint_A \nabla \times \vec{H} \cdot \mathrm{d}\vec{a} = \oint_{\partial A} \vec{H} \cdot \mathrm{d}\vec{l}, \tag{A.8}$$

where $\mathrm{d}\vec{l}$ is an infinite small vector along the boundary ∂A. In engineering practise the current is usually confined to a wire, hence the right hand side of (A.7) reduces to i, the current in the wire, or $n_c i$ if the line integral contains n_c windings of the wire. The quantity $n_c i$ is sometimes referred to as magnetomotive force. Now (A.7) can be written as:

$$\oint_{\partial A} \vec{H} \cdot \mathrm{d}\vec{l} = n_c i. \tag{A.9}$$

In words, (A.9) states that the closed integral of the magnetic field equals the current flowing through the area it encloses.

To actually calculate the field intensity H along the line l, its divergence need to be known:

$$\begin{aligned} \nabla \cdot \vec{H} &= \mu_0 \nabla \cdot \left(\mu_r \vec{B}\right) \\ &= \mu_0 \mu_r \nabla \cdot \vec{B} + \mu_0 \vec{B} \cdot \nabla \mu_r \\ &= \mu_0 \vec{B} \cdot \nabla \mu_r \end{aligned} \tag{A.10}$$

where $\nabla \mu_r$ is the gradient of μ_r. In other words, the field intensity changes when going from one medium to another (with different relative permeability).

A.1.2 Lumped Model of a Magnetic Circuit

In this subsection a magnetic circuit with a current carrying coil is considered. In the analysis of magnetic circuits it is useful to think of flux instead of flux density:

$$\Phi = \iint_A \vec{B} \cdot \mathrm{d}\vec{a}. \tag{A.11}$$

By using ferromagnetic materials in a magnetic circuit the generated flux has a clear preference for (a) certain path(s). A magnetic flux path is defined as a tube with encloses

the coil, each cross-section containing the same amount of magnetic flux[7]. By breaking up each flux path in patches, (A.9) simplifies to:

$$n_c i = \sum^{n_p} H_k l_k, \tag{A.12}$$

where n_p is the number of patches, H_k the magnetic field intensity in and l_k the length of the k^{th} patch. Using (A.6) and (A.11), (A.12) can be written as:

$$\begin{aligned} n_c i &= \sum^{n_p} \frac{B_p l_p}{\mu_0 \mu_k} \\ &= \Phi_t \sum^{n_p} \frac{l_p}{A_p \mu_0 \mu_p} \\ &= \Phi_t \sum^{n_p} \mathcal{R}_p = \Phi_t \mathcal{R}_t, \end{aligned} \tag{A.13}$$

where Φ_t is the flux in each flux path, $\mathcal{R}_k$ the magnetic resistance $[\mathrm{A/T/m^2}]$ of each patch and $\mathcal{R}_t$ the magnetic resistance of the flux path. Hence, the magnetic resistance of a flux path is calculated the same as the electric resistance of a series of resistors.

The total flux generated by the coil is the sum of the flux in all the flux paths:

$$\begin{aligned} \Phi &= \sum^{n_t} \Phi_t \\ &= n_c i \sum^{n_t} \frac{1}{\mathcal{R}_t} \\ &= \frac{n_c i}{\mathcal{R}}, \end{aligned} \tag{A.14}$$

in which n_t is the number of flux paths. In other words the total magnetic resistance is calculated the same as having resistors in parallel.

The advantage of using equations like (A.14), is that there are no more vector products involved in the analysis.

A.1.3 Force in a Magnetic Circuit

To calculate the forces on a ferromagnetic body there are two approaches. One is to use the Maxwell's stress tensor, where the body forces are calculated by a Lorentz type interaction between the applied magnetic field and the domain currents due to the magnetization (see [50, 28, 61]).

Another approach is to consider the change in magnetic and mechanical energy in the system, which is more intuitive. The magnetic energy density is per definition equal to: $\int_0^B H \mathrm{d}B$. Thus the total magnetic energy in the lumped model is given by:

$$E_m = \sum^{n_p} A_k l_k \int_0^B H_k \mathrm{d}B_k. \tag{A.15}$$

[7] A magnetic path is the same as a so-called magnetic flux line, with the difference that the cross-area of the "line" is much smaller than that of the circuit considered.

Using the equations of (A.13), it is easy to verify that (A.15) can also be written as:

$$E_m = \int_0^{\lambda} i \, \mathrm{d}\lambda, \tag{A.16}$$

where λ is the flux linkage of the coil:

$$\lambda = n_c \Phi = \frac{n_c^2}{\mathcal{R}} i = L i, \tag{A.17}$$

with L the inductance of the coil [H].

If an external force is applied and the geometry of a magnetic circuit changes, this change must overcome the internal forces holding the system, which changes the internal energy. Under the assumption that the magnetic circuit is conservative, i.e. eddy current losses, magnetic hysteresis cycles or mechanical friction are neglected, the change of energy can be expressed as:

$$W_f(\lambda_0, x_0, \lambda, x) = \int_{(\lambda_0, x_0)}^{(\lambda, x)} \left(\sum^{n_c} i_k \mathrm{d}\tilde{\lambda}_k - \sum^{n_g} f_k \mathrm{d}\tilde{x}_k \right), \tag{A.18}$$

where n_c is the number of coils, n_g the number of generalized coordinates, x_k the k^{th} DoF of the system and f_k the generalized force **done by the system** along x_k. Because it is assumed that the circuit has no losses, W_f is a *state function*, which means that the change of energy W_f is independent on the path taken and completely described by the begin and end states. The force can then be found by:

$$f_k = -\frac{\partial W_f(\lambda, x)}{\partial x_k}. \tag{A.19}$$

However, to derive the force this way, first the change of energy W_f must be found which requires that force is known! This contradiction can be solved if a convenient path is chosen going from (λ_0, x_0) to (λ, x), which is allowed since W_f is a state function. First of all, it can be assumed that the initial state has zero flux, since the change in energy going from $(0, x_0)$ to (λ_0, x_0) does not contribute to (A.19). Then, as first part of the path, the geometry is changed going from $(0, x_0)$ to $(0, x)$, in which no work is done. In the second part the geometry is fixed, so that W_f can be found solving:

$$W_f(0, x_0, \lambda, x) = W_f(0, x, \lambda, x) = \int_{(0,x)}^{(\lambda, x)} \left(\sum^{n_c} i_k \mathrm{d}\tilde{\lambda}_k \right). \tag{A.20}$$

Thus to find the change in energy W_f, only the current i as function of position x and flux linkage λ is needed, which has been derived for the lumped model. Stacking the n_c fluxes into a vector and assuming zero flux leakage, (A.20) can be written in compact notation:

$$W_f(\lambda, x) = \tfrac{1}{2} \lambda^{\mathrm{T}} L(x)^{-1} \lambda. \tag{A.21}$$

Note that (A.21) denotes the magnetic energy in the system as defined by (A.16). The quantity $W_f(\lambda, x)$ is the *Hamiltonian* of the system.

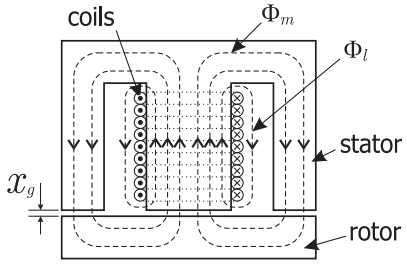

Figure A.1. *An example of a magnetic circuit consisting of an E-core with coil (an electromagnet) and a rotor (an I-core). The current through the coil generates the flux, indicated by the the flux lines. Stray flux do not follow the magnetic circuit completely and take a short cut through air. The magnetic energy stored in the air-gap results in an attracting force.*

Co-energy

Since the flux linkage is also dependent on the geometry of the magnetic circuit, the calculation of the force through (A.19) is a bit extensive. This can be simplified if the *Legendre transformation* of the energy is used:

$$W_c(i,x) = \lambda^{\mathrm{T}} i - W_f(\lambda,x), \tag{A.22}$$

where W_c is called *co-energy* [J]. The co-energy is the Langrangian of the Hamiltonian. It follows that:

$$\frac{\partial W_c}{\partial x_k} = -\frac{\partial W_f}{\partial x_k} = f_k. \tag{A.23}$$

Combining (A.21) and (A.22), gives:

$$W_c(i,x) = \tfrac{1}{2} i^{\mathrm{T}} L(x) i. \tag{A.24}$$

Since it is assumed that the system is linear, the co-energy equals the energy.

A.1.4 Force of a Reluctance Type Actuator

Consider the magnetic circuit as given in Figure A.1. It is a commonly used Reluctance Type Actuator (RTA), consisting of an E-core with coil (the Electromagnet (EM)) and an I-shaped target, the rotor. The core and target are made of a material with a high relative permeability, such as iron.

Neglecting the leakage flux in the RTA, the reluctance becomes:

$$\mathcal{R}_m = \frac{l_i}{\mu_0 \mu_i A_i} + \frac{2x_g}{\mu_0 \mu_a A_a}, \tag{A.25}$$

where μ_i and μ_a represent the relative permeability, A_i and A_a the cross section of the magnetizing flux path of iron and air, respectively and l_i the length of the flux path through

iron. Assuming that the cross section areas of iron and air are the same (namely that of the centre leg), the co-energy in the circuit becomes

$$W_c(i,x_g) = \frac{\mu_0 A n_c^2 i^2}{2\left(\frac{\mu_i}{l_i} + \frac{\mu_a}{2x_g}\right)}. \tag{A.26}$$

Finally, the force of the RTA can be calculated:

$$f_{\text{rta}} = \frac{\partial W_c}{\partial x_g} = -\frac{\mu_0 A n_c^2 i^2}{\mu_a\left(\frac{2x_g}{\mu_a} + \frac{l_i}{\mu_i}\right)^2} = \frac{n_c^2 i^2}{\mu_0 \mu_a A \mathcal{R}_m^2}. \tag{A.27}$$

Notice the sign; the force always acts to decrease the air gap. From here on it is assumed known that the force is always attracting, and the sign omitted. is Now assuming that $\frac{l_i}{\mu_i} \ll \frac{2x_g}{\mu_a}$, (A.27) can be further reduced to:

$$f_{\text{rta}} \approx \tfrac{1}{4}\mu_0 \mu_a n_c^2 A \frac{i^2}{x_g^2} = k_{\text{rta}} \frac{i^2}{x_g^2}. \tag{A.28}$$

Equation (A.28) is mostly used in magnetic bearing literature when considering the controller design. However, in arriving to it, many assumptions and simplifications were made. For this reason FEM is usually used to refine a design based on the analytical formulas.

In the design phase of RTAs, it can be useful to write f_{rta} as a function of flux density. Using (A.14) the magnetic flux density can be written as:

$$B = \frac{n_c i}{\mathcal{R}_m A}, \tag{A.29}$$

where $\mathcal{R}_m$ is given by (A.25). Combining the above equation with (A.27) results in:

$$f_{\text{rta}} = \frac{B^2 A}{\mu_0 \mu_a}, \tag{A.30}$$

gives the same result as (A.28). Assuming that a flux density of 1 T can be realized, than the force tension is:

$$\frac{f_{\text{rta}}}{A} = \frac{B^2}{\mu_0 \mu_a} \approx 8 \cdot 10^5 \text{ N/m}^2. \tag{A.31}$$

With careful design of the magnetic circuit and material selection, flux densities of 1.4 T can be realized, which gives a force tension twice as big.

A.1.5 Discrepancies with the Assumptions

In the derivation of the force in an RTA, two assumptions were made that requires a lot of attention in reality to be approximately true.

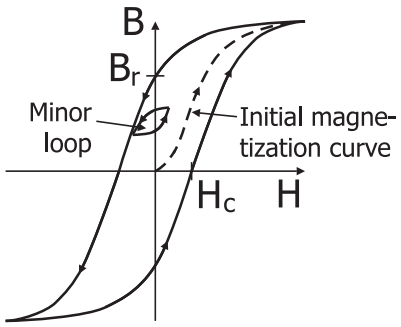

Figure A.2. *Illustration of a hysteresis loop in magnetic materials.*

Magnetic Hysteresis

For equation (A.6), the assumptions were made that the material is isotropic, homogeneous and linear. Especially the latter is essentially not true. Generally, the relation between the field intensity H and the flux density B is not linear and all (ferro)magnetic materials show hysteresis.

The non-linearity of the relationship (A.6), is for a large part due to the saturation of the material. When increasing the field intensity, the flux will increase due to magnetization. Above some flux saturation level, the increase in magnetization will become less and less until the material is fully saturated, and the relative permeability has become one, as shown in Figure A.2.

Hysteresis is the effect that when a magnetic field intensity goes from some value to zero, the material remains magnetized and a certain flux density remains. The *residual magnetic flux density* or *remanence* B_r is the flux density that remains after going from a saturated circuit to zero field intensity. The magnitude of the field intensity needed to have zero flux again, H_c, is called the *coercive force* or shortly *coercivity*.

Permanent magnets use the hysteresis effect and are made of material with an as high as possible coercive force. In applications like transformers, where energy losses due to cycles are to be minimized, materials with a minimal coercivity are used. These materials are called *transformer steel*, and are usually iron alloys with a small amount of silicon, [28].

Eddy Currents

Another important aspect is the occurrence of eddy currents. Eddy currents are explained by another one of Maxwell's equations:

$$\nabla \times E = -\frac{\partial B}{\partial t} \tag{A.32}$$

In words, the line integral of the electric field around a loop equals minus the time derivative of the magnetic flux density through the loop. Thus if the magnetic flux is changed in a conductive material, there will be a current loop in the material such that the resulting

flux from the current loop is in the opposite direction as the change of flux! These are called *eddy currents*.

Eddy currents are thus a frequency dependent phenomenon. In a magnetic circuit, it results in a phase lag between the current in the coil and the flux density. Used as an actuator in a AMB system, eddy currents thus result in additional phase lag in the loop. The eddy currents are greatly reduced using laminated material or a ferromagnetic material with low conductivity, such as ferrites.

A.2 Characterization RTAs of One DoF Setup

This section describes the measurements and modelling of the RTAs used in the experimental setup with one DoF, as described in Section 4.7. Accurate modelling of the RTAs is required for the non-linear compensation control.

A.2.1 Force-Current-Position Relation Measurement

Measurement Setup Description

To measure the force-current-position relationship of the RTAs used, a separate setup shown in Figure A.3 was used[8]. The setup is able to measure the force between the electro-magnet, in this case an E-core, and the target. The target consists of a holder made of aluminum which is fixed to the frame. In the target holder the target material, laminated I-shaped transformer steel, is clamped using brass screws. The electromagnet, laminated E-shaped transformer steel, is glued to the E-core holder. The E-core holder is connected to a force sensor[9], which is attached to an Ω-shaped bridge. The bridge can be adjusted in height through three adjustment screws. With the same screws the tip and tilt of the E-core, with rotations through the air gap can be adjusted. The position, tip and tilt of the E-core relative to the target is measured with four eddy-current sensors[10].

The lamination thickness of the E-core as well as the target material has a thickness of 0.35 mm. The characteristic measure d_{rta} of the RTA is 7 mm, see Figure A.4. The width of the target material is 10 mm.

Measurement Procedure

A total of 4 E-cores were measured; two with 120 windings and two with 200 windings. The (static) force was measured for positions from 0.2 up to 0.9 mm in 14 steps, while the current was set to 0 up to 0.95 A in 20 steps. For each position and current set-point, both position and force was measured during 0.5 s (sample rate 9.6 kHz) and averaged. Each E-core was measured two times, to provide enough data for the fitting procedure.

[8]The setup is property of Philips Applied Technologies, to which the author is grateful for being allowed to use it.

[9]From PCB Piezotronics, model 1102-02A

[10]From Baumer, model IPRM 12I9505

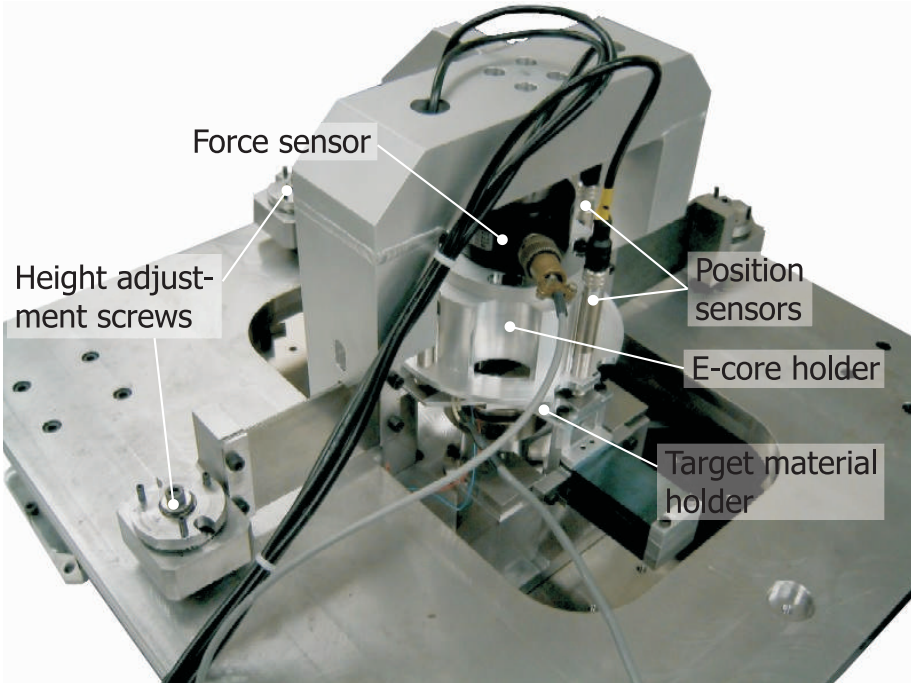

Figure A.3. *Experimental setup.*

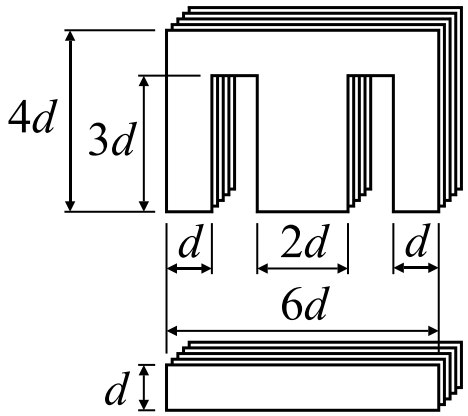

Figure A.4. *A sketch of a standard sized, laminated E-core RTA with target. The thickness (depth) of the RTA (and target) depends on the number of sheets used and the thickness of each sheet. Typically, the thickness of the sheets used in this thesis is 0.35 mm.*

The accuracy of the force measurements was limited by the drift in the force sensor during the measurements for varying currents at a certain position. The drift was measured by zeroing the sensor before a current sweep and after the sweep, when the current was set to zero again. The difference in offset values is the result of drift in the sensor and hysteresis effects. When zero-ing the sensor after a period of time with no measurements, the values for drift were found to be in the same order of magnitude, as when after a current sweep. This indicates that the hysteresis effects were not significant with the materials used, with respect to the drift. A force drift of 5 mN during a current sweep was typical, the highest drift observed in a sweep was 21 mN.

A.2.2 Fitting Procedure

With the procedure above 280 points on the curve $f_{\text{rta}}(i,x_g)$ have been found. To find a function which best describes the measured data, a technique called *linear regression* has been used. Suppose the function $f_{\text{rta}}(i,x_g)$ can be written as the sum of a set of basis functions $g(i,x)$:

$$f_{\text{rta}}(i,x) = \sum_{i=1}^{n} c_k\, g_i(i,x), \tag{A.33}$$

then a measured data point can be written in matrix form:

$$\begin{bmatrix} g_1(i_j,x_k) & g_2(i_j,x_k) & \cdots & g_n(i_j,x_k) \end{bmatrix} \begin{bmatrix} c_1 \\ c_2 \\ \vdots \\ c_n \end{bmatrix} = \begin{bmatrix} f_{\text{rta}}(i_j,x_k) \end{bmatrix}. \tag{A.34}$$

By stacking all the measured data, the following form is obtained:

$$A_m \vec{c} = \vec{f}_m, \tag{A.35}$$

in which each row of A_m consists of the basis functions evaluated for a measurement point, $\vec{c}$ a vector with the coefficients, and $\vec{f}_m$ the stacked measured forces.

When there are more data points than coefficients, a well known result from linear algebra states that a least squares optimal solution for $\vec{c}$ is given by:

$$\vec{c} = \left(A^{\mathrm{T}}A\right)^{-1} A^{\mathrm{T}} \vec{f}_m \tag{A.36}$$

Using this approach, complex polynomial functions dependent on multiple variables can be found with little computational effort.

A.2.3 Fitting Results

The analysis in Section A.1.3 showed that fundamentally the force is dependent on the inverse of the square of the air gap. Hence the following function for fitting was initially investigated:

$$f(i,x) = \frac{n_{2,3}i^2x^3 + n_{2,2}i^2x^2 + \ldots + n_{2,0}i^2 + n_{1,3}ix^3 + \ldots + n_{0,0}}{x^2}. \tag{A.37}$$

Table A.1. *The maximum and RMS-values of the fitting errors of the two RTAs for the various function classes. The maximum force generated by the RTAs is 20.2 N.*

Function family	RTA 1		RTA 2		RTA 1 & 2	
	max [mN]	RMS [mN]	max [mN]	RMS [mN]	max [mN]	RMS [mN]
Reduced	74.3	8.5	71.2	9.9	472	73.3
$k_{\text{rta}}(x^2)$	184	35.5	180	36.3	579	81.1
k_{rta}	1350	270	1410	287	1790	288
k_{rta} and l_i	147	37.2	123	36.4	492	81.4
Advanced and l_i	83.8	0.75	76.9	0.73	463	2.5

By eliminating the terms with the smallest coefficients, the function complexity could be reduced to the following function with very limited loss of accuracy:

$$f(i,x) = k_{\text{rta}}\frac{i^2}{x^2} + k_1\frac{i^2}{x} + k_2\frac{i}{x} + k_3\, i^2 x + k_4\, i^2. \tag{A.38}$$

The fitting results for this function for the two RTAs are shown in Table A.1, and Table A.2, indicated with "reduced".

Further reducing the complexity is achieved by making RTA constant of (A.28) dependent on the gap, $k_{\text{rta}} = n_2x^2 + n_1x + n_0$, which gives the function:

$$f(i,x) = k_{\text{rta}}\frac{i^2}{x^2} + k_1\frac{i^2}{x} + k_4\, i^2. \tag{A.39}$$

The result with this function class are indicated by "$k_{\text{rta}}(x^2)$".

As a last step in the initial investigation, a constant k_{rta} was fitted on the data, indicated by "k_{rta}". The optimal value for both RTAs was 1.32 $\text{N}\,\text{mm}^2/\text{A}^2$, much lower than the theoretical value of 2.46 $\text{N}\,\text{mm}^2/\text{A}^2$.

After investigation of an another RTA used for the setup described in Section 4.8, it was found that taking into account the relative length of the magnetic flux path, see Equation (A.27), led to a big improvement of the fitting accuracy. This additional constant also accounts for that at zero mechanical air gap, the magnetic air gap is not necessarily zero due to uneven lamination and/or different magnetic properties of the surface material due to machining.

After conducting the experiments described in Section 4.7 the data was re-investigated. In addition the following function was fitted:

$$f(i,x) = k_{\text{rta}}\frac{i^2}{\left(x + l_i\right)^2}. \tag{A.40}$$

The relative length of the flux path through iron was found by varying l_i over a certain range and calculate the fitting error with an optimal k_{rta} for each l_i. A length of $l_i =$

Table A.2. *The coefficients for the various functions that were fitted.*

Coef.	Unit	Reduced	$k_{\text{rta}}(x^2)$	k_{rta}	k_{rta} & l_i	Advanced
k_{rta}	$\text{N}\,\text{mm}^2/\text{A}^2$	0.73	0.88	1.32	1.79	1.84
k_1	$\text{N}\,\text{mm}/\text{A}^2$	2.86	1.84	—	—	−0.24
k_2	$\text{N}\,\text{mm}/\text{A}$	$9.6{\cdot}10^{-3}$	—	—	—	—
k_3	$\text{N}/\text{A}^2/\text{mm}$	2.14	—	—	—	—
k_4	N/A^2	−4.01	−1.19	—	—	—
k_5	N/A	—	—	—	—	0.22
l_i	μm	—	—	—	47.5	47.5

47.5 μm and and RTA constant of $k_{\text{rta}} = 1.79\ \text{N}\,\text{mm}^2/\text{A}^2$ gave the best fitting results. The RTA constant is higher than the RTA constant found without taking into account the relative iron flux path, but still much lower than the theoretical found value ($2.46\ \text{N}\,\text{mm}^2/\text{A}^2$).

Finally, the "advanced" function:

$$f(i,x) = k_{\text{rta}}\frac{i^2}{\left(x+l_i\right)^2} + k_1\frac{i^2}{\left(x+l_i\right)} + k_5\, i, \tag{A.41}$$

was fitted, in which for l_i the value found with (A.40) was used (47.5 μm). This function is based on (4.36) on page 91, but it was found that the complexity could be reduced, with hardly any increase in fitting inaccuracy.

Discussion of Fitting Results

Comparing the fitting results for the various functions, Table A.1 and Table A.2, it becomes clear that including an additional parameter for the relative iron flux path, greatly enhances the fitting accuracy. This additional constant also accounts for that at zero mechanical air gap, the magnetic air gap is not necessarily zero due to uneven lamination and/or different magnetic properties of the surface material due to machining.

A difference in the RTA constant k_{rta} of up to 35% was found in different experiments. Possible causes for this difference can be that stray flux (see Figure A.1 on page 164) is neglected and that flux fringing (see [75, p.408]) leads to a smaller flux density in the gap than in the iron, which is also not accounted for.

B

Mechanical Model of the Rotating Demonstrator

B.1 State Space Modelling of Mechanical Plants

B.1.1 Force Input

A linear mechanical system is easily converted to state space by setting the state vector χ to: $\chi = [x,\ \dot{x}]^{\mathrm{T}}$ with which the system can be written as:

$$\dot{\chi} = \underbrace{\begin{bmatrix} 0^{n_m \times n_m} & I^{n_m \times n_m} \\ -M^{-1}K & -M^{-1}D \end{bmatrix}}_{A_{ss}} \chi + \underbrace{\begin{bmatrix} 0^{n_m \times n_a} \\ M^{-1}F \end{bmatrix}}_{B_{ss}} f. \tag{B.1}$$

From the state space vector χ and the force input f, it is easy to select the position, velocity and acceleration as output

$$x = \underbrace{\begin{bmatrix} I^{n_m \times n_m} & 0^{n_m \times n_m} \end{bmatrix}}_{C_{ss}} \chi + \underbrace{\begin{bmatrix} 0^{n_m \times n_m} \end{bmatrix}}_{D_{ss}} f \tag{B.2}$$

$$\dot{x} = \underbrace{\begin{bmatrix} 0^{n_m \times n_m} & I^{n_m \times n_m} \end{bmatrix}}_{C_{ss}} \chi + \underbrace{\begin{bmatrix} 0^{n_m \times n_m} \end{bmatrix}}_{D_{ss}} f \tag{B.3}$$

$$\ddot{x} = \underbrace{\begin{bmatrix} -M^{-1}K & -M^{-1}D \end{bmatrix}}_{C_{ss}} \chi + \underbrace{M^{-1}F}_{D_{ss}} f \tag{B.4}$$

B.1.2 Displacement as Input

Position Input and Output

A system with n_m DoFs with displacement input is called linear mechanical if it can be written in the following form:

$$M\ddot{x}_o + D_o\dot{x}_o + K_o x_o = D_i\dot{x}_i + K_i x_i \tag{B.5}$$

with $M, D_o, K_o \in \mathbb{R}^{n_m \times n_m}$ and $D_i, K_i \in \mathbb{R}^{n_m \times n_i}$. This is converted to state space by setting the state vector to: $\chi = [x_o\,,\, \dot{x}_o - M^{-1}D_i x_i]^{\mathrm{T}}$, with which the system can be written as:

$$\dot{\chi} = \underbrace{\begin{bmatrix} 0^{n_m \times n_m} & I^{n_m \times n_m} \\ -M^{-1}K_o & -M^{-1}D_o \end{bmatrix}}_{A_{ss}} \chi + \underbrace{\begin{bmatrix} M^{-1}D_i \\ M^{-1}K_i - M^{-1}D_o M^{-1}D_i \end{bmatrix}}_{B_{ss}} x_i \tag{B.6}$$

$$x_o = \underbrace{\begin{bmatrix} I^{n_m \times n_m} & 0^{n_m \times n_m} \end{bmatrix}}_{C_{ss}} \chi + \underbrace{\begin{bmatrix} 0^{n_m \times n_i} \end{bmatrix}}_{D_{ss}} x_i \tag{B.7}$$

Velocity Input and Position Output

Now the input vector must first be integrated, hence the model increases with n_i states. When the state vector is set to: $\chi = [x_o,\, \dot{x}_o,\, x_i]^{\mathrm{T}}$ the system can be written as:

$$\begin{aligned} \dot{\chi} &= \underbrace{\begin{bmatrix} 0^{n_m \times n_m} & I^{n_m \times n_m} & 0^{n_m \times n_i} \\ -M^{-1}K_o & -M^{-1}D_o & M^{-1}K_i \\ 0^{n_i \times n_m} & 0^{n_i \times n_m} & 0^{n_i \times n_i} \end{bmatrix}}_{A_{ss}} \chi + \underbrace{\begin{bmatrix} 0^{n_m \times n_i} \\ M^{-1}D_i \\ I^{n_i \times n_i} \end{bmatrix}}_{B_{ss}} \dot{x}_i \\ x_o &= \underbrace{\begin{bmatrix} I^{n_m \times n_m} & 0^{n_m \times n_m} & 0^{n_m \times n_i} \end{bmatrix}}_{C_{ss}} \chi + \underbrace{\begin{bmatrix} 0^{n_m \times n_i} \end{bmatrix}}_{D_{ss}} \dot{x}_i \end{aligned} \tag{B.8}$$

B.2 Notation

The variable x is used to indicate position, the variable f for force. For the modelling of the demonstrator, several coordinate frames are introduced. Table B.1 gives an overview of these frames. The coordinate frame which a position and force vector uses is indicated by a superscript symbol, given in the same table. In Figure B.1 the origin of the coordinate frames r, m, f are indicated.

Vectors of length eight have the following entries: up/right, up/left, up/back, up/front, down/right, down/left, down/back, down/front, indicated with subscripts: ur, ul, ub, uf, dr, dl, db, df, respectively.

Most vectors of length contain positions or force in three translation directions x, y and z, and two rotation directions r^x and r^y. There are two exceptions, the first being the coordinate frame referring to the capacitive sensors, which refers to x, y, z_1, z_2 and z_3, the displacement measured from the centre of the air gap of the capacitive sensors in metres, and the coordinate frame referring to the ground movement, which refers to x_1, y_1, z_1, z_2 and z_3, the displacement at the bottom of the supports of the granite table.

Displacements and positions have unit metre, and forces have unit Newton.

Transformation matrices are denoted by T, with a two letter subscript, indicating between which coordinate systems the transformation applies. A superscript a indicates that the transformation acts on forces (the actuators), if omitted, the transformation acts on positions. Hence, T_{cv} denotes the transformation: $x^v = T_{cv}x^c$.

Table B.1. *Coordinate frames used for mechanical modelling.*

symbol	description	dimension
v	Refers to a **v**irtual five DoF actuator and sensor at the geometrical centre of actuators and optical sensors	5
r	Refers to the CoG of the **r**otor	5
o	Refers to the air gap at the **o**ptical sensors	8
c	Refers to the gaps measured by the **c**apacitive sensors	5
a	Refers to the air gaps and forces of the **a**ctuators	8
f	Refers to the coordinate system of the **f**orce frame. The origin coincides to where the demonstrator is mounted at the granite table	5
g	Represents the movement of the **g**round	5
m	Refers to the CoG of the **m**etrology frame	5

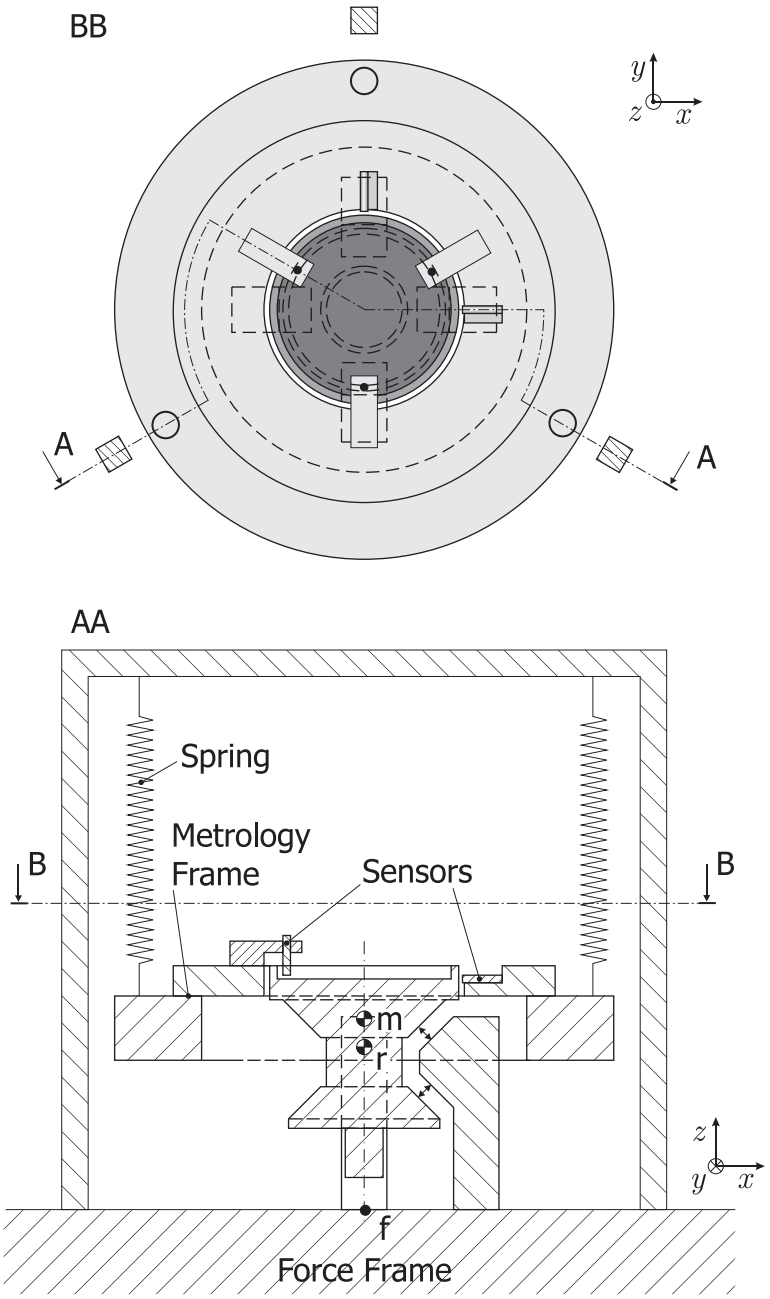

Figure B.1. *Schematic drawing of the complete mechanical design of the rotating demonstrator. Indicated are the rotor, the metrology frame and the force frame. Also indicated are the points r, m and f at which coordinate systems are attached.*

B.3 Model of the Force Frame

B.3.1 Modelling Goal and Assumptions

The stator frame holds the actuators and the motors, on which the reaction forces (of the forces that are exerted on the rotor) act. The stator frame is part of the force frame, the other part being the granite block on which the stator is bolted.

The goal for the force frame model is to describe its movement as function of the the reaction forces of the actuators and the ground vibrations. For the inclusion of reaction forces in the model, the inertia of the force frame in five DoF is to be included in the model. To incorporate the interaction of the ground vibrations in the model, the support of the force frame must be included.

To model the force frame the following assumptions are made:

- All the mass and inertia of the force frame are determined by the granite block.
- The granite block and the stator are infinitely stiff connected and act as a single rigid body with 5 DoFs.
- The damping in the system is viscous, i.e. the forces due to damping are proportional to the velocity.
- The supports of the granite block have zero length.
- Rotations are considered small enough, so that $\sin\alpha \approx \alpha$.

B.3.2 Model Derivation

In Figure B.2 the dimensions of the granite block is given. The base of the stator frame is mounted at the point f (which coincides with the rotation axis of the rotor). The equations of motion are evaluated around point f. The mass matrix is given by:

$$M_f = \text{diag}\,(m_f, m_f, m_f, J_{xf}, J_{yf}), \tag{B.9}$$

with m_f the mass of the force frame, and J_{xf} and J_{yf} the inertia around the x and y axis at point f, respectively. The values of the mass ($\approx 725\text{kg}$) and inertia can be calculated from the dimensions and the density of the granite of 3000 kg/m^3.

To calculate the stiffness matrix, it is useful to introduce an auxiliary local coordinate frame textsfs giving the elongation of each spring in x, y, and z direction. The vector that gives the elongation of the springs is given by:

$$x^s = [x_1,\ y_1,\ z_1,\ x_2,\ y_2,\ \ldots,\ z_3]^{\mathrm{T}} \tag{B.10}$$

The elongation of the springs is given by:

$$x^s = T_{fs}\, x^f - T_{gs}\, x^g, \tag{B.11}$$

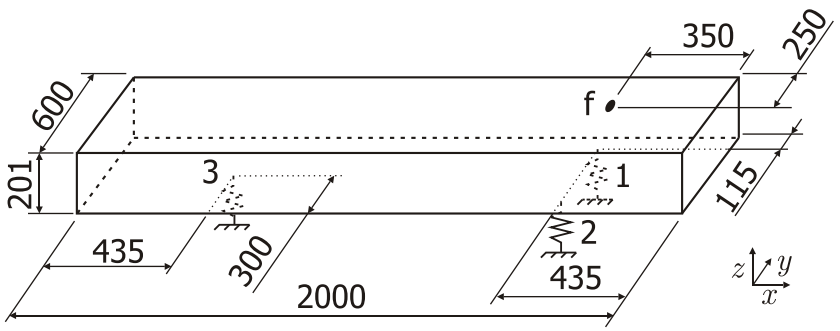

Figure B.2. *Sketch of the force frame with dimensions [mm]. Indicated are the positions (*1, 2, 3*) of the springs (which have stiffness in* x, y *and* z*-direction) and the position at which the rotating prototype is mounted,* f.

where x^f is the displacement vector at point f and x^g a displacement vector representing the movement of the floor:

$$\begin{aligned} x^f &= [x,\, y,\, z,\, r_x,\, r_y]^{\mathrm{T}} \\ x^g &= [x_1,\, y_1,\, z_1,\, z_2,\, z_3]^{\mathrm{T}}. \end{aligned} \tag{B.12}$$

The two transformation matrixes are gives by:

$$T_{fs} = \begin{bmatrix} 1 & 0 & 0 & 0 & -0.201 \\ 0 & 1 & 0 & 0.201 & 0 \\ 0 & 0 & 1 & 0.135 & 0.085 \\ 1 & 0 & 0 & 0 & -0.201 \\ 0 & 1 & 0 & 0.201 & 0 \\ 0 & 0 & 1 & -0.235 & 0.085 \\ 1 & 0 & 0 & 0 & -0.201 \\ 0 & 1 & 0 & 0.201 & 0 \\ 0 & 0 & 1 & -0.05 & 1.215 \end{bmatrix} \tag{B.13}$$

and

$$T_{gs} = \begin{bmatrix} 1 & 0 & 0 & 0 & 0 \\ 0 & 1 & 0 & 0 & 0 \\ 0 & 0 & 1 & 0 & 0 \\ 1 & 0 & 0 & 0 & 0 \\ 0 & 1 & 0 & 0 & 0 \\ 0 & 0 & 0 & 1 & 0 \\ 1 & 0 & 0 & 0 & 0 \\ 0 & 1 & 0 & 0 & 0 \\ 0 & 0 & 0 & 0 & 1 \end{bmatrix}. \tag{B.14}$$

The forces exerted by the springs are given by:

$$f^s = K_s x^s, \tag{B.15}$$

where $K_s = \text{diag}\,(k_x, k_y, k_z, k_x, k_y, k_z, k_x, k_y, k_z)$. The value of k_z is chosen such that the resonance frequency in the z-direction is 20 Hz, the frequency at which the measured ground vibrations show a big peak. Hence, the stiffness k_z equals:

$$k_z = \tfrac{1}{3} m_f (20 \cdot 2\pi)^2. \tag{B.16}$$

The values for k_x and k_y are chosen equal to k_z.

The forces at point f exerted by the springs are given by:

$$\begin{aligned} f^f &= {T_{fs}}^{\mathrm{T}} f^s \\ &= -{T_{fs}}^{\mathrm{T}} K_s x^s \\ &= -{T_{fs}}^{\mathrm{T}} K_s (T_{fs} x^f - T_{gs} x^g) \\ &= -K_f x^f + K_{gf} x^g, \end{aligned} \tag{B.17}$$

in which $f^f = [f_x,\ f_y,\ f_z,\ m_x,\ m_y]^{\mathrm{T}}$. The damping matrix is constructed likewise:

$$\begin{aligned} f^f &= -{T_{fs}}^{\mathrm{T}} D_s (T_{fs} \dot{x}^f - T_{gs} \dot{x}^g) \\ &= -D_f \dot{x}^f + D_{gf} \dot{x}^g, \end{aligned} \tag{B.18}$$

where $D_s = \text{diag}\,(d_x,\ d_y,\ d_z,\ d_x,\ d_y,\ d_z,\ d_x,\ d_y, d_z)$. Note that K_f and D_f are symmetric, since they relate displacement (velocities) at point f to forces at the same point, whereas K_{gf} (and D_{gf}) are not symmetric, since they relate the displacements (velocities) of the ground to forces at point f.

Now, the complete motion equations of the force frame can be written as:

$$M_f \ddot{x}^f + D_f \dot{x}^f + K_f x^f = D_{gf} \dot{x}^g + K_{gf} x^g + F_f f^f, \tag{B.19}$$

where F_f is a 5×5 identity matrix and f^f the reaction forces of the actuators acting on point f.

The resulting model has five resonance modes with frequencies of 9.32, 10.3, 20.0, 23.8, 29.9 Hz.

B.4 Model of the Metrology Frame

B.4.1 Modelling Goal and Assumptions

The metrology frame is attached by three springs (see Figure 5.15 on page 124) to an aluminium frame, which is mounted to the force frame. The goal of the metrology frame model is to describe its motions as function of the position of the force frame.

For the modelling of the metrology frame the following assumptions are made.

- The metrology frame is a rigid body with 5 DoFs (rotation is not seen by the sensors).

- The dampening introduced by the dampers is viscous.
- For the derivation of the transformation matrices, the air gaps are neglected, since they are much smaller than the dimensions of the rotor.
- Rotations are considered small enough, so that $\sin\alpha \approx \alpha$.

B.4.2 Model Derivation

The modelling procedure of the derivation of the model is the same as for the force frame and is described in [90]. Because of the symmetry around the z-axis, it was practical to first write the motion equations in 6 DoF, and then to delete the entries related to the rotation around the z-axis.

The motion equations of the metrology frame, are completely described by:

$$M_m\ddot{x}^m + D_m\dot{x}^m + K_m x^m = D_{fm}\dot{x}^f + K_{fm}x^f + F_m f^m. \tag{B.20}$$

Of the five eigenmodes two modes have an eigenfrequency of 0.92 Hz, two an eigenfrequency of 2.98 Hz and one of 2.01 Hz. The latter eigenfrequency corresponds to the mode in which the whole metrology frame moves in z-direction.

B.5 Motion Sensors

For the derivation of the mechanical model of the rotor, some transformation matrices are needed that are related to the motion sensors. The motion sensors measure the position of the rotor with respect to the force frame and the metrology frame. Figure B.3 gives an overview of the transformation matrices related to the motion sensors.

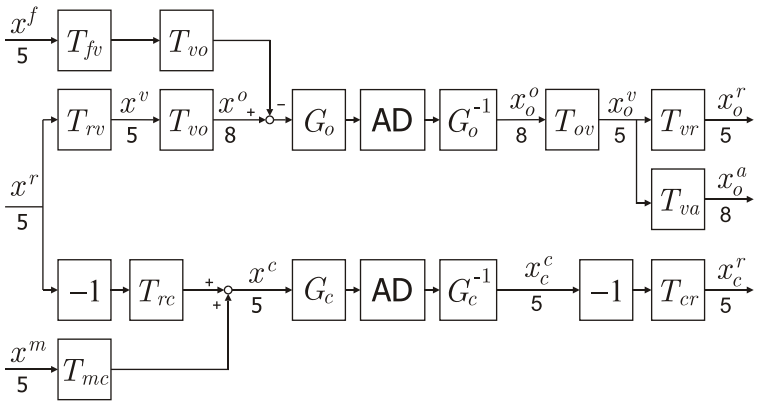

Figure B.3. *Overview of the transformation matrices related to the motion sensors.*

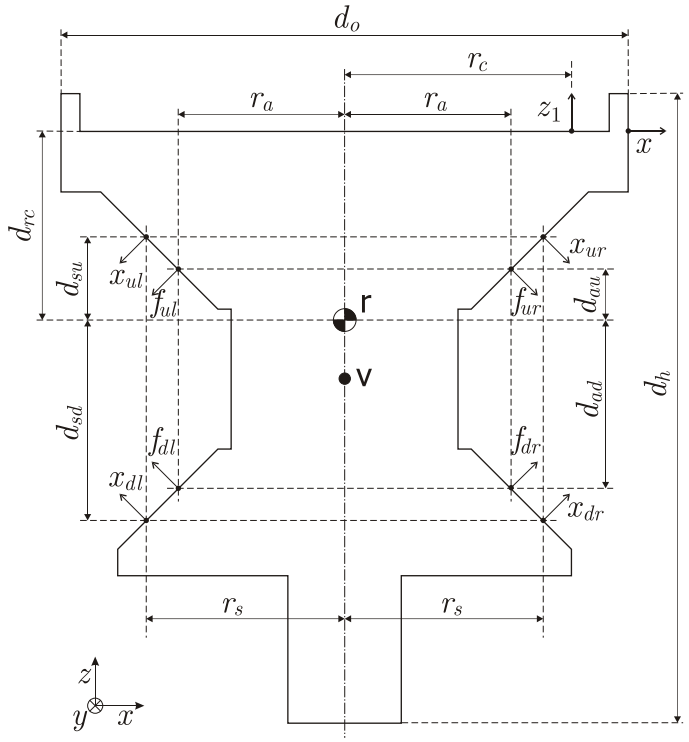

Figure B.4. *A sketch of the Five DoF Rotating Prototype indicating the symbols for the sizes.*

B.5.1 Force Frame Sensors

The position of the rotor with respect to the force frame are measured with eight optical sensors. The eight optical sensors are positioned close to the actuators. The air gaps measured with the optical sensors at the position of the actuators are denoted x_o^a, and at the position of the sensors x_o^o. In Figure B.4 a schematic cross section of the rotor is shown, in which the position of the measured air gaps and actuators is given. The values of the dimensions shown in Figure B.4 are given in Table B.2.

The vector $x^o = [x_{ur}, x_{ul}, x_{ub}, x_{uf}, x_{dr}, x_{dl}, x_{db}, x_{df}]^{\mathrm{T}}$ contains the air gaps at the position of the optical sensors. The gap between the rotor and the force frame depends on the movement of the rotor as well as the movement of the force frame, as indicated in Figure B.3:

$$x^o = T_{vo}\left(T_{rv}x^r - T_{fv}x^f\right) \tag{B.21}$$

The first transformation of (B.21) is from the position at v to the positions at the sensors, $x^o = T_{vo}x^v$. A displacement in x-direction at v, results in an upper-left displacement

Table B.2. *The values of the dimensions of the rotor.*

Symbol	Value [mm]
d_o	150
d_h	166.5
r_s	50.85
r_a	40.25
r_c	63
d_{su}	22.6
d_{sd}	48.9
d_{au}	12
d_{ad}	38.3
d_{rc}	49.2

of: $x_{ul} = \frac{1}{2}\sqrt{2}x$. The transformation matrix T_{vo} becomes:

$$T_{vo} = \frac{1}{2}\sqrt{2}\begin{bmatrix} 1 & 0 & -1 & 0 & d_t \\ -1 & 0 & -1 & 0 & -d_t \\ 0 & 1 & -1 & -d_t & 0 \\ 0 & -1 & -1 & d_t & 0 \\ 1 & 0 & 1 & 0 & -d_t \\ -1 & 0 & 1 & 0 & d_t \\ 0 & 1 & 1 & d_t & 0 \\ 0 & -1 & 1 & -d_t & 0 \end{bmatrix}, \tag{B.22}$$

where $d_t = d_{sv} + r_s$ and $d_{sv} = \frac{1}{2}(d_{su} + d_{sd})$ as illustrated in Figure B.5.

Since eight position sensors are used for measuring five DoF, there is some redundancy. To find the position of point v the sensor positions are averaged. For example, the displacement in x-direction becomes:

$$x = \frac{\sqrt{2}}{4}(x_{ur} + x_{dr} - x_{ul} - x_{dl}). \tag{B.23}$$

Applying averaging in the other directions, gives the transformation matrix T_{ov}:

$$T_{ov} = \frac{1}{8}\sqrt{2}\begin{bmatrix} 2 & -2 & 0 & 0 & 2 & -2 & 0 & 0 \\ 0 & 0 & 2 & -2 & 0 & 0 & 2 & -2 \\ -1 & -1 & -1 & -1 & 1 & 1 & 1 & 1 \\ 0 & 0 & -2/d_t & 2/d_t & 0 & 0 & 2/d_t & -2/d_t \\ 2/d_t & -2/d_t & 0 & 0 & -2/d_t & 2/d_t & 0 & 0 \end{bmatrix} \tag{B.24}$$

To check integrity of the transformation matrices, the following relation must be true:

$$T_{ov} \cdot T_{vo} = I^{5\times 5}, \tag{B.25}$$

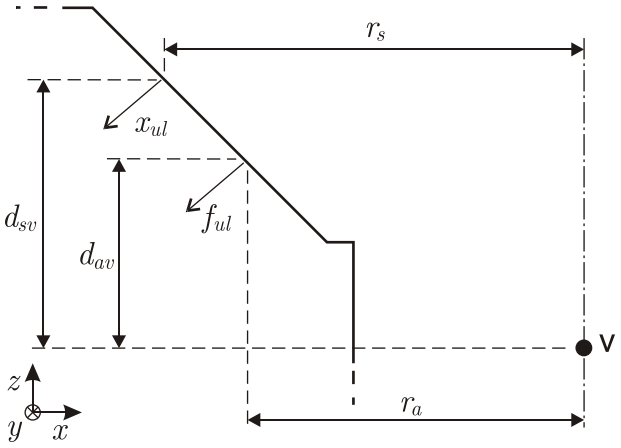

Figure B.5. *Close up of Figure B.4.*

which is indeed the case.

The next transformation of (B.21) is the transformations from CoG to point v, $x^v = T_{rv}x^r$ in which:

$$T_{rv} = \begin{bmatrix} 1 & 0 & 0 & 0 & -\frac{1}{2}(d_{ad} - d_{au}) \\ 0 & 1 & 0 & \frac{1}{2}(d_{ad} - d_{au}) & 0 \\ 0 & 0 & 1 & 0 & 0 \\ 0 & 0 & 0 & 1 & 0 \\ 0 & 0 & 0 & 0 & 1 \end{bmatrix}. \tag{B.26}$$

The transformation from point v to CoG is simply $T_{vr} = T_{rv}^{-1}$.

The electronics consists of the Philtec fiber optic sensors, the anti-aliasing filter and the AD-converter. The bandwidths of the electronic sensor components are considered to be infinitely high. The voltages from the sensors is given by:

$$v_x^o = g_{sens}(s) = k_{os}k_{aa} \cdot x^o, \tag{B.27}$$

with k_{os} the gain of the optic sensors $[\mathrm{V/m}]$ and k_{aa} the gain of the anti-aliasing filters, $[\mathrm{V/V}]$. So:

$$v^o = k_{os}\,k_{aa} \cdot I^{8\times 8}\,x^o = G_o\,x^o, \tag{B.28}$$

with $v^o = [v_{ur}^o \ldots v_{df}^o]^{\mathrm{T}}$ the voltage outputs of the system, $x^o = [x_{ur} \ldots x_{df}]^{\mathrm{T}}$. The gains are: $k_{os} = 2835$ V/m and $k_{aa} = 4$ V/V, which makes the total gain for the sensors: 11.34 V/mm.

The transformation matrix T_{va}, which maps the position of v, x^v, to the gaps at the actuators, x^a, is exactly as T_{vo}, with $d_t = d_{av} + r_a$ and $d_{av} = \frac{1}{2}(d_{au} + d_{ad})$.

The transformation matrix to go from positions at the sensor to positions at the actuators, is:

$$T_{oa} = T_{va} \cdot T_{ov}. \tag{B.29}$$

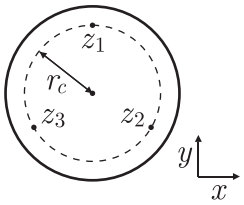

Figure B.6. *The naming convention for the three capacitive sensors measuring on the top of the rotor.*

B.5.2 Capacitive Sensors

The positions of the three capacitive sensor measuring on the top surface are defined in Figure B.6. The gaps measured by the capacitive sensors, depend on the movement of the rotor, as well as the movement of the metrology frame (MF):

$$x^c = T_{mc}\, x^m - T_{rc}\, x^r, \tag{B.30}$$

in which the two transformation matrices are:

$$T_{rc} = \begin{bmatrix} 1 & 0 & 0 & 0 & d_{rc} \\ 0 & 1 & 0 & -d_{rc} & 0 \\ 0 & 0 & 1 & r_c & 0 \\ 0 & 0 & 1 & -\frac{1}{2} r_c & -\frac{1}{2}\sqrt{3} r_c \\ 0 & 0 & 1 & -\frac{1}{2} r_c & \frac{1}{2}\sqrt{3} r_c \end{bmatrix} \tag{B.31}$$

where d_{rc} and r_c are given in Figure B.4 and

$$T_{mc} = \begin{bmatrix} 1 & 0 & 0 & 0 & -d_{mc} \\ 0 & 1 & 0 & d_{mc} & 0 \\ 0 & 0 & 1 & r_c & 0 \\ 0 & 0 & 1 & -\frac{1}{2} r_c & -\frac{1}{2}\sqrt{3} r_c \\ 0 & 0 & 1 & -\frac{1}{2} r_c & \frac{1}{2}\sqrt{3} r_c \end{bmatrix} \tag{B.32}$$

with d_{mc} the distance from CoG of the metrology frame to the surface of the rotor.

The transformation from measured rotor position at the capacitive sensors to the CoG of the rotor, is given by: $x_c^r = T_{cr}\, x_c^c$, where $T_{cr} = \left(T_{rc}\right)^{-1}$.

The electronics that convert the measured distances to voltages, consists of the capacitive sensors, sensor amplifiers and the custom made ADC (which include anti-aliasing filters). Since the bandwidth of the the electronics are much higher than frequency range of interest, the sensor electronics are modelled with a gain:

$$v^c = G_c\, x^c = k_{cs} \cdot I^{5\times 5}\, x^c, \tag{B.33}$$

with $v^c = [v_x, v_y, v_{z1}, v_{z2}, v_{z3}]^{\mathrm{T}}$ the voltage outputs of the capacitive sensors and $k_{cs} = 0.4 \cdot 10^6$ V/m the gain of the optic sensors.

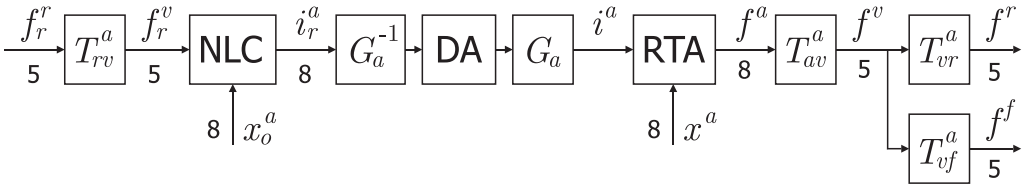

Figure B.7. *Block scheme of the electrical actuators sub-block.*

B.6 Model of the Rotor

B.6.1 Modelling Goal and Assumptions

The goal of the rotor model is to describe its position as function of the actuator forces and force frame position.

The assumptions made for modelling the rotor are:

- The rotor is a rigid body with 5 DOFs (rotation is not seen by the sensors nor excited by the actuators).
- The position dependent forces from the gravity compensator and the linearized reluctance actuators are linear.
- The remaining position dependency of the NLC in combination with the actuators are modelled with a stiffness of 1000 $\mathrm{N/m}$ at each actuator.
- The damping introduced by eddy currents and hysteresis, are modelled with a viscous damping of 3 $\mathrm{N/(m/s)}$.
- The gravity compensator is modelled with a spring stiffness of -250 N/m in z-direction and -125 N/m in x- and y-direction.
- For the remaining stiffness of the ironless motor is a spring with a stiffness of 500 $\mathrm{N/m}$ is taken.
- Rotations are considered small enough, so that $\sin\alpha \approx \alpha$.

B.6.2 Electrical Actuators

First the electrical actuators are modelled. The electrical actuators convert the reference force inputs f_r^r to into realized force inputs f^r acting on the rotor and the reaction force f^f acting on the force frame. Because of the Non-Linear Compensation (NLC), the electrical actuators are considered as black boxes with unit gain. As a result the model of the electrical actuators include a part of the physical system as well as the digital to analogue converter and the NLC implementation in dSPACE®.

In Figure B.7 the block scheme of the electrical actuators is given.

Actuator Transformation Matrixes

The first transformation matrix of Figure B.7 maps the forces at the CoG to point v: $f^v = T^a_{rv} f^r$, in which

$$T^a_{rv} = \begin{bmatrix} 1 & 0 & 0 & 0 & 0 \\ 0 & 1 & 0 & 0 & 0 \\ 0 & 0 & 1 & 0 & 0 \\ 0 & -\frac{1}{2}(d_{ad} - d_{au}) & 0 & 1 & 0 \\ \frac{1}{2}(d_{ad} - d_{au}) & 0 & 0 & 0 & 1 \end{bmatrix}. \tag{B.34}$$

The matrix T^a_{vr} maps the forces at point v to the CoG and equals $T^a_{rv} = \left(T^a_{vr}\right)^{-1}$.

The transfer function G_a models the amplifiers and equals:

$$G_a = \text{diag}\,(k_{\text{amp}},\ ...,\ k_{\text{amp}}), \tag{B.35}$$

in which $k_{\text{amp}} = 0.1$ A/V is the gain of each amplifier.

The transformation matrix to go from actuator forces f^a, to forces at point v, f^v, is defined as:

$$T^a_{av} = \tfrac{1}{2}\sqrt{2} \begin{bmatrix} 1 & -1 & 0 & 0 & 1 & -1 & 0 & 0 \\ 0 & 0 & 1 & -1 & 0 & 0 & 1 & -1 \\ -1 & -1 & -1 & -1 & 1 & 1 & 1 & 1 \\ 0 & 0 & -d_m & d_m & 0 & 0 & d_m & -d_m \\ d_m & -d_m & 0 & 0 & -d_m & d_m & 0 & 0 \end{bmatrix}, \tag{B.36}$$

in which $d_m = r_a + \frac{1}{2}(d_{au} + d_{ad})$.

Finally, the reaction forces of the actuators are transformed to forces to base f by: $f^f = T^a_{vf} T^a_{av} f^a$, where

$$T^a_{vf} = \begin{bmatrix} 1 & 0 & 0 & 0 & 0 \\ 0 & 1 & 0 & 0 & 0 \\ 0 & 0 & 1 & 0 & 0 \\ 0 & -d_{fv} & 0 & 1 & 0 \\ d_{fv} & 0 & 0 & 0 & 1 \end{bmatrix}. \tag{B.37}$$

in which $d_{fv} = 0.11$ m is the distance between the points f and v.

To decouple the system around the capacitive sensors, as discussed in Section 6.4, the transformation from forces at the sensor positions to the centre of the rotor is needed. The corresponding transformation matrix is given by:

$$T^a_{cr} = \begin{bmatrix} 1 & 0 & 0 & 0 & 0 \\ 0 & 1 & 0 & 0 & 0 \\ 0 & 0 & 1 & 1 & 1 \\ 0 & -d_{rc} & r_c & -r_c/2 & -r_c/2 \\ d_{rc} & 0 & 0 & -r_c\sqrt{3}/2 & -r_c\sqrt{3}/2 \end{bmatrix} \tag{B.38}$$

Derivation of Actuator Stiffness

The non-linear compensation (NLC) will not compensate perfectly, and a position dependent force component does remain. This position dependency is approximated with a positive stiffness, defined by the equation $f_{ur} = -k_{act} x_{ur}$ and the sign convention of Figure B.4. In order to write down the equation of motion, the stiffness term for each actuator must be translated to a stiffness at the CoG.

First, the actuator stiffness matrix is defined as:

$$f^a = -\text{diag}\,(k_{act},\ \ldots\ , k_{act})\, x^a = -K_a x^a. \tag{B.39}$$

The air gaps at the actuators, depend on movement of the rotor, as well as the movement of the force frame:

$$x^a = T_{va}\, T_{rv}\, x^r - T_{va}\, T_{fv}\, x^f. \tag{B.40}$$

In the above equation only T_{fv} has not been defined yet. It transforms the displacement at point f to point v, $x^v = T_{fv}\, x^f$, in which

$$T_{fv} = \begin{bmatrix} 1 & 0 & 0 & 0 & d_{fv} \\ 0 & 1 & 0 & -d_{fv} & 0 \\ 0 & 0 & 1 & 0 & 0 \\ 0 & 0 & 0 & 1 & 0 \\ 0 & 0 & 0 & 0 & 1 \end{bmatrix}, \tag{B.41}$$

with d_{fv} the distance from point f on the table to point v at the centre of the actuators.

With the transformations defined above, the stiffness matrix in the CoG coordinate system can be calculated as follows:

$$\begin{aligned} f^r &= T^a_{vr}\, T^a_{av} f^a \\ &= -T^a_{vr}\, T^a_{av}\, K_a \left(T_{va}\, T_{rv}\, x^r - T_{va}\, T_{fv}\, x^f\right) \\ &= -K^a_r\, x^r + K_{fr}\, x^f. \end{aligned} \tag{B.42}$$

The gravity compensator is located at the CoG of the rotor, hence its stiffness can be written down directly:

$$K^{gc}_r = -\text{diag}\,(55,\ -55,\ -110,\ 0,\ 0) \tag{B.43}$$

Hence,

$$f^r = -\left(K^{gc}_r + K^a_r\right) x^r + K_{fr}\, x^f \tag{B.44}$$

To introduce damping to the system, damping is assigned to each actuator (stemming from hysteresis effects and eddy currents). The diagonal matrix $D_a \in \mathbb{R}^{8\times 8}$ is then transformed to D_r and D_{fr} following the same transformations as in (B.42).

By writing the degrees of freedom as $x^r = [x^r\ y^r\ z^r\ r^r_x\ r^r_y]^{\mathrm{T}}$, and the force input as $f^r = [f^r_x\ f^r_y\ f^r_z\ m^r_x\ m^r_y]^{\mathrm{T}}$, the motion equations around the CoG can be written as:

$$M_r \ddot{x}^r + D_r \dot{x}^r + K_r x^r = D_{fr} \dot{x}^f + K_{fr} x^f + F_r f^r, \tag{B.45}$$

where $M_r = [m_r\ m_r\ m_r\ J_x\ J_y]^{\mathrm{T}}$ the mass matrix, with $m_r = 2.69$ kg and $J_x = J_y = 7.62 \cdot 10^{-3}$ kg/m^2, and $F_r = I^{5\times 5}$.

B.6.3 Total Mechanical Model

Model for Controller Design

Since the target bandwidth of the controller is much higher than the resonance frequencies of the rotor, force frame and metrology frame, the dynamics of the transfer function from actuator force to rotor position is determined by the inertia of the rotor. Hence, the model described by (B.45), with omission of the force frame position input, is sufficient for the controller design.

Model for Dynamic Error Budgeting

The total motion equation can be written as:

$$\begin{bmatrix} M_r & 0 & 0 \\ 0 & M_f & 0 \\ 0 & 0 & M_m \end{bmatrix} \begin{bmatrix} \ddot{x}^r \\ \ddot{x}^f \\ \ddot{x}^m \end{bmatrix} + \begin{bmatrix} D_r & -D_{fr} & 0 \\ -D_{rf} & D_f & -D_{mf} \\ 0 & -D_{fm} & D_m \end{bmatrix} \begin{bmatrix} \dot{x}^r \\ \dot{x}^f \\ \dot{x}^m \end{bmatrix} + \begin{bmatrix} K_r & -K_{fr} & 0 \\ -K_{rf} & K_f & -K_{mf} \\ 0 & -K_{fm} & K_m \end{bmatrix} \begin{bmatrix} x^r \\ x^f \\ x^m \end{bmatrix} = \begin{bmatrix} 0 \\ D_{gf} \\ 0 \end{bmatrix} \dot{x}^g + \begin{bmatrix} 0 \\ K_{gf} \\ 0 \end{bmatrix} x^g + \begin{bmatrix} I^{5\times 5} \\ -T^a_{vf} T^a_{rv} \\ 0 \end{bmatrix} f^r. \quad \text{(B.46)}$$

In the above equation four matrices have not been defined yet: K_{rf} and D_{rf} which give the forces on the force frame due to rotor movement and K_{mf} and D_{mf} which give the forces on the force frame due to metrology frame movement. The forces on the force frame due to rotor position is given by:

$$f^f = K_{rf} x^r = T^a_{vf} T^a_{av} K_a T_{va} T_{rv} x^r. \quad \text{(B.47)}$$

Comparing the transformation matrices in the above equation with those in (B.42), shows that $K_{rf} = K_{fr}^{\mathrm{T}}$. The same goes for D_{rf}, K_{mf} and D_{mf} which are the transforms of D_{fr}, K_{fm} and D_{fm}, respectively.

The gaps at the capacitive sensors is given by $x^c = T_{mc} x^m - T_{rc} x^r$ and the rotor position derived from the capacitive sensors $x^r_c = x^r - T_{cr} T_{mc} x^m$. These outputs are easily made, by setting these matrices in the state space output matrix C_{ss}.

B.7 Five DoF Non-Linear Compensation

As can be seen in Figure B.4 eight RTAs are used, which control five DoF. Since the RTAs can only generate attracting forces, the forces calculated at point V are split in positive and

negative parts. Hence $f_x(t) = f_{x+}(t) - f_{x-}(t)$. These positive values are then distributed over the eight RTAs in the following way:

$$\underbrace{\begin{bmatrix} f_{ur} \\ f_{ul} \\ f_{ub} \\ f_{uf} \\ f_{dr} \\ f_{dl} \\ f_{db} \\ f_{df} \end{bmatrix}}_{f_a} = \underbrace{\frac{1}{4}\sqrt{2}\left[\begin{array}{ccccc:ccccc} 2 & 0 & 0 & 0 & 2/d_m & 0 & 0 & 1 & 0 & 0 \\ 0 & 0 & 0 & 0 & 0 & 2 & 0 & 1 & 0 & 2/d_m \\ 0 & 2 & 0 & 0 & 0 & 0 & 0 & 1 & 2/d_m & 0 \\ 0 & 0 & 0 & 2/d_m & 0 & 0 & 2 & 1 & 0 & 0 \\ 2 & 0 & 1 & 0 & 0 & 0 & 0 & 0 & 0 & 2/d_m \\ 0 & 0 & 1 & 0 & 2/d_m & 2 & 0 & 0 & 0 & 0 \\ 0 & 2 & 1 & 2/d_m & 0 & 0 & 0 & 0 & 0 & 0 \\ 0 & 0 & 1 & 0 & 0 & 0 & 2 & 0 & 2/d_m & 0 \end{array}\right]}_{T_{va}^a} \begin{bmatrix} f_{x+} \\ f_{y+} \\ f_{z+} \\ m_{x+} \\ m_{y+} \\ f_{x-} \\ f_{y-} \\ f_{z-} \\ m_{x-} \\ m_{y-} \end{bmatrix}, \quad \text{(B.48)}$$

where $d_m = d_{ar} + \frac{1}{2}(d_{au} + d_{ad})$ represents the momentum arm and $[f_x\ f_y\ f_z\ m_x\ m_y]^{\mathrm{T}}$ are the forces and momentums inputs in 5 DoF of the virtual actuator, with the plus and minus signs indicating the positive and negative parts of the signals.

As a check, one can easily see that:

$$T_{av}^a \cdot T_{va}^a = \begin{bmatrix} I^{5\times5} & -I^{5\times5} \end{bmatrix} \quad \text{(B.49)}$$

The NLC then calculates the currents such that the forces f^a of the RTAs results in that $f_r^v = f^v$.

C

Additional Experimental Results

C.1 Operating Procedure

The operating procedure for the setup is extensively discussed in [16], here a short summary is given. The operating procedure is explained by the state flow given in Figure C.1. For clarity's sake not all the transitions which are implemented are shown. In the state flow the blocks indicate the states of the system and the lines indicate the transitions between the states. A transition is made either at each sample time or when an event (written next to the line) occurs. An event is generated by 1) a transition from one state to another, 2) an if/then branch or 3) user interaction.

Initially the rotor rests on the force frame. By pressing the Start button, the systems enters the Start Up state. In this state the low bandwidth controller is switched on and the system follows a smooth set-point curve from rest position to the nominal position.

After the set-point curve is finished, Startup Ready becomes true, and the setup enters the Cloop w.r.t. Force Frame state. By pressing the To MF button, the reference of the closed loop system switches to the Metrology Frame (MF) sensors and the rotor will follow the MF. This transition is only possible if the MF sensors are in range. The position of the MF with respect to the Force Frame (FF) changes due to temperature induced expansion of the MF. Hence, before switching to the MF sensors, an additional offset is subtracted from the sensor values, such that at the moment of switching the MF sensors give zero positions. This ensures that there is a smooth transition from having the system in closed loop with respect to the Force Frame (FF) to having the system in closed loop with respect to the MF.

By pressing the To High BW button, the system switches to the high bandwidth controller. This transaction is only allowed if the rotor is in closed loop with respect to the metrology frame (Cloop w.r.t. Metro Frame). To guarantee a bumpless transition between the controllers, a special block-scheme is implemented, which is discussed in Section 6.4.

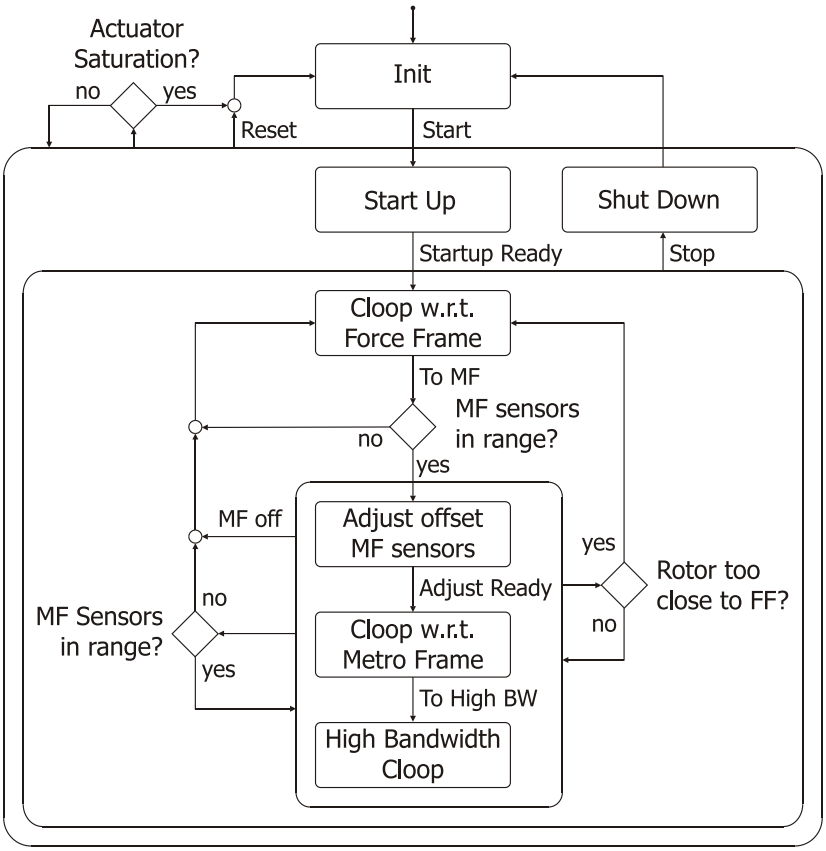

Figure C.1. *State flow of the operating procedure. Initially, the rotor rests on the force frame. By pressing the "Start" button the rotor is brought in closed loop (cloop) with respect to the force frame.*

C.1.1 Safety

For safe operation of the system, several precautions are implemented. When the rotor is in closed loop with respect to the metrology frame, and for some reason the rotor moves out of range of one of the five metrology frame sensors, the system switches back to using the force frame sensors.

Another possible dangerous situation occurs when the rotor is in closed loop with respect to the MF, and the MF makes a large motion. If the rotor approaches the FF too closely, the system switches back to the FF sensors.

Finally, when a general malfunction occurs, such as sensor failure or a mechanical blocking, the whole system should switch off. This situation is detected by monitoring the current to the actuators. If the current of any actuator starts to saturate for more than half a second, the system switches off and go back to the Init state. The rotor will then be supported by the auxiliary ball bearings.

C.1.2 Bumpless Control Transfer

In dSPACE® two controllers are active; one achieving a low bandwidth, used to start the system up, and one achieving a high bandwidth, applied when the system has switched to tracking the metrology frame. In order to be able to switch between the two controllers at any time, a "bumpless" switching scheme is implemented, as shown in Figure C.2b. In this scheme the controller that is not in the main loop forms another loop with an additional controller. The principle is illustrated in Figure C.2a, where the additional controller K_K forces the output of the controller K to track the reference output u. The controller K_K is chosen such that the loop gain $K_K K$ is a pure integrator, with unity gain at 1000 Hz. Switching the three switches in Figure C.2b gives a smooth transition between the two control signals.

C.2 Linearity Measurements

Here the results for the linearity test in the r_x- and r_y-directions are given, as referred to in Subsection 6.2.3.

C.3 Full Measured Transfer Functions

In Figure C.6 the full five by five bode magnitude of the measured transfer function is given.

In Figure C.7 the full five by five bode phase of the measured transfer function is given.

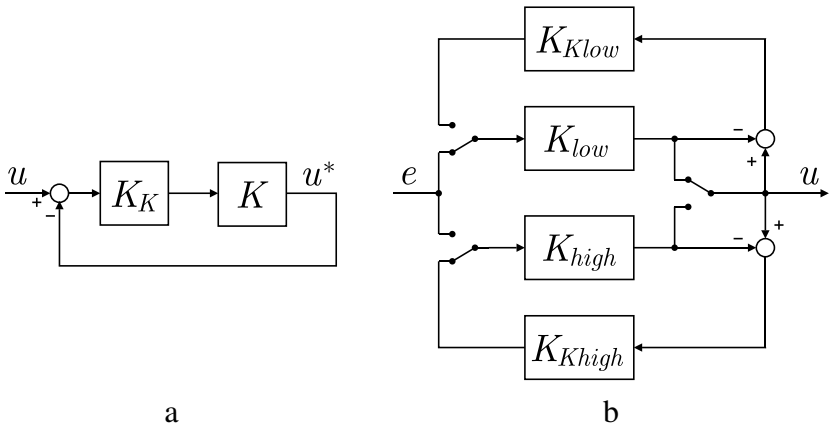

Figure C.2. *a) The additional controller K_K forces the output of the controller K to track the reference output u. b) Bumpless switching scheme for the low bandwidth controller (K_{low}, used for startup) and the high bandwidth controller (K_{high}). In the situation shown K_{low} is in loop with the plant, while the output of K_{high} is forced to follow the output of K_{low}.*

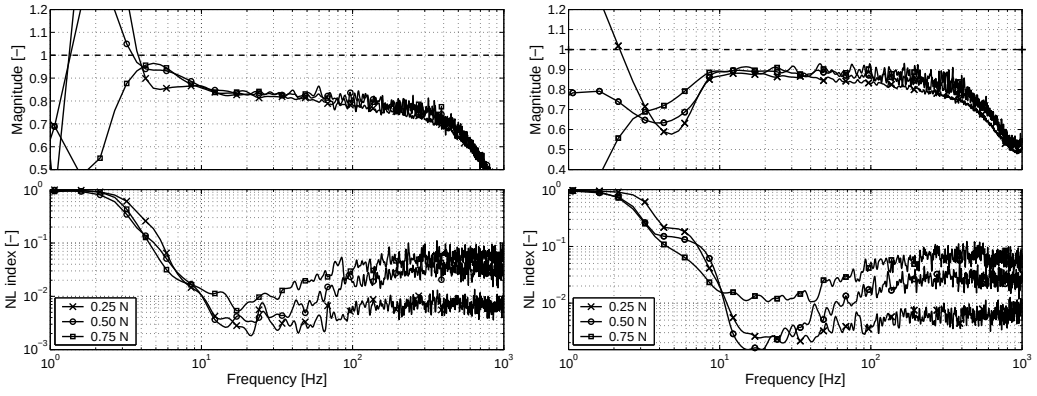

Figure C.3. *Results of the non-linearity test with white noise excitation in the r_x- and r_y-direction. The figures on the top give the gain between the input to the NLC and the estimated moment output. The figures below gives the function one minus the coherence.*

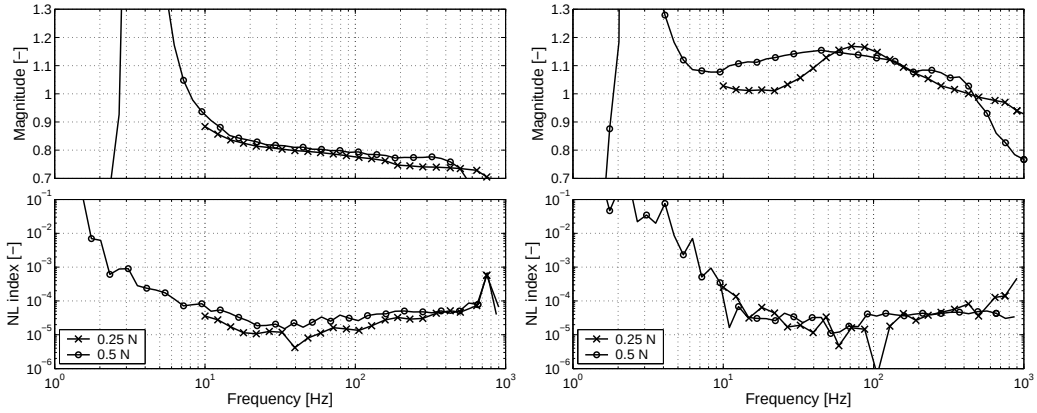

Figure C.4. *Results of the non-linearity test with sinusoid excitation in the* r_x*- and* r_y*-direction. The figures on the top give the gain between the input to the NLC and the estimated output of the RTAs. The figure below gives the power at the higher harmonics divided by the power at the base frequency of the estimation of the generated force*

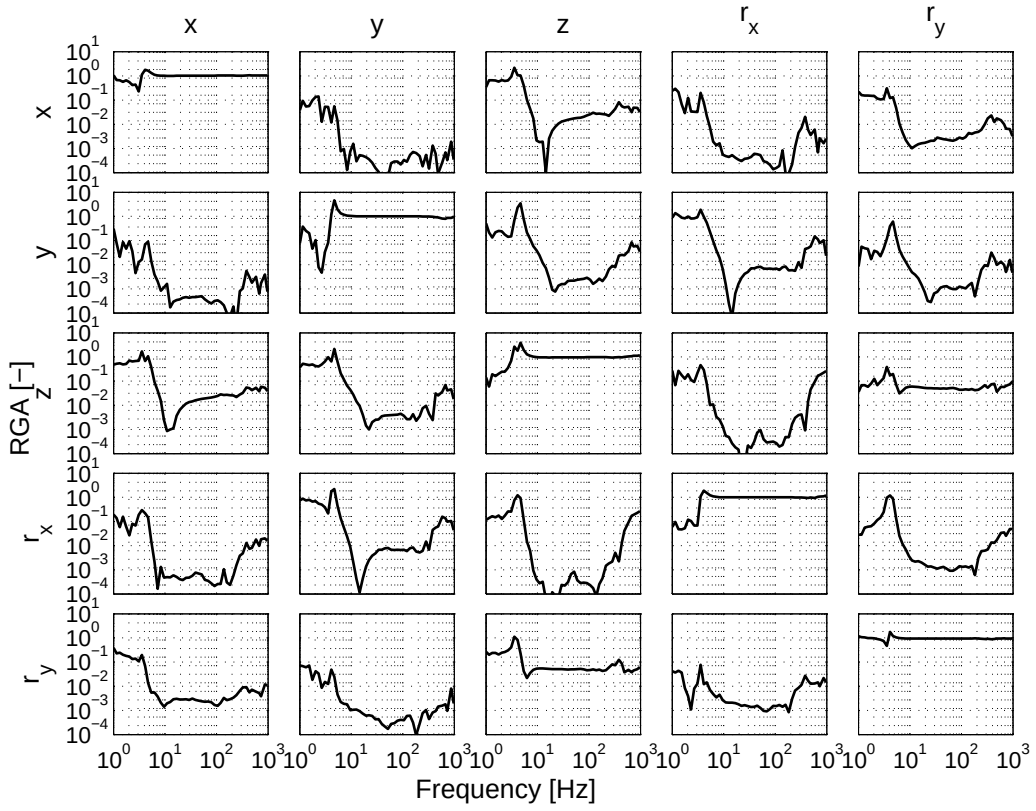

Figure C.5. *Relative Gain Array.*

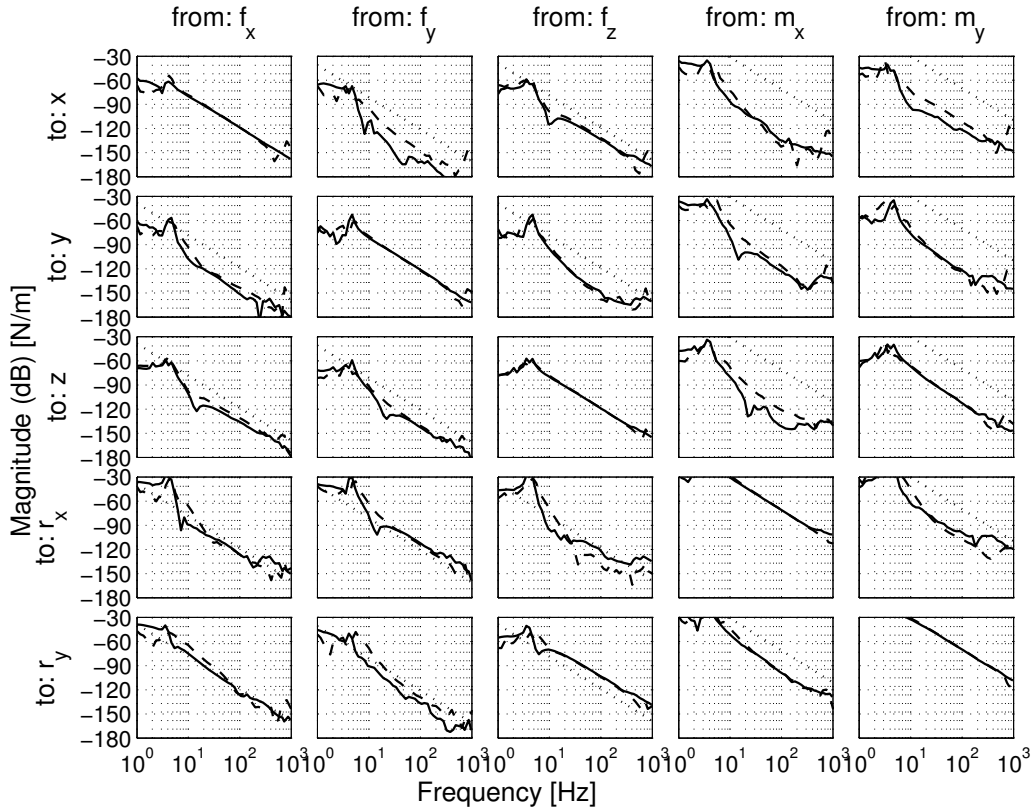

Figure C.6. *Measured bode magnitude of the full five by five transfer function matrix of the plant.*

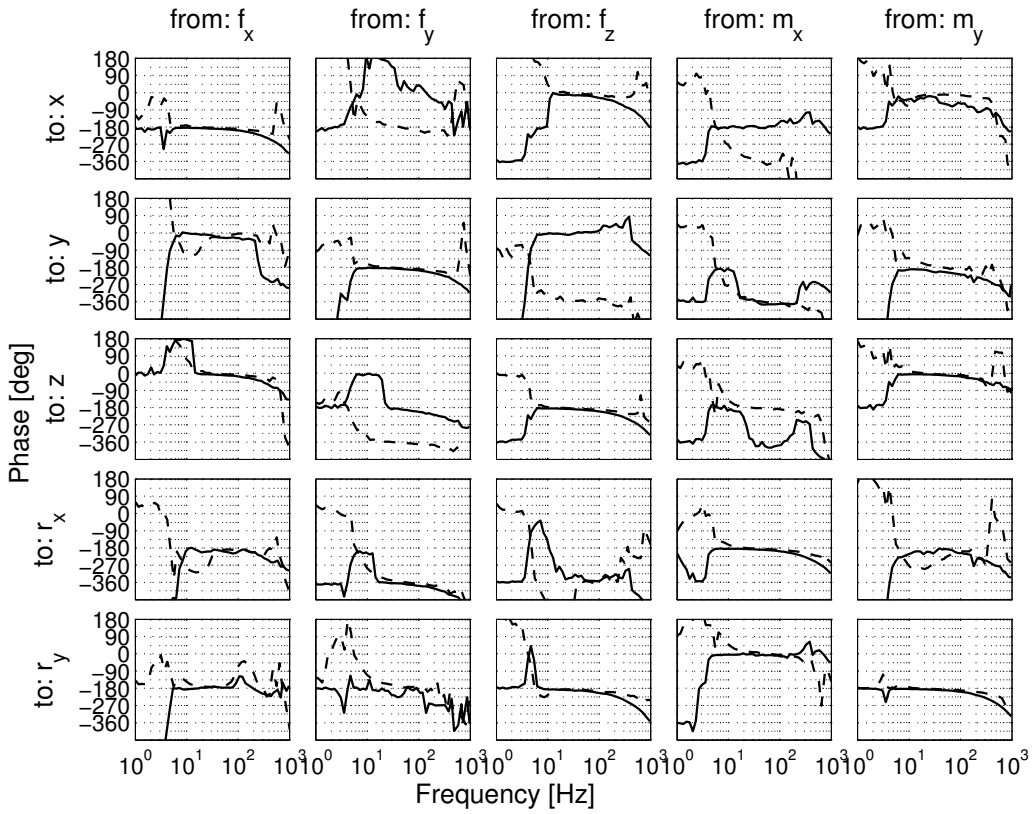

Figure C.7. *Measured bode phase of the full five by five transfer function matrix of the plant.*

D

Spectrum Calculation

Here the functional part of the MATLAB® script is given that is used to calculate the CPS from time data. The interested reader may contact[1] the author for a full version.

```
function [PSD,CPS,frq] = spectra(x,Ts,filter,Nfft,Noverlap);
%   Calculates the spectra of time data.
%   Input:
%     x:       matrix, with time data in columns.
%     Ts:      sample time.
%     filter: filter to be used, 'none',['hanning'].
%     Nfft:    samples used for fft, such that the spectra are
%              averaged length(x)/Nfft times.
%     Noverlap: number of samples overlapping.
%   Output:
%     PSD:      One sided Power Spectral Density [SI^2/Hz].
%     CPS:      Cumulative Power Spectrum [SI^2].
%     frq:      Frequency vector [Hz].

[L,n_sig] = size(x);              % data assumed column-wise
Av        = mean(x);
Var       = mean(x.^2)-Av.^2;     % ac-power of x, ~equal to var(x)
CoVar     = cov(x);
n_it      = floor((L-Noverlap)/(Nfft-Noverlap));
frq       = 1/Ts*(0:ceil(Nfft/2)-1)'/Nfft;
d_f       = 1/(Nfft*Ts);          % delta f of frequency grid
Pxx       = zeros(n_sig,n_sig,Nfft);
index     = 1:Nfft;

for i=1:n_it
  x_tmp = detrend(x(index,:));    % remove first order trend
  index = index+(Nfft-Noverlap);
  if strcmpi(filter,'hanning')
    x_tmp = x_tmp.*repmat(hann(Nfft),1,n_sig);
```

[1] jabius@gmail.com

```
  end
  Wx  = fft(x_tmp)/Nfft;          % Discrete Time Fourier Transform
  for j=1:n_sig
    for k=1:n_sig
      % Two sided Power Spectrum Pxx [SI^2]
      Pxx(k,j,:) = Pxx(k,j,:)+
                   reshape((Wx(:,k).*conj(Wx(:,j)))/n_it,1,1,Nfft);
    end
  end
end

% Make power correction for the used filters
if strcmpi(filter,'hanning')
  Pxx      = Pxx/mean(hann(Nfft).^2);
end
Sxx     = Pxx/d_f;                % Two sided PSD [SI^2/Hz]
Pxx1(:,:,1) = Pxx(:,:,1);         % One sided Power Spectrum
Pxx1(:,:,2:ceil(Nfft/2)) = 2*Pxx(:,:,2:ceil(Nfft/2));
PSD     = Pxx1/d_f;               % One sided PSD [SI^2/Hz]

for j=1:n_sig
  for k=1:n_sig
    if j==k
      % Calculate Cumulative Power Spectrum [SI^2] diagonal
      CPS(j,k,:) = cumsum(Pxx1(j,k,:),3);
    else
      % Cumulative Real Cross Power Spectrum [SI^2]
      CPS(j,k,:) = cumsum(real(Pxx1(j,k,:)),3);
    end
    % Scale the CPS such that the start values corresponds to the
    % dc power and the end value to the total power
    CPS(j,k,:) = (CPS(j,k,:)-CPS(j,k,1))*CoVar(j,k)/
                   (CPS(j,k,end)-CPS(j,k,1))+Av(j)*Av(k);
  end
end

PSD(:,:,1)  = Av.'*Av/d_f;        % gives correct dc-value of PSD
Pxx = fftshift(Pxx,3);            % Make two sided from -f to +f
Sxx = fftshift(Sxx,3);            % Make two sided from -f to +f

if n_sig ==1
  Pxx     = squeeze(Pxx);
  Sxx     = squeeze(Sxx);
  PSD     = squeeze(PSD);
  CPS     = squeeze(CPS);
end

end
```

Bibliography

[1] D. Abramovitch, T. Hurst, and D. Henze. Decompensition of Baseline Noise Sources in Hard Disk Position Error Signals Using the PES Pareto Method. In *Proceedings of the 1997 American Control Conference*, pages 2901–2905, Albuquerque, NM, USA, June 1997.

[2] D. Abramovitch, T. Hurst, and D. Henze. The PES Pareto Method: Uncovering the Strata of Position Error Signals in Disk Drives. In *Proceedings of the 1997 American Control Conference*, pages 2888–2895, Albuquerque, NM, USA, June 1997.

[3] M. Ahrens and L. Kučera. Cross Feedback Control of a Magnetic Bearing System. In *Proceedings of the 3rd International Symposium on Magnetic Suspension Technology*, Tallahassee, FL, USA, December 1995.

[4] K. Aki and P.G. Richards. *Quantitative Seismology*. University Science Books, Sausalito, California, 2nd edition, 2002.

[5] American Society of Mechanical Engineers. *Axis of Rotation: Methods for Specifying and Testing. ANSI Standard B89.3.4M-1985*.

[6] L. Balmer. *Signals and Systems*. Prentice Hall, 2nd edition, 1998.

[7] M. Baloh, G. Tao, P. Allaire, and E. Maslen. Feedback Linearization of Magnetic Bearing Actuator. In *Proceedings of the 7th International Symposium on Magnetic Bearings*, pages 23–25, Zurich, Switzerland, August 2000.

[8] A. Barzilai, T. VanZandt, and T. Kenny. Technique for Measurements of the Noise of a Sensor in the Presence of Large Background Signals. *Review of Scientific Instruments*, 69(7):2767–2773, July 1998.

[9] BD Association, Available on: www.blu-raydisc.com, last accessed 10-12-2006. *White Paper Blu-ray Disk—Physical Format Specifications*, 4nd edition, 2005.

[10] J.S. Bendat. *Nonlinear Systems Techniques and Applications*. John Wiley & Sons, New York, 1998.

[11] W.R. Bennet. *Electrical Noise*. McGraw-Hill Book Company, New York, 1960.

[12] B.J. Bennett. A New Filter Synthesis Technique—The Hourglass. *IEEE Transactions on Circuits and Systems*, 35(12):1469–1477, December 1988.

[13] L.L. Beranek, editor. *Noise and Vibration Control*, chapter 2. McGraw-Hill Book Company, 1971.

[14] F. Betschon and C.R. Knospe. Reducing Magnetic Bearing Currents via Gain Scheduled Adaptive Control. *IEEE/ASME Transactions on Mechatronics*, 6(4):437–443, December 2001.

[15] M. Boerlage, M. Steinbuch, and G. Angelis. Frequency Response Based Multivariable Control Design for Motion Systems. In *Proceedings of the IEEE Conference on Control Applications*, Toronto, Canada, August 2005.

[16] S.G.A. Boschker. Linearizing Control of a 5 DoF Rotating Platform. Master's thesis, Mechanical Engineering, Delft University of Technology, Delft, The Netherlands, 2005.

[17] G. Bouwhuis, J. Braat, A. Huijser, J. Pasman, G. van Rosmalen, and K. Schouhamer Immink. *Principles of Optical Disk Systems*. Adam Hilger, Ltd., 1985.

[18] S. Boyd and C. Barrat. *Linear Controller Design—Limits of Performance*. Prentice Hall, 1991.

[19] P.M.T. Broersen. Automatic Spectral Analysis with Time Series Models. *IEEE Transactions on Instrumentation and Measurement*, 51(2):211–216, April 2002.

[20] B.C. Callen and T.A. Welton. Irreversibility and Generalized Noise. *Physical Review*, 83(1):34–40, July 1951.

[21] A. Charara, J. De Miras, and B. Caron. Nonlinear Control of a Magnetic Levitation System Without Premagnetization. *IEEE Transactions on Control Systems Technology*, 4(5):513–523, September 1996.

[22] B.G. Dijkstra. *Iterative Learning Control—With Applications to a Wafer Stage*. PhD thesis, Mechanical Engineering, Delft University of Technology, The Netherlands, 2003.

[23] J.C. Doyle, K. Glover, P.P. Khargonekar, and B.A. Francis. State-space solutions to standard $\mathcal{H}_2$ and $\mathcal{H}_\infty$ control problems. *IEEE Transactions on Automatic Control*, 34(8), August 1989.

[24] S. Earnshaw. On the Nature of the Molecular Forces, which Regulate the Constitution of the Luminiferous Ether. *Transactions of Cambridge Philosophical Society*, 7:97–112, 1842.

[25] ECMA, Available on: www.ecma.ch, last accessed 3-2-2003. *Standard ECMA-267*, 2nd edition, 2001.

[26] M.H. El-Husseini, A. Bennani, J.W. Spronck, H. Polinder, J.C. Compter, and J. van Eijk. Evaluation of the Dynamic Radial Stiffness of an Ironless Motor for Precision Engineering Application. In *Proceedings of the 16th International Conference on Electrical Machines*, pages 817–822, Cracow, Poland, September 2004.

[27] M.H. El-Husseini, C.J. Slinkman, H. Polinder, J.W. Spronck, and J. van Eijk. Low Noise Linear Power Amplifier for Precision Active Magnetic Bearings Application. In *Proceeding of Power Conversion Intelligent Motion PCIM*, Nuremberg, Germany, May 2003.

[28] R.P. Feynman, R.B. Leighton, and M. Sands. *The Feynman Lectures on Physics—Vol.II Mainly Electromagnetism and Matter*. Addison-Wesley, Reading, Massachusetts, 1964.

[29] P.J. Fish. *Electronic Noise and Low Noise Design*. McGraw-Hill, New York, 1994.

[30] U. Forssell and L. Ljung. Closed-loop Identification Revisited. *Automatica*, 35:1215–1241, 1999.

[31] J.S. Freudenberg, C.V. Hollot, R.H. Middleton, and V. Toochinda. Fundamental Design Limitations of the General Control Configuration. *IEEE Transactions on Automatic Control*, 48(8), August 2003.

[32] T. Glad and L. Ljung. *Control Theory : Multivariable & Nonlinear Methods*. CRC Press, 2000.

[33] C.G. Gordon. Generic Vibration Criteria for Vibration-Sensitive Equipment. In C.G. Gordon, editor, *Vibration Control in Microelectronics, Optics and Metrology*, volume 1619, pages 71–85. SPIE, 1991.

[34] R. Grejda, E. March, and R. Vallance. Techniques for Calibrating Spindles with Nanometer Error Motion. *Precision Engineering*, 29(1):113–123, 2005.

[35] D-W Gu, P.H. Petkov, and M.M. Konstantinov. $\mathcal{H}_\infty$ and $\mathcal{H}_2$ Optimization Toolbox in SLICOT. Technical report, Katholieke Universiteit Leuven, September 1999.

[36] H.M. Gutierrez and P.I. Ro. Parametric Modeling and Control of a Long-Range Actuator Using Magnetic Servo Levitation. *IEEE Transactions on Magnetics*, 34(5):3689–3695, September 1998.

[37] H.M. Gutierrez and P.I. Ro. Sliding-Mode Control of a Nonlinear-Input System: Application to a Magnetically Levitated Fast-Tool Servo. *IEEE Transactions on Industrial Electronics*, 45(6):921–927, December 1998.

[38] R. Haber and Keviczky. *Nonlinear System Identification—Input-Output Modeling Approach*, volume 2: Nonlinear System Structure Identification. Kluwer Academic Publishers, Dordrecht, NL, 1999.

[39] J.W. Hardy. *Adaptive Optics for Astronomical Telescopes*. Oxford University Press, 1998.

[40] E. Hecht. *Optics*. Addison-Wesley, 4$^{\text{th}}$ edition, 2002.

[41] J.L. Herder. *Energy Free Systems—Theory, Conception AND Design of Statically Balanced Spring Systems*. PhD thesis, Mechanical Engineering, Delft University of Technology, Delft, The Netherlands, 2001.

[42] D. Hobbelen. System Design of 5 DoF Ultra High Precision, Magnetically Suspended Rotating Platform. Master's thesis, Mechanical Engineering, Delft University of Technology, Delft, The Netherlands, 2003.

[43] S.A.J. Hol. *Design AND Optimization of a Magnetic Gravity Compensator*. PhD thesis, University of Eindhoven, The Netherlands, 2004.

[44] M. Holmes and D. Trumper. Magnetic/Fluid-Bearing Stage for Atomic-Scale motion control (the Angstrom stage). *Precision Engineering*, 18:38–49, 1996.

[45] T. Hu, L. Lin, and P.E. Allaire. Reducing Power Loss in Magnetic Bearings by Optimizing Current Allocation. *IEEE Transactions on Magnetics*, 40(3):1625–1635, May 2004.

[46] T. Hurst, D. Abramovitch, and D. Henze. Measurements for the PES Pareto Method of Identifying Contributors to Disk Drive Servo System Errors. In *Proceedings of the 1997 American Control Conference*, pages 2896–2900, Albuquerque, NM, USA, June 1997.

[47] IDEMA, Available on: www.idema.org, last accessed 3-2-2003. *IDEMA Standard document no. T17-91*, 2nd edition.

[48] L. Jabben, D. Hobbelen, and J. van Eijk. Non-linear Control of Reluctance Type of Actuators for Ultra High Precision Applications. In *Proceedings of the 3rd Euspen International Conference 2002*, pages 179–182, Eindhoven, The Netherlands, May 2002.

[49] F. Jay. *IEEE Standard Dictionary of Electrical and Electronics Terms*. The Institute of Electrical and Electronic Engineers, Inc., New York, 1977.

[50] E.M.H. Kamerbeek. *On the Theoretical and Experimental Determination of the Electromagnetic Torque in Electrical Machines*. PhD thesis, University of Eindhoven, The Netherlands, 1970.

[51] A.C.P. de Klerk, G.Z. Angelis, and J. van Eijk. Design of a Next Generation 6 DoF Stage for Scanning Application in Vacuum with Nanometer Accuracy and mGauss Magnetic Stray Field. In *Proceedings of ASPE 19th Annual Meeting*, Orlando, Florida, USA, October 2004.

[52] C. Knospe and C. Yang. Gain-Scheduled Control of a Magnetic Bearing with Low Bias Flux. In *Proceedings of the 36th Conference on Decision & Control*, San Diego, CA, USA, December 1997.

[53] P.V. Kokotovic. The Joy of Feedback: Nonlinear and Adaptive. *IEEE Control Systems*, 1991.

[54] H. Kwakernaak and R. Sivan. *Linear Optimal Control Systems*. Wiley Interscience, New York, 1972.

[55] J.D. Lindlau and C.R. Knospe. Feedback Linearization of an Active Magnetic Bearing With Voltage Control. *IEEE Transactions on Control Systems Technology*, 10(1):21–31, January 2002.

[56] P.B. Lock. Design of a Permanent Magnetic Gravity Compensator. Master's thesis, Mechanical Engineering, Delft University of Technology, Delft, The Netherlands, 2001.

[57] S. Ludwick, D. Trumper, and M. Holmes. Modeling and Control of a Six-Degree-of-Freedom Magnetic/Fluidic Motion Control Stage. *IEEE Transactions on Control Systems Technology*, 4(5):553–564, September 1996.

[58] S.J. Ludwick. Modeling and Control of a Six Degree of Freedom Magnetic/Fluidic Motion Control Stage. Master's thesis, Mechanical Engineering, Massachusetts institute of Technology, Delft, The Netherlands, 1996.

[59] J.M. Maciejowski. *Multivariable Feedback Design*. Addison-Wesley, Wokingham, England, 1989.

[60] E.H. Maslen, P.E. Allaire, M. Noh, and C.K. Sortore. Magnetic Bearing Design for Reduced Power Consumption. *ASME Journal of Tribology*, 118(4):839–846, October 1996.

[61] M. Maslen. Magnetic Bearings. http://people.virginia.edu/~ehm7s/MagneticBearings/mag_brgs.pdf, June 2000.

[62] G.K. McConnell. *Vibration Testing—Theory and Practice*. John Wiley & Sons, New York, 1995.

[63] Memorex, Available on: www.memorex.com, last accessed 10-12-2006. *White Paper—Reference Guide for Optical Media*, 2006.

[64] A. Molenaar. *A Novel Planar Magnetic Bearing and Motor Configuration A applied in a Positioning Stage*. PhD thesis, Mechanical Engineering, Delft University of Technology, Delft, The Netherlands, 2000.

[65] W. Monkhorst. Dynamic Error Budgeting—A Design Approach. Master's thesis, Mechanical Engineering, Delft University of Technology, Cambridge, MA, USA, 1996.

[66] C.D. Motchenbacher and J.A. Connelly. *Low-Noise Electronic System Design*. John Wiley & Sons, 1993.

[67] P.G. Nelson. Understanding and Measuring Noise Sources in Vibration Isolation Systems, 1993. www.techmfg.com/company/papers_intro.html, last accessed Jan. 2005.

[68] H. Nijmeijer and A.J. van der Schaft. *Nonlinear Dynamical Control Systems*. Springer-Verlag, New York, 1990.

[69] G.J.P. Nijsse. *Linear Motion Systems—A Modular Approach for Improved Straightness Performance*. PhD thesis, Mechanical Engineering, Delft University of Technology, Delft, The Netherlands, 2001.

[70] A.V. Oppenheim, R.W. Schafer, and J.R. Buck. *Discrete-Time Signal Processing*. Prentice-Hall, Inc., New Jersey, 2nd edition, 1998.

[71] P.M. Overschie, L. Jabben, F. Savenije, J.W. Spronck, R. Munnig Schmidt, and J. van Eijk. Mechatronic Design of an Ultra Precision Magnetically Supported Rotor for Optical Disk Mastering. In *Proceedings of the Seventh International Conference of the European Society for Precision Engineering and Nanotechnology*, Bremen, Germany, May 2007.

[72] P.M. Overschie, L. Jabben, J.P. van Schieveen, J.W. Spronck, and J. van Eijk. Capacitive Sensing System Design for a Rotating AMB with Sub-Nanometer Positioning Accuracy. In *Proceedings of the Tenth International Symposium on Magnetic Bearings*, Martigny, Switzerland, August 2006.

[73] A. Papoulis. *Probability, Random Variables and Stochastic Processes*. McGraw-Hill, 3th edition, 1991.

[74] J. Peterson. Observations and Modeling of Seismic Background Noise, Open-File Report 93-322. http://aslwww.cr.usgs.gov/Publications, last accessed March 2005, 1993. Albuquerque Seismological Laboratory, New Mexico.

[75] M.A. Plonus. *Applied Electro-Magnetics*. McGraw-Hill, Inc., 1978.

[76] M.B. Priestley. *Spectral Analysis and Time Series*. Academic Press, London, 1989.

[77] M.S. de Quieroz and D.M. Dawson. Nonlinear Control of Active Magnetic Bearings: A Backstepping Approach. *IEEE Transactions on Control Systems Technology*, 4(5):545–552, December 1996.

[78] M.A. Riedesel, R.D. Moore, and J.A. Orcutt. Limits of Sensitivity of Inertial Seismometers with Velocity Transducers and Electronic Amplifiers. *Bulletin of the Seismological Society of America*, 80(6):1725–1752, December 1990.

[79] G.R. Ritchie, J.C. Candy, and W.H. Ninke. Interpolative Digital-to-Analog Converters. *IEEE Transactions on Communications*, COM-22:1797–1806, November 1974.

[80] E.I. Rivin. Vibration Isolation of Precision Equipment. *Precision Engineering*, 17(1):41–56, January 1995.

[81] P.W. Rodgers. Frequency Limits For Seismometers as determined from Signal-to-Noise Ratios—The Electromagnetic Seismometer. *Bulletin of the Seismological Society of America*, 82(2):1071–1098, April 1992.

[82] C. Rojer. System Identification of the Planar Active Magnetic Bearing. Master's thesis, Mechanical Engineering, Delft University of Technology, Delft, The Netherlands, 2002.

[83] D. de Roover. *Motion Control of a Wafer Stepper—A Design Approach for Speeding Up IC Production*. PhD thesis, Mechanical Engineering, Delft University of Technology, Delft, The Netherlands, 1997.

[84] A.H. Sayed and T. Kailath. A Survey of Spectral Factorization Methods. *Numerical Linear Algebra With Applications*, 8:467–496, 2001.

[85] C. Scherer, P. Gahinet, and M. Chilali. Multiobjective Output-Feedback Control via LMI Optimization. *IEEE Transactions on Automatic Control*, 42(7):896–911, July 1997.

[86] J.P. van Schieveen. Data-Acquisition for Optical Disc Mastering Unit. Master's thesis, Mechanical Engineering, Delft University of Technology, Delft, The Netherlands, 2004.

[87] G. Schweitzer, H. Bleuler, and A. Traxler. *Active Magnetic Bearings—Basics, Properties and Applications of Active Magnetic Bearings*. ETH-Zurich (Swiss Federal Institute of Technology), Zurich, 1994.

[88] S. Skogestad and I. Postlethwaite. *Multivariable Feedback Control—Analysis and Design*. John Wiley & Sons, West Sussex, England, 1998.

[89] A.H. Slocum. *Precision Machine Design*. Prentice-Hall, Inc., New Jersey, 1992.

[90] F.B.M.B. Soetens. Analysis of a Metrology Frame—Working Principle, Disturbance Response and Final Performance. Master's thesis, Mechanical Engineering, Delft University of Technology, Delft, The Netherlands, 2004.

[91] M.W. Spong and M. Vidyasagar. *Robot Dynamics and Control*. John Wiley & Sons, New York, 1989.

[92] G. Stein. Respect the Unstable. *IEEE Control Systems Magazine*, 23(4):12–25, August 2003.

[93] P.K. Subrahmanyan. *A Modal Approach to Precision Motion Control*. PhD thesis, Mech. Eng., Massachusetts Institute of Technology, Boston, USA, 1999.

[94] Texas Instruments Incorporated. Noise Analysis in Operational Amplifier Circuits—Application Report. Available on: www.techonline.com/community/tech_group/analog/tech_paper/21477, last accessed Jan. 2005, 1998.

[95] D.L. Trumper, S.M. Olson, and K. Subrahmanyan. Linearizing Control of Magnetic Suspensions Systems. *IEEE Transactions on Control System Technology*, 5(4):427–438, July 1997.

[96] D.L. Trumper, J.C. Sanders, T.H. Nguyen, and M.A. Queen. Experimental Results in Nonlinear Compensation of a One Degree-of-Freedom Magnetic Suspension. In *NASA International Symposium on Magnetic Suspension Technology*, August 1991.

[97] B.V. Tryggvason, R.F. Redden, R.A. Herring, W.M.B. Duval, R.W. Smith, K.S. Rezkallah, and S. Varma. The Vibration Environment on the International Space Station: Its Significance to Fluid-Based Experiments. *Acta Astronautica*, 48(2–3):59–70, January–February 2001.

[98] P. Tsiotras and B.C. Wilson. Zero- and Low-Bias Control Designs for Active Magnetic Bearings. *IEEE Transactions on Control Systems Technology*, 11(6):889–904, November 2003.

[99] D. Vaes, J. Swevers, and P. Sas. Optimal Decoupling for MIMO-Controller Design with Robust Performance. In *Proceedings NASA International Magnetic Suspension Technology*, Boston, Massachusetts, USA, June 2004.

[100] W.C. van Etten. *Introduction to Random Signals and Noise*. John Wiley & Sons, Ltd, 2005.

[101] M. van de Wal. Advanced Feedback Control of Electromechanical Servo Systems: Theory, Tools, and Applications to ASML Stages. Technical Report CTB595-00-2168, Philips, October 2000.

[102] P.M.R. Wortelboer. *Frequency-weighted Balanced Reduction of Closed-loop Mechanical Servo-systems*. PhD thesis, Mechanical Engineering, Delft University of Technology, Delft, The Netherlands, 1994.

[103] P.M.R. Wortelboer, M. Steinbuch, and O.H. Bosgra. Iterative Model and Controller Reduction Using Closed-loop Balancing, With Application to a Compact Disc Mechanism. *International Journal Robust and Nonlinear Control*, 4(3):123–142, March 1999.

[104] M. Young. *Optics and Lasers—Including Fibers and Optical Waveguides*. Springer-Verlag, Berlin, 5th edition, 2000.

[105] K. Zhou, J.C. Doyle, and K. Glover. *Robust and Optimal Control*. Prentice Hall, Upper Saddle River, New Jersey, 1996.

Summary

The mastering process of an optical disk is a good example of a high precision process of which ever increasing performance is desired due to the demands made by a modern society which is craving for information. A promising potential technology to increase the performance of optical disk mastering is the use of magnetic bearings. Magnetic bearings work contact free and can operate in a vacuum. A magnetic bearing system is inherently unstable and requires feedback control for stabilization. The use of feedback control make magnetic bearings a typical mechatronic technology. With the design of such a mechatronic system usually many disciplines are involved. To optimize the performance of the total system, the design effort should be a balance between these disciplines. The Dynamic Error Budgeting (DEB) analysis procedure, which is developed in this thesis, aims for the optimal balancing of the design efforts.

A design process starts with the development of a concept design. In order to make the fundamental concept choices, the specifications for Blu-ray mastering are derived from DVD specifications, since they are not publicly available. The driving requirement for the design is the Asynchronous Radial Error Motion (AREM). This motion causes track pitch variations during the mastering process. The AREM for the magnetic platform during rotation should be smaller than 1 nm (RMS).

Since the AREM does not relate to synchronous movements, stochastic (or random) disturbances are by large the main contributors to the AREM. Ground vibrations were identified in an early stage as one of the stochastic disturbances with the most impact. Measurements showed that the ground vibrations in the laboratory have higher levels than would be allowed for a wafer scanner of ASML. For this reason it was decided to separate the metrology frame with the force frame. Resulting from this choice, other decisions were made, such as the use of a gravity compensator to minimize the actuator forces and to use non-linear control to linearize the actuators and minimize the mechanical stiffness.

The use of active magnetic bearing technology was a starting point for the design of the rotor. Active magnetic bearings use *Reluctance Type Actuators* (RTAs) which have a strong non-linear behaviour with respect to the current and the air

gap. The common applied technique to linearize an RTA is to use pre-loading with half the maximum current. Drawbacks of this approach are a constant power dissipation in the actuators and a strong mechanical coupling between the rotor and the frame holding the actuators. This coupling conflicts with the concept of separating the force and the metrology frame which requires actuators with a low stiffness. A technique described in literature to minimize these effects is *Non-Linear Compensation* (NLC). In this thesis the sensitivity of NLC to parameter changes is analysed and the technique is validated using two experimental setups. With these experiments it was found that the mechanical stiffness can be reduced by a factor 20 to 100, depending on the complexity of the NLC and the working range of the actuators.

To evaluate the various design decisions, the DEB analysis procedure was used. The DEB analysis takes into account that the performance is determined by a closed loop system, and that this performance is adversely affected by stochastic disturbances. Using the superposition principle, the contribution from each stochastic disturbance source to the error can be analysed separately. The outcome of the DEB analysis is a plot which indicates which disturbances are the most dominant. The design effort then aims to minimize the influence of these disturbances. As the plot also indicates the power distribution over frequency, DEB provides valuable information in the design phase on how to improve the controller design and/or the plant design. This procedure can be applied to a broad range of mechatronic systems, which is why DEB is described in this thesis in a general sense.

After translating the concept design into an initial design which could be modelled, the design proceeded using DEB. Based on evaluations using DEB various design decisions were made, the most important of which were the choice for an ironless motor and the decision to start the development of an improved analogue-to-digital converter. The asynchronous radial error motion that was predicted for the final design was less than 0.5 nm (STD), which gives a margin of two compared to the specification. Using DEB during the design process of the rotor greatly helped to identify the performance limiting components and disturbances.

A magnetically levitated platform has been realized, with a measured performance around 0.5 nm (RMS up to 1000 Hz) when not rotating. Because a suitable motor was not yet available during the realization of the system, the performance could not be evaluated with a rotating system. Since the specification for the Asynchronous Radial Error Motion (AREM) is 1 nm (RMS), the system has a budget for non-synchronous disturbances introduced by rotation of about 0.5 nm (RMS), which is a promising result.

Curriculum Vitae

Leon Jabben (1974) received in 1999 his M.S. degree in Mechanical Engineering at the Delft University of Technology. During his studies he did an internship in 1998 at the nuclear research facility (CERN) in Geneva. Subject of his M.S. final project was the control design for a part of an optical instrument in a weather satellite. The project was performed at the company CSEM in Neuchâtel. In 2000 he started his Ph.D. project on the system design of an ultra-precise positioned rotor in the group of Advanced Mechatronics at the Delft University of Technology. The goal of this research was to achieve the specifications of the mastering process for the next generation optical disks with magnetic bearing technology. In the scope of this research, he did an internship in 2004 at Philips Applied Technologies in San Jose (CA, USA). In 2005 he worked as Control Engineer at the same company in Eindhoven. From 2006 onwards he works as Systems and Control engineer at TNO Industry and Technology in Delft, for Vision Dynamics (Eindhoven).